Bank erosion hotspots in the Msimbazi River, Tanzania

Assessment of Catchment Changes

Master Thesis

Quinten Oostwegel

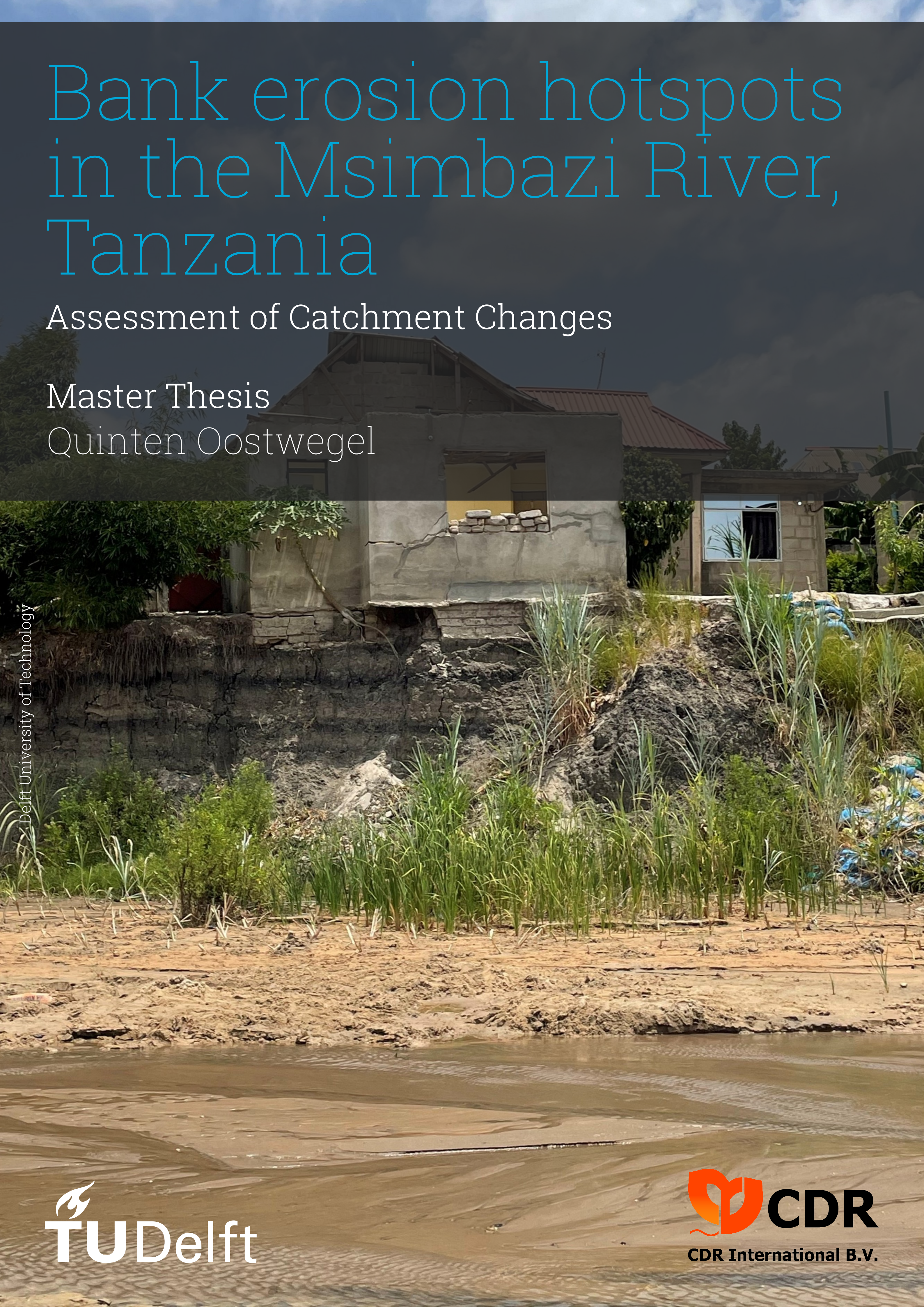

Delft University of Technology

CDR International B.V.

This page is intentionally left blank

Bank erosion hotspots in the Msimbazi River, Tanzania

Assessment of Catchment Changes

by

Quinten Oostwegel

to obtain the degree of Master of Science at the Delft University of Technology,
to be defended publicly on June 5th, 2025 at 9:30 AM.

Head of committee:	Dr. ir. A. (Astrid) Blom	Delft University of Technology
Daily supervisor:	Dr. ir. K.B.J. (Kieran) Dunne	Delft University of Technology
Daily supervisor:	MSc. B.M.C. (Bram) Loef	CDR International B.V.
Committee member:	Prof. Dr. ir. N.C. (Nick) van de Giesen	Delft University of Technology

Project Duration:	November, 2024 - May, 2025
Faculty:	Faculty of Civil Engineering and Geosciences, Delft
Student number:	4812328

Cover: Site visit upper middle Msimbazi Basin, February 2025

Preface

Dear reader,

In front of you lies my thesis titled: “Bank Erosion Hotspots in the Msimbazi River, Tanzania”. As a young boy, I was fascinated by the enormous size of our shared planet. And of course, being from the generation in which climate and sustainability became hot topics, I was raised with the idea that we should leave behind a better world for our children than the one we inherited. As I grew older, it became clear what role I could play in that global challenge.

When I asked myself why I am so privileged to have been born in the Netherlands, with a functioning education system and plenty of opportunities for personal growth, I realized that the foundation of our Dutch society is well organized. At home, I had a tap supplying clean drinking water to my family. I never questioned whether our house might flood or whether we’d be able to evacuate in time. We have roads, stable buildings, and so many things that seem obvious.

But imagine living in a place on this planet where none of this is guaranteed. Would you be able to follow a full-time study if you had to walk several miles just to fetch drinking water? Could you create economic opportunities for your community if everyone had to leave their homes multiple times a year due to flooding?

With these questions in mind, I discovered the field of Civil Engineering. It is a discipline that not only encourages reflection on such issues but also provides the tools to take meaningful action and contribute to the greater good. This path led me to study Hydraulic Engineering, and for my thesis, I focused on the people living along the highly dynamic Msimbazi River. Not because I have the power to directly help them, but because I believe that science allows us to understand why these communities are so vulnerable. It is through this understanding that action becomes possible.

I would like to express my gratitude to Kieran Dunne, for his continued support and enthusiasm. Without your understanding and feedback this experience would not have been possible. The same applies to Bram Loef (CDR-International) whose practical guidance and local insight grounded the study. I also mean to thank Astrid Blom and Nick van de Giesen for their valuable guidance, engagement, and support in improving the scientific quality of this thesis.

I am grateful to the Lamminga Fund and FAST Fund for their generous support, which enabled my travel to Tanzania and fieldwork along the Msimbazi River, greatly enhancing the research.

During this trip, I received great support from Bas van de Sande and Jenny Pronker (CDR International), whose guidance and availability made the research trip both meaningful and enjoyable. I also thank Eng. Mussa Natti (World Bank) for facilitating connections with local stakeholders and providing insights into institutional efforts addressing changes in the Msimbazi River. Furthermore, I appreciate the contributions of Prof. Joel Norbert and Dr. Augustina Alexander (University of Dar es Salaam), Iddy Chazua, Amour Nyalusi, and Asha Mustapher (OpenMap Development Tanzania), Eng. Nanai (President’s Office – Regional Administration and Local Government), Mr. Alfred Mbyopo and Eng. Benjamin Mboya (Dar es Salaam City Council), Hamisi Msangi and Peterson Olang’u (Tanzania Railway Corporation), and drivers Frank and Tumain, whose local knowledge was essential for this research.

Last, but certainly not least, I want to thank my family and friends. For all those discussions and moments of support and laughter. You not only stood by me during this thesis project, but throughout my whole academic journey. Your encouragement, as well as the moments of joy and distraction you offered when I needed them most, have meant more than I can express.

Quinten Oostwegel
Amsterdam, May 2025

Abstract

In rapidly growing urban areas, river dynamics have become major hazards, endangering vulnerable populations and their environments. The Msimbazi River Basin in Dar es Salaam, Tanzania, demonstrates these challenges, where unplanned urban expansion, deforestation, and infrastructure development have influenced river morphodynamics. Although prior studies have addressed flood risks, sedimentation, and bank erosion, an understanding of the river's migration patterns, widening trends, and key drivers at the full catchment scale has been lacking. This research applies a descriptive approach combining manual riverbank tracking from satellite imagery, identification of potential morphological change drivers, and hotspot mapping based on hazard severity and exposure susceptibility. From 2007 to 2024, the Msimbazi River experienced significant lateral migration and localized widening, with notable episodes of instability after 2017. These changes are primarily driven by land cover transformations, such as urbanization and deforestation, which have led to gradual shifts in river morphology, rather than being the result of changing precipitation patterns. In contrast, abrupt and localized changes, particularly after 2017, appear to be associated with infrastructural developments like the Standard Gauge Railway, as well as the coincidence of the El Niño phase with the cyclone season, which contributed to elongating the wet seasons. Findings reveal that river migration rates and widening trends fluctuate considerably, often doubling or tripling during periods of rapid change, with the highest vulnerability observed in the upper catchment. By identifying zones where hazard severity and exposure intersect, this study provides a framework for prioritizing mitigation in the Msimbazi Basin and other urban rivers in rapidly developing regions.

Contents

Nomenclature

Abbreviations

Abbreviation	Definition
ArcGIS	Geographic Information System software
CDF	Cumulative Distribution Function
CHIRPS	Climate Hazards Group InfraRed Precipitation with Station data
DSAS	Digital Shoreline Analysis System
ECMWF	European Centre for Medium-Range Weather Forecasts
ERA5	Fifth-generation ECMWF atmospheric reanalysis of the global climate
GEE	Google Earth Engine
GPM	Global Precipitation Measurement Mission
GSMaP	Global Satellite Mapping of Precipitation
HEC-HMS	Hydrologic Engineering Center – Hydrologic Modeling System
HRU	Hydrological Response Unit
IMERG	Integrated Multi-satellite Retrievals for GPM
IQR	Inter-Quartile Range
ITCZ	Intertropical Convergence Zone
KS	Kolmogorov-Smirnov (statistical test)
LB	Lower Basin
LMB	Lower Middle Basin
LRR	Linear Regression Rate
LULC	Land Use and Land Cover
MNDWI	Modified Normalized Difference Water Index
NASA	National Aeronautics and Space Administration
NDWI	Normalized Difference Water Index
NMR	Normalised Migration Rate
POT	Peak over Threshold
SAR	Synthetic Aperture Radar
SGR	Standard Gauge Railway
SWIR	Short-Wave Infrared
TAHMO	Trans-African Hydro-Meteorological Observatory
ToC	Time of Concentration
UB	Upper Basin
UMB	Upper Middle Basin
WLR	Weighted Linear Regression

1

Introduction

1.1. Research problem and objective

Flooding in Dar es Salaam, Tanzania's largest city, has showed the urgent need for enhanced flood resilience, particularly following an early 2018 disaster that claimed 15 lives and severely damaged critical infrastructure, including roads, bridges, and public services. Over three million residents, many living in informal settlements near the Msimbazi River, were left especially vulnerable, prevailing the government to declare a state of emergency. Jangwani, an unplanned neighbourhood along the Msimbazi River, was among the hardest hit areas. In response to the widespread damages, the Tanzanian government, supported by the World Bank and other development partners, has been working with local communities to develop a more resilient river basin and better manage future flood risks (UNDRR, 2018).

The Msimbazi River originates in the Pugu Hills and flows into the Indian Ocean. Along its course, it passes through areas that were formerly agricultural land or forest. These have gradually been transformed into predominantly informal settlements. Today, an estimated 70% of development within the basin is unplanned. This leaves large parts of the area highly vulnerable to flood-related hazards such as riverbank erosion (Izdori et al., 2022; Kazi, 2019; Nabeta, 2022) In fact, over 80% of the riverbanks in the lower Msimbazi Basin are classified as being at "high" to "critical" risk of erosion, endangering local populations (Alexander et al., 2024).

Despite ongoing efforts to mitigate these risks, including the provision of alternative land and the enforcement of evictions, residents continue to settle in erosion-prone areas (Kironde, 2016). Informal settlements within the basin, such as those in Jangwani, are directly exposed to frequent flash floods, heavy sedimentation, and riverbank erosion, all of which are intensified by inadequate disaster risk management strategies (Kazi, 2019; Machiwa et al., 2021; Mkilima, 2021). These interrelated issues present significant challenges for managing the highly dynamic Msimbazi River system, where upstream erosion contributes to heavy downstream sedimentation, leading to a shifting river course, observed channel widening, and the development of steep, unstable banks, alterations that significantly increase flood risks (Kazi, 2019). Figure 1.2 shows an example of the impact of the Msimbazi river dynamics, the river shifted its course, which in this specific case resulted in a meander around the existing bridge.

Recognizing these threats, local authorities and the World Bank launched the Msimbazi Basin Development Program in 2022, aimed at strengthening flood resilience, improving discharge capacity, and promoting integrated urban development within the flood-prone basin. The project focuses on enhancing critical infrastructure, restoring degraded land, and preventing further encroachment into flood-prone areas, with erosion control forming a crucial sub-component of this initiative (World Bank Group, 2024)

Despite extensive research on flooding, sedimentation, and bank erosion along the Msimbazi River in Dar es Salaam, considerable uncertainty persists regarding the primary drivers of its rapid morphodynamic changes and the river's likely future trajectory. Fundamental questions remain unresolved: How is the river truly evolving over time? What are the underlying causes of these changes? And, when institutions implement mitigation strategies, how well is information on which areas are most at risk and where interventions will be most effective in mitigating the risks?

This research aims to provide a deeper understanding of the catchment changes driving the rapid morphological evolution of the Msimbazi River. To effectively mitigate impacts such as bank erosion, it is crucial to first understand how and why the river itself is changing. Therefore, this study focuses on channel migration and potential widening or narrowing of the river. Additionally, based on observed channel migration patterns, critical areas within the river basin will be identified to guide mitigation strategies and prioritize intervention efforts.

Given the Msimbazi River's relatively short length of 32 kilometers and its basin area of approximately 289 square kilometers (Kironde, 2016), this research will cover the entire basin to ensure a comprehensive analysis of the river's dynamics and associated risks. While the river has multiple tributaries, as shown in Figure 1.3, this study focuses on the main channel.

1.2. Research questions

To achieve the objective of this study, in light of the described scope, the research questions are:

1. *How is the Msimbazi River evolving in terms of channel migration and morphological changes?*
2. *What are the key drivers behind the morphodynamic changes occurring in the Msimbazi River?*
3. *Where are the critical erosion hotspots along the Msimbazi River?*

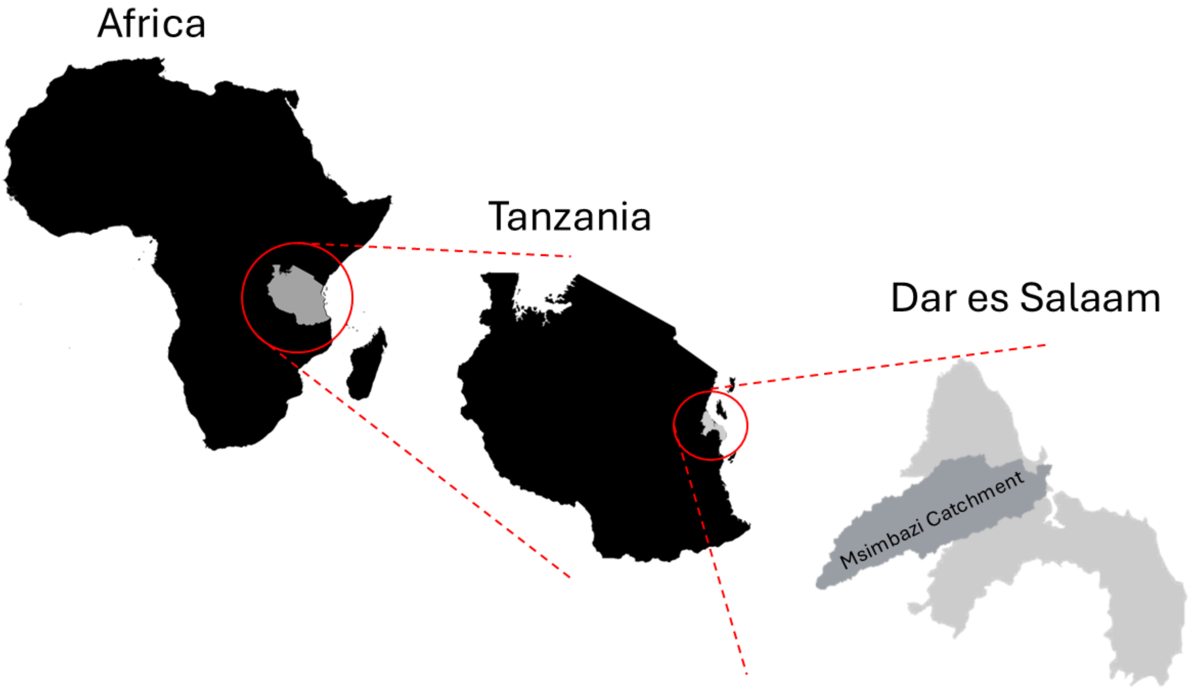

Figure 1.1: Location of the Msimbazi River Basin within Africa, Tanzania and the city of Dar es Salaam (van de Sande & Laboyrie, 2021)

Figure 1.2: The impact of the Msimabazi river dynamics are shown. The river shifted its course, which in this specific case resulted in a meander around the existing bridge located in the Upper Middle Basin.

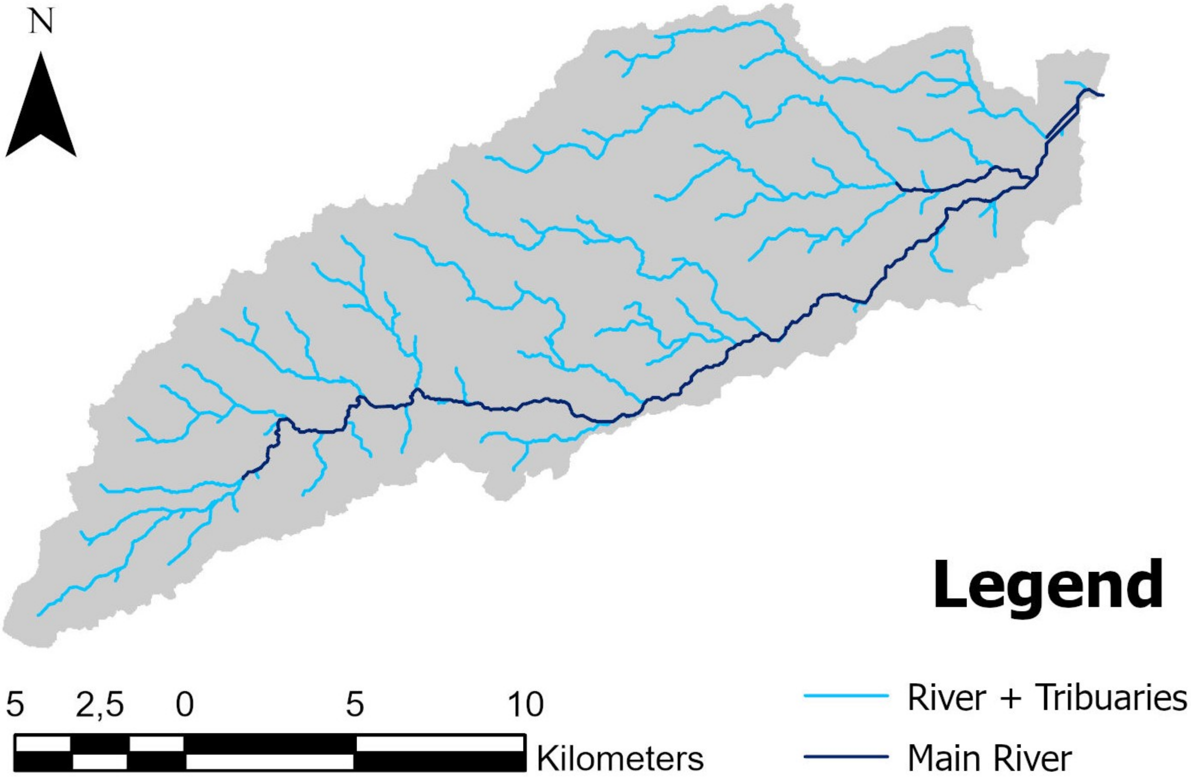

Figure 1.3: Main Msimbazi river and its tributaries

2

Research method

To address the research questions, a stepwise methodology is adopted, focusing on three key components: (1) analyzing river migration patterns, (2) quantifying catchment changes, and (3) developing erosion hotspot maps to guide future mitigation strategies.

2.1. Assessment of river migration and widening patterns

The first step in analyzing river migration is determining the river's position over time. This is achieved by detecting the riverbanks and deriving the centerline from satellite imagery obtained from Landsat 4-9 (1982–Present) and Sentinel-2 (2015–Present) within Google Earth Engine (GEE). Landsat imagery has a resolution of 30×30 meters, while Sentinel-2 provides higher-resolution images at 10×10 meters. The centerline serves as a representative indicator of the river's course, allowing for a systematic comparison of its position across different time periods (Xia et al., 2021).

Ideally, the detection of water bodies and subsequent extraction of riverbanks and centerlines would be automated using remote sensing techniques such as the Modified Normalized Difference Water Index (MNDWI), Normalized Difference Water Index (NDWI), or Synthetic Aperture Radar (SAR). These methodologies are detailed in Appendix A. However, the Msimbazi River's relatively narrow width, ranging from 4-15 meters in the early 2000s to its current 30–70 meters, poses a challenge. The spatial resolution of available satellite imagery is insufficient for reliable automated extraction, limiting the applicability of these methods.

Instead, riverbanks are manually delineated by visually interpreting satellite imagery, tracing the riverbanks based on distinguishable reflectance differences between water and land (Figure 2.1). Riverbanks were manually delineated at a scale of 1:17,500, providing an optimal balance between detail and accuracy. The centerline was then derived as the exact midline between the two detected banks, ensuring a balanced representation of the river's central flow path. To reduce errors caused by temporary water level fluctuations, only satellite images captured outside the time of concentration (ToC) period were used (Iowa Organization of Natural Resources, 2023). More details on the ToC the centerline detection procedure are provided in Appendix B and Appendix C, respectively.

To quantify the uncertainty in the centerline position, the error propagation formula for averaging independent measurements is applied (Ku, 1966). This formula is used because the river centerline is derived as the midline between two independently determined bankline positions. Since these positions are derived from the same satellite image, the error in each measurement contributes evenly to the overall uncertainty of the centerline. The formula for error propagation allows us to estimate how these independent errors affect the final result.

In this case, the uncertainty in the centerline position is calculated by considering the standard deviation (σ_X) of the independently digitized bankline positions. The uncertainty (σ_C) in the centerline is given by Equation 2.1.

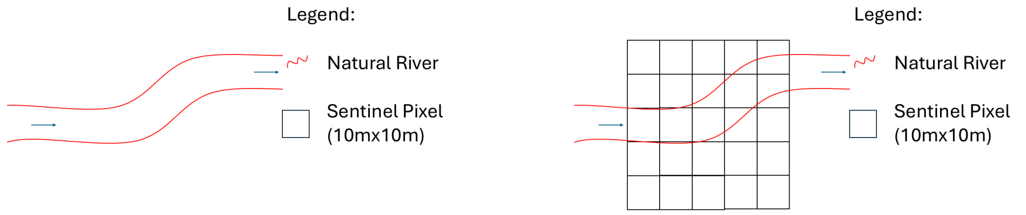

(a) Step 1: The river is located somewhere within the wider catchment area. In this case a small stretch of the river is considered.

(b) Step 2: A satellite image of the catchment is obtained from Landsat or Sentinel. In this case the image is a Sentinel image which has a 10 x 10 meter resolution.

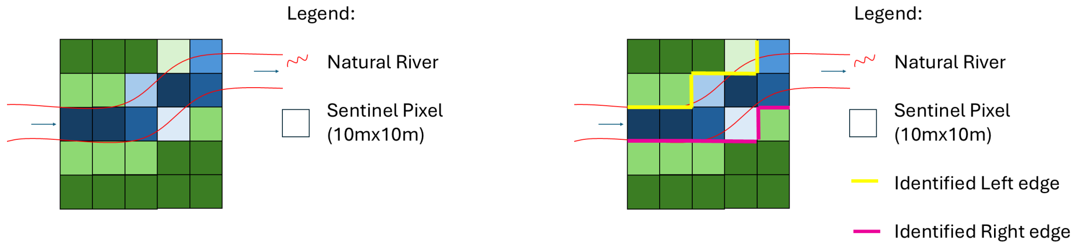

(c) Step 3: Band selection and image enhancement make the river water surface identifiable. See Appendix C (Figure C.3) for further explanation of this process.

(d) Step 4: The edges of the water surface are delineated, aiding in centerline identification. See Appendix C for further explanation.

Figure 2.1: Stepwise method for detecting river water cover boundaries using satellite imagery.

Once the banklines and centerlines are delineated, the next step is to assess their migration over time. River migration refers to the lateral displacement of the river channel over time, while the migration rate quantifies the speed of this movement, typically expressed in meters per year (m/yr). To calculate these rates, the Digital Shoreline Analysis System (DSAS) is used, a tool designed to evaluate shoreline dynamics, which can also be applied to riverbank or centerline analysis. DSAS enables the calculation of change rates across a series of riverbank or centerline positions over multiple time periods (see Figure 2.2) (Himmelstoss et al., 2021). Initially, river positions from different years are imported into the tool. A baseline is then established, with transects created at 15-meter intervals along the Msimbazi River. The rate of change for each transect is computed using the Weighted Linear Regression (WLR) technique (Tha et al., 2022).

Along with the detection of the centerlines, the width of the identified channels was also recorded. Consequently, the temporal variations in channel width and their rates of change will also be analyzed.

$$\sigma_C = \frac{\sigma_X}{\sqrt{2}} \tag{2.1}$$

In this study, migration and widening rates are compared across different temporal extents. As described by Eggert et al. (2015), shorter time periods tend to emphasize more extreme values, as such variations are less likely to be averaged out compared to longer observation periods. While de Vries (1975) defines long-term river morphological change as occurring over several decades to centuries, this study adopts a more pragmatic distinction between short- and long-term for the sake of analytical clarity and readability. Here, long-term refers to the full duration for which satellite imagery is available, spanning from 2007 to 2024. In contrast, short-term refers to sub-periods within that timeframe, typically ranging from 2 to 5 years, depending on the specific analysis.

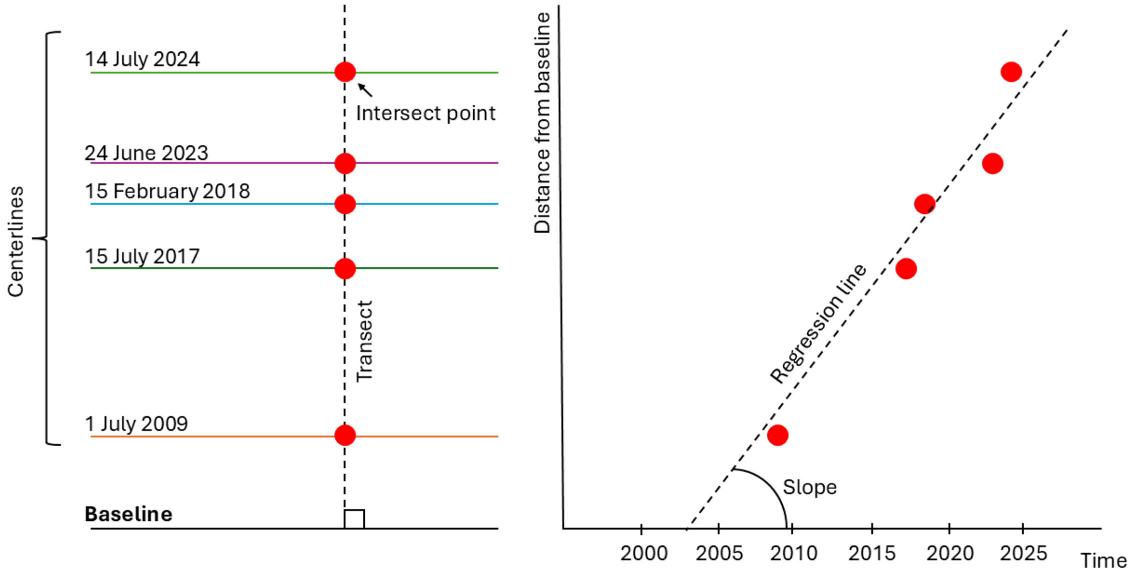

Figure 2.2: The left side of the figure shows river centerlines delineated for multiple dates, alongside a predefined baseline that follows the river's general course and consists of known coordinates. Perpendicular to this baseline, transects are generated at 15-meter intervals. The intersection between each transect and a centerline provides a distance from the baseline at a specific point in time. In the right side of the figure these distances are plotted against time. By fitting a regression line to these points, the slope represents the rate of lateral channel movement, i.e., the migration rate (Himmelstoss et al., 2021). For a detailed explanation of the DSAS methodology, see Appendix E.

2.2. Identification and quantification of catchment changes

The key factors influencing the morphodynamic changes observed in the Msimbazi River include precipitation variations, landcover changes, urbanization, deforestation, and infrastructure development.

Changes in precipitation patterns, such as increased rainfall, altered rainfall duration, or more frequent and intense extreme events, could significantly impact the river's dynamics (Redolfi et al., 2023). For this analysis, two years were considered particularly important: 2007 and 2018. The year 2007 is notable as it marks the first year the Msimbazi River became visible in satellite imagery. The year 2018 was selected because it corresponds with the period when significant changes in the river's width were observed, particularly in the early months.

The analysis compared precipitation data from before and after 2007 and 2018 to identify any significant changes that could explain the river's morphological shifts. A Kolmogorov-Smirnov (KS) test was used to assess statistical significance, as it does not assume normality of the data. This non-parametric test compares the distributions of precipitation data across the two periods to determine if the differences are statistically significant (Massey Jr, 1951).

In addition to precipitation, landcover changes are an important factor influencing river dynamics, as they directly affect runoff and river discharge. Changes in the landscape, such as increased urbanization or deforestation, can reduce the land's capacity to absorb water, leading to higher runoff and potentially increased erosion (U.S. Geological Survey, 2019). Runoff is the portion of precipitation that does not infiltrate the soil but instead flows over the land surface and eventually reaches rivers and streams (James & Lecce, 2013; Kayitesi et al., 2022; Tang & Lettenmaier, 2012; Wohl, 2004).

Landcover changes were quantified using data from the Institute of Resource Assessment (IRA) at the University of Dar es Salaam and the European Space Agency (ESA).

Urbanization and deforestation are two major landcover changes that significantly influence river morphology. Urbanization, marked by the expansion of built-up areas, increases the total paved surface, leading to higher runoff and flood risks. Deforestation, on the other hand, reduces the vegetation that protects the soil. This decreases the area's ability to absorb water, contributing to increased erosion and altered water flow in the catchment (Li et al., 2024).

The extent of urbanization was quantified by analyzing landcover change data combined with building block data from OpenMap Development Tanzania. This data, which includes detailed information on the location, shape, and size of individual buildings, allowed for tracking the growth of built-up areas over time. Deforestation was assessed using similar landcover change data, enabling the identification of areas where vegetation had been cleared or degraded. Both urbanization and deforestation influence the catchment's runoff, which in turn affects the river's dynamics. Therefore, changes in runoff are also assessed.

Human interventions, such as infrastructure development, also play a significant role in shaping river dynamics. A notable example in the Msimbazi catchment is the construction of the Standard Gauge Railway (SGR) in early 2018, located upstream (TanzaniaInvest, 2024). This development was identified during fieldwork as a potential influence on river morphology, particularly regarding sedimentation and water flow. To assess its impact, a combination of satellite image analysis, field observations, and a review of environmental reports related to the railway construction was conducted.

2.3. Development of erosion hotspot maps

Migration rates of river channels can vary widely, often differing by several orders of magnitude. In certain regions, these rates may exceed tens or even hundreds of meters annually (Langhorst & Pavelsky, 2023). Given that a significant portion of the global population resides near rivers, such high rates of bank erosion present substantial risks to nearby infrastructure and human settlements (Noh et al., 2024). The Msimbazi river is no exception.

In this study, riverbank erosion hotspots are defined in terms of vulnerability, which is the result of exposure and hazard. Dilley et al. (2005) define a ”hotspot” as a specific area or region that is at relatively high risk of loss from one or more natural hazards. However, this study focuses specifically on vulnerability, rather than risk, because risk inherently involves the consideration of potential consequences, such as economic losses or other impacts, which are outside the scope of this research. Vulnerability, on the other hand, refers to the degree of susceptibility of people, communities, and assets to the impacts of hazards. A hazard is any event or process that can cause harm, such as erosion, while exposure refers to the presence of people, infrastructure, or assets in areas prone to such hazards (Dilley et al., 2005; Stone et al., 2011). Therefore, vulnerability to riverbank erosion is determined by both the degree of exposure to erosion-prone areas and the severity of the hazard itself (Climate Investment Funds, 2023).

The first step in identifying a hotspot is to determine both the location and the magnitude of the hazard. In this study, the hazard is defined as river migration or river widening.

Since a hotspot reflects the vulnerability of a location to future hazardous events, the location of the hazard is taken as the most recent position of the river, which, based on available data, corresponds to the location of the Msimbazi River in May 2024.

The magnitude of the hazard is represented by the migration rate or widening rate of the river. To distinguish between long-term patterns, which are primarily driven by gradual catchment-scale changes, and short-term responses of the river system to sudden events (e.g., abrupt landcover changes or extreme rainfall events), both long-term (2007-2024) and short-term (2020-2024) rates for both migration and widening are considered in the hotspot analysis (Tha et al., 2022).

This approach produces four distinct hotspot maps: one illustrating vulnerability to long-term hazards (2007–2024), based on gradual river migration rates; one capturing vulnerability to short-term hazards (2020–2024), reflecting event-driven river responses; and two additional maps representing vulnerability to long-term and short-term river widening rates, respectively.

The hazard will be assigned a severity value value between 1 and 5, where 1 indicates minor severity,

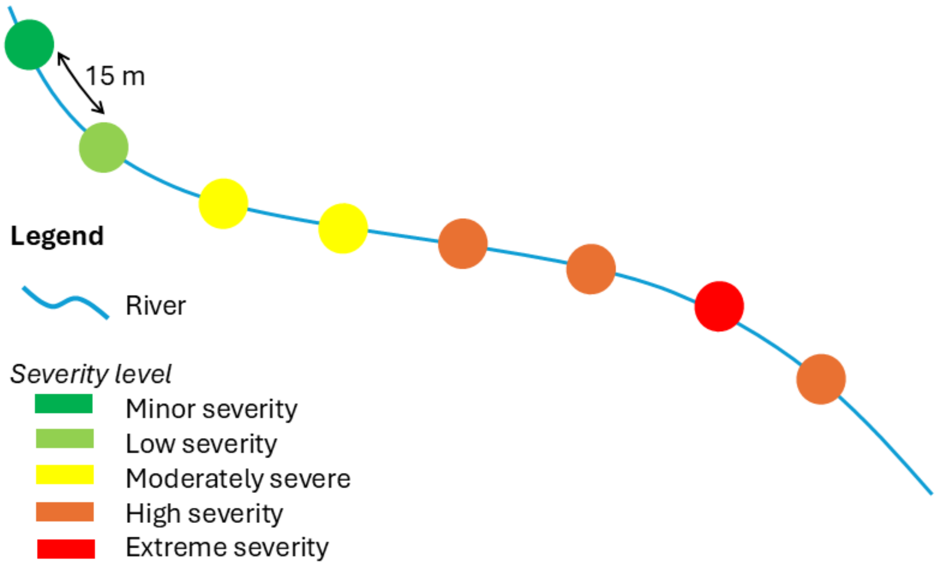

Figure 2.3: Because both migration rates and widening rates have been calculated at 15 meter intervals along the river, these values can be stored at corresponding point locations. The rates are classified by severity using the Natural Breaks (Jenks) method, which groups similar values together and identifies class boundaries based on natural gaps in the data. Identifying where along the river certain severity levels occur allows for the assessment of locational vulnerability.

3 corresponds to a moderately severe hazard and 5 represents an extreme severe hazard. In terms of migration rates, the distribution of migration rates is divided into 5 equal intervals where the smaller rates correspond to the minor severe hazard and the largest rates to the extremely severe hazard. Similarly, for river widening, narrowing and stable trends are assigned very low severity and extreme widening rates correspond to very high severity. As is shown in Figure 2.3.

It is important to note that both hazard severity and, by extension, vulnerability are assessed relative to the behavior of the specific river system being studied. In this analysis, migration rates, used as an indicator of hazard severity, are classified using the Natural Breaks (Jenks) method. This classification technique groups similar values together and places class boundaries where there are relatively large jumps in the data. The goal is to highlight meaningful patterns by maximizing the similarity within each class while emphasizing the differences between them (de Smith et al., 2018). This approach helps to identify the areas experiencing the most severe river migration within the Msimbazi system.

Although the hazard is defined for two different timeframes, Long-term (2007-2024) and short-term (2020-2024), the exposure remains constant across both analyses. Exposure refers to the objects within the catchment area that are potentially affected by the hazard (IPCC, 2014). Since the river has an average width of approximately 50 meters (ranging between 30 and 70 meters), the susceptible zone is defined as a buffer of roughly 10 times the river width, resulting in a zone of about 500 meters on either side of the river (Rinaldi et al., 2013). This zone represents the area susceptible to potential river migration or widening.

The first step in exposure mapping involves identifying what lies within this susceptible area that could be impacted by river migration, such as residential buildings, critical infrastructure, and other assets (Stone et al., 2011; UNISDR, 2009). The aim is to spatially quantify where these elements are located.

The second step concerns susceptibility, that is, how sensitive these exposed elements are to harm. Stone et al. (2011) define susceptibility as "the propensity of the people, property or other receptors to experience harm." One intuitive assumption is that proximity to the river plays a key role: the closer an object (e.g. a house) is to the migrating river, the more susceptible it is to erosion or damage. Therefore, distance to the river is adopted as a metric to quantify susceptibility within the exposed area. Elevation, by contrast, was not included as a factor in this analysis. Erosion processes can undermine high riverbanks irrespective of their elevation relative to the channel. Field observations confirmed that even buildings situated more than 12 meters above the river can become destabilized when the supporting bank material is eroded. This is particularly relevant given that the riverbanks consist of alluvium which is highly susceptible to planar erosion, as supported by both field evidence and the findings of Van Camp et al. (2014). Therefore, susceptibility was quantified using distance to the river, as elevation does not meaningfully reduce the vulnerability of erosion-related damage in this setting.

Figure 2.4 illustrates the susceptibility of buildings, which is also a value between 1 and 5. Where 1 equals minor susceptibility and 5 is equal to extremely susceptible. This same approach is applied to other objects within the defined exposed zone. As shown in the figure, some objects are situated near the boundaries of the distance classes. To ensure consistency in the analysis, the centroid (geometric center) of each object is used to assign it to a specific susceptibility class.

In this study, the objects considered within the exposed area are buildings and infrastructure, such as roads and railways. Research by Tha et al. (2022) has shown that exposure mapping can be based on landcover and population density. However, in the case of the Msimbazi River, which flows predominantly through a densely populated area, this approach may not provide the most informative results. To distinguish more vulnerable areas from less vulnerable ones within this overall high-populated catchment, buildings and infrastructure are considered as an objective metric.

Once hazard severity and exposure susceptibility have been mapped, spatial hotspots, areas with the highest vulnerability, can be identified. These vulnerability values are derived using the relationship defined in Equation 2.2, where vulnerability is a function of both hazard severity (quantified by the rate of river migration or widening) and exposure susceptibility (measured as the distance of exposed elements to the river).

$$\text{Hotspot (Vulnerability)} = \text{Hazard (Severity)} \times \text{Exposure (Susceptibility)} \tag{2.2}$$

Equation 2.2 aligns with established risk assessment frameworks in which risk is defined as the product of hazard, exposure, and vulnerability (IPCC, 2014; UNDRR, 2017; Wisner et al., 2004). As emphasized by Turner et al. (2003), vulnerability depends not only on exposure but also on the sensitivity and resilience of the affected system. Since resilience is not yet quantified in this study due to data limitations, the resulting vulnerability map should be seen as a proxy, useful for informing initial mitigation strategies, with further refinement possible as more data becomes available.

The practical implementation of vulnerability mapping involves combining object susceptibility with hazard severity. This is achieved using the Near tool in ArcGIS (Figure 2.5), which calculates the nearest distance and direction between points (Esri, 2024). In this case, the origin point is a feature within the exposed area (e.g., a building), and the target point is a location along the river where a migration rate has been recorded. This method not only identifies the closest hazard source but also attributes its migration rate to the exposed object. This spatial linkage enables the calculation of vulnerability and, subsequently, the delineation of hotspot zones.

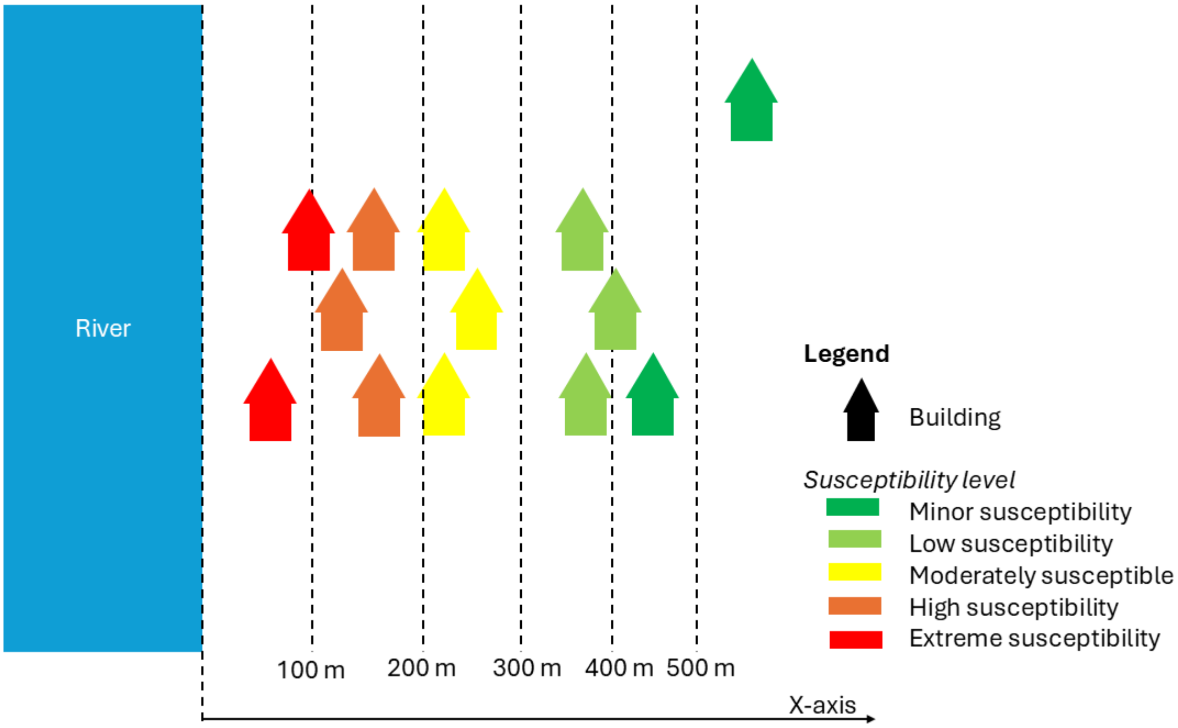

Figure 2.4: Susceptibility of objects within the exposed area, quantified by their distance to the river. This measure of susceptibility is used to determine locational vulnerability.

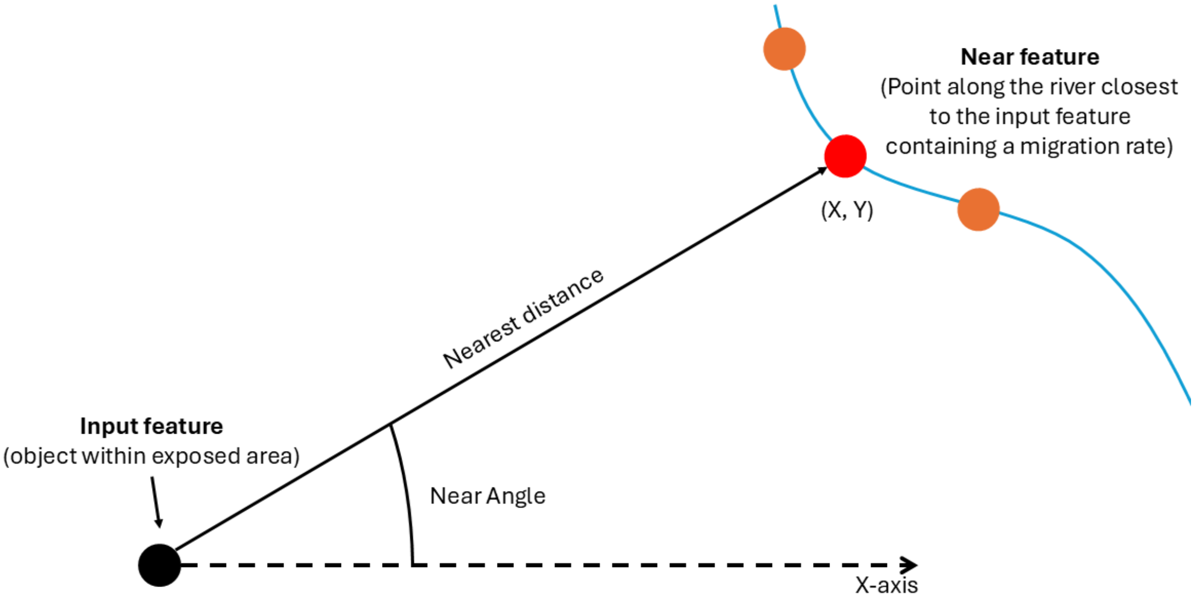

Figure 2.5: Schematization of ArcGIS's Near tool. The black dot represents an object located within the exposed area. The tool calculates the nearest distance from this object to the river, thereby determining its susceptibility. In addition, the severity of the nearest hazard point along the river is identified. By assigning this severity value to the object, it is provided with all the necessary information to compute its vulnerability using Equation 2.2 (Esri, 2024).

3

The study area

The Msimbazi River flows through Dar es Salaam, Tanzania's commercial capital, where rapid urbanization has dramatically reshaped the landscape (Izdori et al., 2022; Kazi, 2019; Shibayama & Esteban, 2022; van de Sande & Laboyrie, 2021). With one of the fastest-growing populations in the world, Dar es Salaam is experiencing unprecedented urban expansion, contributing to significant environmental and infrastructural challenges (Kazi, 2019). The Msimbazi Basin is home to 27% of Dar es Salaam's population (Kazi, 2019; Kironde, 2016). The most severe flooding occurs in the Lower and Lower Middle Basins, which is why the World Bank-led Msimbazi Development Program has primarily focused on mitigation efforts in these areas.

Land use and settlement patterns vary across the Msimbazi Basin, with distinct zones identified throughout the area (see Figure 3.1). In the Upper Basin, peri-urban expansion is rapidly converting agricultural land and forests into residential areas. The Upper Middle Basin is more densely populated and highly urbanized, while the Lower Middle Basin has also seen substantial urban development, with much of its infrastructure already consolidated (Alexander et al., 2024; Kazi, 2019). The Lower Basin, covering 400 hectares, is characterized by floodplains, mangrove forests in the tidal zone near the river mouth, wetlands, and sandy plains formed by sediment deposition after flash floods (Kazi, 2019; Kironde, 2016). Despite the high flood risk in these areas, unplanned informal settlements continue to spread across the floodplains, showing the basin's vulnerability (Kazi, 2019).

This research distinguishes between several sub-basins within the overall catchment to facilitate localized analyses. Figure 3.1 illustrates the spatial subdivision of the catchment area. In general, a river system evolves from steep upper basins to flatter lower basins. In the upper basins, runoff is generated from precipitation, and sediment is mobilized through active erosion. Further downstream, sediment is transported, stored, and eventually deposited in lowland floodplains or deltas. As slope and energy decrease, the dominant processes shift accordingly, with each sub-basin playing a distinct role in shaping the river's hydrological and morphological characteristics (Charlton, 2008; Leopold et al., 1995; Mackin, 1948).

Satellite imagery, as presented in Figures 3.2 to 3.7, clearly illustrates that the river is undergoing significant transformation. A longitudinal comparison of these Google Earth images shows the exact same stretch of the river. The river, once a relatively narrow stream (as shown in Figure 3.2), has progressively claimed more space over the years.

In addition to this gradual expansion, the river appears to have responded to abrupt events. This is particularly evident when comparing Figure 3.4 (January 2018) with Figure 3.5 (March 2018). The extent of change observed within a three-month period, during which the channel width nearly tripled, suggests a sudden and substantial shift in river morphology. Such rapid changes, occurring over just three months, go well beyond the gradual alterations typically seen in natural river migration, which generally unfolds over decades to centuries, particularly in urban alluvial systems (de Vries, 1975).

In response, the Msimbazi Development Program has initiated various projects to mitigate the impacts of these dynamics.

One of the biggest problems for research in East Africa is the lack of good, trustworthy data. In many parts of the continent, poor data quality makes it hard to build useful knowledge and to support decision-making with solid evidence (Kinyondo & Pelizzo, 2018). This is especially true for climate data, which is often difficult to access or simply not available (Dinku, 2019). Unfortunately, the Msimbazi catchment is no exception.

Field observations conducted in February 2025, aimed at gathering data, provided insight into the current geomorphological and anthropogenic conditions along the river. In the Upper Basin, recent reforestation efforts were evident, characterized by young vegetation and riverbanks reinforced with large boulders (see Figure 3.8), indicating a degree of stabilization. Progressing downstream toward the upper Middle Basin, the morphology of the banks shifted, from gradually sloping, protected banks to steep, unprotected banks where residential structures are located dangerously close to the river's edge (see Figure 3.9a). Elevation does not appear to protect these buildings from erosion, as the dominant process is clearly bank undermining. This downstream shift coincides with the start of more urbanized areas, where solid waste begins to appear along the banks.

Further downstream, point bars and cut banks become increasingly distinguishable. The point bars are characterized by gently sloping profiles, whereas the cut banks show pronounced vertical erosion. In the Lower Middle Basin, evidence was observed of community-led engineering interventions: local residents have constructed embankments to mitigate flood risks. The elevation of these manually constructed banks ranges from approximately 1–3 meters in the Lower Middle Basin to as high as 8–10 meters in the Lower Basin. The Lower Basin also showed sand mining activities within the channel, see Figure 3.9

Along the full length of the river, the bank material mainly consists of coarse to very coarse sand. A downstream trend is observed in which sediment angularity decreases and grain sorting improves, reflecting typical fluvial sorting processes (Knighton, 2014). Appendix D provides more detailed information about the findings during the fieldwork.

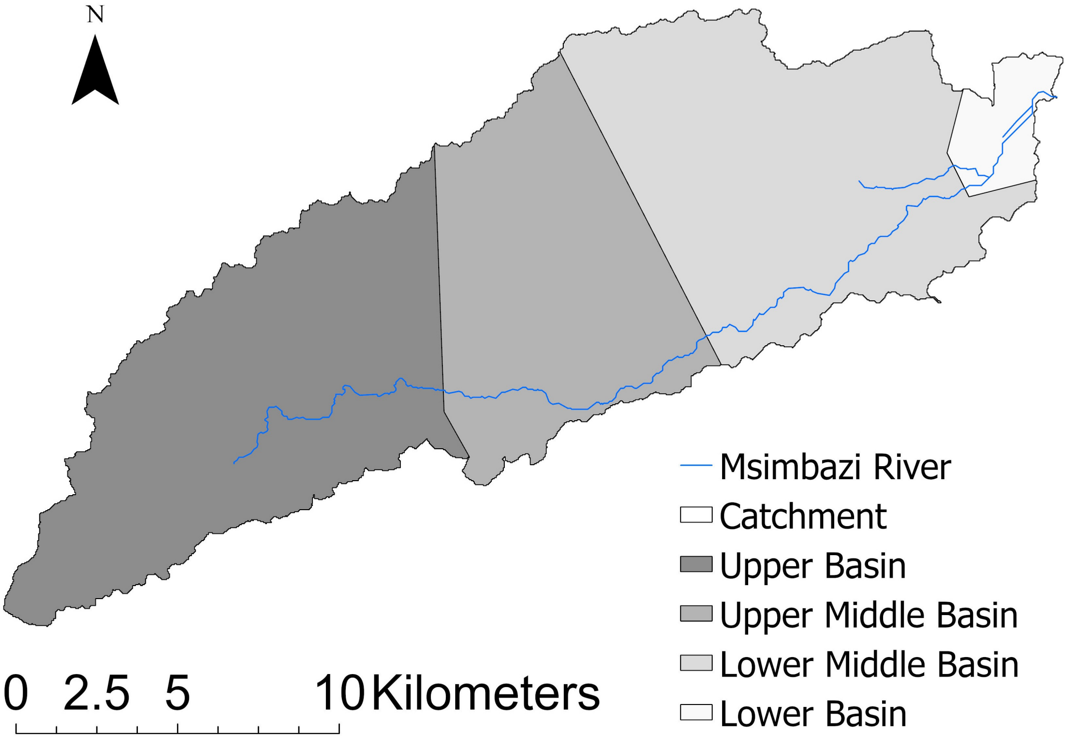

Figure 3.1: Map of sub-basins within the Msimbazi River Basin (Kazi, 2019).

Figure 3.2: Observed river morphology on May 8, 2013. The Msimbazi River appears as a narrow stream, making it barely distinguishable in the satellite imagery.

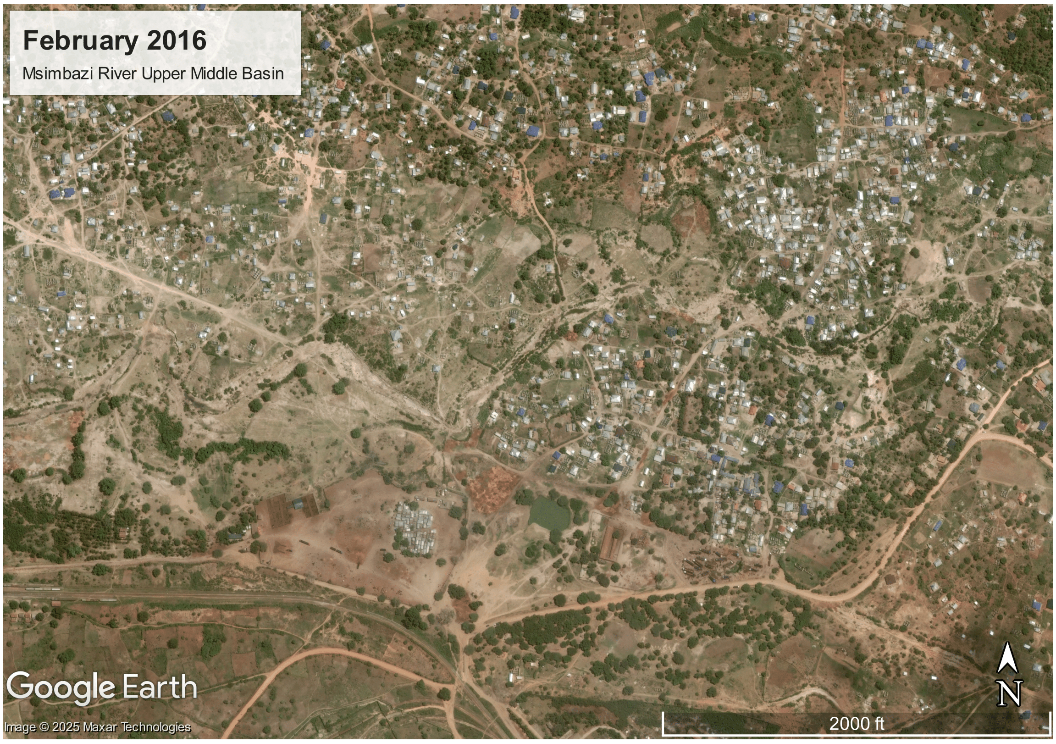

Figure 3.3: Observed river morphology on January 27, 2016. The Msimbazi River has slightly widened, but it remains difficult to clearly identify in the satellite image due to its narrow appearance.

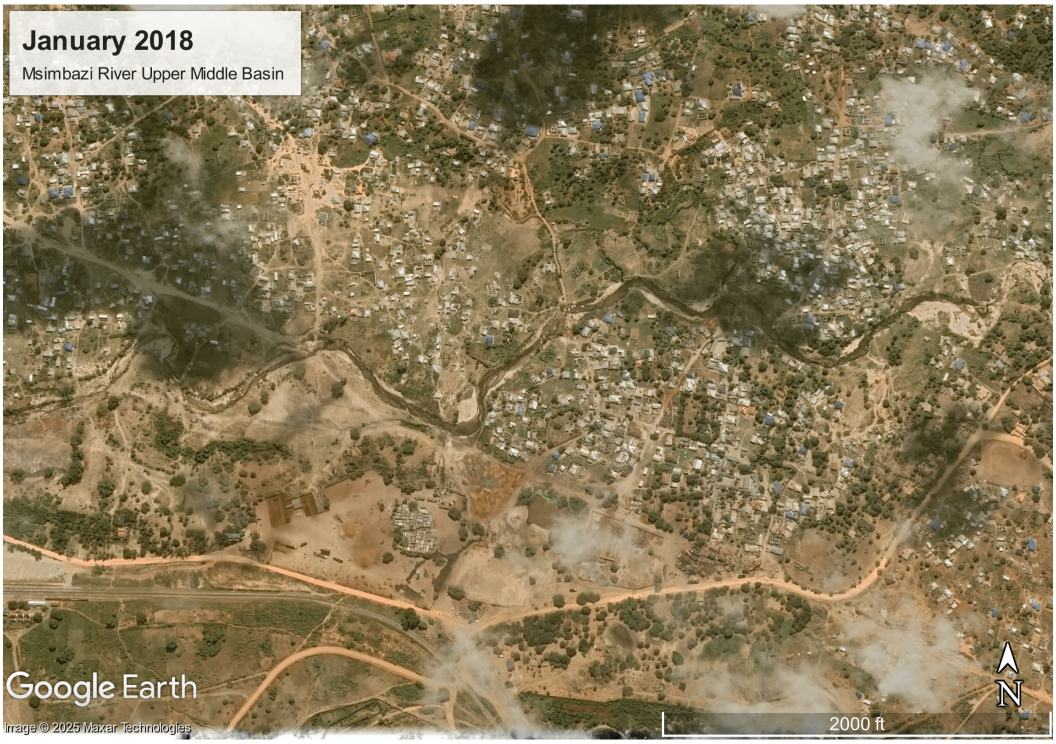

Figure 3.4: River morphology on January 1, 2018. Continued widening of the Msimbazi River enhances its visibility due to greater contrast with the surrounding landscape.

Figure 3.5: River morphology on March 17, 2018. Compared to January 2018 (Figure 3.4), the river appears to have roughly tripled in width, indicating rapid morphological change. The lighter water surface reflection indicates a higher concentration of dissolved sediment.

Figure 3.6: Observed river morphology on May 9, 2022. The river remains wide, with substantial sediment deposits clearly visible within the channel.

Figure 3.7: Observed river morphology on May 3, 2024. The river appears to have widened further, as shown by houses now located directly along the riverbanks. It should also be noted that the number of buildings has increased considerably between Figures 3.2 and 3.7.

Figure 3.8: Photograph from the February 2025 site visit illustrating the protected and re-vegetated banks in the Upper Basin.

(a) Residential building located on the 5-meter-high riverbank in the Upper Middle Basin, observed during the February 2025 site visit as the first house along the river. Clearly, elevation alone does not guarantee protection from erosion.

(b) Active sand mining operations observed in the Lower Basin.

Figure 3.9: Photographs from the February 2025 site visit illustrating key features in the Upper Middle and Lower Basins of the Msimbazi River.

4

River migration and widening

This chapter describes the movement of the Msimbazi river. It explains how the river is changing in terms of centerline migration (section 4.1) and river widening (section 4.2). Therefore it gives answer to the first research question: ”How is the Msimbazi River evolving in terms of channel migration and morphological changes?”

4.1. Centerline migration

Centerline migration refers to the lateral displacement of the river’s centerline in time. The computations conducted for all centerlines from 2007 to December 2024 yield the results presented in Table 4.1. These results represent the overall migration behavior of the entire river system. Although the underlying analysis is based on point movements spaced at 15-meter intervals along the river, the reported outcomes summarize the migration characteristics at the system scale.

Table 4.1: Long-term (2007-2024) centerline Weighted Linear Regression (WLR) summary statistics according to DSAS (Thieler et al., 2003)

Metric	Value
Total number of transects	1851
Average rate (m/yr)	-0.46
Average confidence interval	2.76
Reduced number of independent transects (n_{red})	105.19
Uncertainty of average rate using n_{red}	0.27
Average rate with uncertainty (m/yr)	-0.46 ± 0.27
Number of erosional transects	1007
Percent of transects erosional (%)	54.40
Statistically significant erosion (%)	30.90
Maximum erosion rate (m/yr)	-18.01
Transect ID (max erosion)	364
Average erosional rate (m/yr)	-3.85
Number of accretional transects	844
Percent of transects accretional (%)	45.60
Statistically significant accretion (%)	23.82
Maximum accretion rate (m/yr)	16.50
Transect ID (max accretion)	946
Average accretional rate (m/yr)	3.59

The results in Table 4.1 indicate that 54.4% of all transects exhibit erosion, while 45.6% show accretion. With an average migration rate of -0.46 m/year (negative value corresponds to erosion thus leftward directed), the long-term migration rate of the river’s centerline appears relatively stable. According to

Hooke (2003) and Langhorst and Pavelsky (2023), rivers typically migrate at a rate of 0.1–2% of their width per year. Given that the Msimbazi River ranges from 30 to 70 meters in width, an expected migration rate would fall between 0.03 and 1.4 m/year, aligning well with the observed rate.

The short-term Weighted Linear Regression (WLR) results in Appendix F (Table F.1) show fluctuations in the Msimbazi River's centerline migration between 2007 and 2024. The proportion of transects experiencing leftward movement (erosion) is consistently higher than those undergoing rightward movement (accretion). The percentage of erosional transects ranges from 51% to 55%, while accretional transects vary between 45% and 49%. This indicates a net tendency for the river to shift leftward over time, although rightward migration remains a significant counteracting force. However, this kind of directional trend is probably not caused by one specific factor, but instead emerges from many local influences that shape how the river moves (Schwenk et al., 2015).

A key observation from the migration rates is the considerable variation across different periods. While the long-term migration rate was relatively stable at -0.46 m/year, the short-term rates fluctuate significantly. The highest leftward migration occurred between 2021–2023, with an average rate of -1.0 m/year, whereas the 2019–2021 period briefly exhibited a slight rightward shift (+0.15 m/year). The extreme values at certain points along the river in both directions, such as -138 m/year (2023–2024) for leftward movement and +140 m/year (2017–2019) for rightward movement, highlight the river's instability.

Overall, the results for the entire river system show that the river's centerline has moved both to the left and right over time, with a slight dominance of leftward movement, indicating more erosion on that side. The large variation in migration rates confirms that the river is highly dynamic.

To gain a more detailed understanding of how the river has changed over time and across different locations, it is valuable to examine the movement of individual points along the river centerline. This approach enables the detection of local variations in river migration that may not be apparent at a broader, system-wide scale. The absolute migration rates at these specific points are presented in Figures 4.1 to 4.9. By using absolute values, the direction of movement is disregarded, allowing the analysis to focus solely on the magnitude of migration. This is particularly relevant when considering river movement as a potential hazard for nearby communities, where the impact is determined by the extent of displacement rather than whether the river shifts to the left or right.

Long-term trends (2007-2024)
As previously explained, the river appears relatively stable over the full 2007–2024 period, as illustrated in Figure 4.1, with most migration rates ranging between 0 and 4 m/yr. These values exceed the commonly cited rule of thumb that rivers typically migrate at a rate of 0.1–2% of their width per year (Hooke, 2003; Langhorst & Pavelsky, 2023). For the Msimbazi River, which had an estimated width of approximately 30-70 meters (Gorelick et al., 2017), this would correspond to expected migration rates of roughly 0.03 to 1.4 m/yr. Nevertheless, slightly higher rates are not uncommon in dynamic fluvial environments, and isolated instances of extreme migration exceeding 10 m/yr are also observed.

According to Table 4.3, the Upper Middle Basin (UMB) shows the highest mean migration rate (4.0 m/yr) and the highest standard deviation (3.97), reflecting its overall higher variability and migration intensity over time. In contrast, the Lower Basin (LB) remains the most stable, with the lowest mean migration rate (3.4 m/yr) and one of the lowest standard deviations (3.63).

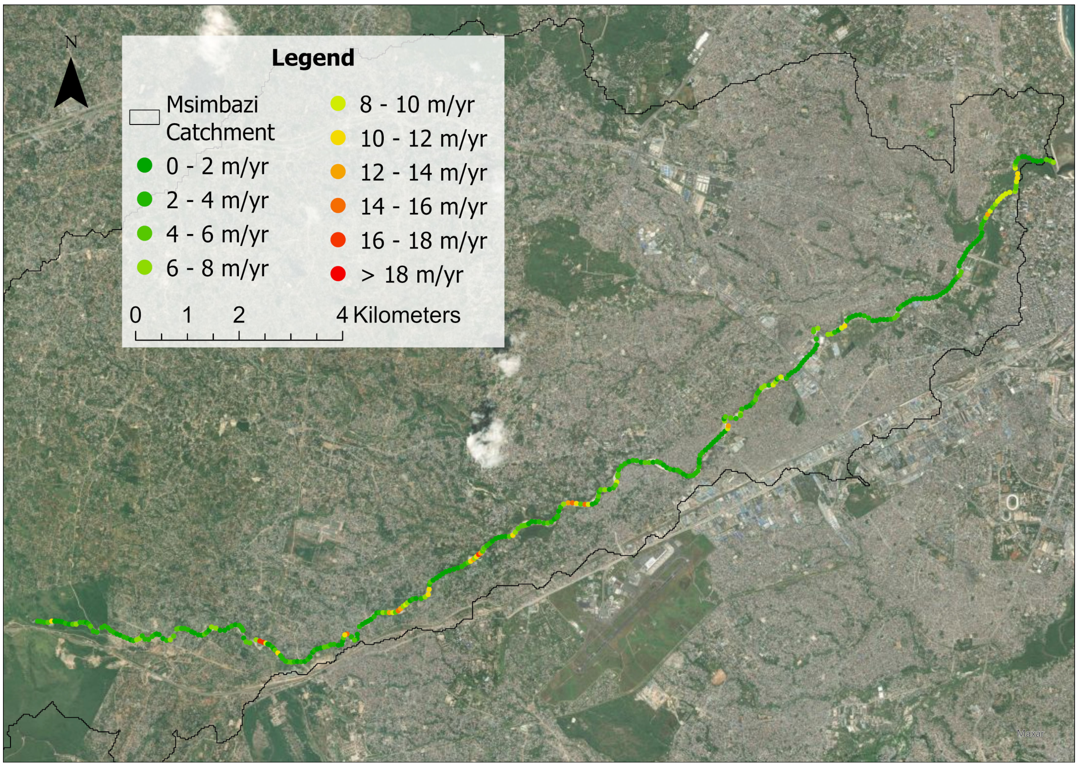

Figure 4.1: Migration rates along the Msimbazi River averaged over 2007-2024.

A deeper understanding of the changes in migration trends over time can be achieved by shifting the focus to short-term migration. Among this analysis the normalized migration values of consecutive periods are observed. Normalised migration rates are the migration rates of the later period divided by the migration rates for the previous period, as shown in Equation 4.1. This shows the magnitude of change of the rates between the two periods. Table 4.2 illustrates the result interpretation: a value of 3 indicates that the migration rate in the observed period (Period 2) is three times higher than in the baseline period (Period 1), while a value of 0.5 indicates a rate that is half as large.

The temporal segmentation into five distinct periods: 2007–2017, 2017–2019, 2019–2021, 2021–2023, and 2023–2024, was chosen to reflect data availability and event relevance. The first period spans a decade due to limited availability of centerlines (approximately one per year), while subsequent periods are shorter (2–3 years) to provide a more detailed representation of migration dynamics. These intervals were selected to capture key events such as the 2023/2024 El Niño phenomenon and the start of the Standard Gauge Railway (SGR) construction around 2017–2018.

$$\text{Normalized Migration Rate} = \frac{\text{Migration Rate}_{\text{Period 2}}}{\text{Migration Rate}_{\text{Period 1}}} \tag{4.1}$$

Table 4.2: Interpretation of the Normalised Migration Rate

Normalised Migration Rate	Interpretation
> 1	Faster migration in the second period.
≈ 1	Similar migration rate, same direction
$0 <$ Normalised Migration Rate < 1	Slower migration in the second period.
≈ 0	Very slow migration in the second period

Short-term changes (2007-2017)
During the 2007–2017 period, migration activity was larger in the Upper Basin and Upper Middle Basin compared to the long-term rates, although the rates remained moderate, as indicated by the dominance of green values in Figure 4.2 and the small whiskers in Figure 4.11. In contrast, the Lower Middle Basin appears relatively stable, showing limited channel movement. Interestingly, the Lower Basin exhibited less activity during this decade compared to the overall 2007–2024 trend, suggesting that more dynamic changes in that region may have occurred after 2017.

This observation aligns with the findings presented in Table 4.3. The migration rates during this period were relatively stable across all sub-basins, with the Lower Basin (LB) showing the lowest mean migration rate at 3.3 m/yr and the Upper Middle Basin (UMB) having the highest at 5.0 m/yr. The standard deviations were similar across all sub-basins, with the Lower Basin (LB) showing the lowest variability (3.75), indicating more stable migration behavior in this region. Figure 4.11 shows a visualization of the rates and variability presented in Table 4.3.

Some river sections are missing in the figure. This is due to cloud cover or low satellite image quality, which occasionally prevented accurate delineation of the river centerline. To calculate a migration rate, the centerline must be available for at least two different points in time for a given section of the river.

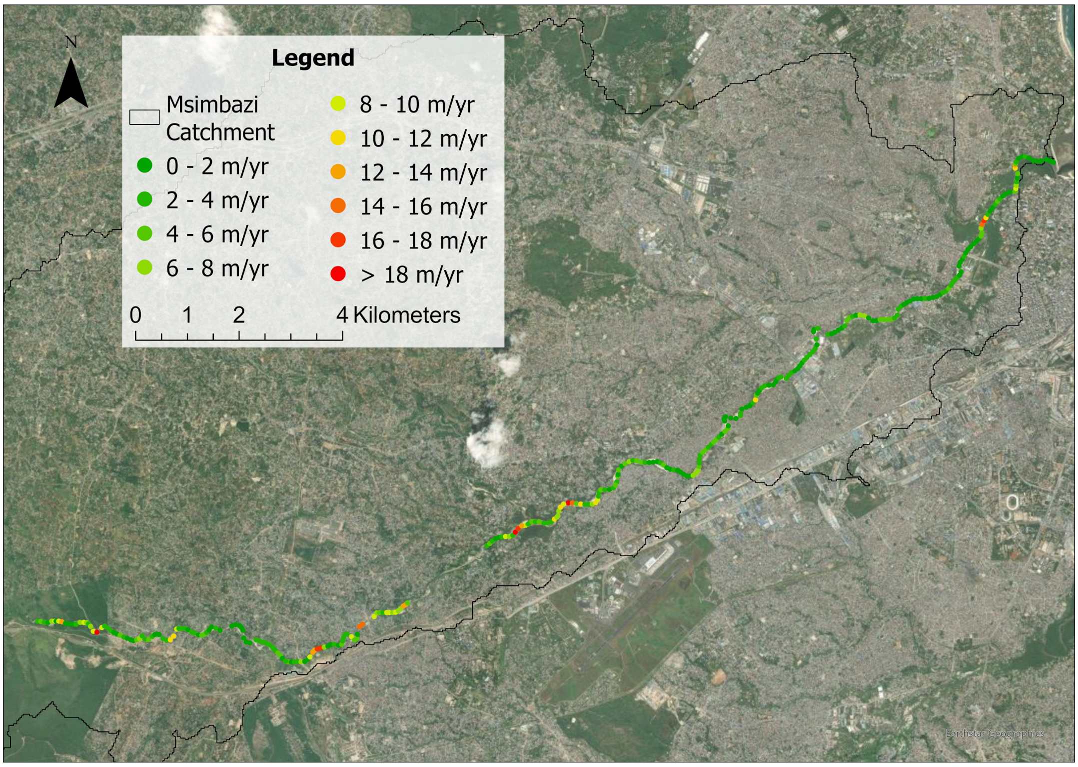

Figure 4.2: Migration rates along the Msimbazi River averaged over 2007-2017.

2017-2019: Rise in migration rates
A comparison with the 2017–2019 period, a three-year span coinciding with the start of the SGR construction, reveals a clear increase in migration intensity across several parts of the river (Figure 4.3). A rise in river migration rates indicates that the river channel is migrating faster than during the previous period, in this case, compared to 2007–2017. Not only have overall migration rates increased, but the frequency of extreme migration events has also risen. This is particularly evident in the growing number of locations displaying very high rates, indicated by dark red. The most pronounced changes are observed in the Upper Middle Basin and the Lower Middle Basin, where the most extreme rates occur.

This aligns with the data in Table 4.3 and Figure 4.11, where a noticeable increase in migration rates is observed during this period. The Upper Middle Basin (UMB) shows the highest mean migration rate at 10.5 m/yr, while the Lower Basin (LB) also sees a significant increase, with a mean of 6.6 m/yr. The standard deviations increase significantly, especially in the Lower Middle Basin (LMB) and Upper Middle Basin (UMB), indicating more extreme migration behavior during this period.

Figure 4.4, which compares the 2017–2019 period to the 2007–2017 baseline, illustrates substantial shifts in migration dynamics. The color scheme helps to interpret these changes: green areas indicate a decrease in migration rate, while light green to yellow reflects zones where migration rates remained relatively stable between the two periods. In contrast, red colors denote a drastic increase in migration intensity, with dark red highlighting the most extreme cases.

Across the Upper Basin, the map is predominantly orange, indicating that migration rates approximately doubled. A similar pattern is visible in the Upper Middle Basin, where several areas show rates that more than doubled. In the Lower Middle Basin, migration rates have also generally more than doubled, and the spatial extent of extreme increases (dark red) has grown considerably. The Lower Basin exhibits a more moderate response relative to the other sub-basins, where extreme changes are limited.

To evaluate the statistical relevance of the observed changes, a Kolmogorov–Smirnov (KS) test was performed at a 5% significance level. The KS test was selected due to its non-parametric nature, which makes it suitable for comparing distributions without assuming normality, unlike the commonly used t-test. The results, summarised in Table 4.4, demonstrate that several changes in migration rates between time periods are statistically significant. For instance, the comparison between 2007–2017 and 2017–2019 yields an extremely low p-value (9.59×10^{-31}), confirming that the shift in migration rate distribution is highly significant.

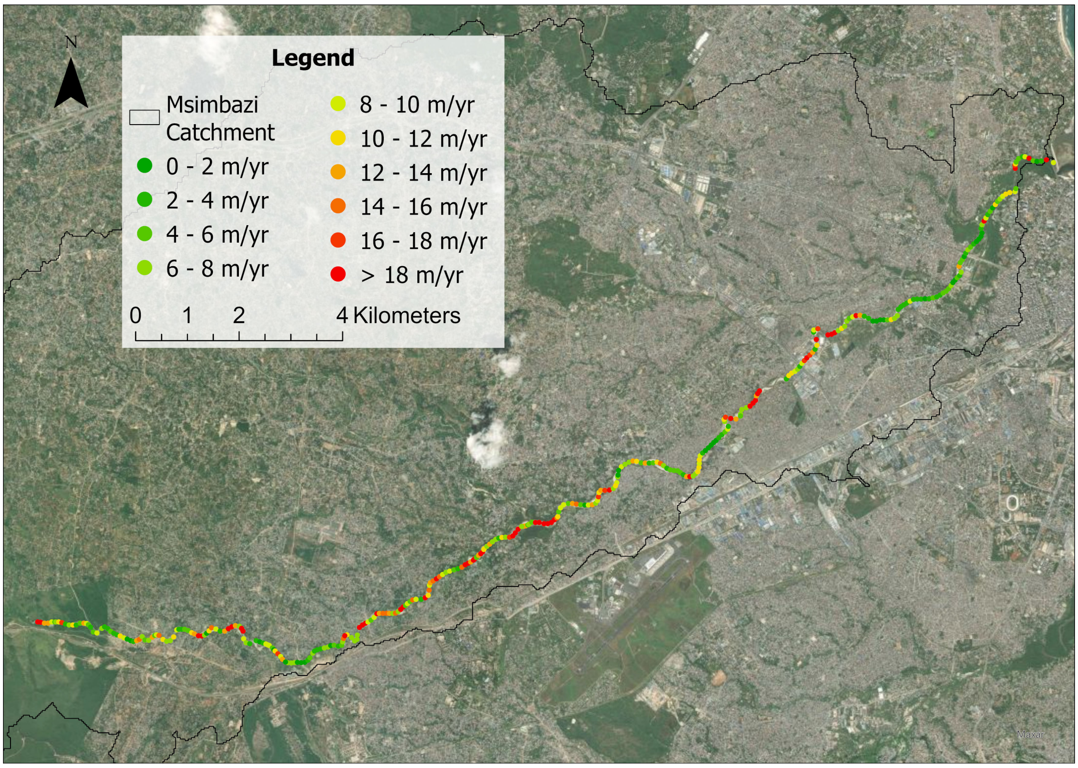

Figure 4.3: Migration rates along the Msimbazi River averaged over 2017-2019.

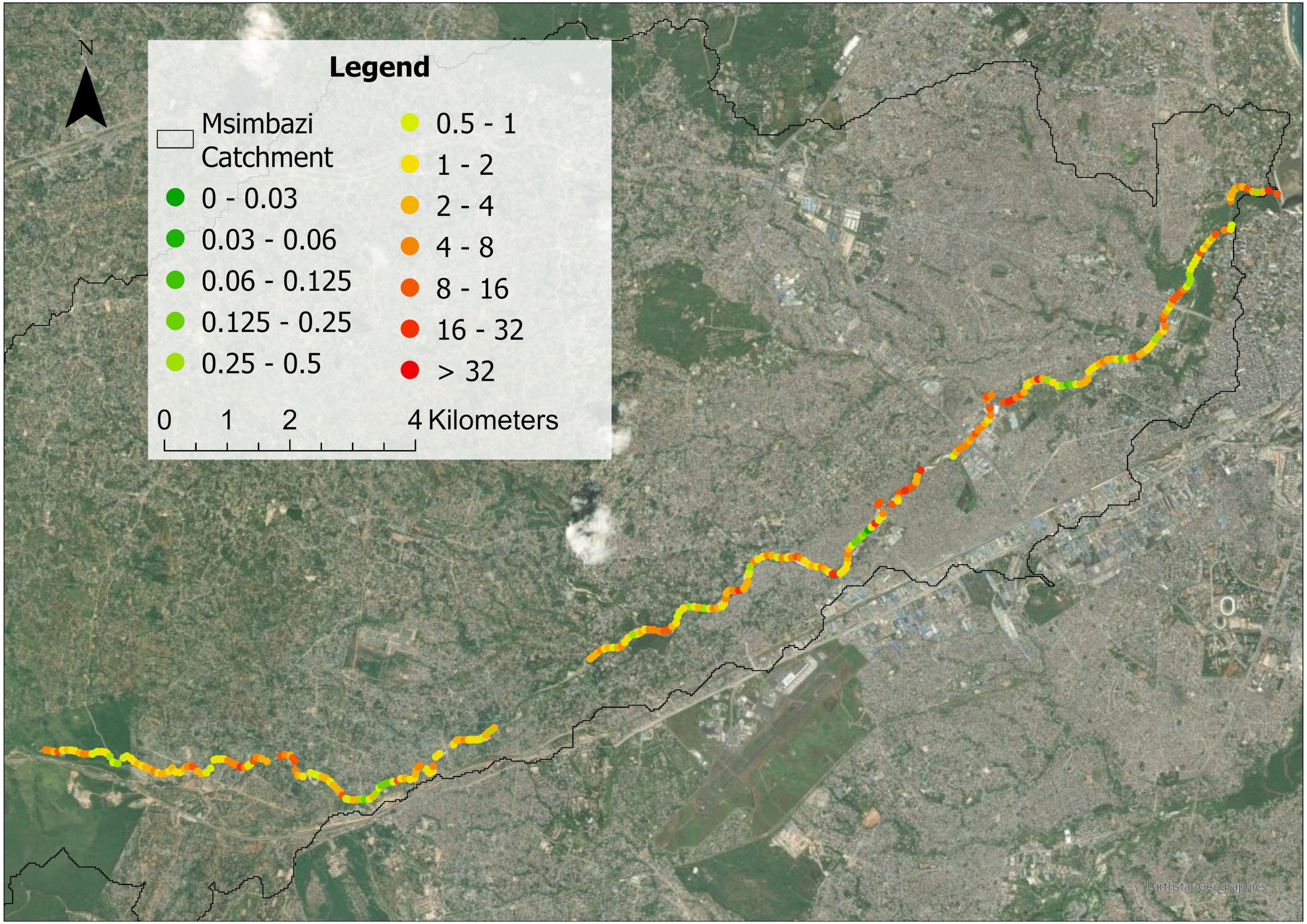

Figure 4.4: Normalized river migration rates for 2017–2019, relative to baseline rates from 2007–2017.

2019-2021: Continued increase in extreme migration rates
Figure 4.5 shows the migration rates for the period 2019–2021. Migration rates remains large during this interval. Notably, the number of locations showing extreme migration rates has further increased compared to the previous period.

This aligns with the data in Table 4.3 and Figure 4.11, where the period 2019–2021 shows the highest migration rates across all sub-basins. The Lower Middle Basin (LMB) and Upper Middle Basin (UMB) show particularly high means of 12.4 m/yr and 12.0 m/yr, respectively. The standard deviations are also at their peak, particularly in the Upper Middle Basin (UMB), with a standard deviation of 12.7, indicating fluctuating and extreme migration rates.

Comparing the 2019–2021 period with the 2017–2019 baseline (Figure 4.6) reveals a relatively stable pattern across the basin, which aligns with the remaining high migration rates. While increased migration rates are dominant, decreases also occur frequently. In the Upper Basin, changes mostly range between 0.5 and 2 times the previous migration rate. For the Upper Middle and Lower Middle Basins, the variation is more pronounced, ranging from 0.06 to 16 times the earlier rate. The Lower Basin shows a consistent increase, with rates generally ranging from 1 to 4 times those of the preceding period.

This apparent stabilization is supported by the results of the KS-test (Table 4.4), which yields a p-value of 0.193. As this exceeds the 0.05 significance threshold, the observed differences between the two periods are not statistically significant.

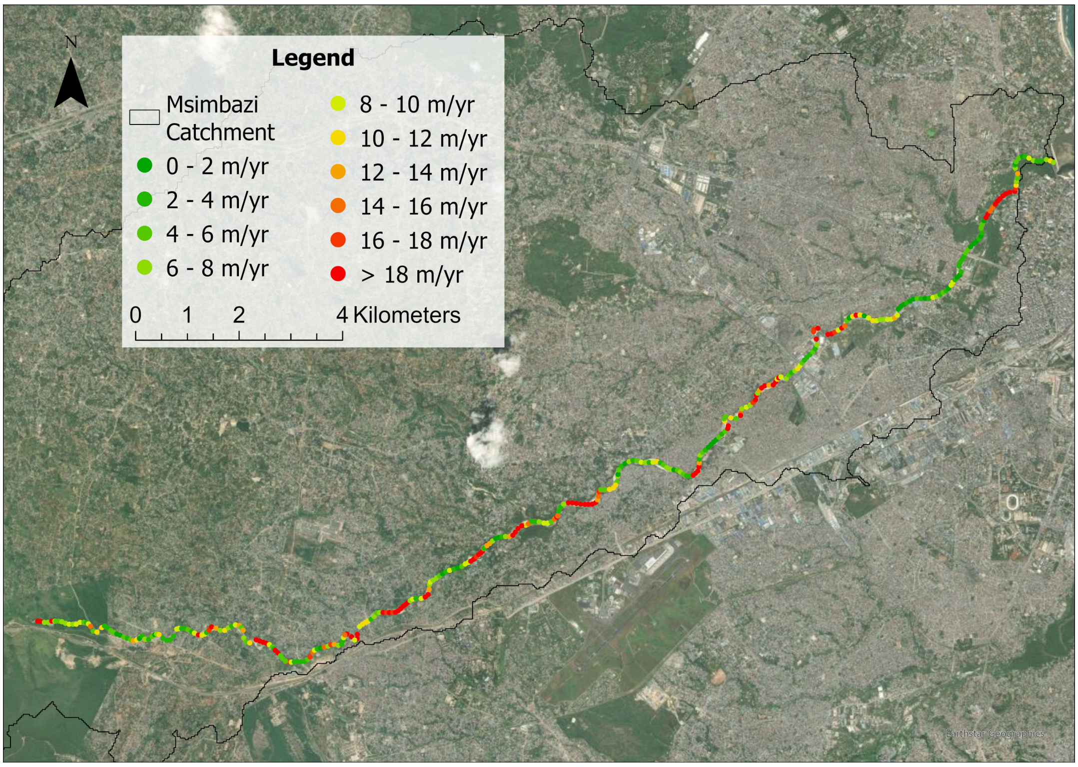

Figure 4.5: Migration rates along the Msimbazi River averaged over 2019-2021.

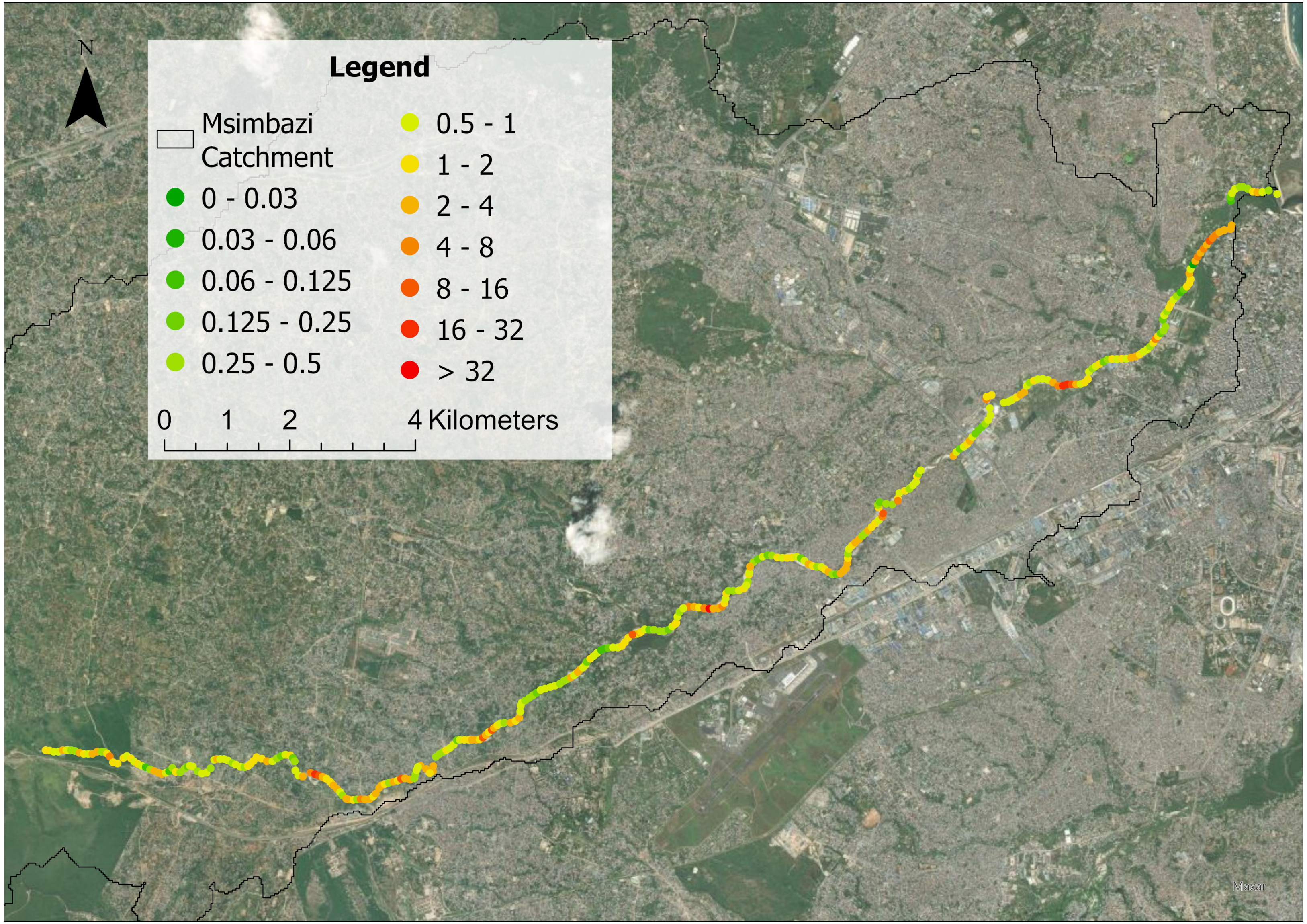

Figure 4.6: Normalized river migration rates for 2019–2021, relative to baseline rates from 2017–2019.

2021-2023: Decreasing migration rates

Figure 4.7 illustrates the migration rates during the 2021–2023 period. Compared to previous time intervals, the frequency and magnitude of extreme migration events have noticeably declined. Overall migration rates are lower, and fewer locations show extremely high migration rate values. This suggests a potential return to more stable conditions, aligning more closely with the migration rates observed over the 2007–2024 period.

This aligns with the findings in Table 4.3, where the 2021–2023 period shows a clear decline in migration rates. Notably, the Upper Basin (UB) experiences a sharp drop from 10.8 m/yr to 2.5 m/yr, while the Lower Basin (LB) shows more moderate decreases, returning from 9 m/yr to a more stable, lower migration rate of 4.2 m/yr. The standard deviations have also decreased, particularly in the Upper Basin (UB), suggesting less fluctuation in migration (as can also be seen from teh whiskersizes in Figure 4.11).

Accordingly, Figure 4.8, examines changes in migration rates between the 2021–2023 and 2019–2021 periods. Overall, a decreasing trend in migration rates is observed. In the Upper Basin, green values (indicating reduced rates) are predominant. The Upper Middle and Lower Middle Basins show a mix of increasing and decreasing rates, though decreases are more frequent. In the Lower Basin, the dominant rate change is around 0.5, suggesting that migration rates have generally halved compared to the previous period ,which aligns with the data in Table 4.3.

This observed decrease in migration rates is statistically confirmed by the KS-test results shown in Table 4.4, with a p-value of 4.95×10^{-20}, indicating that the changes are highly significant.

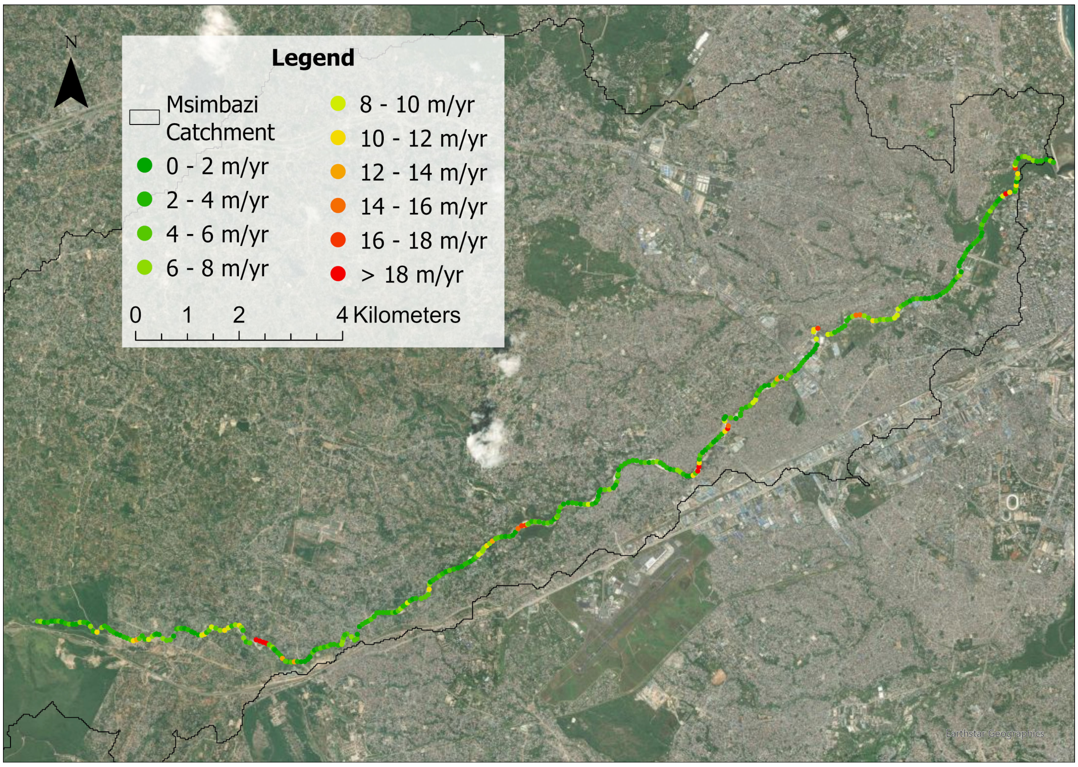

Figure 4.7: Migration rates along the Msimbazi River averaged over 2021-2023.

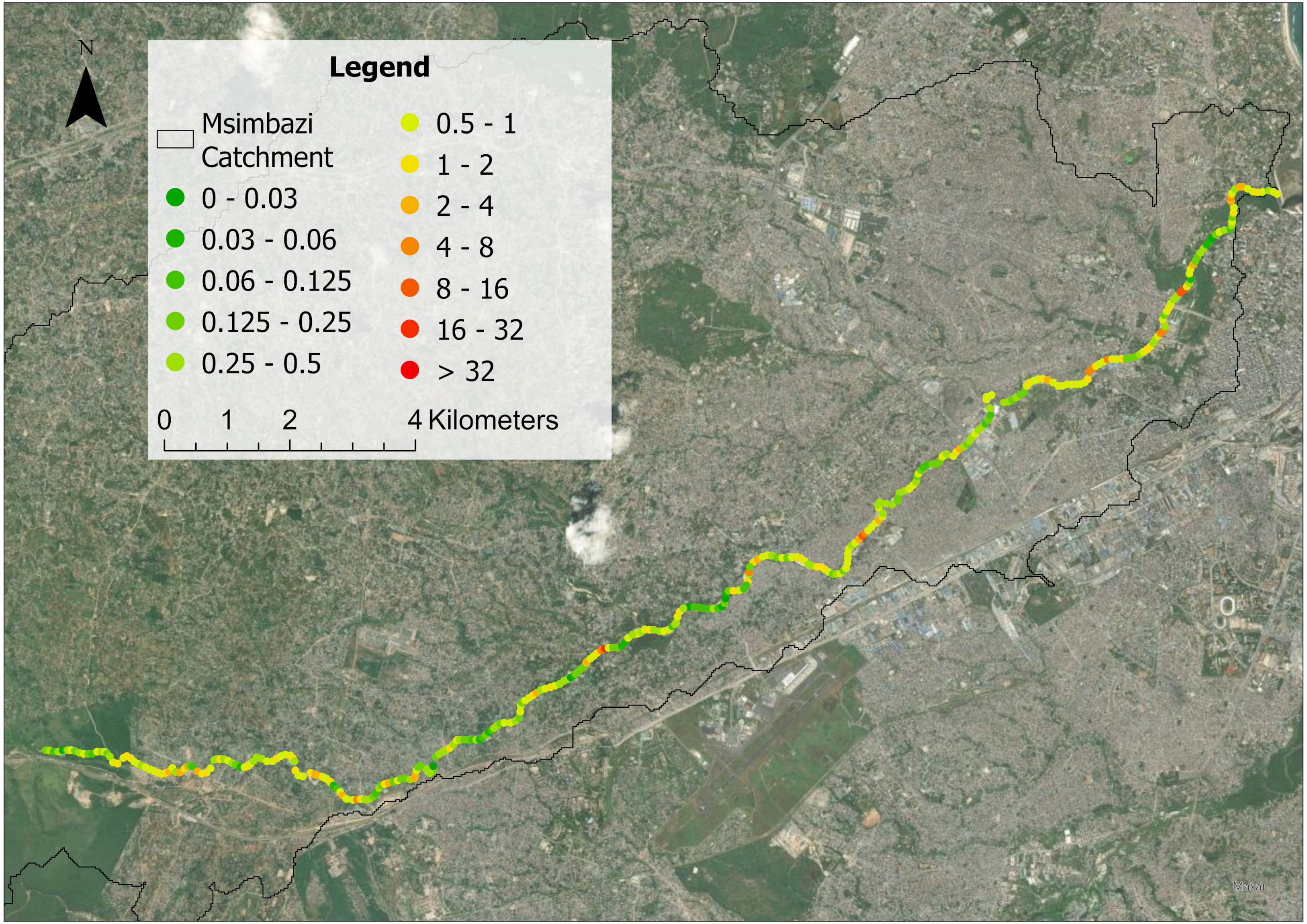

Figure 4.8: Normalized river migration rates for 2021–2023, relative to baseline rates from 2019–2021.

2023-2024: Reemergence of extremes
The final period observed, 2023–2024 (Figure 4.9), coincides with the El Niño phase and Cyclone Hidaya (further discussed in Chapter 5), and reveals a notable increase in the river's migration rates. Extreme migration events are now much more frequent and are observed across nearly all sub-basins. However, the Lower Basin remains relatively calm in comparison, showing less pronounced migration activity during this period.

This aligns with the findings in Table 4.3, where migration rates have increased again, particularly in the Lower Middle Basin (LMB) and Upper Middle Basin (UMB), with very high means of 14.5 m/yr and 15.0 m/yr, respectively. Standard deviations also peak in these basins, indicating a rise in both intensity and variability of migration. See Figure 4.11 for comparison.

Figure 4.10 illustrates the change in river migration rates between the 2021–2023 and 2023–2024 periods. The figure is predominantly shaded in red, indicating widespread increases in migration rates, consistent with the observations shown in Figure 4.9.

In the Upper Basin, several areas appear in dark orange, representing increases ranging from 4 to 16 times compared to the previous period. In the Upper Middle Basin, increases are somewhat less extreme, typically between 2 and 8 times, but remain significant. The Lower Middle Basin shows a more moderate rise, with rates increasing by approximately 2 to 4 times. In contrast, the Lower Basin exhibits relatively limited changes, with increases generally falling between 1 and 2 times. These patterns are supported by Table 4.3.

Table 4.4 confirms that the changes between 2021–2023 and 2023–2024 are statistically significant, with a p-value of 2.70×10^{-23}.

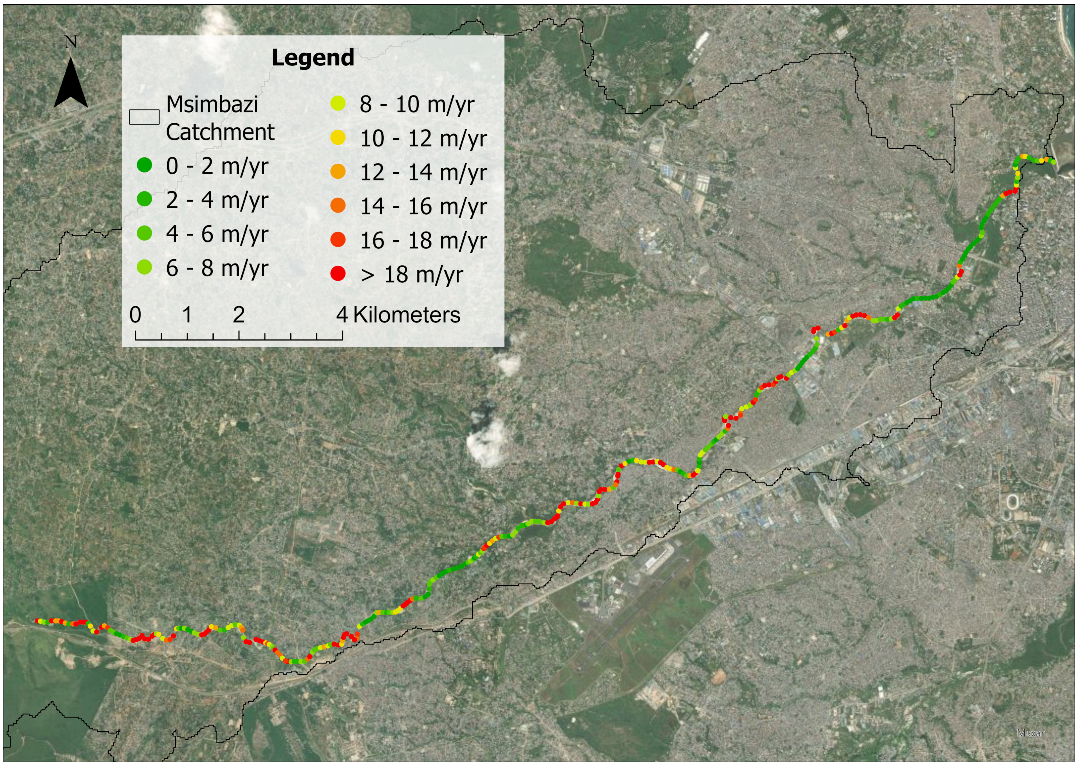

Figure 4.9: Migration rates along the Msimbazi River averaged over 2023-2024.

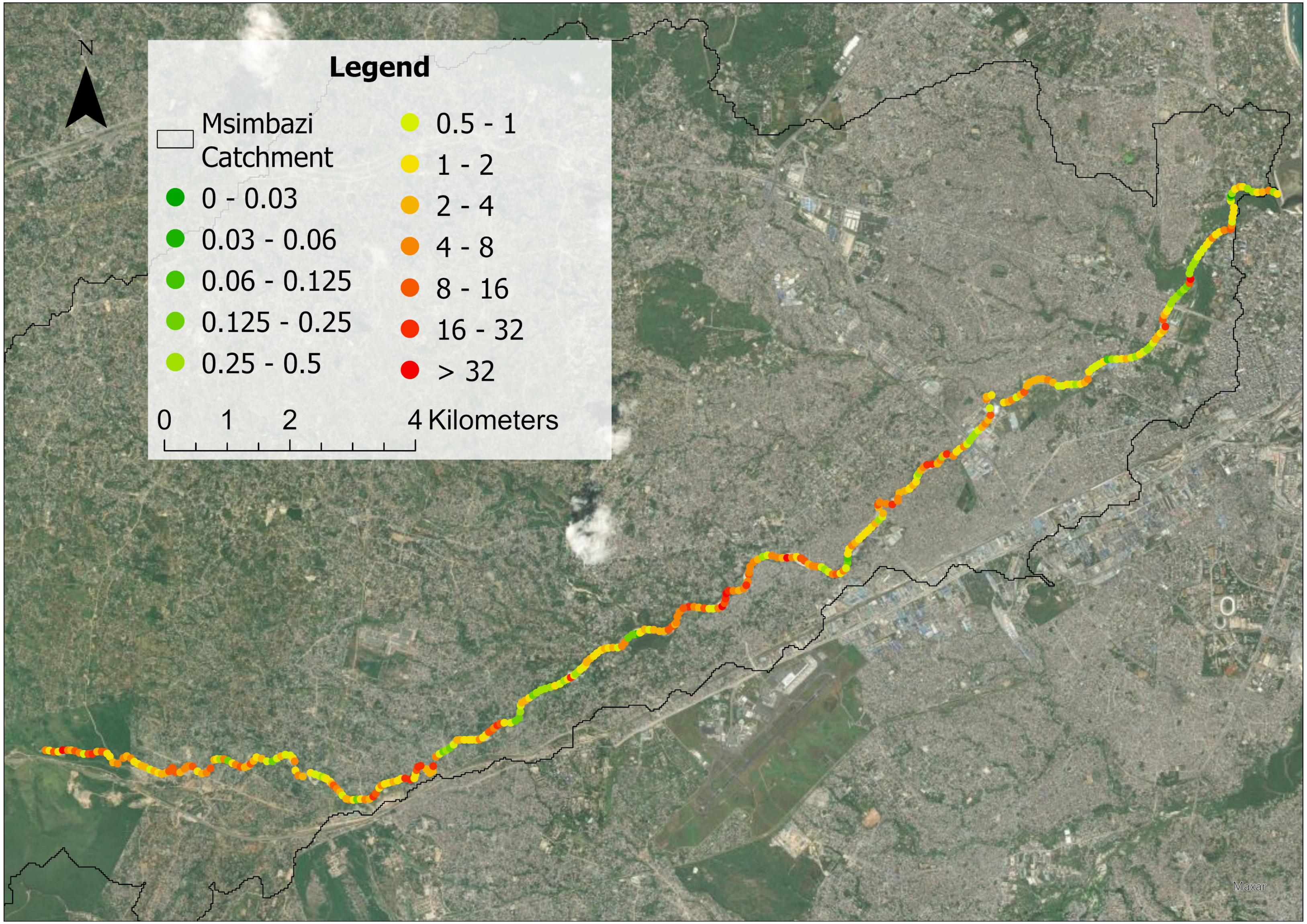

Figure 4.10: Normalized river migration rates for 2023–2024, relative to baseline rates from 2021–2023.

Table 4.3: Mean and standard deviation of absolute river migration rates per sub-basin and time period (2007–2024) within the Msimbazi catchment (Thieler et al., 2003).

Period	**Mean of Absolute River Migration Rate [m/yr]**					**Std of River Migration Rate [m/yr]**				
	LB	**LMB**	**UMB**	**UB**	**Whole basin**	**LB**	**LMB**	**UMB**	**UB**	**Whole basin**
2007–2017	3.3	4.0	5.0	4.7	4.2	3.8	4.2	4.5	4.5	4.3
2017–2019	6.6	10.7	10.5	9.2	9.9	9.0	9.5	11.3	5.4	7.4
2019–2021	9.0	12.4	12.0	10.8	11.6	11.8	12.7	12.7	8.0	12.5
2021–2023	4.2	5.1	5.7	2.5	5.1	4.1	4.9	8.1	2.2	6.3
2023–2024	6.6	14.5	15.0	15.3	13.4	10.1	15.0	18.6	10.2	16.0
2007–2024	3.4	3.5	4.0	4.0	3.7	3.6	3.4	4.0	3.5	3.7

LB = Lower Basin, LMB = Lower Middle Basin, UMB = Upper Middle Basin, UB = Upper Basin.

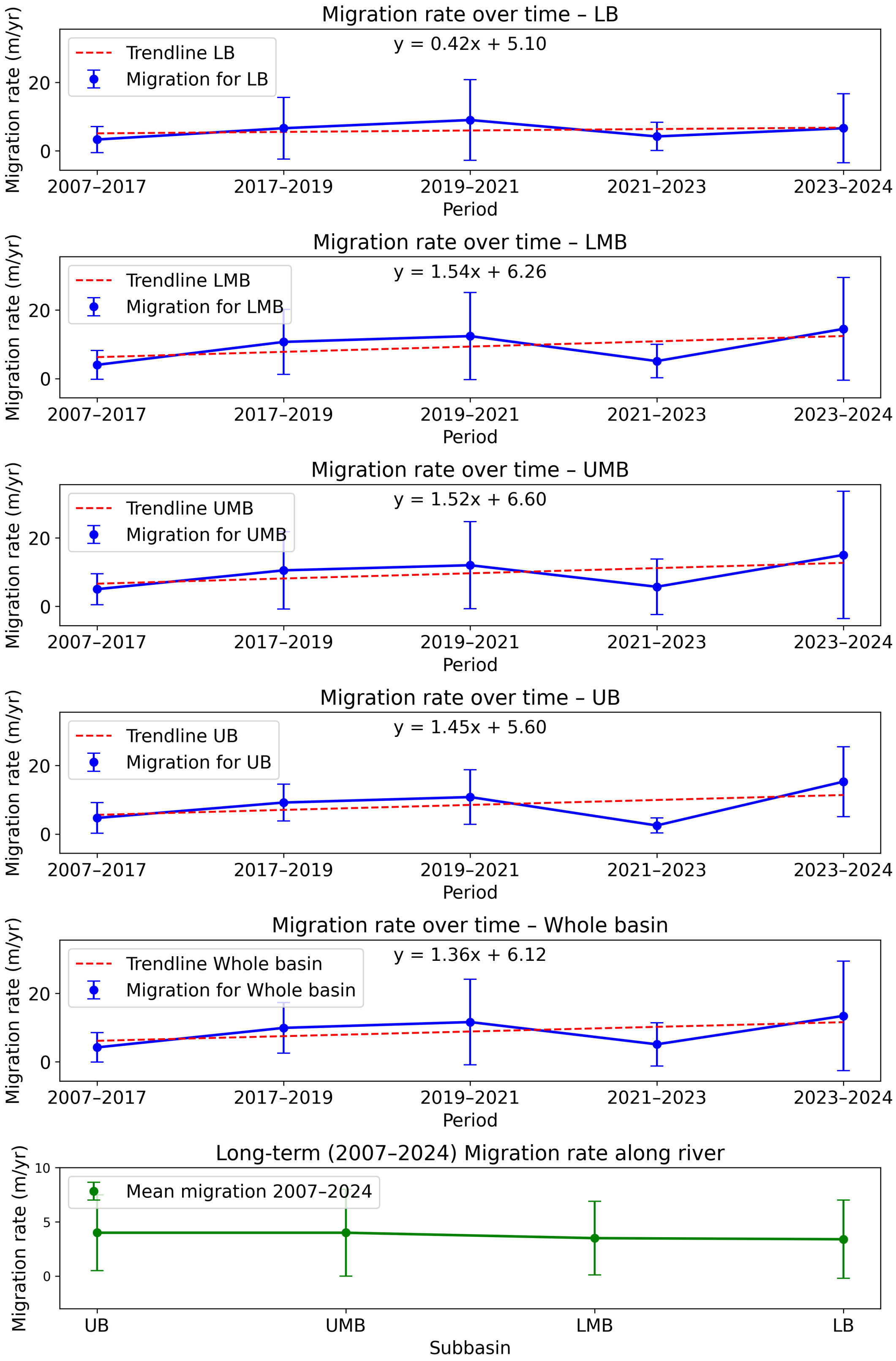

Figure 4.11: Changes in migration rate along the river's sub-basins between 2007 and 2024. The dots show the time- and spatial averaged migration rate. The whiskers denote the variability in migration rate but are also spatially averaged over the (sub-)basin. The red-dotted trend lines represent the long-term gradual changes of the river's migration rate.

Table 4.4: KS-significance test for Weighted Linear Regression (WLR) rates across different periods between 2007 and 2024

Compared periods	KS-statistic	p-value	Significance
2007–2017 vs. 2017–2019	0.4405	9.59×10^{-31}	Yes
2017–2019 vs. 2019–2021	0.0789	0.193	No
2019–2021 vs. 2021–2023	0.3459	4.95×10^{-20}	Yes
2021–2023 vs. 2023–2024	0.3730	2.70×10^{-23}	Yes

Over the full 2007–2024 observation period, river migration rates show clear temporal and spatial variability. Between 2007 and 2017, migration activity was relatively moderate and stable across all sub-basins, with mean rates generally below 5 m/yr and limited variability. A pronounced shift occurs after 2017: the 2017–2019 period marks a sharp increase in migration intensity, with rates doubling or more in many areas compared to the 2007–2017 baseline. This intens migration continues into the 2019–2021 period, particularly in the Upper and Lower Middle Basins, which reach average rates exceeding 12 m/yr and record-high standard deviations, reflecting extreme channel shifts.

Following this peak, a temporary decline is observed during 2021–2023, especially in the Upper Basin. However, this trend reverses dramatically in the final period (2023–2024), with widespread, and in some locations extreme, increases in migration rates across the basin.

Spatially, the Upper Middle Basin consistently shows to be the most dynamic segment, recording the highest mean migration rates in every time interval. It reaches a time averaged peak of 15 m/yr in 2023–2024, along with the highest observed standard deviation (18.6 m/yr), indicating intense and variable channel migration. In contrast, the Lower Basin remains the most stable sub-basin over time, with a long-term mean of just 3.4 m/yr, despite brief periods of increased activity.

A downstream gradient in migration behavior is clear: the Upper Basin shows moderate variability, with increases primarily concentrated in specific intervals (e.g., 2017–2019). The Upper Middle- and Lower Middle Basins display the most pronounced fluctuations, with substantial rate increases during 2017–2019, 2021–2023, and 2023–2024. Meanwhile, the Lower Basin generally exhibits more moderate and consistent changes, with migration rate shifts typically within a 1- to 4-fold range across the entire study period.

4.2. River width changes

As shown in the satellite imagery presented in Chapter 3), the river is not only migrating laterally but also undergoing local widening. Accurately tracing these changes requires information on river width over time. However, the resolution of the available satellite images is too low to reliably delineate riverbanks, introducing significant uncertainty in their exact position. Nevertheless, water cover could be detected, allowing for the derivation of the river centerline.

To assess river widening (or narrowing), changes in the extent water cover are used as a proxy for variations in river width. This method draws on studies that employ automated water body detection techniques, such as Synthetic Aperture Radar (SAR) or Normalized Difference Water Index (NDWI) to delineate river widths (Innoter, 2024; O'Leary et al., 2019). For instance, Mengen et al. (2020) developed continuous time series of river width using high-resolution, weather-independent SAR imaging, allowing for precise width measurements over time. Similarly, Gao et al. (2024) explored channel structure characteristics by analyzing water and non-water indices. While water cover is not a direct indicator of river width, it is generally assumed that an increase in the water-covered area reflects a widening trend in the river channel. Nevertheless, it is important to recognize the limitations of this approach.

Particularly for smaller rivers, such as the Msimbazi, the resolution of available satellite imagery can hinder accurate delineation of riverbanks, introducing uncertainty in the true river width. Narrow channels are often poorly represented in commonly used water masks, leading to underestimation or omission of narrower sections (Feng et al., 2022; Yamazaki et al., 2014). In this study, changes in water-covered area are therefore used as proxies for relative widening or narrowing trends over time, rather than as precise measurements of river width. These interpretations provide useful insights but should be treated with caution.

While water cover width does not always directly reflect changes in the actual positions of the riverbanks, it remains a useful, although imperfect, indicator for understanding the morphological dynamics. Small variations in water cover may simply represent discharge seasonality, rather than actual lateral expansion. However, this metric provides value because it consistently captures the deepest and most persistent part of the channel. Due to ongoing sediment deposition in the Msimbazi River, this deepest section is gradually aggregating. As a consequence, the water is forced to spread laterally, which can result in the widening of the channel. Therefore, significant increases in water cover width may suggest actual changes in river width. Although water cover width does not perfectly represent morphological change, consistent trends in widening, especially when the water cover exceeds the established channel width, can serve as indirect evidence of bank movement. To validate these indications, field observations or high-resolution satellite imagery are required.

To minimize the influence of individual storm events, care was taken to exclude satellite images captured within the catchment's Time of Concentration (ToC). The ToC refers to the time it takes for water to travel from the most distant point in a catchment to the river outlet following a rainfall event (Iowa Organization of Natural Resources, 2023; Mehta et al., 2022). See Appendix B, for the computation of the ToC. By analyzing only satellite imagery captured outside this period, the influence of seasonality is minimized, as this approach isolates the baseflow component of the river. Additionally, the analysis uses temporally and spatially averaged width values, which further minimize the influence of any remaining seasonal effects that may have been unintentionally captured, as these variations tend to cancel out (Eggert et al., 2015). Although the water cover width is a imperfect proxy for channel width, it is a relevant best option given the data-scarce environment.

The widening trend was analyzed using two complementary approaches. The first involves tracking the movement of the delineated edges of the water cover. Which is the boundary between land classified pixels and water classified pixels. A schematic of these water cover boundaries is shown in Figure 4.12. By comparing the displacement of the left and right edges over time, relative changes in width can be presumed. The second approach focuses directly on the distance between these edges, which serves as an estimate of the water cover width. This width is stored in the metadata during the centerline delineation process. Further details on the extraction of water cover edges and centerlines are provided in Appendix C.

The analysis of the edges between water-classified and land-classified pixels reveals both long-term (2007–2024) and short-term variations in the river's width. These changes are driven by the movement of the left and right edges relative to the baseline located on the right side. According to DSAS (see Appendix E), movement of the right water cover edge towards the baseline corresponds to erosion, while movement of the left edge towards the baseline (which is on the right) indicates accretion. Conversely, movement away from the baseline signifies accretion for the right edge and erosion for the left edge. Therefore, the sign of the migration rates must be interpreted differently for each edge: for the left edge, a positive $(+)$ value means accretion and a negative $(-)$ value means erosion; for the right edge, the opposite applies, with 'plus' indicating erosion and 'minus' indicating accretion (Himmelstoss et al., 2021). To avoid confusion, the following analysis describes erosion and accretion based on their actual definitions: movement towards the centerline indicates accretion, while movement away from the centerline indicates erosion.

Over the long term (2007–2024), the left edge has experienced an average migration rate of -0.22 m/yr, indicating a mild trend of erosion. In contrast, the right edge shows a slightly greater erosional trend with an average migration rate of -0.37 m/yr, suggesting that the river as a whole is undergoing a net narrowing. Despite this, the similar magnitude of these rates for both edges indicates a relatively stable system over the long term.

In the short term, width changes exhibit more episodic behavior, with alternating periods of narrowing and widening. Between 2007 and 2017, the left edge experienced mild erosion (-0.48 m/yr), while the right edge also eroded (0.71 m/yr), resulting in a widening trend. From 2017 to 2019, the left edge eroded (-1.09 m/yr) and the right edge remained almost stable (0.05 m/yr), suggesting localized

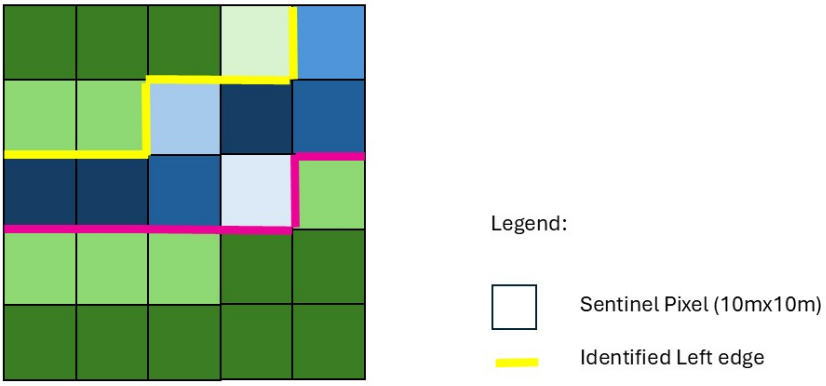

Figure 4.12: Identified edges of the water cover. The distance between these boundaries is used to determine the water cover width. See Appendix C for further explanation.

widening. During the 2019 to 2021 period, the left edge exhibited mild accretion (0.12 m/yr), while the right edge accreted slightly (-0.04 m/yr), signaling stabilization rather than significant narrowing. Between 2021 and 2023, the left edge remained stable (0.03 m/yr), while the right edge experienced notable accretion (-1.27 m/yr), marking a period of narrowing. Finally, from 2023 to 2024, the left edge showed substantial erosion (-1.97 m/yr), while the right edge eroded (1.05 m/yr), indicating a net widening phase.

These alternating trends highlight the dynamic nature of the river's width. The most significant widening occurred between 2023 and 2024, with substantial erosion on the left edge. However, extreme erosion rates during the 2023–2024 period, with occasions of -140 m/yr on the left bank and occasions of -129 m/yr on the right bank, are likely due to localized hydrodynamic forces, possibly resulting from extreme weather events or human interventions. The observed variability in erosion and accretion rates further explains the episodic nature of the river's width changes.

The Msimbazi River has experienced alternating widening and narrowing phases, with the most substantial widening occurring between 2021 and 2023. While the long-term trend suggests a mild widening, short-term variations indicate localized widening and narrowing driven by movement of the water cover edges.

Table 4.6 presents the median and standard deviation of water cover width for the Lower Basin (LB), Lower Middle Basin (LMB), Upper Middle Basin (UMB), Upper Basin (UB), and the whole basin over the period 2007–2024. Overall, the average water cover width for the whole basin increases from 33.7 meters in 2007–2017 to a peak of 37.1 meters in 2021–2023, indicating a general trend of water cover widening over time.

The Upper Middle Basin shows the most notable increase, with a rise in median width from 30.7 meters to 37.7 meters between 2007–2017 and 2021–2023. The Upper Basin also shows a considerable widening during the same period, from 36.6 meters to 39.3 meters. However, observations over different periods actually reveal a narrowing. The Lower Basin increases more modestly from 31.9 meters to 35.9 meters, while the Lower Middle Basin experiences a relatively stable width. It is evident that the Upper Middle Basin experienced the largest increase in width over time, while changes in the Lower and Lower Middle Basins were more limited.

The standard deviation of water cover width, which reflects spatial variability within each sub-basin, also increases during this period. For the whole basin, it rises from 11.1 meters in 2007–2017 to 12.2 meters in 2021–2023, indicating that differences in width between locations along the river became more pronounced. This increase in variability is especially evident in the Upper Basin, where the standard deviation grows from 10.9 to 14.6 meters, suggesting that the water cover widened more unevenly across this region. The Upper Middle Basin similarly sees an increase from 9.9 to 13.1 meters. The Lower Middle Basin maintains relatively high variability around 12 to 13 meters, while the Lower Basin shows less fluctuation, remaining near 9 meters.

These trends suggest that while the overall water cover showed a general widening, this change was not uniform across the entire river; some areas experienced more pronounced local variations in width than others. Interestingly, these observations contradict the edge migration rate analysis, which indicated a net narrowing of the river in long-term. This discrepancy arises from the fact that the migration rate analysis focused on the movement of the river's edges across the entire system, while the width measurements were taken at intervals of 15 meters along the river. As such, these more localized width measurements provide a more detailed and reliable assessment. Based on this, it is concluded that the river is undergoing a net widening, despite the earlier indication of net narrowing from the edge migration rates.

According to Table 4.5 the observed changes are all statistically significant.

Table 4.5: KS-significance test for water cover width across different periods between 2007 and 2024

Compared periods	KS-statistic	p-value	Significance
2007–2017 vs. 2017–2019	0.1712	5.22×10^{-222}	Yes
2017–2019 vs. 2019–2021	0.0436	1.42×10^{-24}	Yes
2019–2021 vs. 2021–2023	0.0821	5.58×10^{-101}	Yes
2021–2023 vs. 2023–2024	0.0793	8.00×10^{-86}	Yes

Plotting the river widths over time (2007–2024) as average values for different observed periods, shown in Figure 4.13, reveals how the different basins compare to the long-term average. It is assumed that the red trend line corresponds to a gradual increase in water cover width. Since the plotted values represent averages, it is expected that they generally follow this long-term trend. This long-term change is likely due to gradual modifications in the catchment's morphology. Any significant deviations from this long-term average would indicate more immediate causes of widening or narrowing.

From Figure 4.13, it is clear that the Lower Basin (LB) follows the long-term trend closely, with the exception of the 2021–2023 period. The Lower Middle Basin (LMB) shows a drop in width during the 2017–2019 period, followed by a recovery. The Upper Middle Basin (UMB) clearly shows a steep slope in its trend, indicating that it is undergoing more significant widening compared to the LMB and LB. Additionally, it is evident that the width peaks above the average during both the 2017–2019 and 2021–2023 periods. In contrast, the Upper Basin (UB) demonstrates a decreasing trend in width, indicating the river is becoming narrower. Moreover, the variability in the width data of the Upper Basin appears relatively large, particularly after 2021.

When observing the final figure within Figure 4.13, which plots the width along the river from UB to LB, it is clear that the Upper Middle Basin is the widest part of the river. This is somewhat surprising, as one might expect the width of a river to increase as it moves downstream, based on flow accumulation. As Garbrecht (1991) described: ”The drainage network accumulates upstream sub-watershed runoff into a single downstream response, with runoff accumulating at network junctions.” However, it is important to note that width is just one metric, and there is no information available on changes in channel depth or other influencing factors.

Nonetheless, it can be observed that the river's width is relatively variable in the Upper Middle Basin.

The analysis of river width trends over time suggests that the changes in width are not uniform across the basin. While the general long-term trend indicates a gradual increase in water cover width, certain periods exhibit notable deviations from this trend, implying the presence of more immediate factors influencing the river's morphology. In particular, the Upper Middle Basin (UMB) shows more significant widening, which contrasts with the narrowing trend observed in the Upper Basin (UB). These variations highlight that while gradual changes in catchment morphology likely drive the long-term trend, short-term fluctuations in river width may be linked to localized hydrological or geomorphological processes. The variability in the Upper Basin, particularly after 2021, further suggests that transient or external factors may be contributing to changes in river width

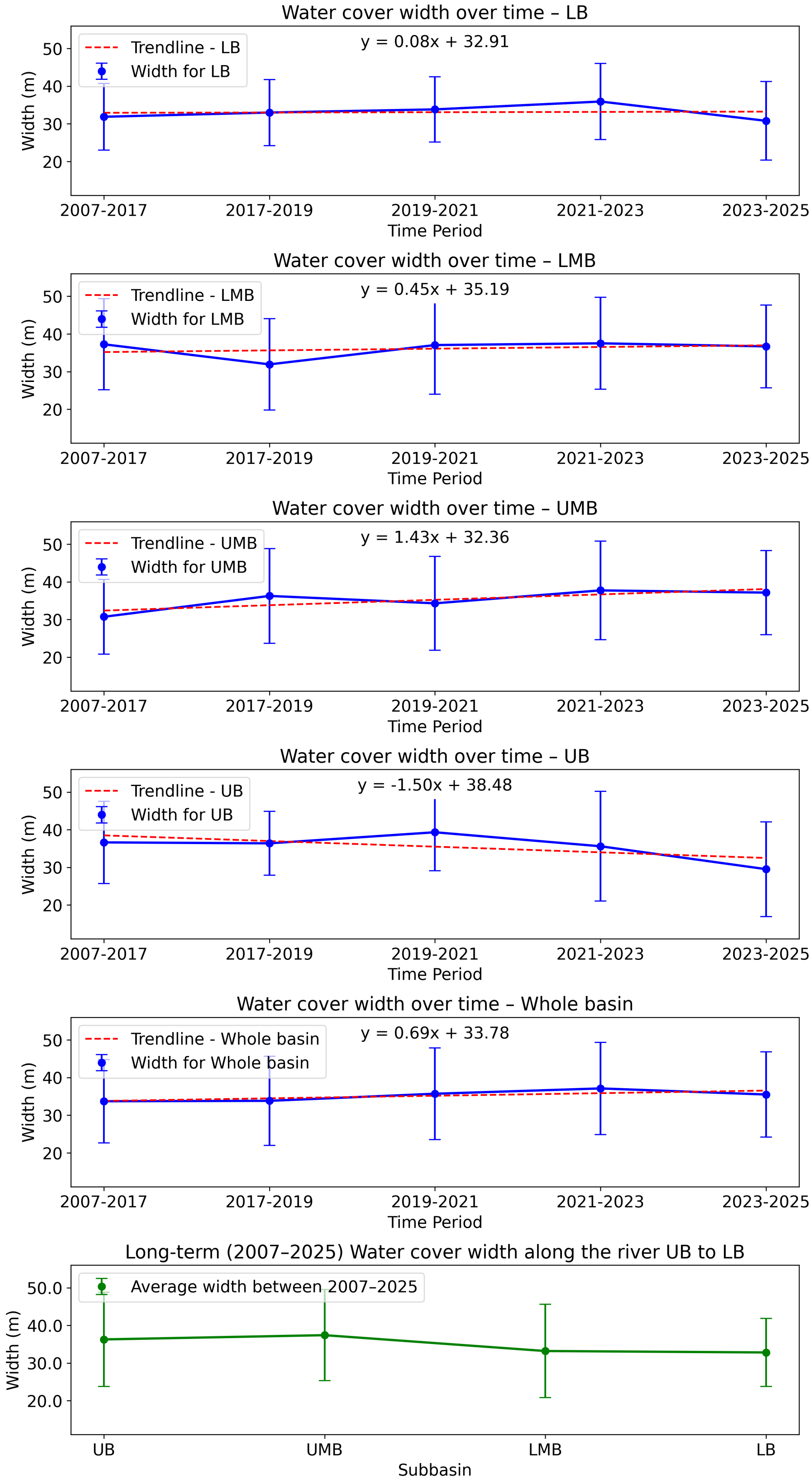

Figure 4.13: Changes in water cover width along the river's sub-basins between 2007 and 2024. The dots show the time- and spatial averaged water cover width at baseflow. The whiskers denote the variability in width but are also spatially averaged over the (sub-)basin. The red-dotted trend lines represent the long-term gradual changes of the river's width.

Table 4.6: Mean and standard deviation of water cover width at baseflow per sub-basin and time period (2007–2024) within the Msimbazi catchment.

Period	Mean of River Width [m]					Std of River Width [m]				
	LB	LMB	UMB	UB	Whole basin	LB	LMB	UMB	UB	Whole basin
2007–2017	31.9	37.3	30.7	36.6	33.7	8.8	12.1	9.9	10.9	11.1
2017–2019	33.0	31.9	36.3	36.4	33.8	8.8	12.2	12.6	8.5	11.9
2019–2021	33.8	37.1	34.3	39.3	35.7	8.7	13.1	12.5	10.2	12.2
2021–2023	35.9	37.5	37.7	35.6	37.1	10.1	12.2	13.1	14.6	12.2
2023–2024	30.8	36.7	37.1	29.5	35.5	10.5	11.0	11.2	12.6	11.3
2007–2024	32.8	33.2	37.4	36.3	34.8	9.0	12.4	12.1	12.5	12.0

LB = Lower Basin, LMB = Lower Middle Basin, UMB = Upper Middle Basin, UB = Upper Basin.

5

Drivers of change

This chapter examines the key drivers behind the morphodynamic changes occurring in the Msimbazi River. The analysis first investigates whether there is a signature of changing climate patterns influencing the river's behavior. The river responds to variations in precipitation, which can manifest in several ways. One possibility is an increase in extreme rainfall, reflected in a rise in annual total precipitation (Zwiers et al., 2013). Alternatively, overall precipitation may have increased without a larger number of extreme events, in which case the annual maximum rainfall would show a change over time, often referred to as changes in intensity (Zwiers et al., 2013). Another factor could be shifts in the duration of rainfall events, which could alter the timeframe over which the catchment must manage the water (Westra et al., 2014).

Following that, this chapter explores the role of land use changes, urbanization, deforestation, and human interventions such as infrastructure development. These factors collectively shape the river's path by influencing sediment dynamics and catchment runoff (James & Lecce, 2013; Kayitesi et al., 2022; Wohl, 2004). Understanding their interplay is essential in explaining the observed changes.

5.1. Precipitation

Many rivers experience changing characteristics such as discharge, flow velocity, and erosion speed due to variations in precipitation (Vörösmarty et al., 2000). The goal of this section is to explain how river morphology is changing as a result of discharge. Discharge is the amount of water that flows through a river (Chow et al., 1988). However, given the lack of available discharge data for the Msimbazi River in Tanzania, precipitation is used as a proxy. Precipitation is widely considered a key driver of river discharge (Fleischmann et al., 2019).

To investigate the role of precipitation in shaping river morphology, we consider four potential ways in which precipitation patterns could influence the river: 1) total precipitation, 2) precipitation intensity, 3) precipitation duration, and 4) precipitation anomalies. The precipitation data used in this research comes from the Global Precipitation Measurement (GPM) mission, an international satellite network operated by NASA. GPM provides global measurements of precipitation and snowfall, serving as a reference standard by unifying precipitation data from various satellites worldwide (Huffman et al., 2014; NASA, 2025).

The GPM data has been extracted for the area of interest from the beginning of the mission until 8 October 2024 for every hour. The earliest available precipitation data for the area of interest in the GPM dataset starts from 3 June 2000. Figure 5.1 shows the precipitation data from 3 June 2000 till 8 October 2024.

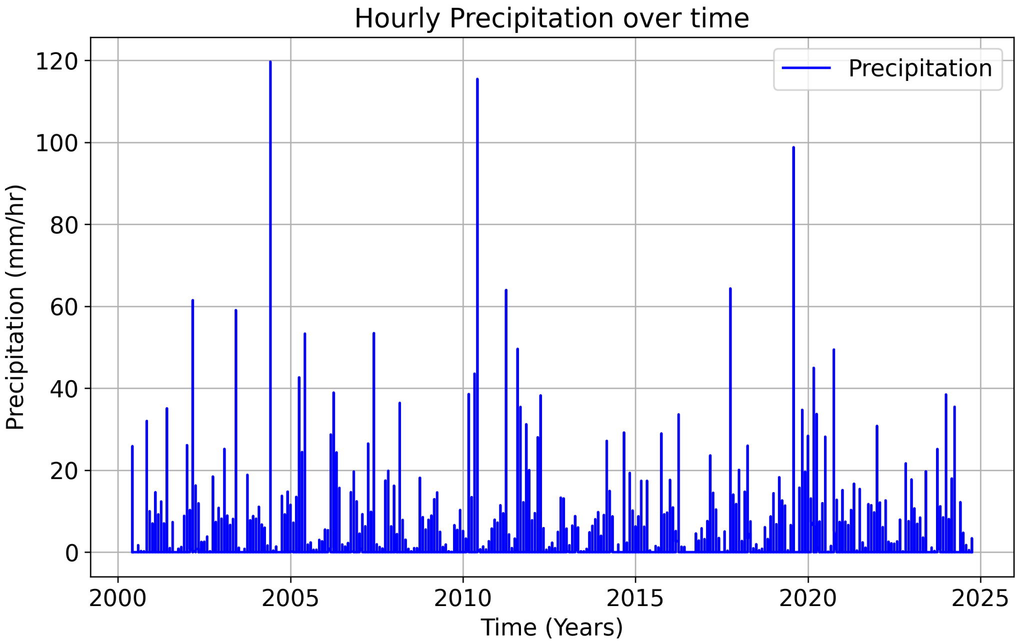

Figure 5.1: Hourly GPM Precipitation between 3 June 2000 and 8 October 2024 (Huffman et al., 2014; NASA, 2025)

5.1.1. Return periods

The bankfull discharge is often considered to be the flow that fills the channel to the top of its banks and occurs, on average, every 1 to 2 years (Rosgen, 1996). This flow is frequently identified as the one that transports the greatest amount of sediment over time, thereby playing a critical role in shaping the form and size of alluvial channels (Leopold et al., 1995). Although the recurrence interval of bankfull flow can vary depending on geomorphological and hydrological conditions, it is generally associated with a flow event that occurs approximately every two years, reflecting a balance between channel-forming energy and flow regularity (Ahilan et al., 2013; Leopold et al., 1995; Mirzaee et al., 2018; Rosgen, 1996). Given its importance in river morphology and sediment transport, the 2-year return period serves as a key threshold for understanding significant geomorphic changes.

Figure 5.2 shows the cumulative distribution function (CDF) for precipitation events in the Msimbazi catchment, illustrating the relationship between precipitation intensity and return periods. The CDF plot shows how the probability of a specific rainfall intensity increases with the return period. As shown in the figure, the precipitation event corresponding to a 2-year return period in the Msimbazi catchment is 38.2 mm/hr. The 2-year, 5-year, 10-year, 25-year, and 50-year return periods were chosen to assess the impact of both frequent, moderate events and rare, extreme events on river morphology, covering a range of typical and extreme discharge conditions critical for understanding sediment transport, erosion, and long-term channel evolution (Mirzaee et al., 2018; Ward et al., 2011).

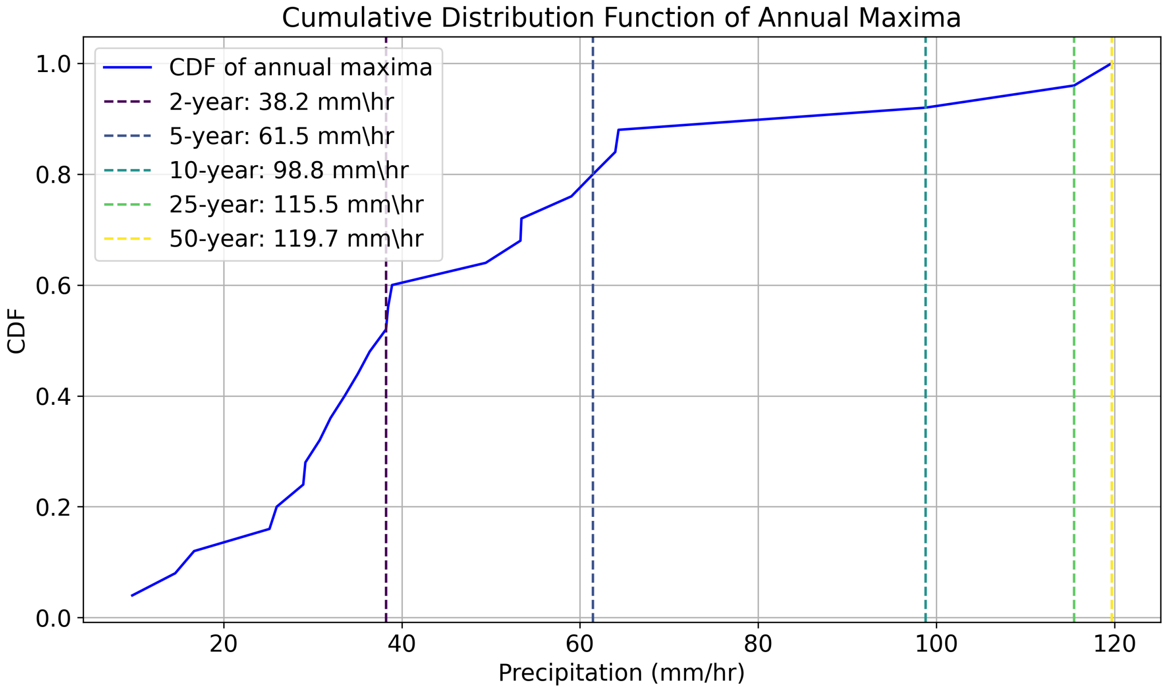

Figure 5.2: Cumulative Distribution Function (CDF) of annual maximum precipitation. The CDF is used to estimate precipitation intensities associated with specific return periods.

5.1.2. Annual total precipitation

To identify these changes, two key years have been selected: 2007 and 2018. The year 2007 is significant because the river was not detectable in satellite imagery before this year but became visible afterward. Meanwhile, 2018 is relevant because, at the beginning of that year, major changes in river width and path were observed in satellite imagery.

Figure 5.3 illustrates the distribution of Annual Total Precipitation across different subsets of the GPM precipitation data. These subsets include: (1) the entire dataset, (2) data collected up to December 31, 2006, (3) data from January 1, 2007, onward, (4) data collected up to December 31, 2017, and (5) data from January 1, 2018, onward, as depicted in Figure 5.4.

Based on the CDF shown in Figure 5.3a and the boxplots in Figure 5.3b, the total precipitation rates across the different subsets appear relatively similar. No differences in precipitation rates are observed a difference between datasets would result in a shift of the curve. The minor deviations between the distributions reflect variations in the underlying datasets comprising each temporal subset.

To verify these observations, a significance test was conducted at a 5% significance level, with results presented in Table 5.1. The Kolmogorov-Smirnov (KS) test was chosen to compare total annual precipitation distributions, as it does not assume normality, unlike the t-test.

Table 5.1: Significance test for distributions of total annual precipitation

Compared subsets	**KS-statistic**	**p-value**	**Significance**
Pre- vs. Post 1 Jan 2007	0.071	0.91	No
Pre- vs. Post 1 Jan 2018	0.17	0.89	No

Since the p-values for both the pre- and post-January 1, 2007, and pre- and post-January 1, 2018, comparisons exceed the 0.05 significance threshold, no statistically significant differences in total annual precipitation are observed between these subsets.

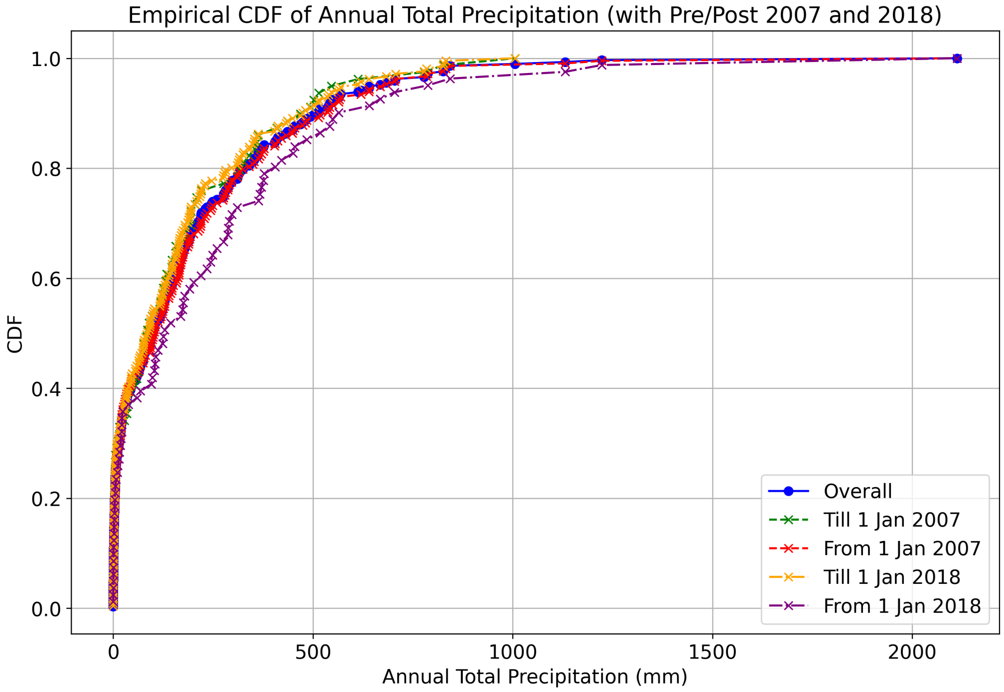

(a) Cumulative distribution function (CDF) of annual total precipitation across five time periods: the full record, pre-2007, post-2007, pre-2018, and post-2018. The CDF illustrates the distribution and variability in total yearly precipitation.

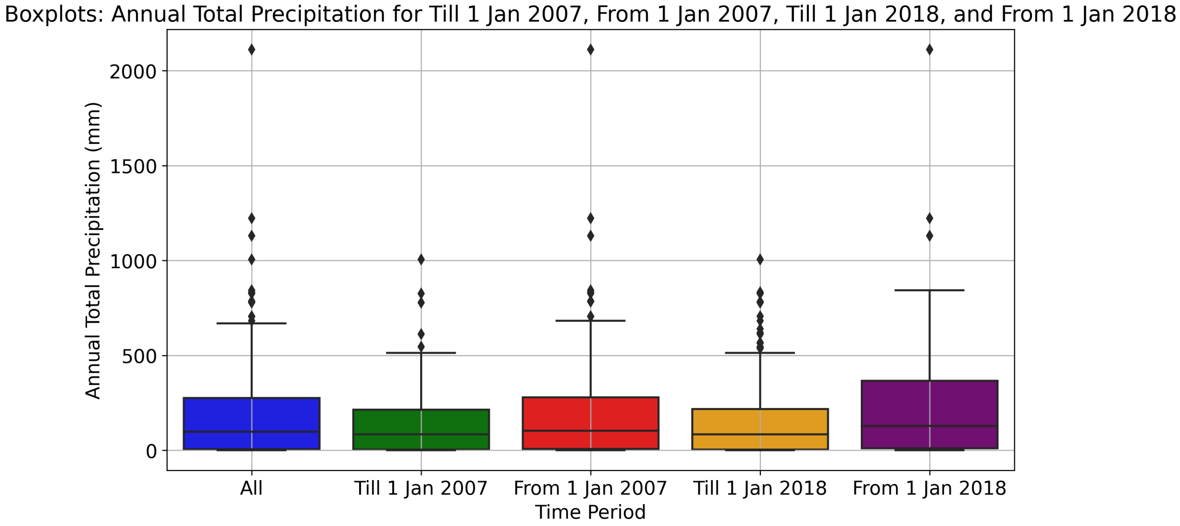

(b) Boxplots of annual total precipitation for the same five time periods. The distributions appear broadly similar, suggesting limited temporal shifts in total annual precipitation relative to the 2007–2024 (All) mean.

Figure 5.3: Annual total precipitation characteristics. Panel (a) presents the cumulative distribution of yearly totals across five periods, while panel (b) compares their median and spread. Together, the plots assess potential temporal changes in annual total precipitation within the study period.

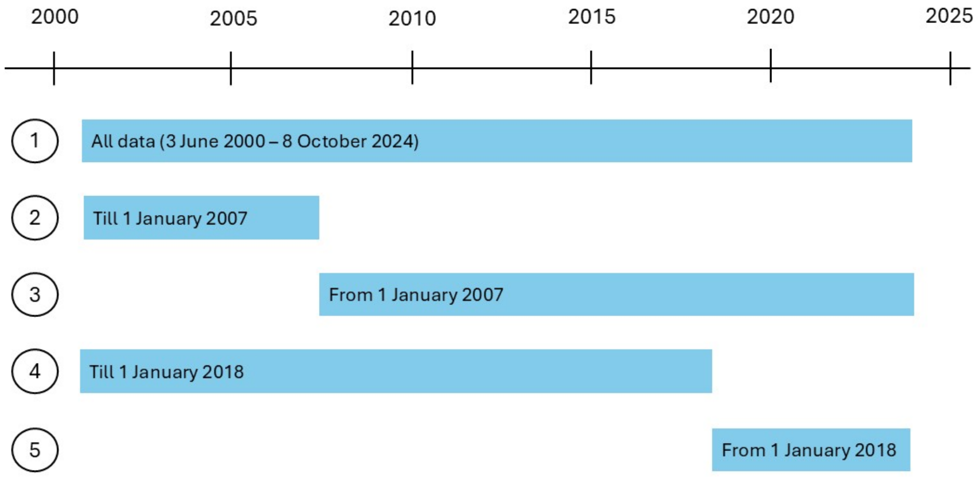

Figure 5.4: Timeline of precipitation data subsets, used to determine whether precipitation is a significant driver of the morphological changes observed within the Msimbazi river.

5.1.3. Annual maximum precipitation

An analysis of annual maximum precipitation was conducted to evaluate potential changes in the intensity of precipitation events over time. The results, presented in Figure 5.5, show that there are no differences in extreme precipitation before and after 2007 and 2018.

This is illustrated by Figure 5.5a, which shows the CDFs of different precipitation subsets. The absence of noticeable shifts in the curves indicates that extreme precipitation levels have remained stable over time. Additionally, the boxplots in Figure 5.5b show comparable means and interquartile ranges (IQRs) across the subsets, further reinforcing this finding.

To statistically verify these findings, a significance test was conducted. As shown in Table 5.2, both p-values exceed the 5% significance threshold, indicating that the differences between the compared subsets are not statistically significant. This shows that the intensity of precipitation events has remained consistent over time, with no substantial increase in annual maximum precipitation.

Table 5.2: Significance test for distributions of annual maximum precipitation

Compared subsets	**KS-statistic**	**p-value**	**Significance**
Pre- vs. Post 1 Jan 2007	0.077	0.85	No
Pre- vs. Post 1 Jan 2018	0.14	0.20	No

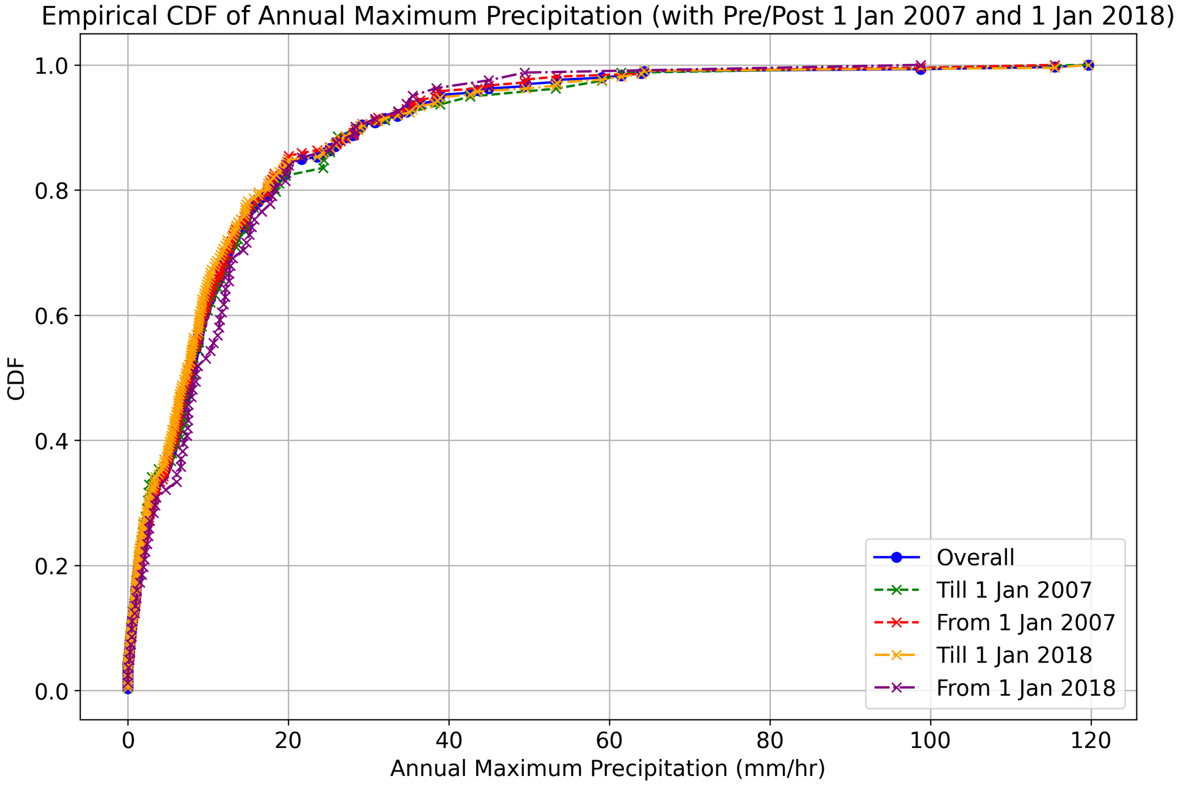

(a) Cumulative distribution function (CDF) of annual maximum daily precipitation. This plot illustrates the distribution of the highest daily precipitation values recorded each year, providing insight into the frequency and magnitude of extreme precipitation events.

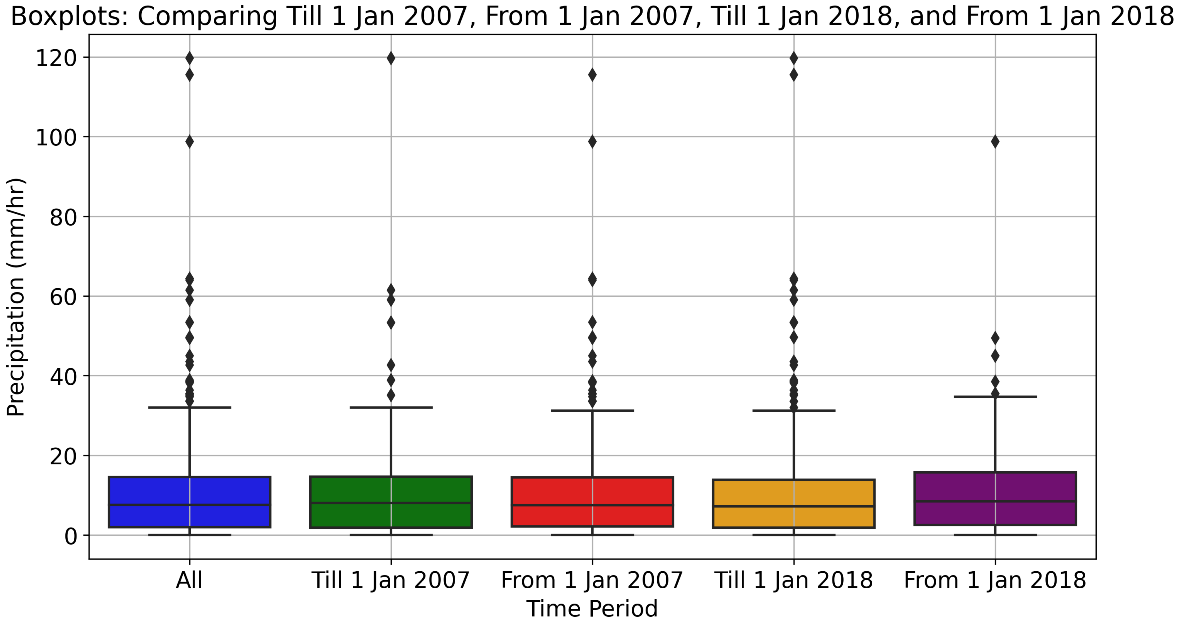

(b) Boxplots of annual maximum precipitation for different time periods. The plot compares the distribution of annual maximum precipitation relative to the 2007–2024 (All) mean across five temporal subsets: the full record, pre-2007, post-2007, pre-2018 and post-2018. The distributions appear broadly similar, indicating limited temporal shifts in annual maximum precipitation patterns over time.

Figure 5.5: Annual maximum daily precipitation characteristics. Panel (a) shows the cumulative distribution function (CDF) of annual maximum daily precipitation, illustrating the frequency and intensity of extreme events. Panel (b) compares distributions across five time periods using boxplots, revealing minimal temporal variation relative to the 2007–2024 mean.

5.1.4. Precipitation durations

Another factor to consider is the duration of precipitation events, as changes in their duration could affect river dynamics by altering the timeframe within which the catchment must manage the water (Westra et al., 2014).

It is possible that either the maximum precipitation events have become longer or that the overall mean precipitation duration has increased. Both possibilities were evaluated using the Peak over Threshold (POT) method, with results for maximum and mean durations shown in Figures 5.6 and 5.7. The POT method was analyzed on how long the precipitation rate remains above the set threshold.

To analyze changes in base precipitation, events with rates between 0 mm/hr and 20 mm/hr were examined (Figure 5.6). A separate analysis for more extreme events, ranging from 10 mm/hr to 100 mm/hr, was also conducted (Figure 5.7).

Figure 5.6 illustrates variations in the duration of the maximum precipitation event over time. However, these differences diminish as the threshold value increases. For example, the mean event duration varies by less than an hour across the observed period. Similarly, Figure 5.7 reveals comparable trends.

Statistical analysis verifies that for thresholds below 6 mm/hr, the differences in event duration are statistically significant, with p-values falling below 0.05 (see Appendix G). This indicates meaningful variations in duration for low precipitation rates. However, for thresholds between 6 and 60 mm/hr, no significant differences in event duration were observed (p-values > 0.05), except at 9 mm/hr.

Statistical significance (p-value < 0.05) indicates that the differences in precipitation durations between periods (e.g., before and after 2007 or 2018) are unlikely to have occurred by chance. However, statistical significance alone does not guarantee that the difference is practically meaningful. Even small changes in event duration, while statistically significant, may not substantially impact river dynamics or erosion risks. For example, slight shifts in precipitation duration, such as a few hours (see Figure 5.6), may not be enough to significantly alter environmental processes.

This is particularly relevant when considering precipitation events corresponding to the determined 2-year return period of 38 mm/hr. At this threshold, no significant differences in event duration were observed. This suggests that although there may be statistical variations in duration for low precipitation rates, such variations are unlikely to have a meaningful impact on river dynamics or erosion risks (Field, 2009). The 2-year return period is important because it typically represents a flow event that occurs roughly every two years, balancing channel-forming energy with flow regularity (Ahilan et al., 2013; Leopold et al., 1995; Mirzaee et al., 2018; Rosgen, 1996).

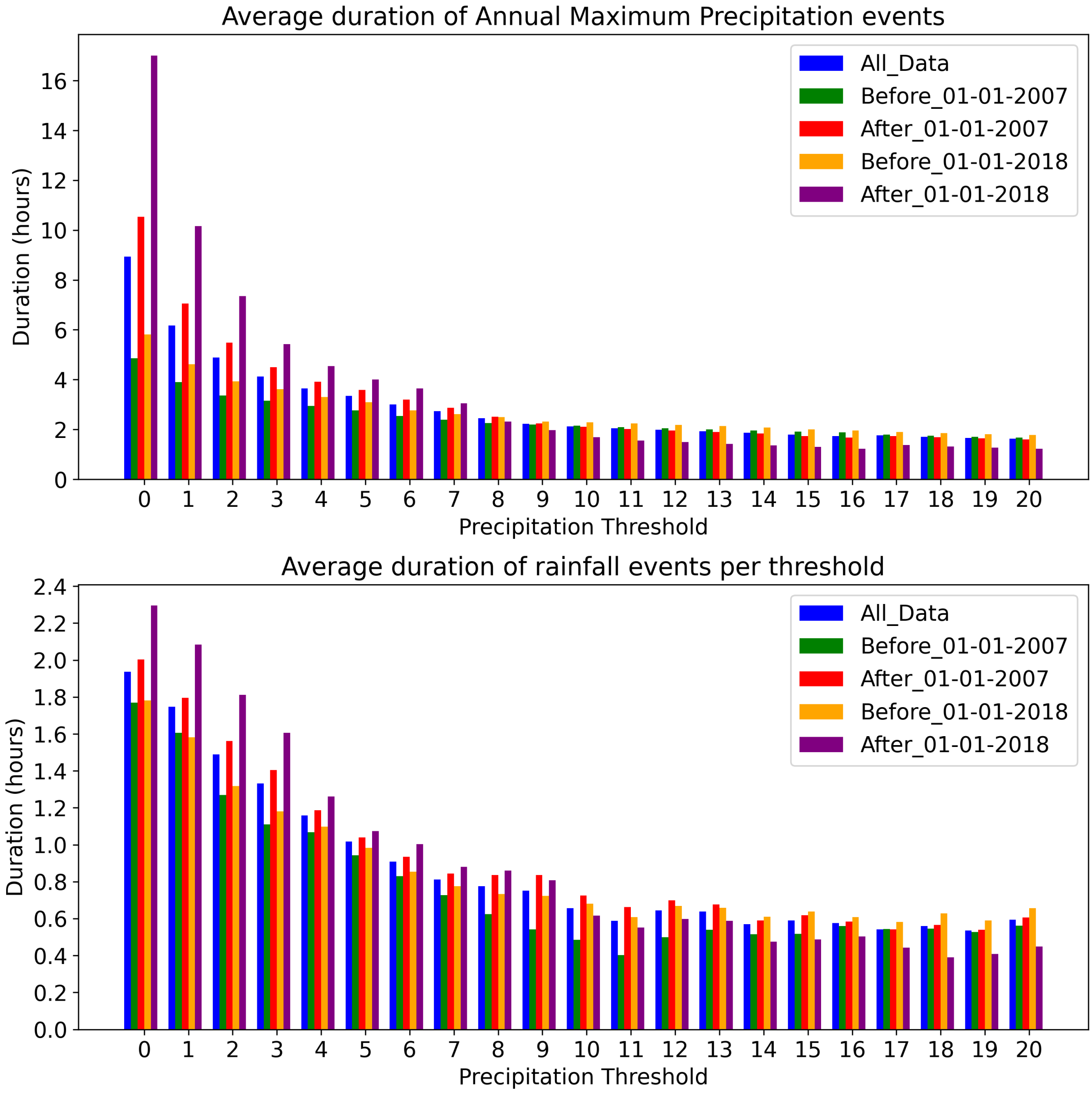

Figure 5.6: Maximum and mean duration of precipitation events with intensities from 0 to 20 mm/hr, shown in 1 mm/hr increments across five time periods. The results reveal minor differences over time, indicating no substantial temporal changes in the duration of low to moderate precipitation events.

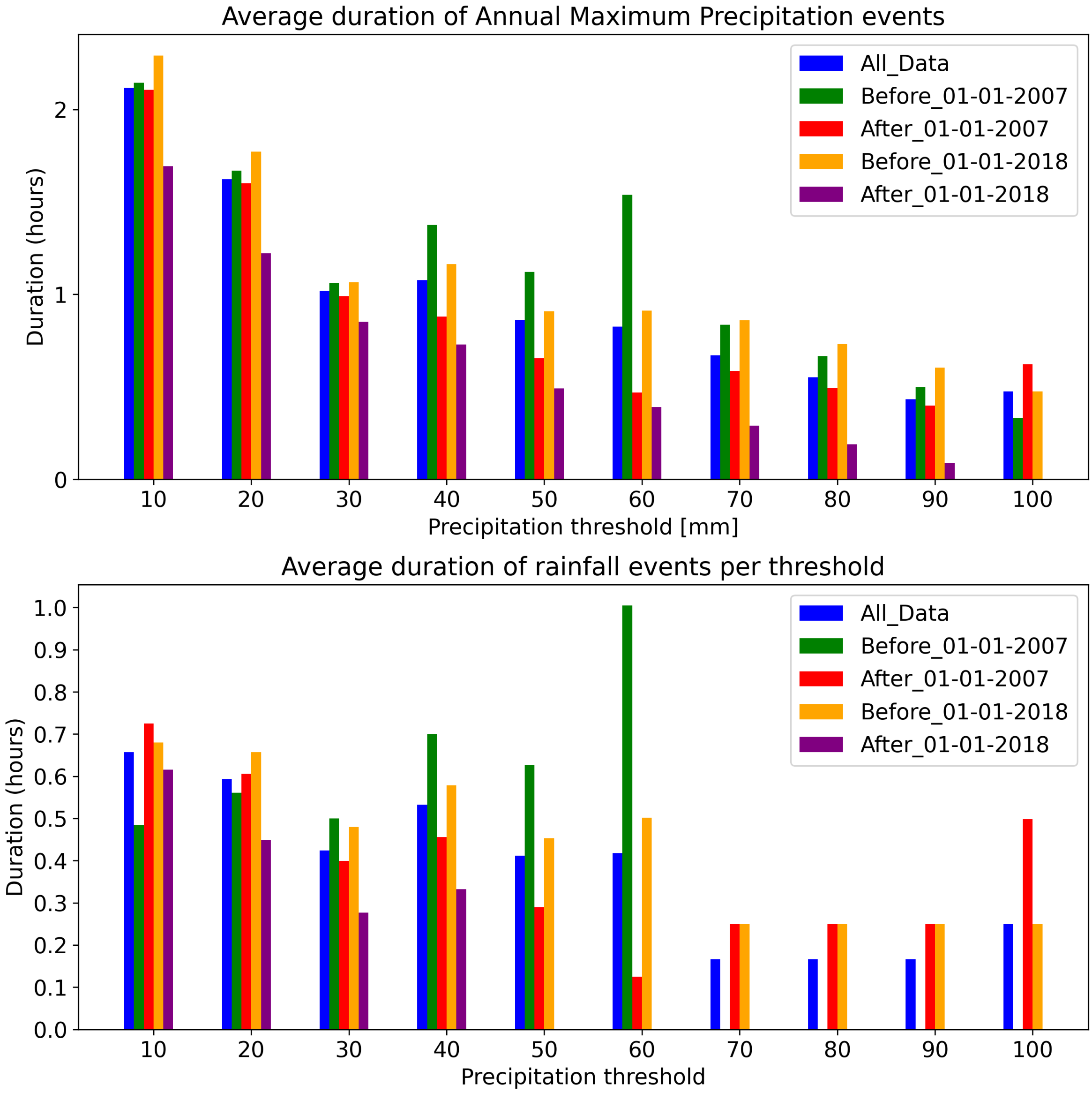

Figure 5.7: Maximum and mean duration of precipitation events with intensities from 10 to 100 mm/hr, shown in 10 mm/hr increments across five time periods. Similar to lower intensities, the duration of more intense precipitation events shows minimal variation over time, indicating stable temporal patterns for heavy precipitation durations.

5.1.5. Precipitation anomalies

In analyzing changes in river width and path within the Msimbazi River catchment, no statistically significant differences were found between precipitation intensity, frequency, or duration across different subsets of the data. This indicates that precipitation patterns are unlikely to be the primary drivers of the observed gradual morphological changes, suggesting that other factors may be influencing these transformations over time.

For this analysis, a reference year was constructed by averaging daily precipitation across the full 23.5-year GPM record. This average annual cycle (Figure 5.8) serves as the baseline for calculating daily precipitation anomalies from 2000 to 2024, defined as deviations from this long-term mean. The anomaly for each day is computed using the Equation 5.1.

$$A_i = P_i - AVG_i \tag{5.1}$$

Where A_i is the anomaly for day i, P_i is the observed precipitation on day i, and AVG_i is the daily average precipitation based on the 23.5 years of data, as shown in Figure 5.8. The resulting anomalies are shown in Figure 5.9, with positive anomalies (blue) indicating days with precipitation above the mean, and negative anomalies (brown) indicating days with precipitation below the mean.

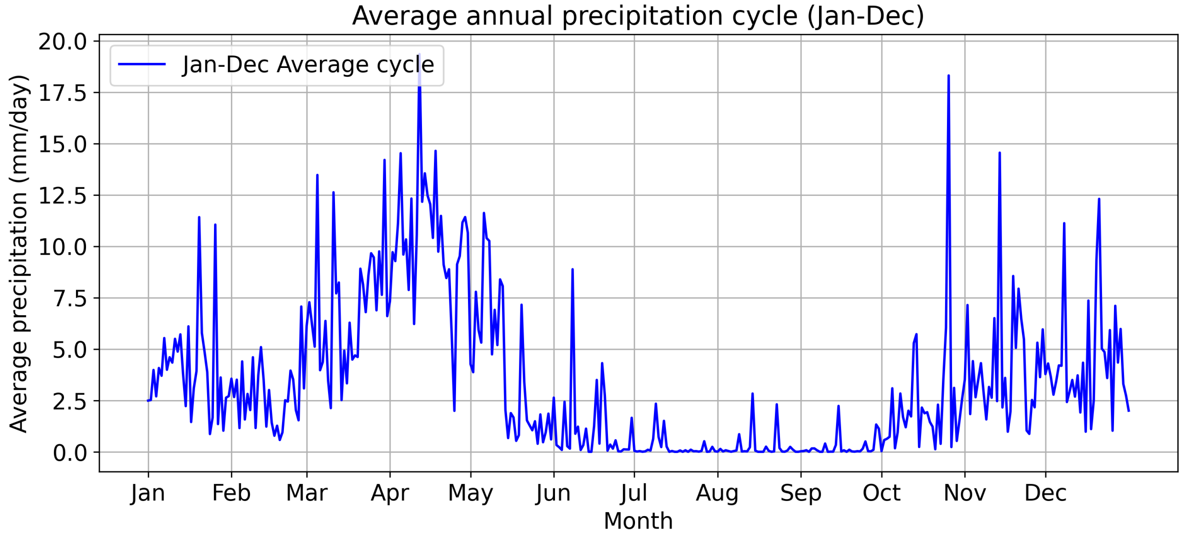

(a) Jan-Dec average precipitation cycle

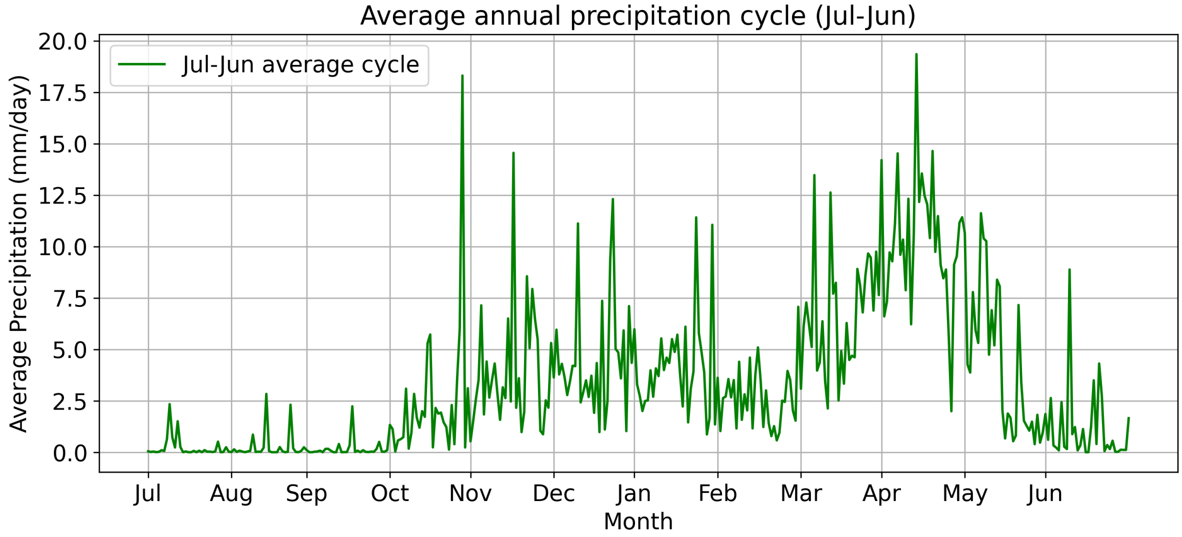

(b) Jul-Jun average precipitation cycle

Figure 5.8: Annual average precipitation cycles

Table 5.3: Significance test for distributions of precipitation anomalies

Compared subsets	KS-statistic	p-value	Significance
Pre- vs. Post 1 Jan 2007	0.013	0.93	No
Pre- vs. Post 1 Jan 2018	0.056	2.8×10^{-5}	Yes

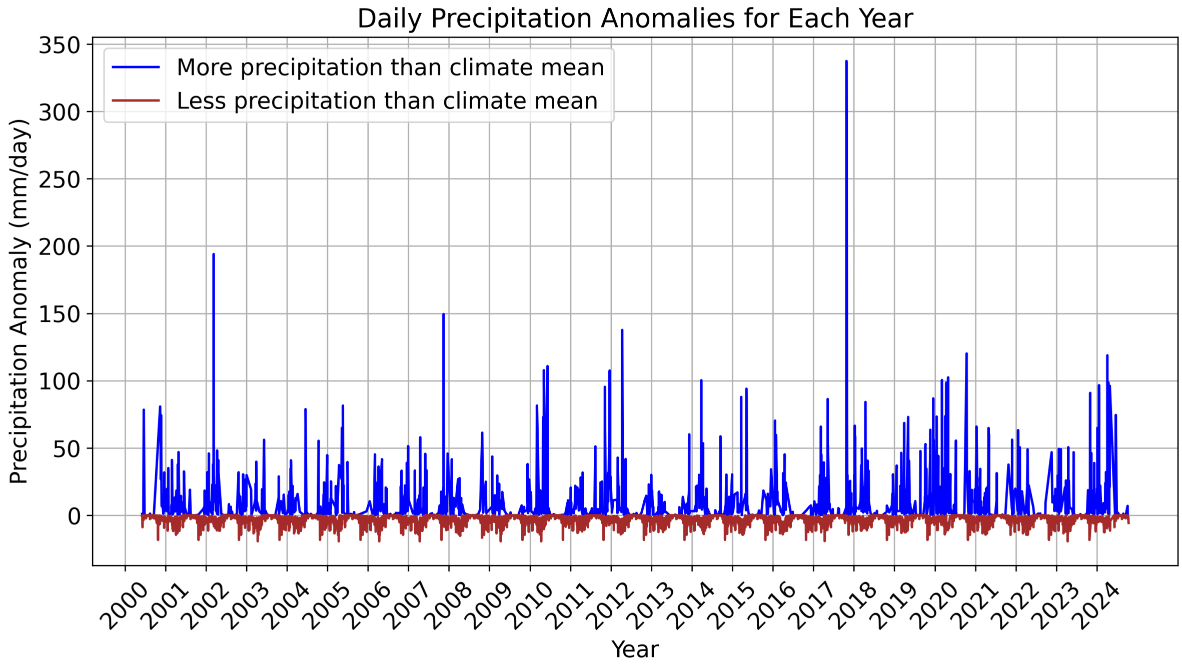

Figure 5.9: Daily precipitation anomalies per year. Anomalies are calculated as the difference between observed daily precipitation and the long-term mean for that calendar day, based on the 2007–2024 average.

The Kolmogorov-Smirnov (KS) test was performed to assess differences in precipitation anomalies before and after 2007 and 2018. The results, presented in Table 5.3, confirm that precipitation anomalies show significant changes after 2018 but not after 2007. The distribution of the anomaly data is given in Figures 5.10 and 5.11.

Additionally, the standard deviation of daily precipitation anomalies is found to be 25.02 mm/day. The standard deviation (σ) is calculated as:

$$\sigma = \sqrt{\frac{1}{n}\sum_{i=1}^{n}(x_i - \mu)^2} \tag{5.2}$$

where x_i are the observed precipitation values, and μ represents the mean of the dataset (Wackerly et al., 2008). The large standard deviation suggests considerable variability in daily precipitation values, implying that fluctuations in precipitation events may be most influential.

As discussed in Chapter 4, the river showed substantial migration between 2023 and 2024. While most of the available precipitation data shows no significant temporal changes and thus likely does not explain the observed morphological changes, as noted in Chapter 3, this conclusion must be approached with caution, as the anomaly analysis clearly shows a significant difference.

Diving deeper into the cause of this, two main factors were identified. The first factor of influence is the occurrence of Cyclone Hidaya (category 1), which stands out as the most intense tropical storm ever documented in the area of Tanzania, making landfall on May 4, 2024 (Erickson & Reiter, 2024). Cyclone Hidaya caused heavy precipitation and powerful winds to East Africa (Igini, 2024). The second factor of influence is the occurrence of El Niño, which lasted from October 2023 till May 2024 (Evarister, 2023; World Meteorological Organization, 2023).

El Niño is a climate phenomenon characterized by unusually warm sea surface temperatures in the central and eastern tropical Pacific Ocean. It occurs when the normal east-to-west trade winds weaken or reverse, leading to significant shifts in atmospheric circulation. These changes disrupt weather patterns globally, including variations in rainfall, temperature, and storm activity. El Niño events typically recur every two to ten years and last for about 9 to 12 months (Evarister, 2023; U.S. Geological Survey, 2024b). In Tanzania, the 2023–2024 El Niño phenomenon contributed to above-average rainfall for two consecutive rain seasons of October - December 2023 (Vuli rains) and March - May 2024 (Masika rains) (Food and Agriculture Organization of the United Nations (FAO), 2024; World Bank, 2024; World Meteorological Organization, 2023).

The anomaly analysis reveals that while precipitation patterns remained largely stable, significant deviations occurred after 2018, with extreme events such as Cyclone Hidaya (May 2024) and the 2023–2024 El Niño phenomenon contributing to increased precipitation.

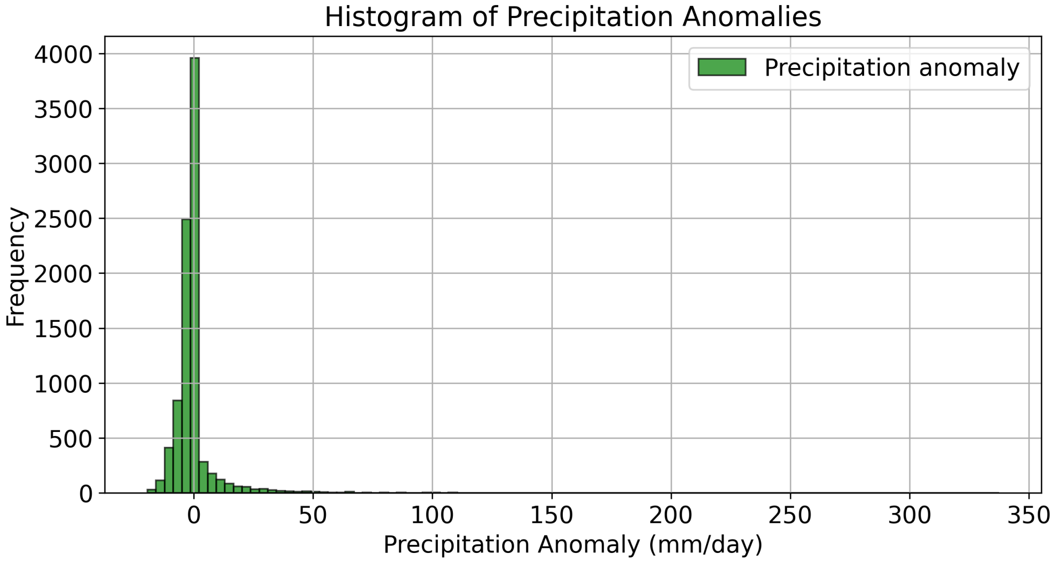

Figure 5.10: Histogram of precipitation anomalies. This histogram shows the frequency distribution of daily precipitation anomalies, calculated as the difference between observed precipitation and the long-term daily mean (2007–2024).

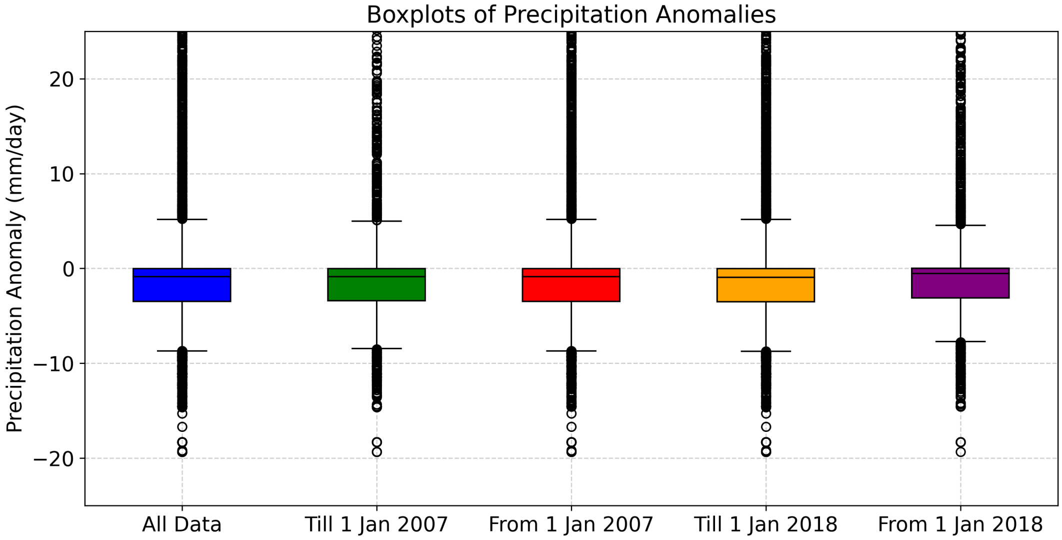

Figure 5.11: Boxplots of daily precipitation anomalies for different time periods. The plot compares the distribution of precipitation anomalies relative to the 2007–2024 mean across five temporal subsets: the full record, pre-2007, post-2007, pre-2018 and post-2018. The distributions appear broadly similar, indicating limited temporal shifts in daily precipitation anomaly patterns over time.

5.2. Landcover changes

One of the key factors influencing river dynamics is landcover and land use, as these factors directly affect runoff and sediment transport. Changes in land use, such as urbanization and deforestation, can alter the catchment's ability to absorb water, leading to increased surface runoff during rainfall events. This, in turn, can amplify river discharge, erosion, and sediment transport, even in the absence of changes to precipitation patterns. When land is cleared or developed, soil permeability decreases, and impervious surfaces (such as roads and buildings) increase, reducing infiltration and promoting faster runoff. This altered runoff regime influences river morphology by modifying sediment supply, flow velocity, and erosion patterns (James & Lecce, 2013; Kayitesi et al., 2022; Wohl, 2004).

This section focuses on quantifying the associated changes. First, population growth is mentioned. Then landcover changes, urbanization and deforestation are addressed. Third, the connection to runoff is assessed. Finally, a case study on the impact of the Standard Gauge Railway (SGR) is presented.

5.2.1. Population growth

Dar es Salaam is experiencing significant population growth, with a current annual increase of around 3% ("World Bank Open Data", 2023). This has led to a catchment population of approximately 1.6 million in 2021, with estimates suggesting this number will rise to 2.5 million by 2030, more than double the 1.2 million recorded in 2011 (Mkilima, 2021).

Figure 5.12 shows the exponential population growth of Dar es Salaam, together with a future prediction of this growth according to the United Nations Department of Economic and Social Affairs et al. (2024).

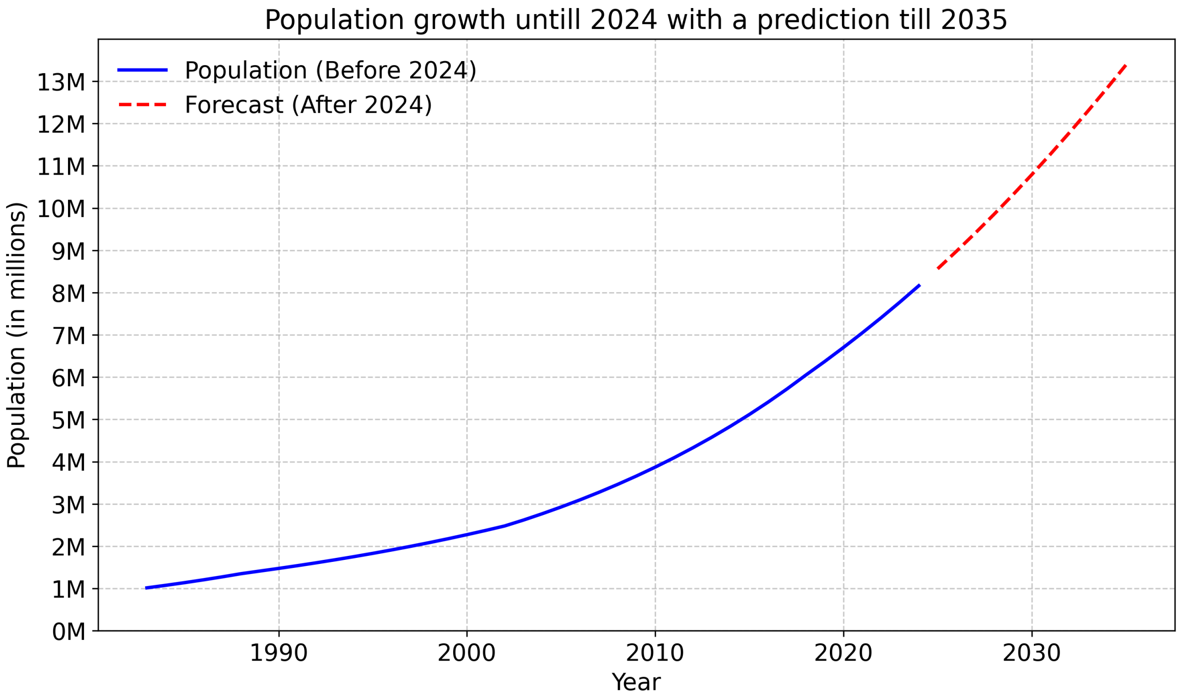

Figure 5.12: Population growth in Dar es Salaam until January 2024 with a prediction till 2035 (United Nations Department of Economic and Social Affairs et al., 2024)

5.2.2. Landcover

Figure 5.13 illustrates the temporal changes in landcover. A comparison between Figures 5.13a and 5.13b shows a noticeable decline in forested areas, particularly in the Upper Basin. These forests have largely been replaced by built-up areas, bushland, and grasslands. Additionally, all sub-basins show a significant increase in built-up areas, reflecting the continued expansion of urban development.

Comparing the 2020 landcover (Figure 5.13c) with that of 2021 (Figure 5.13d) also reveals a transition from forested areas to built-up areas and grasslands. In addition to the westward expansion of the built-up area, the city is also undergoing densification, as grasslands and bare land within previously developed areas are being converted into built-up areas.

The images from 2000 and 2010 (Figures 5.13a and 5.13b, which originate from the Regional Centre for Mapping of Resources for Development (RCMRD)) have a resolution of 30 × 30 m (RCMRD-SERVIRESA et al., 2018a, 2018b). In contrast, the images from 2020 and 2021 (Figures 5.13c and 5.13d, from the European Space Agency (ESA)) have a resolution of 10 × 10 m (Zanaga et al., 2021, 2022). Due to these differences in resolution, the datasets are not directly comparable across sources; however, the 2000 and 2010 images can be compared with each other, as can the 2020 and 2021 images.

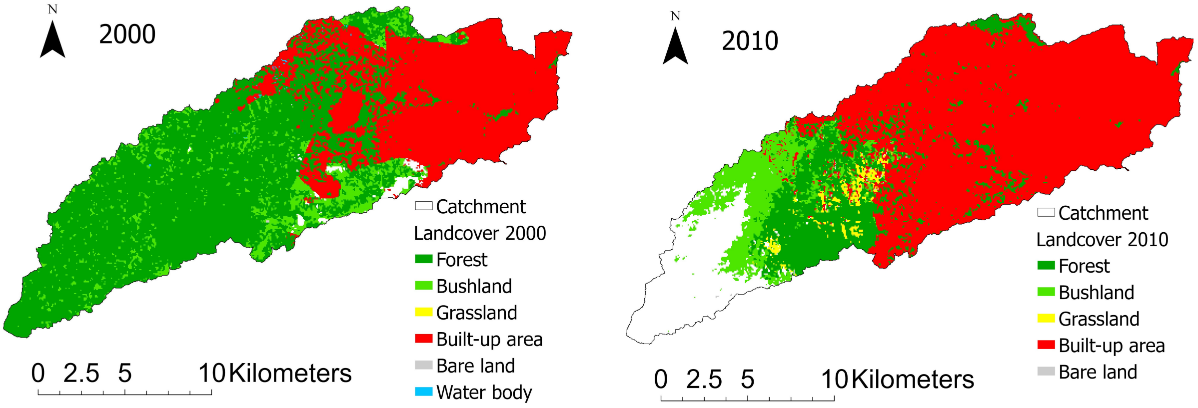

(a) Landcover in 2000 (RCMRD-SERVIRESA et al., 2018a)

(b) Landcover in 2010 (RCMRD-SERVIRESA et al., 2018b). The white stretch corresponds to missing data due to cloud cover.

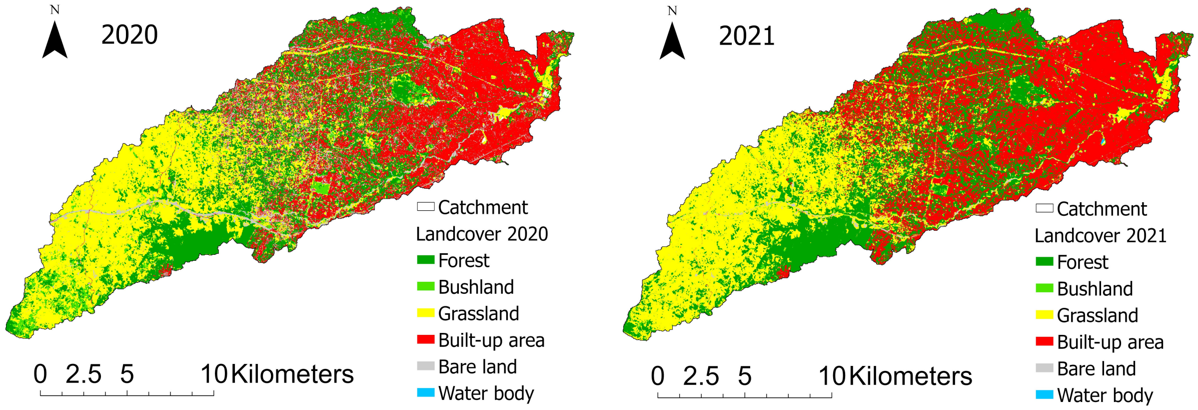

(c) Landcover in 2020 (Zanaga et al., 2021)

(d) Landcover in 2021 (Zanaga et al., 2022)

Figure 5.13: Msimbazi Catchment Landcover for the years 2000, 2010, 2020 and 2021. The images from 2000 and 2010 (RCMRD) have a resolution of 30 × 30 m, while the images from 2020 and 2021 (ESA) have a resolution of 10 × 10 m, making them comparable within their respective timeframes (2000 and 2010 versus 2020 and 2021) but not across sources. The white stretch in Figure 5.13b corresponds to missing data due to cloud cover.

5.2.3. Urbanization

The landcover data confirms ongoing urbanization, but questions remain about its spatial distribution and extent. To address this, building block data from OpenMap Development Tanzania (2025), available for 2016 and 2025, was analyzed. The catchment was divided into a 1×1 km grid, with each cell representing the number of buildings (Figure 5.14) and the total built-up area (Figure 5.15).

A direct comparison of building density (Figure 5.14) suggests an increase from 2016 (Figure 5.14a) to 2025 (Figure 5.14b). However, this is partly misleading, as the total mapped area expanded over time, meaning some areas that appear undeveloped in 2016 may have already contained buildings. To account for this, the data was normalized (Figure 5.16).

The normalized data reveals a general increase in buildings between 2016 and 2025. Some areas show a decrease, which may result from land clearance, evictions, sales, or demolition for new developments. Notably, the highest increase in building density occurs at the western edge of the mapped area, indicating westward city expansion.

Similarly, the analysis of total built-up area (Figures 5.15 and 5.17) reveals a consistent trend. The built-up area has generally increased, with the most significant expansion occurring towards the west.

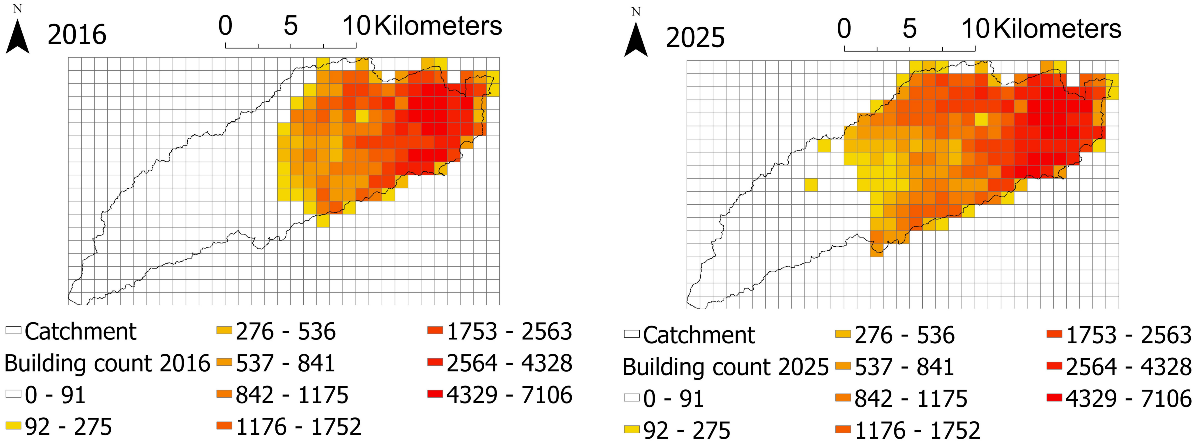

(a) Building density (number of buildings per km^2) in the catchment area in 2016.

(b) Building density (number of buildings per km^2) in the catchment area in 2025, showing urban expansion.

Figure 5.14: Building density (number of buildings per km^2) in the catchment area for 2016 and 2025, illustrating changes in urban expansion (OpenMap Development Tanzania, 2025).

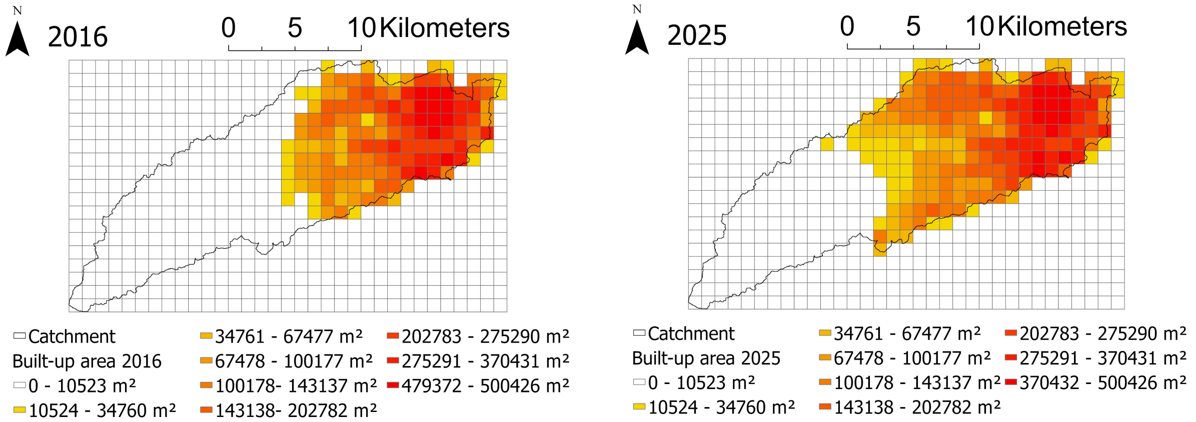

(a) Built-up area (area in km^2 per grid cell) in the catchment area in 2016.

(b) Built-up area (area in km^2 per grid cell) in the catchment area in 2025, showing urban expansion.

Figure 5.15: Built-up area (area in km^2 per grid cell) in the catchment area for 2016 and 2025, illustrating changes in urban expansion (OpenMap Development Tanzania, 2025).

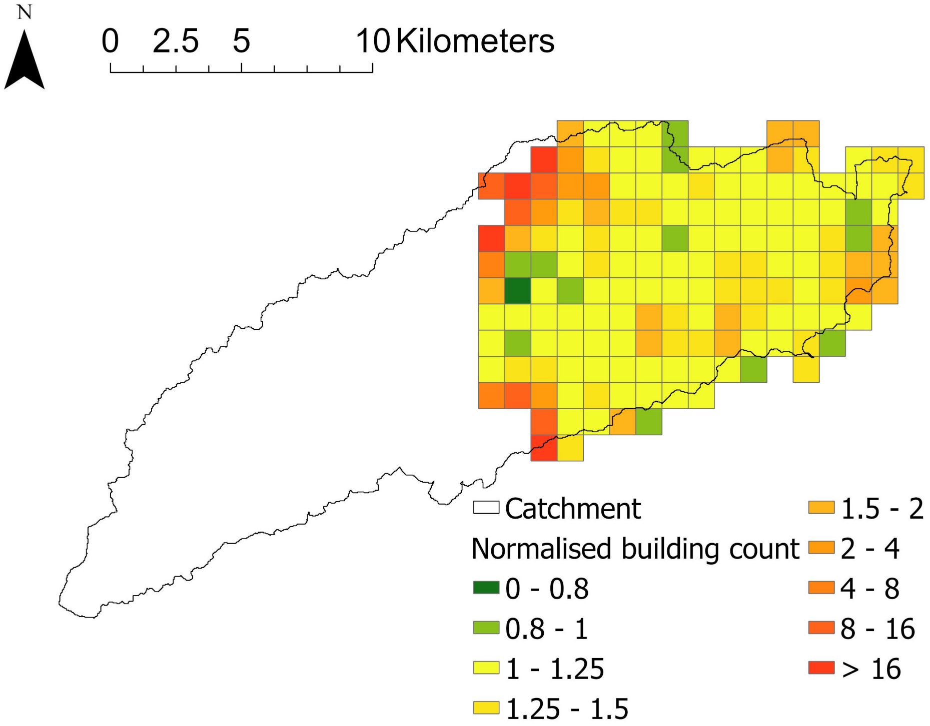

Figure 5.16: Normalized ratio of building density (number of buildings per km^2) between 2025 and 2016 in the catchment area, highlighting spatial patterns of urban expansion and contraction (OpenMap Development Tanzania, 2025).

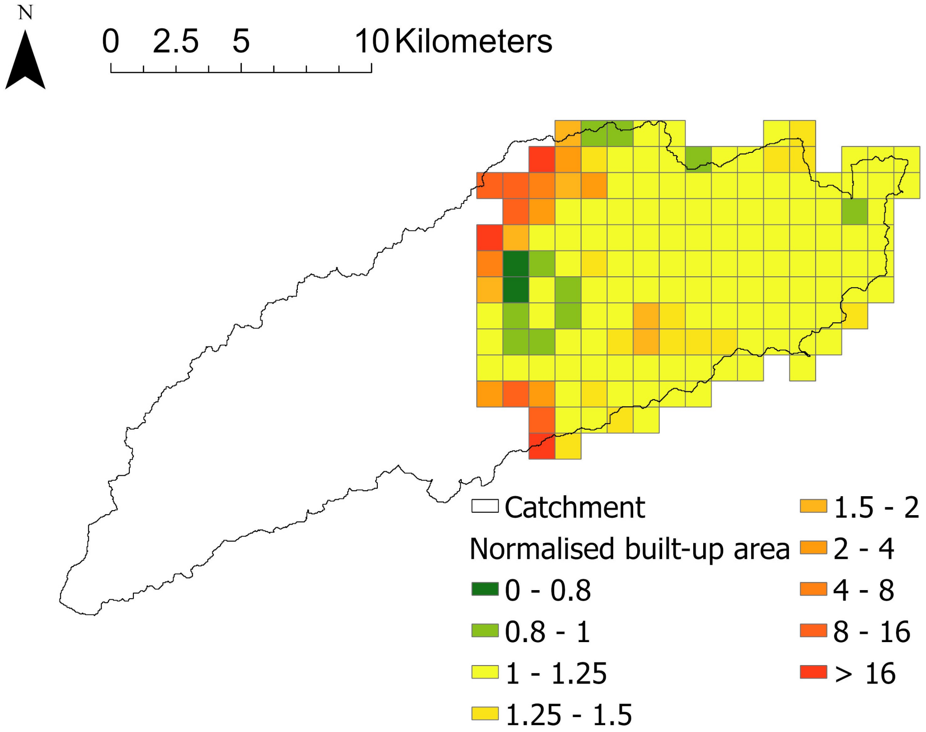

Figure 5.17: Normalized ratio of built-up area (area in km^2 per grid cell) between 2025 and 2016 in the catchment area, highlighting spatial patterns of urban expansion and contraction (OpenMap Development Tanzania, 2025).

5.2.4. Deforestation

From the landcover changes (Figure 5.13), it is evident that deforestation is occurring alongside urbanization in the Msimbazi River catchment. Lupala et al. (2014) highlight that land use changes in Dar es Salaam and surrounding areas have led to an increase in residential and agricultural land, while grazing land and open spaces have declined. Rapid population growth, especially since the 1990s, has driven these shifts, contributing to the degradation of the Pugu and Kazimzumbwi forest reserves, where ecosystem services such as water quality and availability have diminished. Despite efforts to restrain illegal settlements, forest loss continues (Lupala et al., 2014).

Research by Boussougou Boussougou et al. (2018) found that the risk of deforestation is highest in the eastern parts near major urban centers like Pugu and Kisarawe. Vulnerability is particularly pronounced in areas close to major roads and settlements. This aligns with the westward expansion of the city as found for the trends in urbanization (Section 5.2.3).

Figure 5.18 illustrates deforestation trends in the Pugu Nature Reserve, based on Kashaigili et al. (2013). It shows a significant decline in closed forest cover between 1980 and 2010, while open vegetation types, such as bushland and grassland, have increased, confirming the findings.

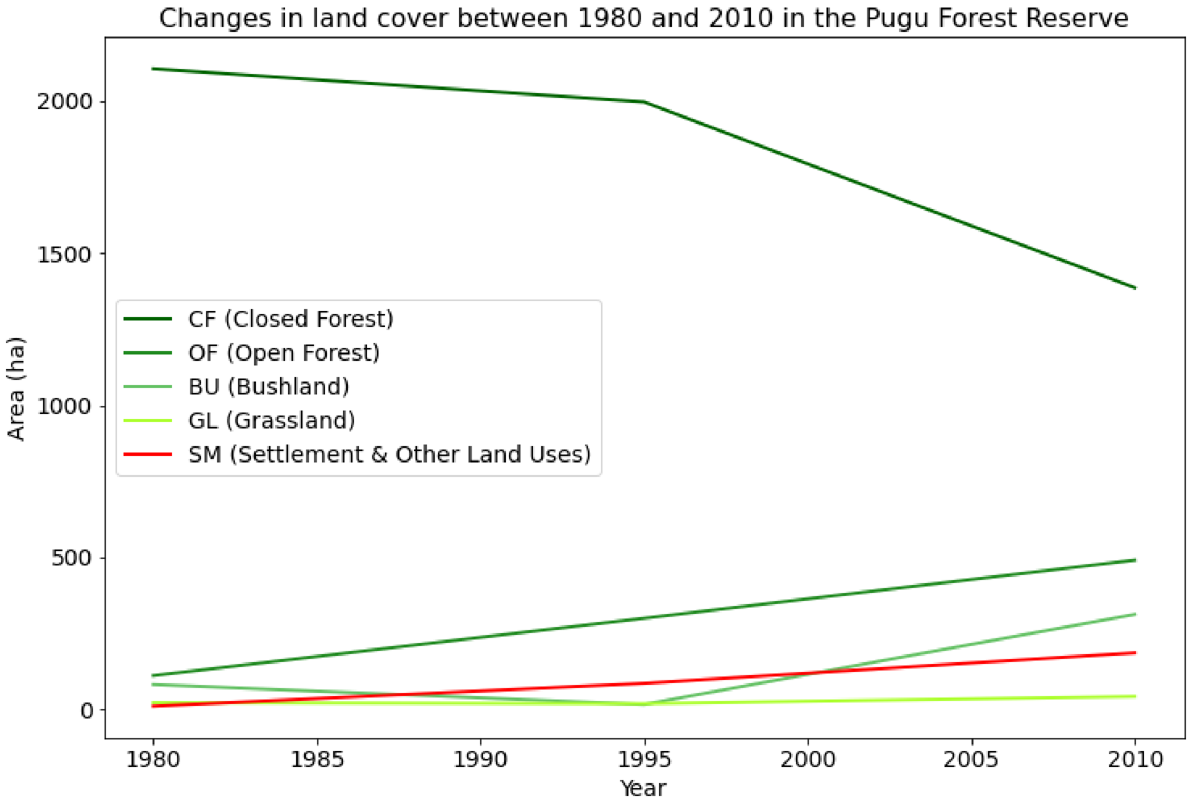

Figure 5.18: Deforestation trends in the Pugu Nature Reserve, located in the upper Msimbazi catchment, between 1980 and 2010 (Kashaigili et al., 2013).

5.2.5. Runoff

Since landcover changes influence the catchment's runoff, it is important to understand runoff as the portion of precipitation that does not infiltrate the soil but instead flows over the land surface and eventually reaches rivers and streams. These changes directly affect how much water enters the river during rainfall events. In particular, landcover transformations such as urbanization and deforestation tend to increase runoff by reducing infiltration capacity and increasing impervious surfaces, leading to greater and faster surface flow (James & Lecce, 2013; Kayitesi et al., 2022; Tang & Lettenmaier, 2012; Wohl, 2004). To quantify this runoff potential, both the catchment's slope and landcover are analyzed.

Literature by Kibugu et al. (2022) and Mkilima (2021) (illustrated in Figures 5.19 and 5.20) indicates an increase in built-up areas and a decline in forested and vegetated land between 2000 and 2010. Given this trend, the observed decrease in runoff potential between 2010 and 2020 is likely an artifact of resolution discrepancies rather than an actual reduction, as shown by Figure 5.13. It is therefore reasonable to assume that the catchment's runoff potential has been consistently increasing over time.

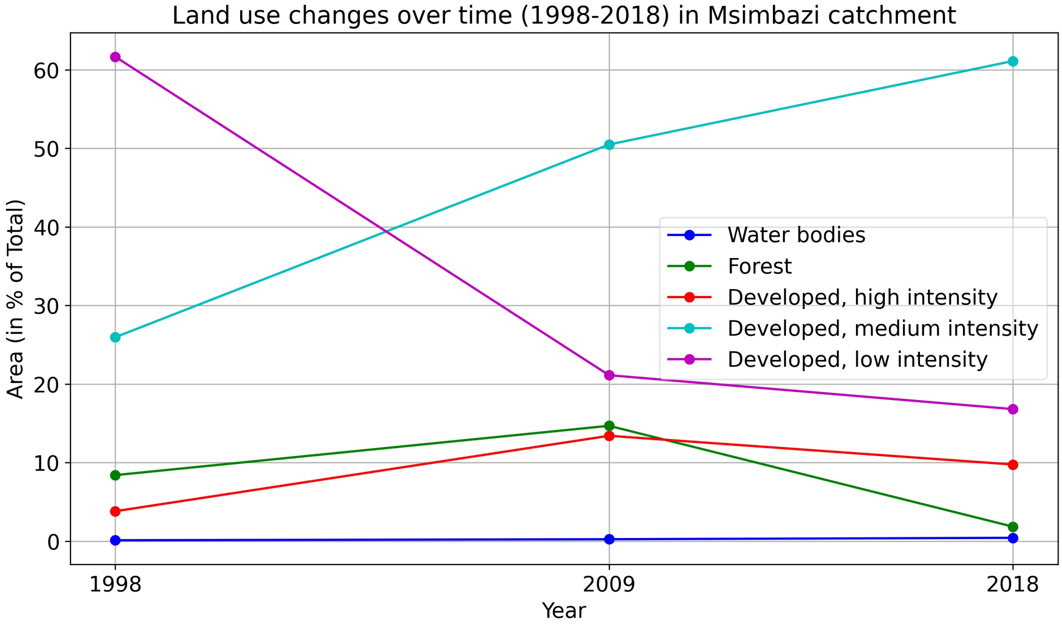

Figure 5.19: Landcover changes between 1998 and 2018 within the Msimbazi catchment according to Mkilima (2021).

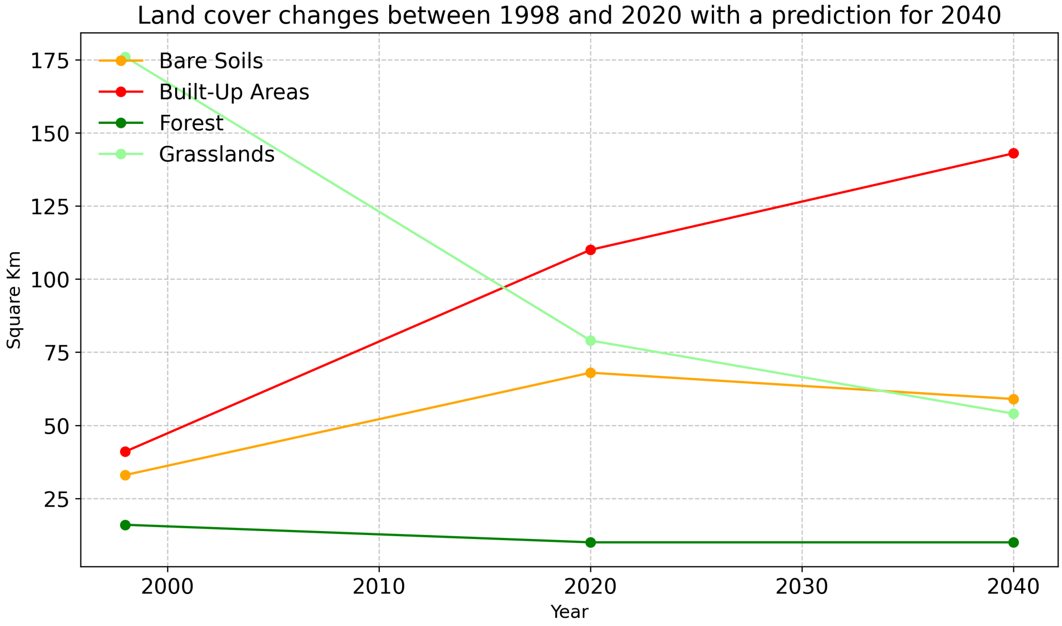

Figure 5.20: Landcover changes (1998-2020) within the Lower Basin with a prediction for 2040 according to Kibugu et al. (2022).

The Ohio Department of Transportation (2020) mentions that impervious surfaces, such as built-up areas, have high runoff coefficients (0.90) due to limited infiltration, while natural landcovers like forest, bushland, and grassland have lower coefficients, reflecting their higher ability to absorb rainfall. Additionally, runoff coefficients increase with slope, as steeper terrains lead to higher flow velocity and runoff volume. Figure 5.23 illustrates the spatial variation in terrain slopes across the Msimbazi catchment. The runoff potential of the catchment, defined as the fraction of precipitation that directly contributes to surface runoff flowing into the river (Tang & Lettenmaier, 2012), is calculated using the following equation:

$$\text{Runoff potential} = \frac{\sum(A_i \cdot C_i)}{\sum A_i} \tag{5.3}$$

where A_i represents the area covered by a specific runoff coefficient, C_i is the corresponding runoff coefficient (Table 5.4), and $\sum A_i$ is the total area of the catchment.

The representative runoff for the catchment is determined using the coefficients provided in Table 5.4. These coefficients are primarily sourced from the drainage design manual by Ohio Department of Transportation (2020). However, to ensure their relevance and accuracy, they have been cross-verified with the findings of Mdee (2015), who applied various models to estimate spatial runoff patterns across Tanzanian catchments. Additionally, the coefficients are compared with local studies by Kibugu et al. (2022) and Igulu and Mshiu (2020), which offer valuable insights into the region's specific runoff dynamics. The quantitative results for the Msimbazi river catchment runoff are presented in Table 5.5.

Table 5.4: Runoff coefficients (Igulu & Mshiu, 2020; Kibugu et al., 2022; Mdee, 2015; Mkilima, 2021; Ohio Department of Transportation, 2020)

Landcover	**Slope**		
	0-2%	**2-10%**	**>10%**
Built-up area	0.90	0.90	0.90
Forest	0.10	0.15	0.20
Bushland	0.25	0.30	0.35
Grassland	0.50	0.50	0.50
Bare land	0.55	0.60	0.65

As shown in Table 5.5, both the total catchment runoff potential and the mean runoff potential increased between 2000 and 2010. A similar increase is observed when comparing 2020 with 2021, though it is less pronounced due to the shorter time span, while the 2000–2010 period covers a decade, the 2020–2021 comparison spans only one year.

Table 5.5: Runoff potential of the catchment

Year	**Total catchment runoff potential**	**Mean runoff potential per m^2**
2000	0.42	0.00045
2010	0.69	0.00073
2020	0.53	0.0062
2021	0.55	0.0064

Interestingly, when comparing 2010 with 2020 (also a 10-year period), a decrease in both the total and mean runoff potential is observed. However, this result is misleading due to differences in data sources and resolution between 2010 and 2020, as previously discussed.

To verify whether the observed changes in runoff potential over the entire catchment are statistically significant, a KS-significance test is performed. Specifically, we compare the collection of runoff potential values per pixel in the runoff maps for the entire catchment, where each pixel is assigned a runoff coefficient (Figure 5.21). The maps are reclassified to ensure they all share the same resolution. These collections of runoff potential values are then subjected to statistical testing. The results, shown in Table 5.8, indicate that the changes are not statistically significant when considering the entire catchment. However, when analyzing individual sub-basins (Figure 5.22), as previously discussed, significant differences are observed between the periods.

Table 5.6: KS-significance test for Runoff potential

Compared subsets	KS-statistic	p-value	Significance
2000 vs. 2010	0.4375	0.0563	No
2020 vs. 2021	0.2941	0.4654	No

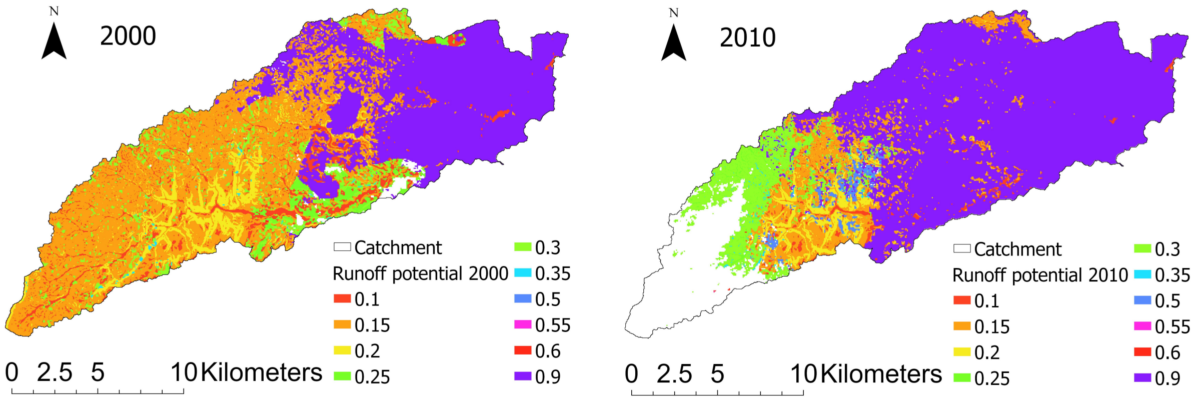

(a) Runoff 2000

(b) Runoff 2010

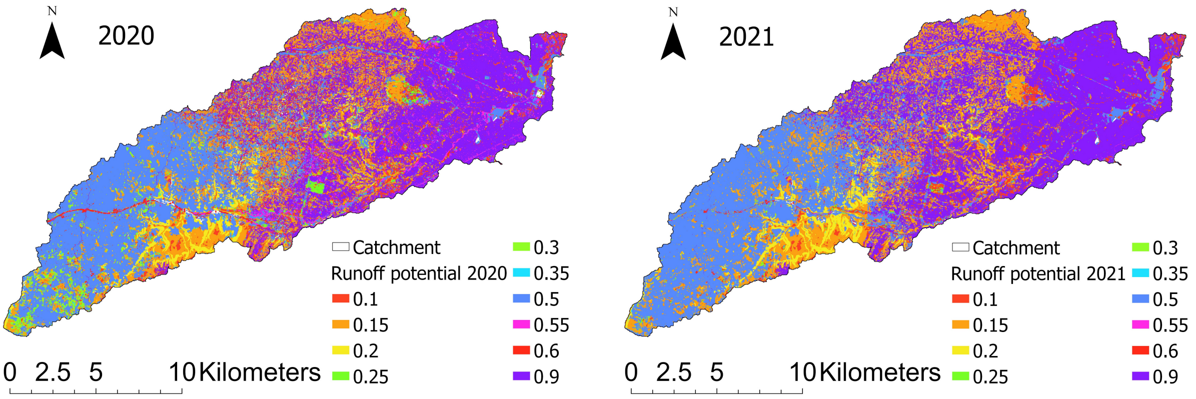

(c) Runoff 2020

(d) Runoff 2021

Figure 5.21: Spatial distribution of the runoff potential in the Msimbazi catchment for each 100 m², over the years 2000, 2010, 2020, and 2021 (Igulu & Mshiu, 2020; Kibugu et al., 2022; Mdee, 2015; Mkilima, 2021; Ohio Department of Transportation, 2020).

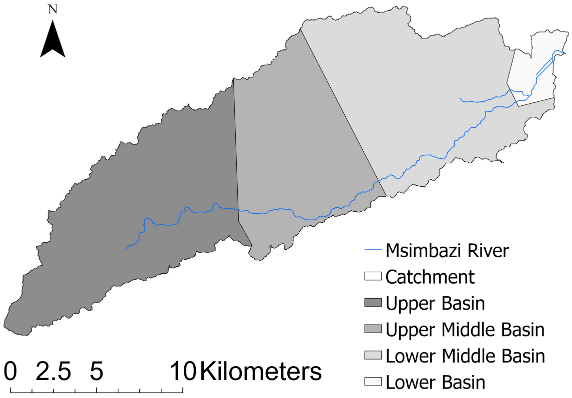

Figure 5.22: The Msimbazi river catchment divided into four sub-basins (van de Sande & Laboyrie, 2021).

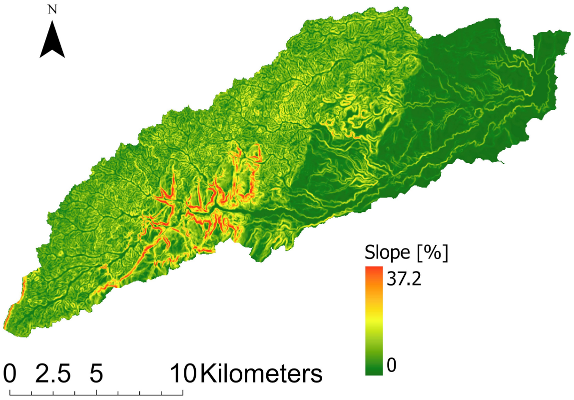

Figure 5.23: Terrain slope distribution [%] across the Msimbazi River basin (U. NASA & SERVIR-RCMRD, 2018).

The evaluation of runoff potential across the four sub-basins within the catchment reveals statistically significant differences when comparing the periods 2000 to 2010 and 2020 to 2021. Specifically, the collections of runoff potential values per pixel in the runoff maps for each sub-basin are analyzed. The results for runoff potential and significance tests are presented in Tables 5.7 and 5.8, respectively.

Between 2000 and 2010, substantial increases in average runoff potential are observed in the Upper Basin (UB), Upper Middle Basin (UMB), and Lower Middle Basin (LMB), see Figure 5.22 for the distinction of these sub-basins. The UB increased from 0.16 to 0.30, while the UMB rose from 0.31 to 0.78. The LMB exhibited a more moderate increase from 0.73 to 0.86. In contrast, the Lower Basin (LB) remained stable at 0.89, indicating that its runoff potential had likely already reached a maximum. These patterns are mirrored in the values expressed per square meter.

Between 2020 and 2021, a consistent increase in runoff potential is evident across most sub-basins. In the UB, the average runoff potential remained unchanged at 0.41, while in the UMB, it increased slightly from 0.51 to 0.55. The LMB rose from 0.65 to 0.67, while the LB increased from 0.68 to 0.70. The smaller magnitudes reflect the shorter one-year interval, whereas greater changes are seen over the ten-year comparison of 2000-2010.

A spatial gradient is visible from Table 5.7, with the downstream sub-basins (LMB and LB) consistently exhibiting higher average runoff potential than the upstream sub-basins (UB and UMB). This is consistent with hydrological expectations, as downstream areas generally experience cumulative flow, higher degrees of development, and lower infiltration capacity (Allan, 2004). Figure 5.21 shows the spatial distribution of the catchment's runoff potential.

The Kolmogorov–Smirnov (KS) test confirms statistically significant changes in runoff potential for most sub-basins. Between 2000 and 2010, UB, UMB, and LMB showed significant distributional changes (KS = 0.28, 0.38, and 0.098 respectively; p$< 10^{-16}$), indicating differing runoff distributions over time. The LB showed no significant change (KS = 0.0038, p = 1), consistent with observed stability. From 2020 to 2021, all sub-basins showed statistically significant changes (KS = 0.014–0.088; p $< 10^{-16}$).

The observed increases in runoff potential, particularly between 2000 and 2010, suggest that land use changes, such as urbanization and deforestation, have directly influenced catchment morphology. These changes, reflected in higher runoff in downstream sub-basins, indicate reduced infiltration and increased surface runoff due to altered landcover. The statistical significance of these shifts supports the conclusion that land use transformations are driving changes in the catchment's runoff characteristics.

Due to varying spatial resolutions in the runoff maps, reliably assessing general changes in runoff potential across the entire catchment from 2000 to 2021 is challenging. However, the Upper Basin offers a clearer signal, as it is free of built-up areas and represents approximately one third of the total catchment area. This absence of urban development reduces classification noise caused by mixed pixels that include both built-up and vegetated landcovers. As a result, the runoff potential in the Upper

Table 5.7: Average runoff potential and per squared meter for different sub-basins and years.

Year	Average Runoff Potential for the Catchment				Average Runoff Potential per m²			
	UB	**UMB**	**LMB**	**LB**	**UB**	**UMB**	**LMB**	**LB**
2000	0.16	0.31	0.73	0.89	0.00018	0.00034	0.00078	0.00095
2010	0.30	0.78	0.86	0.89	0.00032	0.00084	0.00092	0.00096
2020	0.41	0.51	0.65	0.68	0.00044	0.00055	0.00069	0.00074
2021	0.41	0.55	0.67	0.70	0.00044	0.00059	0.00072	0.00075

UB = Upper Basin, UMB = Upper Middle Basin, LMB = Lower Middle Basin, LB = Lower Basin.

Table 5.8: KS-significance test for Runoff potential

Compared subsets	KS-statistic	p-value	Significance
UB (2000 vs. 2010)	0.28	$< 10^{-16}$	Yes
UMB (2000 vs. 2010)	0.38	$< 10^{-16}$	Yes
LMB (2000 vs. 2010)	0.098	$< 10^{-16}$	Yes
LB (2000 vs. 2010)	0.0038	1	No
UB (2020 vs. 2021)	0.014	$< 10^{-16}$	Yes
UMB (2020 vs. 2021)	0.088	$< 10^{-16}$	Yes
LMB (2020 vs. 2021)	0.070	$< 10^{-16}$	Yes
LB (2020 vs. 2021)	0.036	$< 10^{-16}$	Yes

Basin is less affected by landcover heterogeneity, making it a more reliable proxy for assessing broader trends within the catchment. Figure 5.24 illustrates how runoff potential in the Upper Basin has evolved over time.

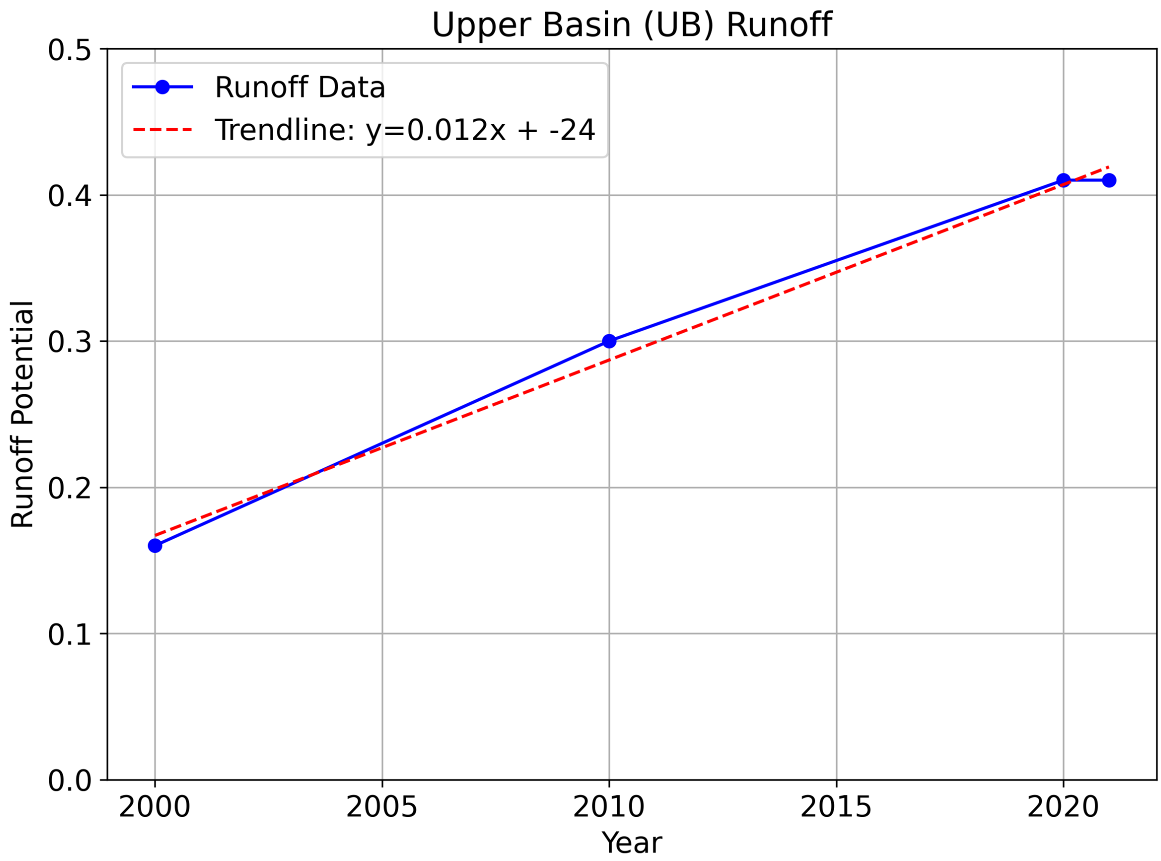

Figure 5.24: Runoff potential in the Upper Msimbazi Basin, which covers over one-third of the total catchment area. The runoff potential gradually increased from 2000 to 2020. Between 2020 and 2021, it appears to stabilize. The short time interval between these points may limit the detection of meaningful changes. Therefore, this stabilization should be interpreted with caution.

Figure 5.24 shows a gradual increase in runoff potential in the Upper Basin from 2000 to 2020. Between 2020 and 2021, this increase appears to stabilize. However, this apparent stabilization may be influenced by the short time interval, only one year, between these two observations, which could reduce the sensitivity of the data to capture meaningful changes in average runoff potential. As such, the observed stabilization should be interpreted with caution, as it may reflect short-term variability rather than a true change in trend.

5.2.6. River width versus runoff

In Chapter 4, the changes in the width of the Msimbazi River were analyzed (see Figure 4.13). To better understand runoff as a potential driver of these observed changes, an analysis was conducted to explore the relationship between runoff potential and river width. This analysis focuses on the Upper Basin, which, as discussed earlier, provides the most reliable data due to minimal noise from built-up areas. River width was calculated for the years for which runoff potential is known, allowing for a direct comparison. Figure 5.25 plots runoff potential on the x-axis and river width on the y-axis, offering insight into how variations in runoff may influence river width.

As illustrated in Figure 5.25, where both axes are spaced linearly, the relationship between water cover width and runoff potential follows a non-linear trajectory, showing a slope-break around 2010. Over this period, the runoff potential in the Upper Basin increases gradually, while the width of the Msimbazi River in this area expands nonlinearly (showing the slope break). Notably, between 2020 and 2021, a sudden drop in river width occurs despite no corresponding change in runoff potential. This change in width occurs without any increase in variability, as the coefficient of variation remains relatively unchanged.

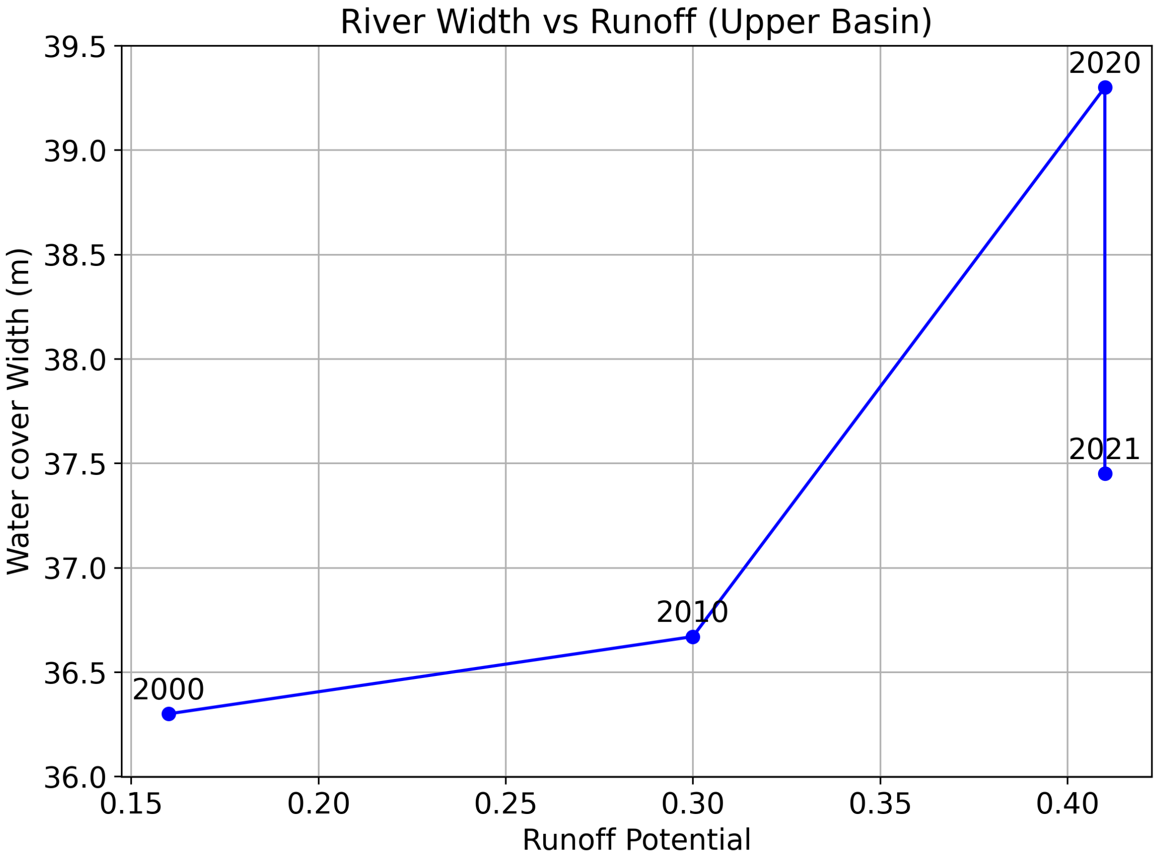

Figure 5.25: Msimbazi River width in the Upper Basin between 2000 and 2021, plotted against varying runoff potentials. The graph indicates a gradual increase in water cover width from 2000 to 2010, followed by a noticeable change in slope after 2010. Although the runoff potential remains constant at 0.41 between 2020 and 2021, the water cover width decreases significantly by nearly 2 meters. This change in width occurs without any increase in variability, as the coefficient of variation remains relatively unchanged.

This indicates that gradual catchment changes, such as urbanization and deforestation, while contributing to the steady increase in runoff potential, do not fully account for the observed morphological changes in river width. Therefore, additional drivers must be influencing the river's dynamics during this period.

5.2.7. Construction of the Standard Gauge Railway (SGR)

Satellite imagery analysis over time revealed an interesting discovery for the Upper Basin. Large amounts of exposed sediment emerge in satellite imagery between January 2018 and March 2018, see Figure 5.26. Given the imminent changes that are found to have occurred in the same timeperiod, it is reasonable to believe the two events are related.

According to TanzaniaInvest (2024), this project is a key component of Tanzania's railway network expansion. The Standard Gauge Railway (SGR) is designed to connect Tanzania from the port of Dar es Salaam on the Indian Ocean to the port of Mwanza on Lake Victoria in the north, with further links to Rwanda, Burundi, and the Democratic Republic of the Congo. The first phase of the project involves constructing the 300 km section between Dar es Salaam and Morogoro, which commenced on April 12, 2017. As part of this phase, excavation work was carried out in the hills near Pugu National Park (TanzaniaInvest, 2024), as can also be identified in Figure 5.26.

The fieldwork findings (as described in Appendix D) support this observation. Figure D.6 indicates that grain sizes do not reach medium to fine fractions, and sediment remains quite angular along a significant stretch of the river. While sorting improves downstream, the lowest observed locations exhibit poor sorting, likely due to ongoing excavation activities exposing deeper soil layers. These findings suggest that the river has experienced a substantial sediment load.

(a) Upper Mismbazi Basin in January 2018

(b) Upper Msimbazi Basin in March 2018

Figure 5.26: SGR construction

Analysis of satellite images from both the SGR construction and the river suggests that the observed sediment flux may be linked to the railway project, as the timing aligns precisely. Additionally, fieldwork observations revealed that the riverbanks exhibited steep profiles well before the first settlements appeared along the river. This rules out increased runoff from urbanization as the sole driver of bank erosion.

Several factors could contribute to bank steepening upstream of urban areas, such as tributary inflows or increased runoff from deforestation. However, the SGR construction may have also played a role.

The project not only exposed large amounts of sediment but also introduced an elevated, dam-like structure in the Upper Basin (see Figure 5.27), which could alter the basin's hydrology. Although no definitive evidence currently supports this, a hydrological assessment of the Upper Basin is recommended to assess the potential influence of the SGR on water flow and sediment dynamics.

Figure 5.27: SGR near Pugu Hills on 20 February 2025, showing protected riverbanks and an elevated, dam-like structure. A railway viaduct connects the hill on the left to the raised dam-like structure on the right.

According to ERM (2019), the environmental assessment reveals that extensive land clearance and excavation during the SGR construction exposed significant sediment. While erosion control measures were implemented, these focused primarily on surface erosion, with limited attention given to the impact on river sedimentation. Stockpiled soil was regulated to minimize erosion, but no provisions were made to assess its effect on sediment influx into the river (ERM, 2019).

While the project adhered to the 60-meter buffer zone regulations around rivers, streams, and water bodies, construction activities within the broader catchment likely altered hydrology. The railway embankment, for instance, could have influenced surface runoff patterns, contributing to localized erosion (ERM, 2019).

Therefore, a hydrological assessment is recommended to better understand the extent of sedimentation impacts and potential changes in riverbank stability due to the SGR project.

Considering the current state of the upstream basin, with protected riverbanks and replanted vegetation, it is likely that future sudden sediment fluxes will not occur due to exposed sediment.

6

Hotspot maps

This chapter evaluates where the Msimbazi River system is most vulnerable. By identifying locations with very high vulnerability, it provides guidance for future mitigation strategies and highlights where interventions are urgent. Accordingly, this chapter addresses the third research question: *Where are the critical erosion hotspots along the Msimbazi River?*

As previously mentioned (Chapter 2), vulnerability hotspots are identified based on the combination of hazard in terms of severity and exposure in terms of susceptibility. As shown in Chapter 4, the Msimbazi River system is subject to two types of changes that pose risks to those within the exposed area. The first hazard is river migration, and the second is river widening.

Exposure is considered the same for both hazards, as it simply represents what lies within the river's exposed area. In this study, exposure is defined as a distance-based metric (see Figure 2.4). Elevation was excluded from the analysis because erosion can undermine high riverbanks regardless of their height, making elevation a poor indicator of erosion vulnerability in this alluvial setting (Van Camp et al., 2014). Figure 6.1 presents the exposure map of the Msimbazi River.

6.1. River migration hotspots

When river migration is considered as a hazard, it is important to distinguish between two temporal scales: long-term, gradual changes within the system, and short-term, rapid responses to events occurring within the catchment. These two rates are calculated over different periods to assess the migration hazard in both contexts, as shown in Figure 6.2. The long-term hazard is assessed for the period 2007–2024, reflecting the gradual shifts in migration, while the short-term hazard is assessed for 2020–2024, focusing on more immediate responses to events such as extreme precipitation. This distinction is critical because, as shown in previous cases, the river can respond abruptly to such events (Izdori et al., 2022; Kazi, 2019; UNDRR, 2018), which is why evaluating vulnerability in response to short-term migration is necessary. Additionally, the temporal extent used to assess migration rates and width changes influences the interpretation of results. Shorter time periods tend to highlight more extreme values, as these are less likely to be averaged out, unlike in longer time frames (Eggert et al., 2015). For each type of hazard, a corresponding hotspot map has been developed.

With the exposure, the hazard (long- and short-term), and the vulnerability equation (Equation 2.2), the hotspot maps are created. Figure 6.4 shows the long-term (2007–2024) river migration hotspot map, and Figure 6.5 shows the short-term (2020–2024) map. In these maps, hotspots are indicated in red, corresponding to areas with very high vulnerability. More detailed images are given in Appendix H.

Discrepancies between the river centerline and the satellite imagery are due to differing acquisition dates: the satellite image is from July 2023, while the centerline is from May 2024. Due to ArcGIS limitations, updating the satellite image is not possible. The centerline was extracted from Sentinel imagery with a 10 × 10 meter resolution, introducing a positional uncertainty of about 7 meters (see Appendix C).

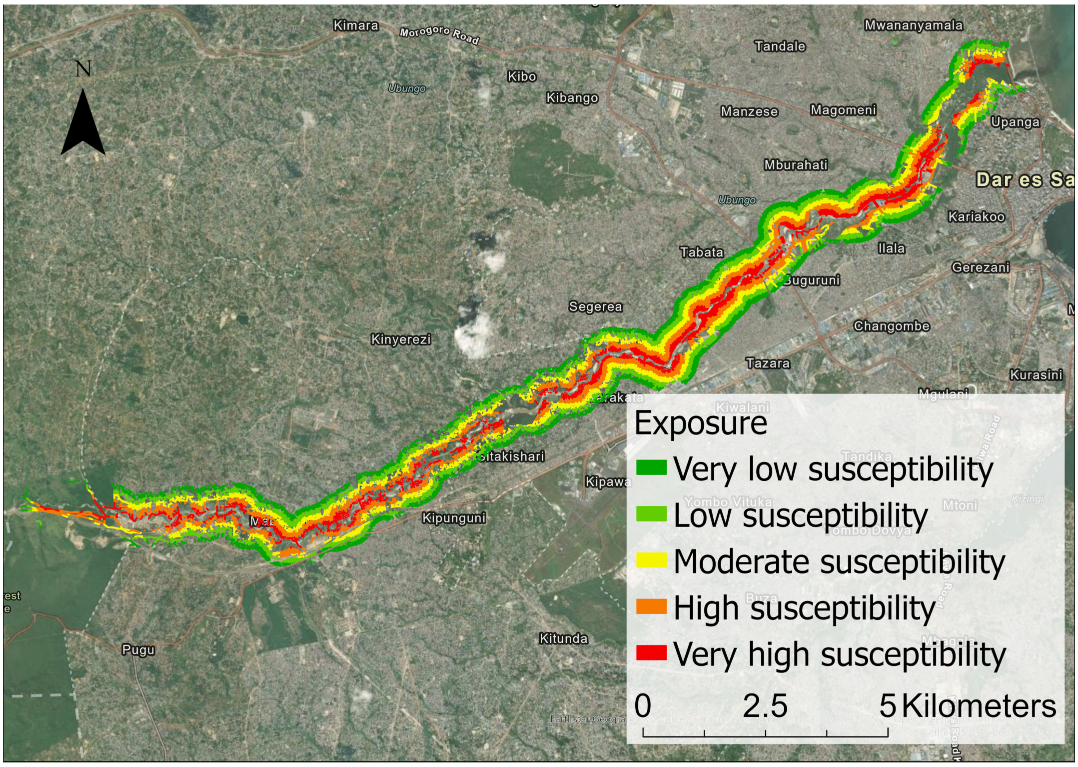

(a) Overview of the exposure map

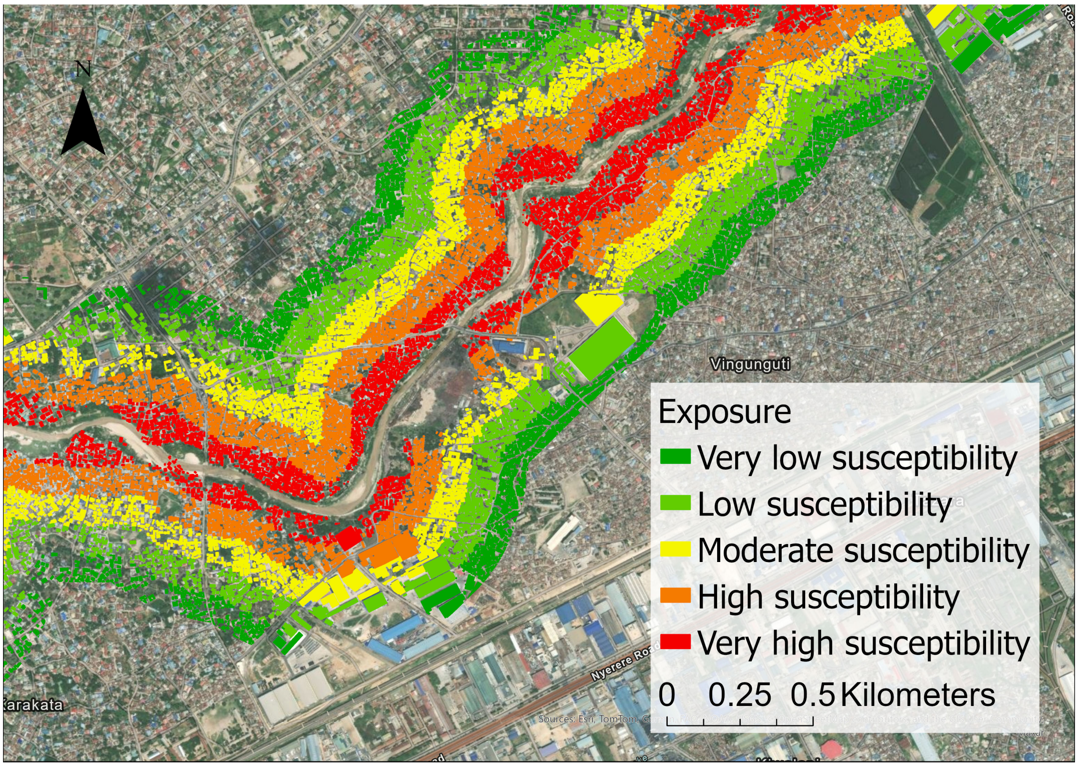

(b) Detailed view of the exposure map

Figure 6.1: Exposure analysis of the Msimbazi River. (a) Overview map showing exposure, based on building footprint data (Nyalusi et al., 2025) and infrastructure data (Humanitarian OpenStreetMap Team (HOT) & OpenStreetMap contributors, 2025), within a 500-meter buffer on either side of the river. (b) Detailed view highlighting a specific section within the Lower Middle Basin of the exposure map.

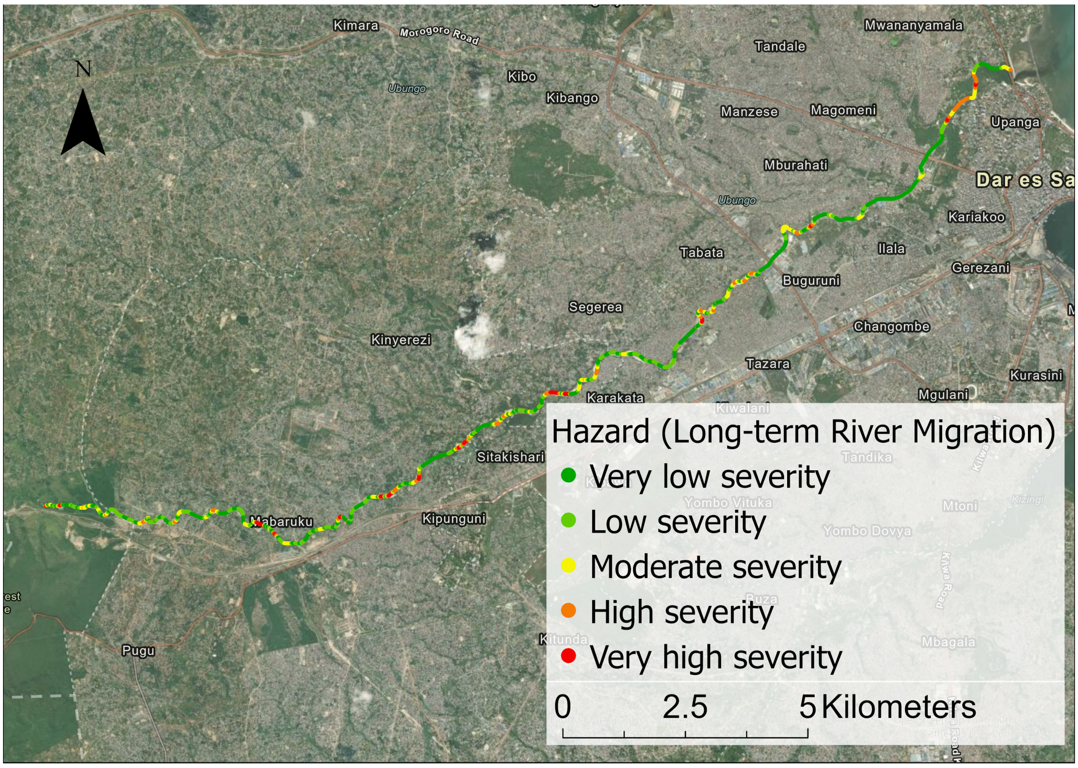

(a) Long-term hazard (River migration rates between 2007 and 2024)

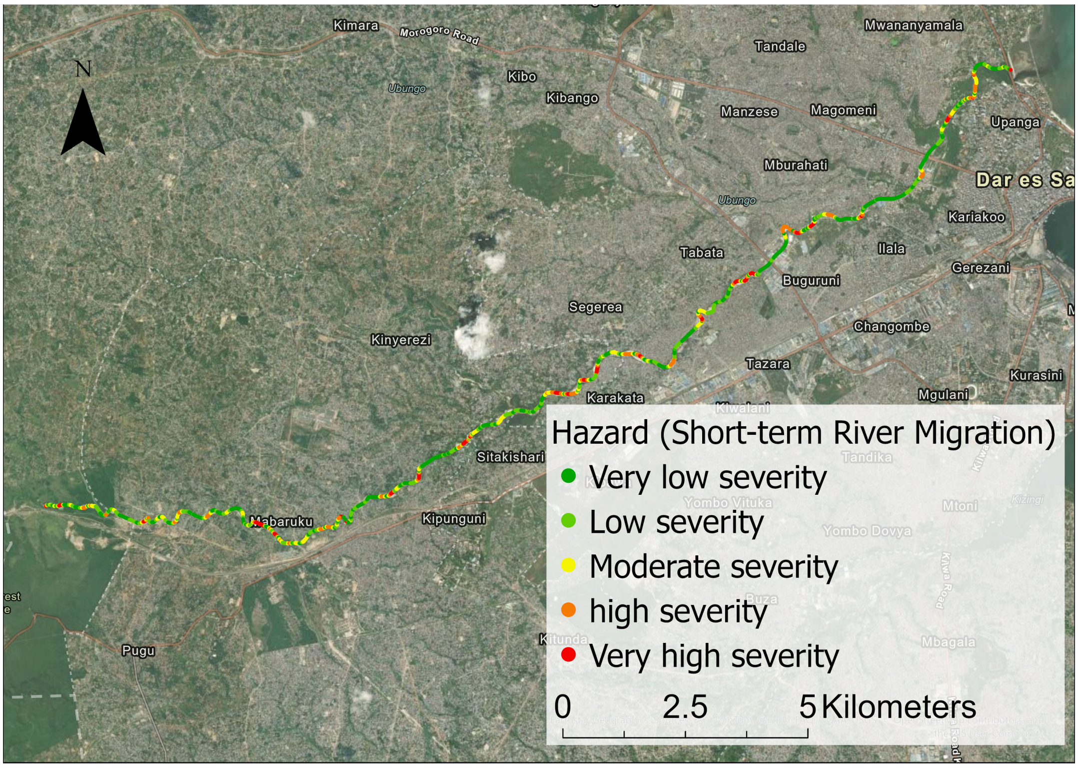

(b) Short-term hazard (River migration rates between 2020 and 2024)

Figure 6.2: Mimbazi river Long- and short-term hazard (River migration)

As described in the methodology, the classification of migration rates into severity levels is based on the Natural Breaks (Jenks) method, which groups similar values to highlight meaningful differences in river behavior (de Smith et al., 2018). As a result, the identified hotspots should always be interpreted in relation to the actual severity values. In river systems with generally low migration rates, some areas may still be classified as hotspots, even if the absolute migration rates are relatively minor. Therefore, the classification should always be cross-checked with the underlying severity values to understand the level of vulnerability in absolute terms.

Given that migration rate is used as a proxy for hazard, the distribution of long-term migration rates is shown in Figure 6.3a. To classify these rates into categories ranging from very low severity to very high severity, the Natural Breaks (Jenks) method, described by de Smith et al. (2018), is applied. To ensure consistency and comparability between hotspot maps based of long-term and short-term migration rates, the class breaks derived from the long-term data are also applied to the short-term migration rates (Figure 6.3b).

In the case of the Msimbazi River, the highest severity class corresponds to migration rates ranging between 12 and 18 meters per year. This is equivalent to approximately 30–50% of the local river width. According to the rule of thumb proposed by Langhorst and Pavelsky (2023), rivers typically migrate at a rate of 0.1–2% of their width, which, for the Msimbazi River, would correspond to a rate of approximately 0.05–1 meter per year.

A comparison between the hotspot map subject to the long-term hazard (Figure 6.4) and the hotspot map subject to the short-term hazard (Figure 6.5) reveals a greater number of very high vulnerability hotspots in the map resulting from short-term migration. In the map resulting from long-term migration, areas with very high vulnerability are primarily concentrated in the Upper Middle Basin. By contrast, the Lower Middle and Lower Basins are predominantly classified as having high, rather than very high, vulnerability. These patterns are consistent with the findings presented in Chapter 4, which identified the Upper Middle Basin as showing the highest rates of migration, thereby representing a significant hazard. The higher number of hotspots observed in the map for the short-term hazard is likely due to two main factors. First, the increased migration rates recorded between 2023 and 2024, which coincide with the El Niño phase and Cyclone Hidaya. Second, short-term rates are averaged over a shorter time period, making them more sensitive to recent changes (Eggert et al., 2015; Pannone & Vincenzo, 2022).

Closer inspection of the hotspot map based on the long-term hazard reveals evidence of past meandering. This is indicated by the May 2024 riverline intersecting built-up areas that are visible in the underlying satellite imagery from July 2023, as shown in Figure 6.6. This spatial mismatch suggests that the river has already migrated through previously developed land. The resulting changes have likely increased the vulnerability of exposed buildings and infrastructure. This is evident from the classification of inland structures, previously farther from the river, as now being within zones of very high vulnerability.

Several locations in the Lower Middle and Lower Basins that were classified as high vulnerability in the hotspot map subject to the long-term migration have been reclassified as very high vulnerability in the short-term analysis. This is due to a increase in severity of the hazard for the short-term period (Pannone & Vincenzo, 2022). The hotspots in the Upper Middle Basin remain largely consistent across both time periods.

As the hotspot map is derived from historical migration data, it effectively serves as a hindcast of vulnerability hotspots. As illustrated in Figure 6.6a, a cutoff has already occurred at this location, likely resulting from chute channeling processes (Pannone & Vincenzo, 2022). Despite the fact that geomorphological changes have already taken place in certain areas, the hotspot mapping remains highly relevant for forecasting purposes for two key reasons. First, many of the identified hotspots are characterized by gradual, progressive riverbank migration, which increasingly increases the vulnerability of adjacent infrastructure and buildings. This increased vulnerability as a result of the gradual catchment changes is dangerous if singular events, like extreme precipitation, occur. Without the implementation of mitigation strategies, these exposed objects remain at significant vulnerability. Second, the Msimbazi River shows dynamic behavior, suggesting that morphological adjustments such as cutoff formation and channel reactivation can recur at previously active locations. This behavior, often involving the reoccupation of former meander bends or migration corridors, is well-documented in fluvial geomorphology. For example, Hooke (2003) provides evidence from long-term studies of meandering rivers that show old meander loops and abandoned channels can be reactivated under changing flow or sediment conditions (Hooke, 2003).

Figure 6.6b provides an example of a meander bend migrating toward a built-up area. The hotspot map clearly indicates that the nearby structures are vulnerable to ongoing and future erosion. Figure 6.7 shows that the identified hotspots align with locations that were observed as vulnerable during field visits.

In conclusion, river migration hotspots are consistently identified in the Upper and Upper Middle Basins in maps resulting from long-term and short-term hazards. In contrast, the Lower and Lower Middle Basins show hotspots only in the short-term analysis. Although these hotspots are identified through a hindcast, they remain highly relevant for future forecasts, as they indicate areas with persistent or emerging vulnerability.

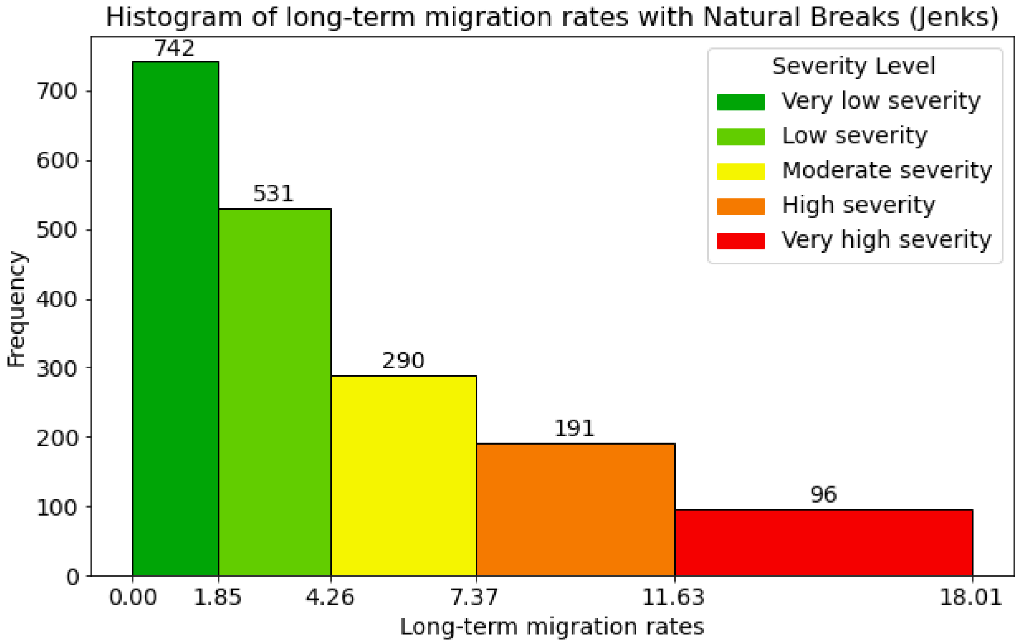

(a) Long-term (2007–2024) migration rate classifications.

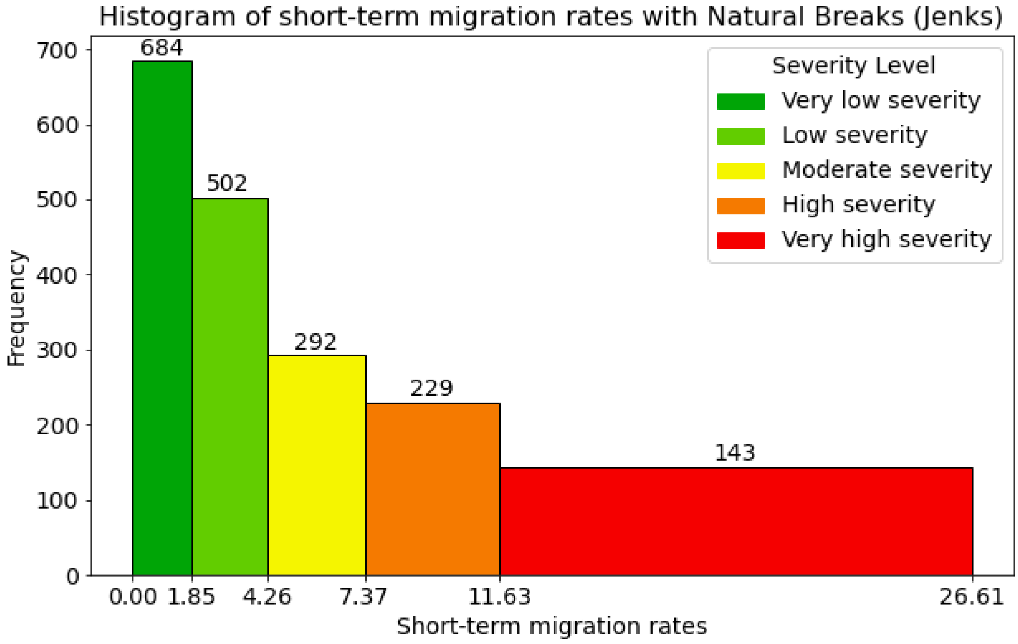

(b) Short-term (2020–2024) migration rate classifications.

Figure 6.3: Histograms of river migration rates classified by Natural Breaks (Jenks) (de Smith et al., 2018). The severity of migration increases from left to right in both graphs. Short-term migration rates are classified according to breaks in long-term migration rate data to facilitate comparability between the two hotspot maps.

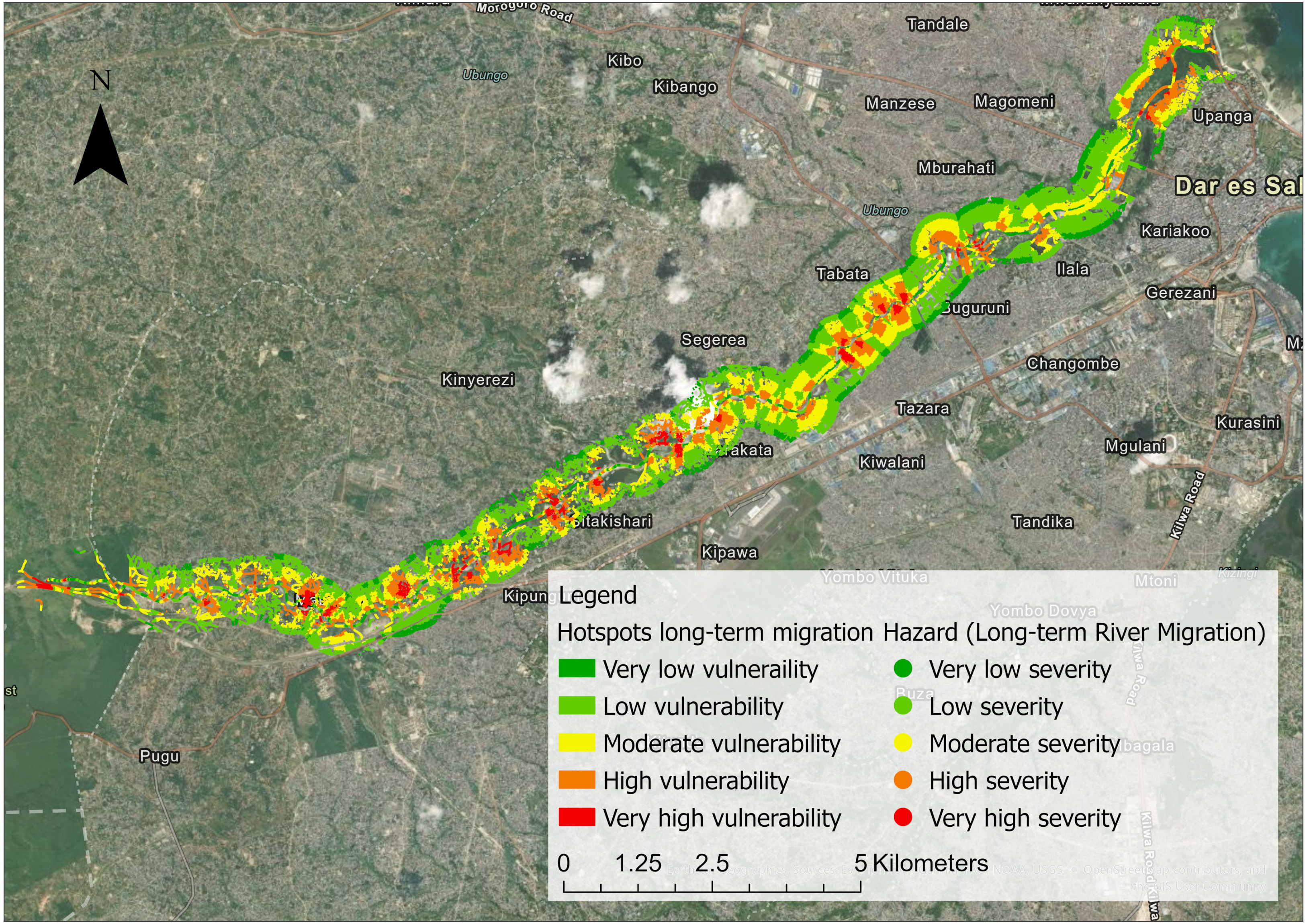

Figure 6.4: Overview of the hotspot map as a result of long-term (2007-2024) river migration.

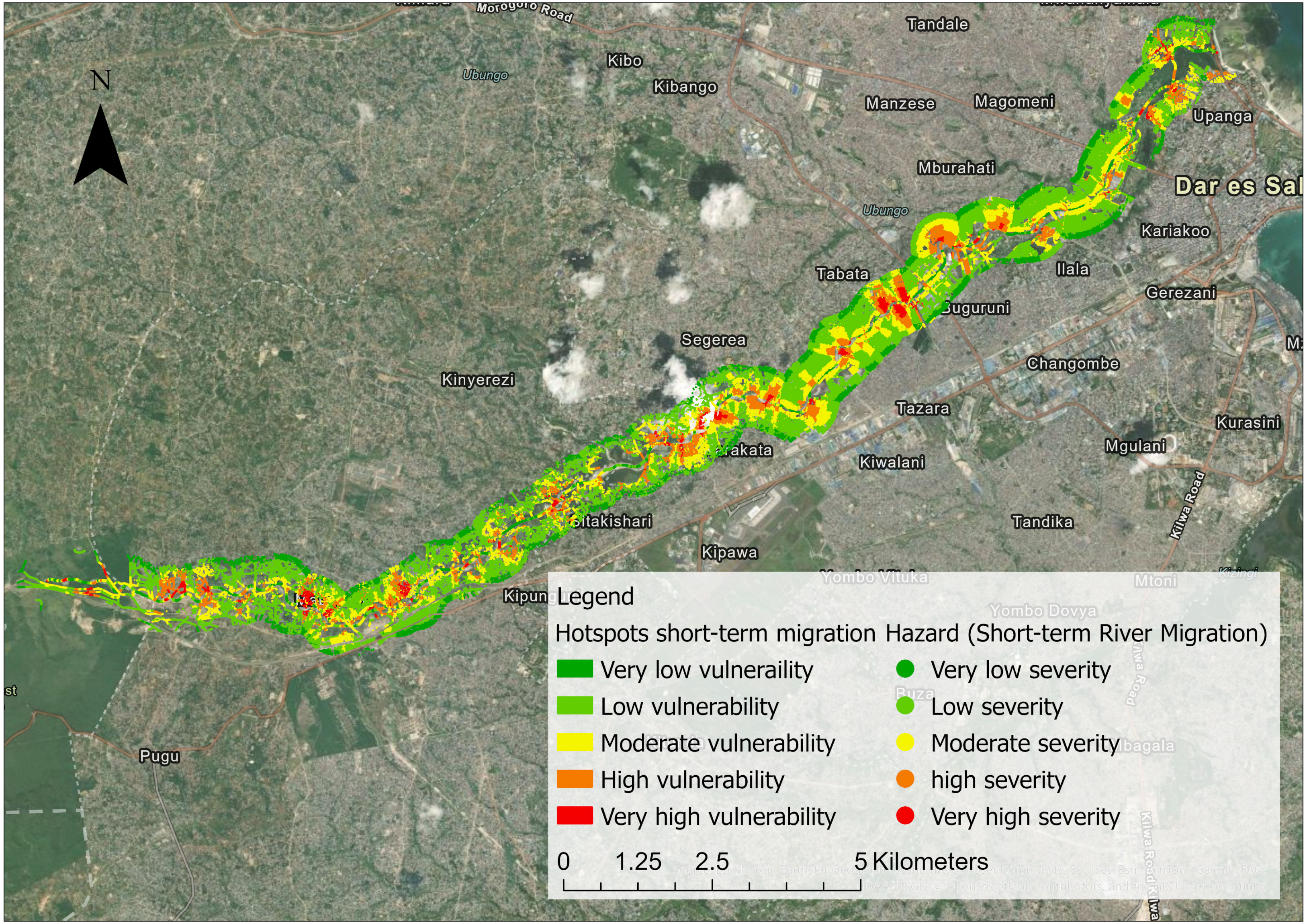

Figure 6.5: Overview of the hotspot map as a result of short-term (2020-2024) river migration.

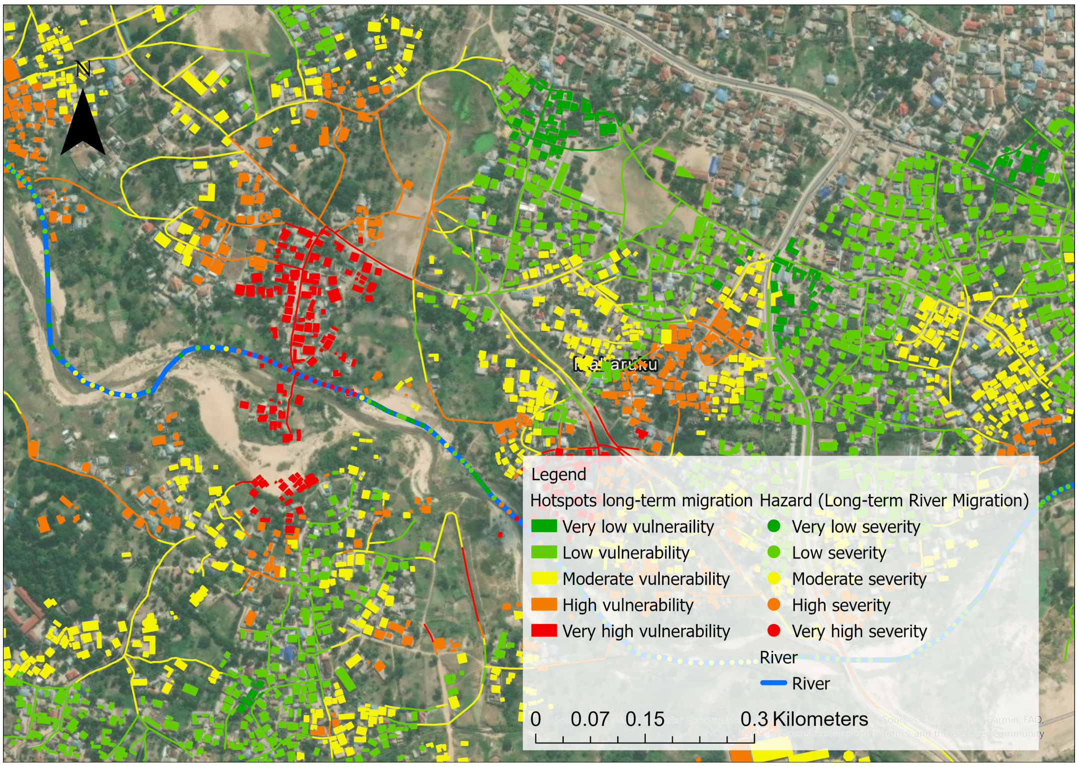

(a) Instance of a Cut-off in the Upper Middle Basin, which has already appeared.

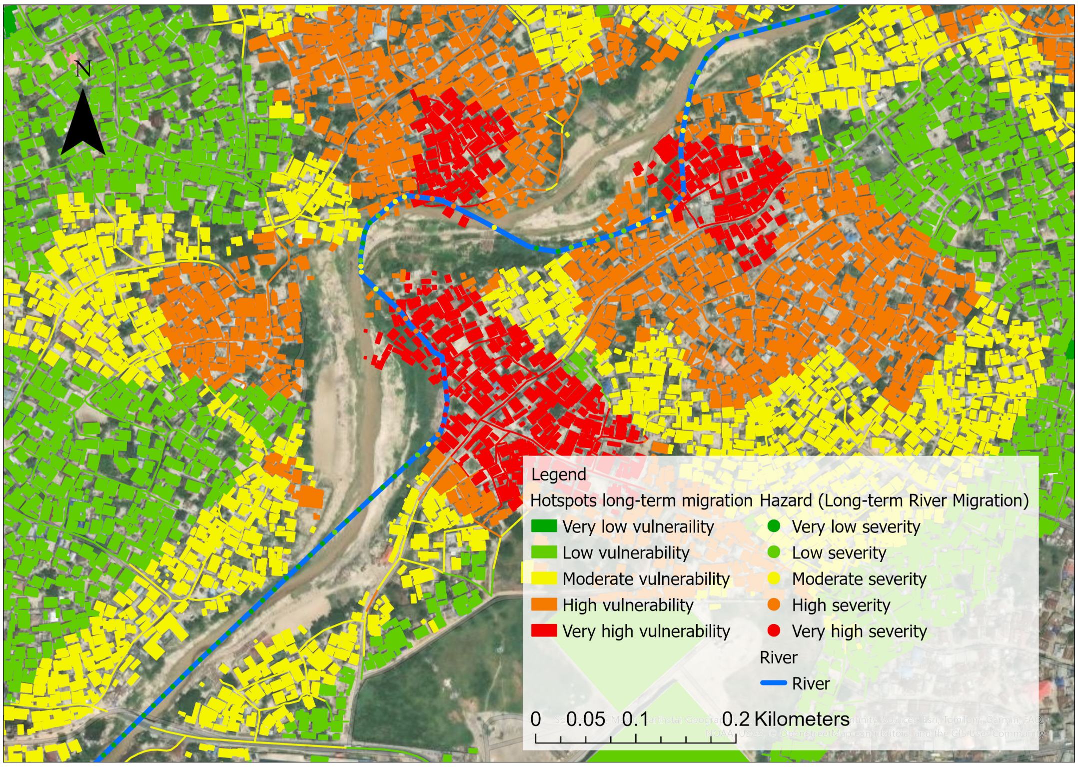

(b) Detailed view of a meander bend in the Lower Middle Basin

Figure 6.6: Detailed views on the hotspot map as a result of long-term (2007-2024) river migration.

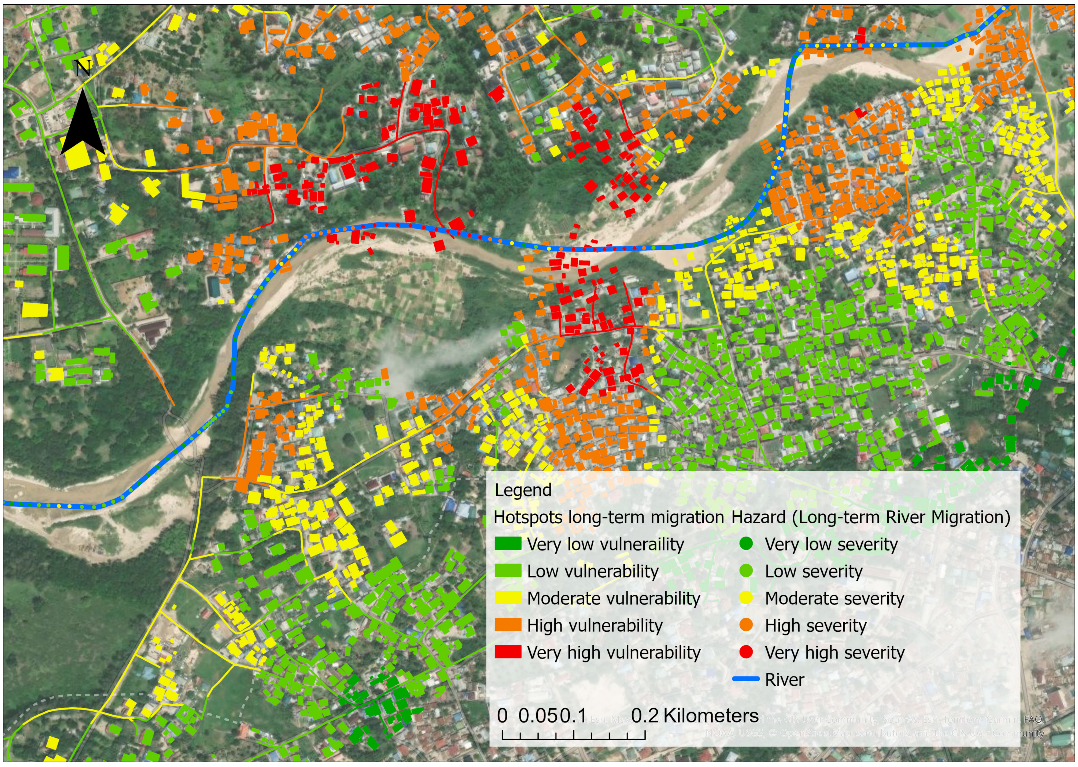

(a) The identified long-term (2007-2024) migration rate hotspot in the Upper Middle Basin

(b) Photo taken in the Upper Middle Basin at the exact location shown in figure 6.7a, during a field visit. The image shows the southern bank, where houses are located close to a steep riverbank. A manually constructed reinforcement is visible in the foreground, built out of loose white sand to protect against erosion.

Figure 6.7: Validation of identified long-term (2007-2024) migration hotspot location using field observations. The hotspot identified in the southern section corresponds to exposed houses observed during field visits, as shown in the accompanying photographs.

6.2. River widening hotspots

Besides river migration river widening also poses a hazard to the objects within the exposed area as described in Chapter 4. Now, the rate of change of the river width is used as the metric for the hazard in terms of severity. Once again, the hazard is determined based on long-term (2007-2024) and short-term (2020-2024) widening rates. Obviously, river narrowing (corresponding to rates of change below 1) are considered as hazards with very low severity as they do not pose a risk for the exposed objects. Figure 6.9 shows the hazard of widening in terms of severity.

As with the analysis on the vulnerability of river migration rates, the interpretation of river widening vulnerability is closely tied to the internal dynamics of the Msimbazi River system. Widening rates are classified based on their distribution within the study area using Natural Breaks (Jenks) (de Smith et al., 2018), which allows for the identification of zones that are experiencing relatively severe widening in the local context. Once again, the breaks computed for the long term changes are also applied to the short term changes to improve comparability between the hotspot maps. See Figure 6.8.

This relative classification means that some areas may be identified as hotspots even if the absolute rates of widening are not extreme given the local context. To accurately assess the degree of exposure and potential vulnerability, it is therefore important to consider the actual widening values alongside the hotspot classification.

It can be seen from Figures 6.8 and 6.9 that the short-term hazard is more severe compared to the long-term hazard.

The hotspot maps for river widening are presented in Figures 6.10 and 6.11. See Appendix H for more detailed images. The hotspot map subject to long-term (2007–2024) widening shows that nearly all buildings and infrastructure within 100 meters of the river are classified as highly vulnerable. Areas of very high vulnerability are relatively rare; however, where they do occur, they are predominantly situated on the left side of the river. This spatial pattern aligns with the observed net tendency of the river to migrate leftward, as was discovered in Chapter 4. Furthermore, the Upper Basin and Upper Middle Basin generally show the highest levels of vulnerability, suggesting that these reaches are particularly dynamic and pose a greater vulnerability to exposed objects.

The increased rates of widening observed during the short-term period (2020–2024) clearly indicate that objects located within 0–300 meters of the river, corresponding to zones of moderate to very high susceptibility, are now frequently classified as highly vulnerable (Figure 6.11). In contrast to the long-term pattern, these highly vulnerable areas are now distributed along the entire length of the river, rather than being concentrated primarily in the Upper- and Upper Middle Basins. Additionally, areas of very high vulnerability are no longer confined to one side; they now appear more evenly distributed between the left and right banks of the river.

Figure 6.12 shows how two locations, one in the Lower Middle Basin and one in the Upper Middle Basin are influenced by the width changes of the Msimbazi river. Figure 6.13 validates that the identified widening hotspots correspond to areas that are indeed vulnerable, as confirmed by field observations.

To conclude, long-term width changes primarily affect objects located within 100 meters of the river, with high vulnerability concentrated in the Upper and Upper Middle Basins. Areas classified as very highly vulnerable are predominantly situated on the left side of the river. In contrast, short-term width changes reveal very high vulnerability on both sides of the river. In this case, highly vulnerable objects are generally located within 300 meters of the river, a pattern observed consistently across all sub-basins. However, as width was estimated based on water cover, some of these patterns may reflect short-term fluctuations in surface water rather than true morphological change (Hooke, 2003; Leopold et al., 1995). A more accurate delineation of channel banks over time would allow for a better assessment of actual erosion dynamics and hazard.

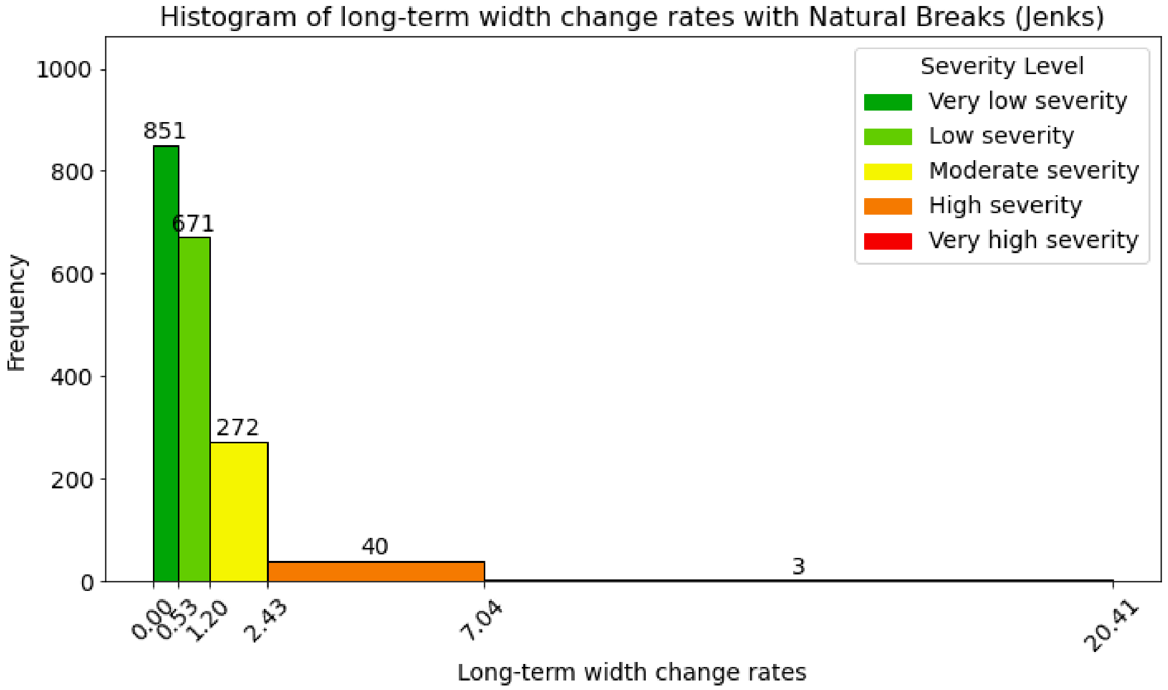

(a) Long-term width change rates (2007–2024).

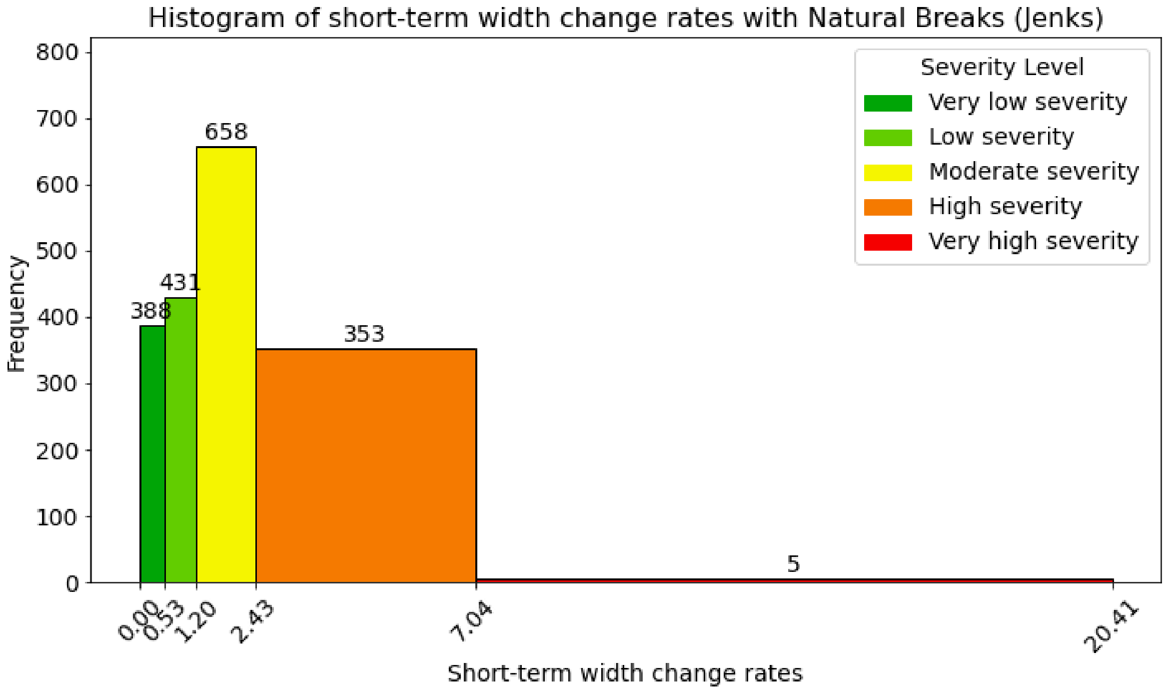

(b) Short-term width change rates (2020–2024).

Figure 6.8: Histograms of river width change rates classified by Natural Breaks (Jenks) (de Smith et al., 2018). The severity of width changes increases from left to right in both graphs.

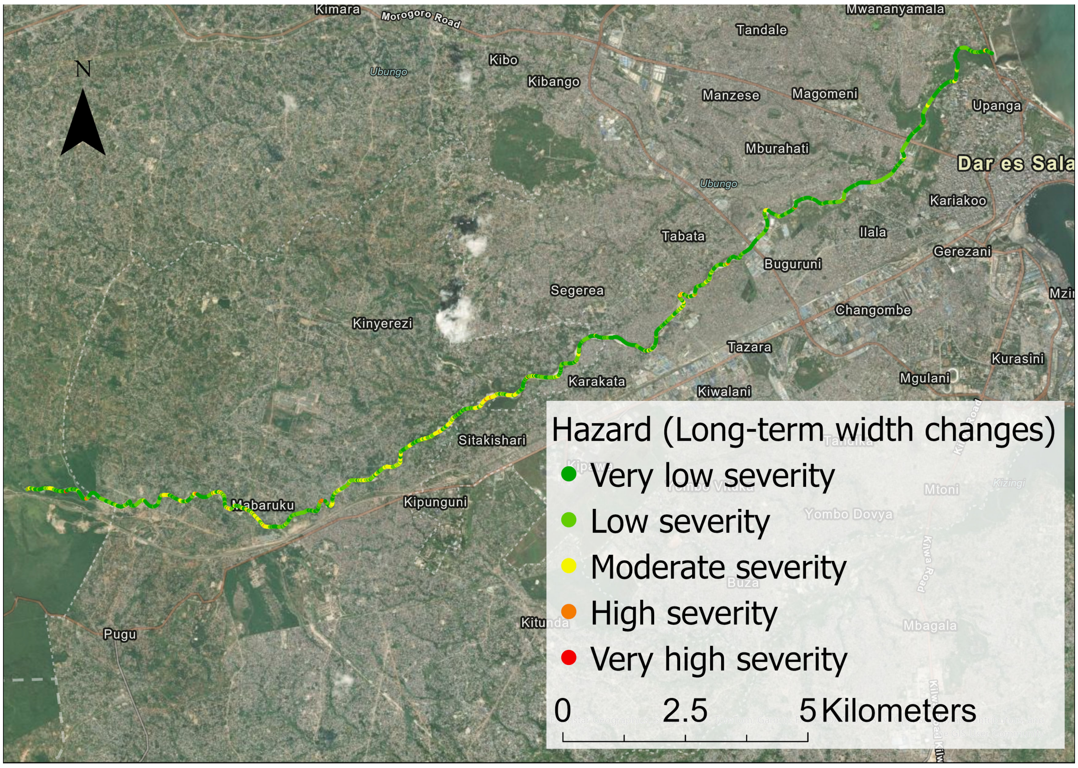

(a) Long-term hazard (River widening rates between 2007 and 2024)

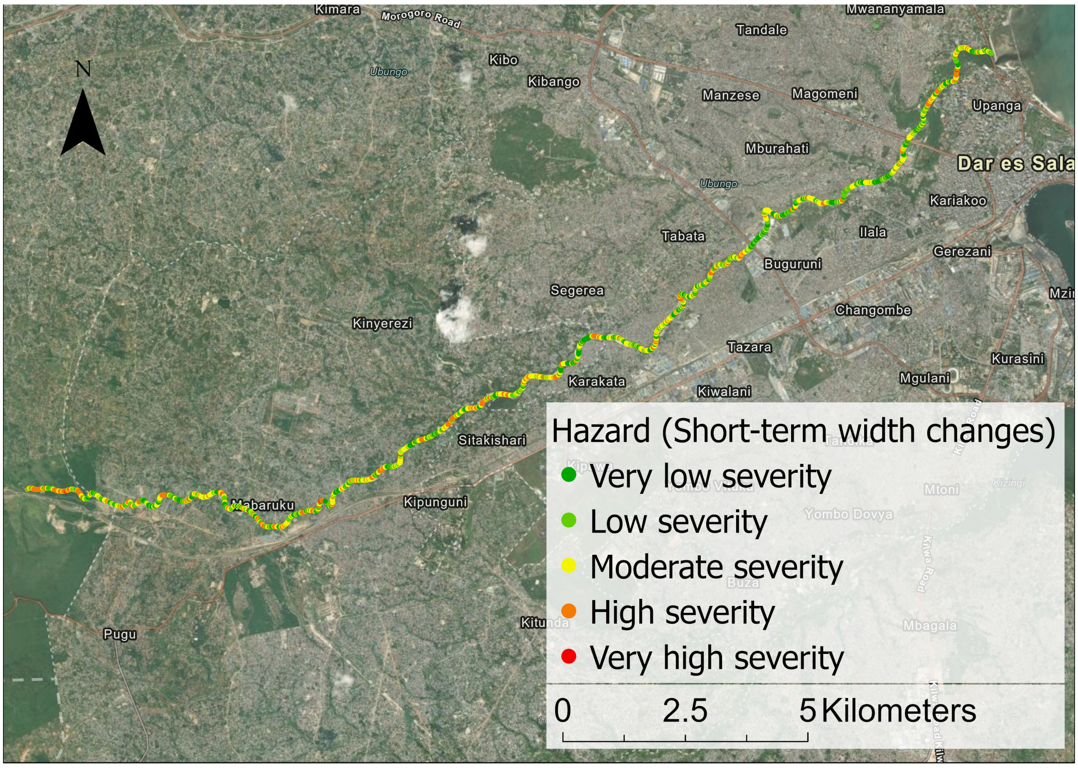

(b) Short-term hazard (River widening rates between 2020 and 2024)

Figure 6.9: Mimbazi river long- and short-term hazard (River widening)

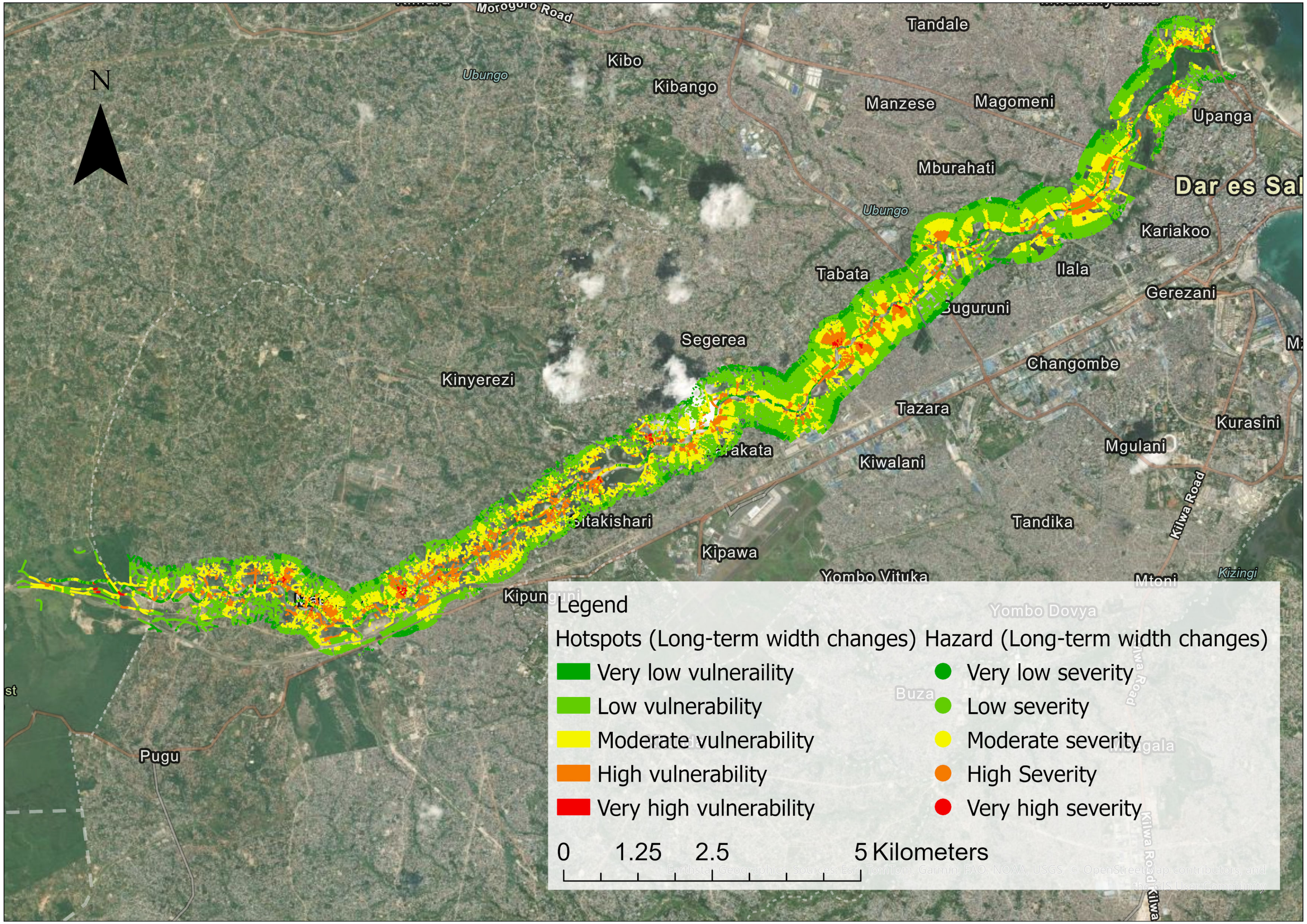

Figure 6.10: Overview of the hotspot map as a result of long-term (2007-2024) river widening.

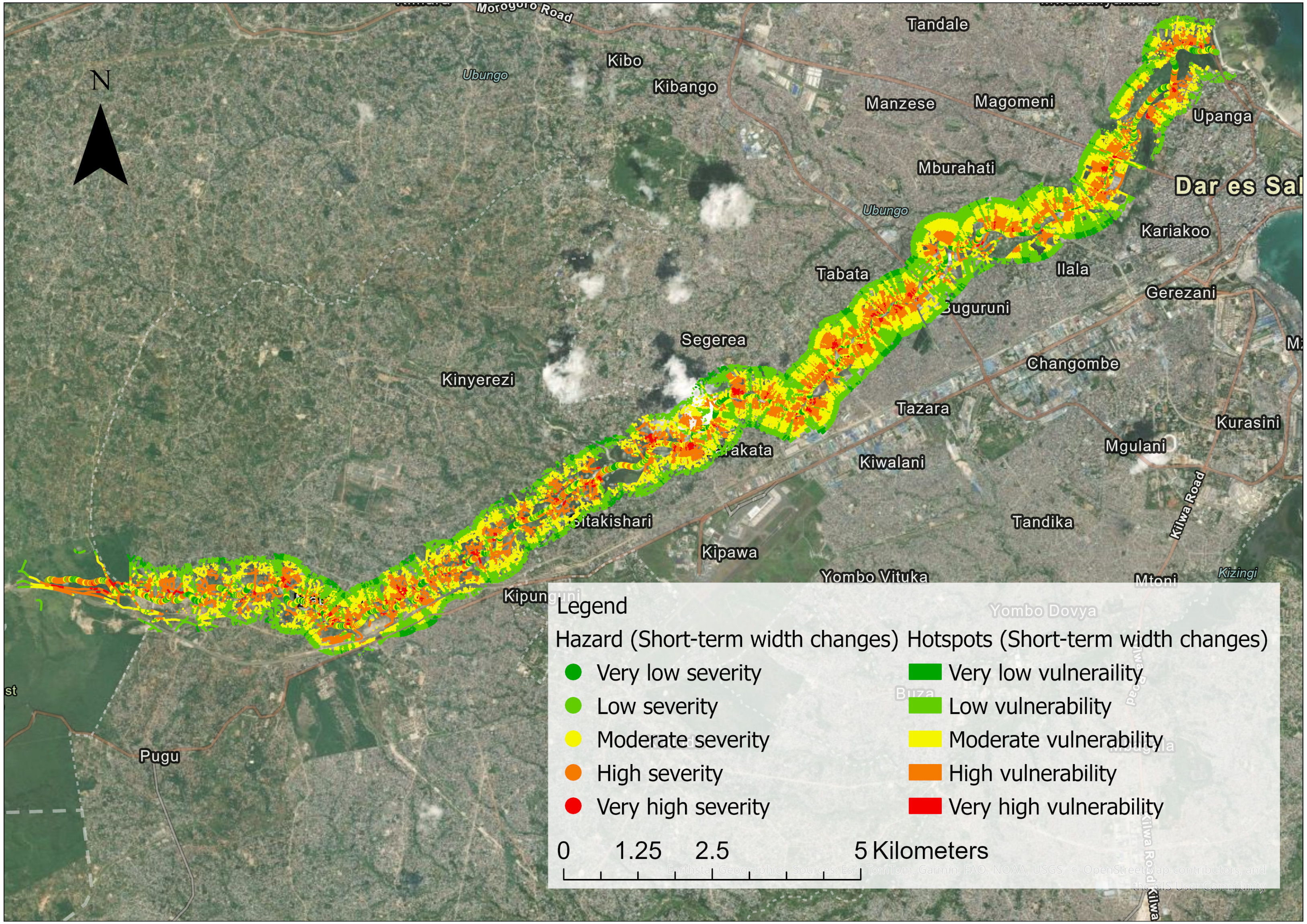

Figure 6.11: Overview of the hotspot map as a result of short-term (2020-2024) river widening.

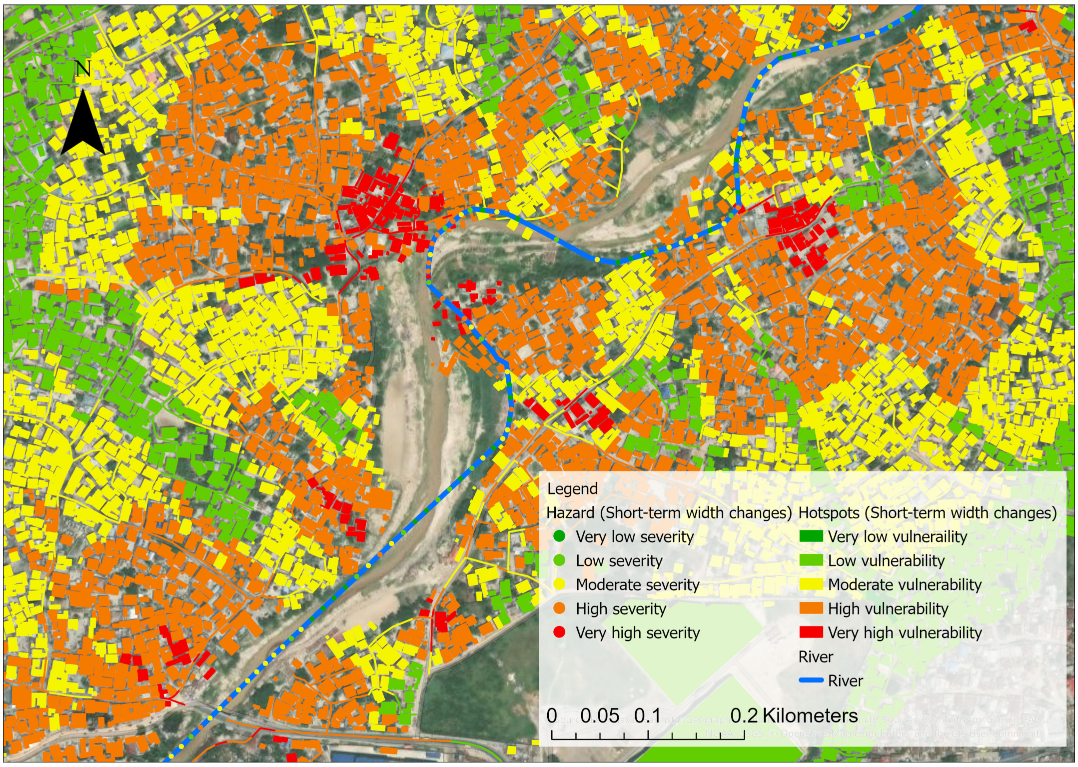

(a) Detailed view on short-term (2020-2024) river widening severity and catchment vulnerability in the Lower Middle Basin.

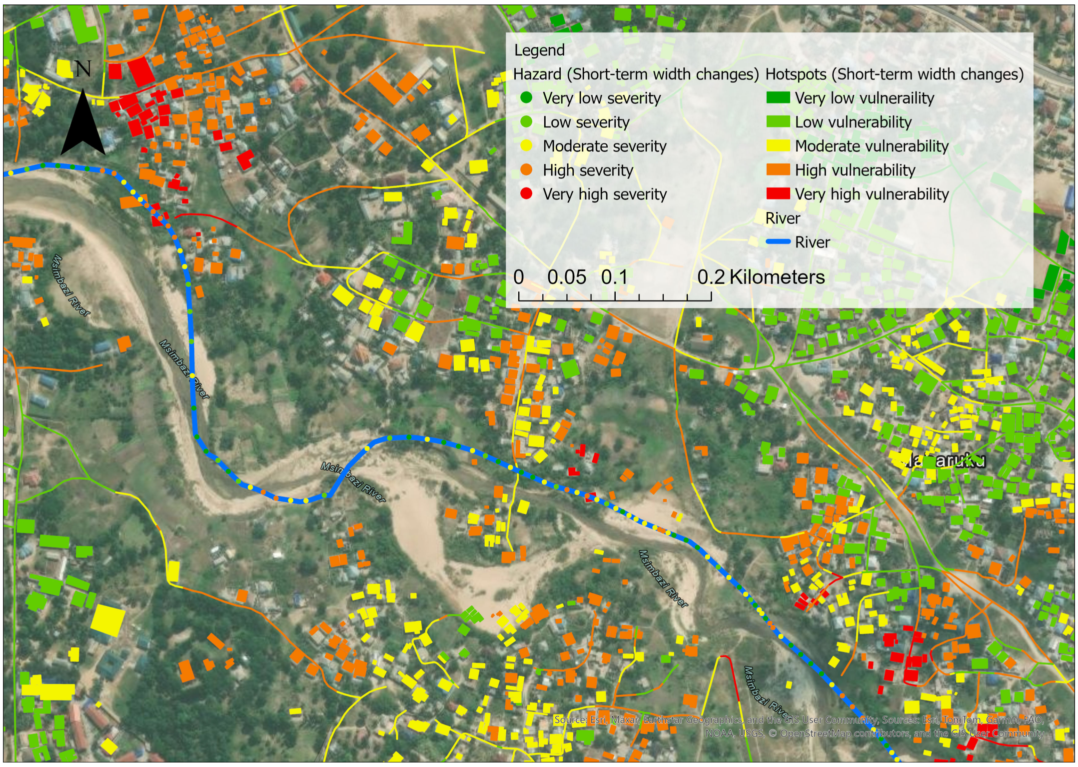

(b) Detailed view on long-term (2007-2024) river widening severity and catchment vulnerability in the Upper Middle Basin.

Figure 6.12: Detailed views on vulnerability in the Lower Middle Basin and Upper Middle Basin as a result of the short-term (2020-2024) widening.

(a) Hotspot location in the Upper Middle Basin, showing houses close to a steep southern riverbank.

(b) Close-up showing early signs of failure in the installed gabions at the same location.

Figure 6.13: Validation of identified long-term (2007–2024) widening hotspot location using field observations. The hotspot in the northern section corresponds to exposed houses observed during field visits, as shown in subfiure (a). Subfigure (b) shows that even recently installed gabions (also visible on the left of subfigure (a)) are already beginning to fail, indicating ongoing erosion risk.

7

Discussion

This chapter reflects on the key findings of this study and their broader implications for understanding river morphodynamics in rapidly urbanizing environments. Between 2007 and 2024, the Msimbazi River experienced substantial channel widening and increased lateral migration. These changes were spatially and temporally variable, driven by both long-term and sudden factors. Long-term influences, such as increased runoff potential due to deforestation in the upper catchment and ongoing urban expansion, likely contributed to gradual morphodynamic shifts. In contrast, abrupt drivers such as the construction of the Standard Gauge Railway (SGR) around 2017–2018, the 2023–2024 El Niño phase, and Cyclone Hidaya triggered rapid, event-based morphological changes. This is evident from the ”Runoff versus Width” analysis. These event-based changes include sedimentation and bank steepening, which were further confirmed by field observations. Furthermore, the hotspot map produced for Dar es Salaam highlights how the intersection of morphodynamic hazards, such as river migration and channel widening, with urban exposure results in spatial patterns of vulnerability.

The results of this study reveal several important implications for how the Msimbazi River may respond to future climate change. The increasing runoff potential, caused by deforestation and urbanization, has been quantitatively shown in this study to influence gradual changes in the river system. Historical events such as Cyclone Hidaya demonstrate that the river is already sensitive to extreme weather conditions, as such events have triggered sudden and significant changes in river morphology. In the absence of mitigation strategies targeting river migration and widening, it is reasonable to expect that the catchment's vulnerability will increase under worsening climate scenarios. Field observations suggest erosion in the upstream areas and sedimentation downstream, which may explain the recurring flood events in the lower parts of the basin (World Bank Group, 2024). These patterns highlight that particularly the Upper Basin and Upper Middle Basin are most vulnerable to future morphological changes, as confirmed by the quantitative results of this study. Regarding infrastructure, the construction of the SGR has clearly changed the Upper Basin, introducing a dam-like structure. However, no hydrological impact assessment of this intervention was performed, and while field observations suggest reforestation practices may reduce sediment input to the river, the influence of the SGR on flow dynamics and sedimentation remains an open question for future research. Given the ongoing land-cover changes and the unpredictability of major storm events, it is essential to continuously update the hotspot map developed in this study. This will ensure that it remains a vital tool for urban planning and mitigation strategies, particularly as human interventions such as urbanization and deforestation continue to influence river dynamics.

Despite the valuable insights provided by this study, several limitations need to be considered when interpreting the results. First, the methodology addresses the spatial variability of the river, as determining the river's position over time is a fundamental step in analyzing river migration. In this study, this was achieved by manually delineating the riverbanks from satellite imagery and deriving the centerline as the midpoint between them. Although automated detection methods using MNDWI, NDWI, or SAR are commonly used for wider rivers (Xia et al., 2021), the relatively narrow width of the Msimbazi River, ranging from 4–15 meters in the early 2000's to 30–70 meters in recent years, makes such methods unreliable due to the limited spatial resolution of available imagery (10–30 m). Consequently, riverbank delineation was performed manually based on visual interpretation of satellite images. The resulting centerline was derived from these banklines, with uncertainty in its position quantified using error propagation principles (Ku, 1966).

While this manual approach enabled the tracking of channel migration and width changes, it also introduces a degree of positional uncertainty due to the image resolutions that may affect the precision of the results. Should future advancements in remote sensing improve the applicability of automated techniques for narrow rivers, a re-delineation using high-resolution methods is recommended. This would not only reduce the risk of bias from manual interpretation but also shift the focus from the centerline to the riverbanks. This approach is more directly useful for risk assessment, because riverbank erosion, rather than shifts in the centerline, poses the real threat to nearby buildings and infrastructure.

Similarly, the analysis of width changes would benefit from this refinement. In this study, river width was approximated using the water cover width derived from satellite imagery. However, water cover can fluctuate within a stable channel without implying morphological change (Hooke, 2003; Leopold et al., 1995). Seasonality was minimized by excluding imagery within the Time of Concentration, and by applying both temporal and spatial averaging to river width measurements. However, a more precise delineation of riverbanks over time would allow for direct measurement of true channel widening or narrowing, thereby offering a more accurate representation of erosion dynamics and potential hazard.

Given the centerline positions in time, the use of the Digital Shoreline Analysis System (DSAS) was used to calculate migration rates. The methodology involves the creation of transects along the river, with a smoothing distance applied to each transect. The smoothing distance of 500 meters (corresponding to approximately 10 times the river width in recent years) is applied to prevent overlap between transects when the baseline curves, ensuring that the transects are more evenly spaced and oriented across the river (Himmelstoss et al., 2021). However, this smoothing distance causes the migration rates to be calculated at an angle that is as close as possible to 90 degrees to the centerline, rather than perfectly perpendicular. This adjustment helps to prevent transect overlap, but it may introduce slight deviations from the true migration rates.

The study on the Msimbazi River's morphodynamic drivers faces several limitations that impact the accuracy of its findings. One key limitation is the absence of discharge data, which restricts the ability to directly link precipitation and landcover changes to river flow, thus introducing uncertainty in understanding their influence on the river's morphology. Furthermore, the reliance on Global Precipitation Measurement (GPM) data, with its coarse spatial resolution, may not fully capture localized precipitation variations within the catchment. This could lead to potential errors when assessing the influence of precipitation on river dynamics (Huffman et al., 2014; NASA, 2025). Despite these limitations, research by Leopold et al. (1995) and Rosgen (1996) has shown that bankfull discharge, corresponding to a 2-year precipitation event, is most capable of driving changes in river morphology. Therefore, variability in precipitation events smaller than the 2-year event has a less significant impact. Additionally, the long-term precipitation trends focused on in this research are less affected by daily variability.

The development of erosion hotspot maps in this study assesses vulnerability along the Msimbazi River by combining hazard severity (for both river migration and widening) with exposure, defined as the susceptibility of nearby infrastructure (Climate Investment Funds, 2023; Dilley et al., 2005; Stone et al., 2011; Tha et al., 2022). Buildings and infrastructure were chosen as the focus for exposure mapping due to the river's densely populated catchment area, allowing for more targeted vulnerability assessments compared to broader methods based on landcover or population density.

Rather than directly assessing risk, the research focuses on vulnerability, using hazard severity and the susceptibility of exposed objects as proxies. However, incorporating potential consequences, such as economic losses or property damage, could provide a more detailed assessment and further enhance the research. The assumption that consequences are uniform across all observed objects may oversimplify the actual impacts. As Turner et al. (2003) points out, vulnerability also depends on sensitivity and resilience, factors that were not included in this study due to data limitations. Future research should incorporate these dimensions to provide a more comprehensive understanding of the vulnerabilities and risks faced by communities along the river, rather than focusing solely on their vulnerability.

The results presented in Chapter 4 discuss the migration and width changes of the river, averaged across the entire basin or specific sub-basins (Upper Basin, Upper Middle Basin, Lower Middle Basin, and Lower Basin). According to Hooke (2003), rivers primarily meander at specific bends rather than shifting uniformly across the entire system or sub-basins. As such, averaging migration across these larger areas offers a broad and simplified understanding of the river's dynamics but fails to capture the localized movements of individual river bends (Wibig et al., 2014).

In contrast, the centerline position and water cover width data is collected at 15-meter intervals, analyzing historical movement patterns, and providing a more precise and detailed perspective on the river's dynamics. This approach ensures that, despite the broader analysis of migration and width changes at the sub-basin or basin level, the underlying data remains detailed and accurate. Furthermore, the use of future high-resolution data that reflects historical movements will offer an even more accurate representation of the river's behavior, capturing finer details and enabling a deeper, more localized understanding of the river's movement.

The temporal extent used to assess migration rates and width changes also plays a critical role in interpreting the results. Shorter time periods tend to highlight more extreme values because the extremes are less likely to be averaged out, unlike in longer time frames (Eggert et al., 2015).

An alternative explanation for the lower migration rates observed over the long-term timeframe (as provided in Table 4.3) could be the increased frequency of satellite imagery available after 2017. With satellite images becoming available monthly instead of annually, this higher frequency may introduce greater variability in the delineated position of the river's centerline. However, it is important to note that the DSAS tool, which was used to compute the migration rates, accounts for the time interval when calculating these rates, thus minimizing the impact of such variability on the results (see Appendix E). Nevertheless, this variability may still influence the results for river widening. Additionally, future research could incorporate field measurements of river width collected over multiple months in different years, which would provide further verification of any widening or narrowing trends observed in the satellite data.

Furthermore, while gradual changes in migration rates and river width are visible throughout the entire study period, the results reveal a clear deviation from this trend between 2017–2019 and 2023–2024. This indicates that the river's dynamics are not solely shaped by long-term processes. As discussed in Chapter 5, precipitation has remained relatively stable, while landcover change has gradually increased runoff potential. However, these changes alone do not fully account for the observed shifts. The pronounced changes during the 2017-2019 and 2023-2024 periods indicate the influence of additional factors, including extreme rainfall events and human interventions such as the construction of the Standard Gauge Railway (SGR). These findings highlight the importance of considering both climatic variability and anthropogenic impacts when interpreting river morphodynamics.

Chapter 5 begins by evaluating the potential climatic impacts on river morphological changes, focusing on factors such as annual total precipitation, maximum precipitation, precipitation durations, and observed anomalies in precipitation rates. The discussion regarding the effects of averaging extremes over the observed temporal extent, as mentioned by Eggert et al. (2015), is also relevant to the observed subsets of the precipitation data. The results suggest no significant changes in precipitation, and therefore, no detectable influence on river morphology. However, in the precipitation anomaly analysis, statistical significance is observed when comparing the pre- and post-2018 periods. Although it is assumed that these changes are negligible due to the large standard deviation, which is likely dominant, the change in anomalies does suggest that precipitation could be a potential driver of change. The post-2018 subset used in this analysis includes the El Niño phase and Cyclone Hidaya, which elongated the wet season and may help explain the statistically significant shift in precipitation patterns (Erickson & Reiter, 2024; Evarister, 2023; Igini, 2024; World Meteorological Organization, 2023).

In addition to precipitation, landcover changes are considered as a potential driver of the observed morphological changes. A connection is made between landcover changes and their influence on runoff potential. The runoff coefficients used to establish this connection are estimated based on existing literature rather than directly delineated using methods such as the curve number approach. While these estimates were thoroughly cross-examined for the local context, they remain less precise. In addition to the challenges posed by data scarcity and variations in data resolution, this study focuses on catchment-level changes, where a broad understanding of how runoff potential evolves over time provides sufficient insight. However, it is recommended that future research more accurately delineate runoff potential, especially if discharge data remain unavailable, as runoff is shown to be one of the main drivers of the river's morphological changes (Tang & Lettenmaier, 2012).

Given the results of comparisons between river width and runoff changes over time, it is hypothesized that other drivers, such as the construction of the Standard Gauge Railway (SGR), may also contribute to the observed changes. It has been noted that since the initiation of the SGR construction, there seems to have been a change in sediment influx to the river. Furthermore, the SGR appears to act as a dam-like structure in the Upper Basin, potentially altering the hydrological flow path. To more accurately assess the impact of these changes, it is recommended to develop a hydrological model. While the hypothesis that the SGR has influenced river dynamics is supported by the elimination of other potential drivers, the direct connection between the SGR and the observed increases in river widening and migration rates remains unproven. Therefore, the conclusion that the SGR has had a significant impact on river behavior should be viewed as preliminary until further evidence is obtained.

Chapter 6 presents hotspot maps for both river migration and river widening as hazards. To enable meaningful comparisons, the severity of the hazard are determined based on long-term (2007-2024) changes in migration and widening rates. The same boundaries for the classification of severity are applied to short-term (2020-2024) changes. It is likely that long-term changes are overestimated, as extreme values tend to be averaged out in long-term trends (Eggert et al., 2015).

A potential limitation of the vulnerability mapping is the assumption of uniform floodplain material. Areas with high clay content, such as old oxbow lake deposits, can limit or prevent river migration in certain directions, which is not captured in this study. This heterogeneity may lead to an overestimation of vulnerability hotspots, as zones with more cohesive, erosion-resistant soils may be less vulnerable despite their proximity to the river (Güneralp & Rhoads, 2011). Another simplification is the exclusion of elevation as a factor in assessing susceptibility. While elevation might intuitively seem protective, field observations have shown that even buildings situated over 12 meters above the river channel can be undermined due to toe erosion and planar collapse. Therefore, distance to the river was considered a more reliable proxy for susceptibility in this context. Incorporating detailed soil composition data, could enhance the accuracy of vulnerability assessments, particularly in areas with significant variability in floodplain material.

The hotspots are identified based on local migration and widening rates, rather than global standards, ensuring they reflect areas of highest vulnerability within the Msimbazi River system. This prevents the entire system from being labeled a hotspot due to the river's dynamic nature.

However, focusing solely on the local context when identifying hotspots introduces limitations in assessing the overall vulnerability of the river system. For instance, areas identified as moderately vulnerable may still be at risk due to migration rates that are considered high according to global standards (e.g., a rate exceeding 2% of the river width per year, as indicated by (Langhorst & Pavelsky, 2023); in our study, for example, 6m/yr exceeds this 2% rule of thumb). Given that the system shows even higher migration rates, this specific 6m/yr rate is considered moderately severe. Comparing the hotspot maps presented in Chapter 6 with those that evaluate hotspots based on global standards for the severity of migration or widening rates would provide valuable insights, offering a broader perspective on vulnerability and helping with a more comprehensive risk assessment.

This research provides a practical method for tracking and understanding the movement of narrow rivers and their drivers in data-scarce regions. It enables the identification of erosion and migration hotspots in densely populated catchments, offering valuable insights for risk management. The results reveal that gradual change, combined with sudden events, creates significant vulnerability for communities along the river. The Msimbazi case clearly demonstrates the hazards of unregulated development and highlights the need for coordinated landscape management to reduce exposure to climate-related and environmental hazards.

In conclusion, this chapter has examined the methodology, limitations, and key findings of the study, showing both the strengths and challenges in understanding the Msimbazi River's morphodynamics and associated vulnerability. The manual delineation of riverbanks, while necessary given the resolution limitations of satellite imagery, introduced some uncertainty in determining the river's centerline and width changes, which could be mitigated by advancements in remote sensing techniques. Despite this, the approach allowed for a detailed analysis of river migration and widening, providing valuable insights into the river's behavior. The application of the DSAS tool was effective in calculating migration rates, though slight deviations due to the smoothing distance were acknowledged. The absence of discharge data posed a significant challenge in linking precipitation and landcover changes to morphodynamic changes of the river, with the reliance on GPM data further complicating the analysis of localized precipitation effects. Nonetheless, long-term trends suggest that precipitation variability may not significantly affect the river's morphology, while landcover changes and other factors, such as the SGR, likely play an important role in shaping the river's dynamics. The hotspot maps presented in this study, derived from local migration and widening rates, offer valuable insights into the most vulnerable areas of the river system. However, the methodology may underestimate the vulnerability of certain locations due to the local context approach, which may overlook globally recognized standards for hazardous migration or widening rates. By comparing these maps with those based on global standards, a more comprehensive understanding of the river's vulnerability could be achieved. Finally, while the limitations of the current study are acknowledged, the results provide a strong foundation for future research, particularly in refining data resolution, incorporating discharge data, and exploring the potential impacts of man-made interventions like the SGR on the river's morphology.

8

Conclusion

The study answers the three research questions introduced in Chapter 1. The first of these is: *How is the Msimbazi River evolving in terms of channel migration and morphological changes?*

One key aspect of this evolution is the shifting position of the river's centerline. From 2007 to 2024, the Msimbazi River showed an overall stable migration pattern, stressed by short-term dynamic episodes. The centerline shifted both leftward and rightward, with a slight tendency towards leftward movement, indicating greater erosion on that side. Migration rates varied clearly across space and time, with some uncertainty due to manual centerline interpretation and varying spatial resolutions.

For sub-periods between 2007 and 2024, the Msimbazi River showed an overall episodic migration pattern, marked by alternating phases of stability and rapid change. From 2007–2017, migration remained relatively stable, followed by a significant increase between 2017–2019, with basin-wide rates more than doubling (+136%). These elevated rates persisted in 2019–2021 (+17%), after which migration sharply declined in 2021–2023 (–56%), before rising again in 2023–2024 (+163%). Spatially, the Upper Middle Basin (UMB) was consistently the most dynamic, while the Lower Basin remained relatively stable. The Upper and Lower Middle Basins exhibited episodic peaks in 2017–2019 and 2023–2024.

River width changes mirrored this pattern. The total widening across the basin was modest (+5.3%), but trends differed per sub-basin. The UMB showed the strongest and most consistent widening (+20.8%), while the Upper Basin experienced marked fluctuations, including a narrowing of nearly 25% in the most recent period. The Lower Basin remained largely stable, and the Lower Middle Basin fluctuated around its initial width.

In summary, migration rates and river widths followed a temporal pattern of stable conditions, then a rise, a period of sustained high values, a decline, and finally a sharp increase. The Upper Middle Basin was the most dynamic throughout. These fluctuations suggest an interplay of gradual changes and abrupt, event-driven influences.

The second research question is: *What are the key drivers behind the morphodynamic changes occurring in the Msimbazi River?*

Precipitation data was analyzed due to the absence of direct discharge measurements for the Msimbazi River. Four aspects were examined, total precipitation, maximum precipitation, event durations, and precipitation anomalies, using satellite data from GPM (2000–2024). Across all metrics, no statistically significant differences were found between key temporal subsets (pre/post 2007 and pre/post 2018). Consequently, precipitation trends do not appear to explain the observed extreme river migration and widening. An exception is the increased precipitation linked to the 2023–2024 El Niño phase and Cyclone Hidaya (May 2024), which may explain the increased channel dynamics observed during that period.

While changes in precipitation are often considered a driver of river dynamics, this analysis highlights that landcover transformations, particularly urbanization and deforestation, play a crucial and likely dominant role in altering the hydrological and morphological behavior of the Msimbazi River. Between 2000 and 2021, the catchment experienced rapid population growth and extensive urban development, accompanied by a notable decline in forested areas. These changes have directly impacted runoff processes by increasing the extent of impervious surfaces, reducing infiltration, and amplifying surface runoff during rainfall events.

The quantified increase in runoff potential, particularly between 2000 and 2020, aligns with landcover changes and is statistically significant across multiple sub-basins. In the Upper Basin, which provides the least disturbed results, the average runoff potential increased by 156% (from 0.16 in 2000 to 0.41 in 2020). Although discrepancies in resolution between datasets limit the comparability of absolute values over the full study period, the spatial and temporal patterns, especially in the Upper Basin, provide strong evidence of a systemic shift in runoff dynamics. These hydrological changes are closely linked to increased river discharge and erosion potential, both of which are known to accelerate river migration and channel widening, independent of precipitation changes.

In addition to the gradual increase in runoff linked to urbanization and deforestation, this study also reveals a more complex picture in terms of river behavior. While urbanization and deforestation have caused a steady increase in discharge, demonstrated by the runoff potential increase, the river itself does not show only gradual changes in migration or widening. This contradiction leads us to hypothesize that other factors may be at play, as illustrated by the ”runoff versus width” analysis. This analysis shows that, while runoff potential gradually increased between 2000 and 2020, the river width expanded non-linearly, with a sudden drop in width between 2020 and 2021 despite no change in runoff potential, suggesting additional drivers influencing the river’s dynamics. Precipitation alone cannot explain the migration rates and widening observed between 2017 and 2021, as these changes occurred during a period of relatively stable precipitation patterns. However, it is during the late 2017 and early 2018 period that construction of the Standard Gauge Railway (SGR) began, coinciding with increased sediment deposition in the river. The river’s morphology appears to be reacting to this influx of sediment, which may exceed its capacity to adapt, leading to the observed accelerated changes in migration and widening. This hypothesis is based on indirect evidence, consisting mainly of the timing of the observed river changes following the start of construction, rather than on direct sediment measurements. Although SGR construction has now been completed, the impacts of the 2023–2024 El Niño phase and Cyclone Hidaya demonstrate that the river system remains highly sensitive to sudden, extreme events. These findings highlight that river behavior in rapidly urbanizing catchments like the Msimbazi River is not only a reflection of natural climatic variability but also a direct response to human-induced landscape alterations.

Finally, the third research question is: *Where are the critical erosion hotspots along the Msimbazi River?*

This study defines erosion hotspots as areas of high vulnerability where high levels of the hazard and exposure coincide. The hazard is defined as either river migration or widening. Exposure is determined by proximity to the river, specifically not as elevation. Vulnerability is assessed using local rates of hazardous migration and widening, which may limit direct comparisons with global standards.

Hotspots of river migration are consistently found in the Upper Basin and Upper Middle Basin, where both long- and short-term migration rates indicate severe morphological activity. In contrast, the Lower and Lower Middle Basins show fewer hotspots as a result of long-term (2007-2024) migration but show emerging hotspots as a result of short-term (2020-2024) river migration.

For river widening, the Upper and Upper Middle Basins again stand out in the long-term analysis, with vulnerability concentrated particularly on the left bank due to the net leftward migration trend. However, short-term widening has intensified across all sub-basins, leading to hotspots along the full river system, including previously less affected downstream sections.

This study emphasizes the interplay between climatic changes and landcover transformations in shaping river morphology, particularly in rapidly urbanizing catchments like the Msimbazi River. It shows that landcover changes alone are capable of driving significant shifts in river dynamics, pointing out the profound impact of human activities. The first research question revealed that the Msimbazi River shows dynamic shifts in channel migration, with distinct periods of increased migration rates, especially from 2017 onward. Regarding the second research question, while precipitation trends alone could not explain these changes, urbanization and deforestation were found to play a dominant role in altering river behavior, with the Standard Gauge Railway construction indicating sediment deposition and likely accelerating morphological changes. Lastly, the vulnerability assessment identified the Upper and Upper Middle Basins as the most vulnerable areas. These findings provide insights into river dynamics in the Msimbazi river basin and offer a foundation for future management strategies.

References

Ahilan, S., O'Sullivan, J., Bruen, M., Brauders, N., & Healy, D. (2013). Bankfull discharge and recurrence intervals in irish rivers. *Proceedings of the Institution of Civil Engineers - Water Management*, *166*(7), 381–393. https://doi.org/10.1680/wama.11.00078

Alexander, A. C., Izdori, F. J., Mulungu, D. M. M., & Mugisha, L. R. (2024). Analysis of msimbazi river banks erosion with regards to soil erodibility. https://doi.org/10.21203/rs.3.rs-4551858/v1

Allan, J. D. (2004). Landscapes and riverscapes: The influence of land use on stream ecosystems. *Annual Review of Ecology, Evolution, and Systematics*, *35*, 257–284. https://doi.org/10.1146/annurev.ecolsys.35.120202.110122

Aqua Veo. (2016, December). Wms:kirpich tc equation. https://www.xmswiki.com/wiki/WMS:Kirpich_Tc_Equation

Boussougou Boussougou, G., Télesphore Brou, Y., & Valimba, P. (2018). Vulnerability of pugu and kazimzumbwi forest reserves under anthropogenic pressure in southeast tanzania. Springer Verlag. https://doi.org/10.1007/978-3-319-95165-2_16

Casal, G. (2022). Assessment of sentinel-2 to monitor highly dynamic small water bodies: The case of louro lagoon (galicia, nw spain). *Oceanologia*, *64*, 88–102. https://doi.org/10.1016/j.oceano.2021.09.004

Charlton, R. (2008). *Fundamentals of fluvial geomorphology*. Routledge. https://text2fa.ir/wp-content/uploads/Text2fa.ir-FUNDAMENTALS-OF-FLUVIAL-1.pdf

Chen, J., Chen, S., Fu, R., Li, D., Jiang, H., Wang, C., Peng, Y., Jia, K., & Hicks, B. J. (2022, February). Remote sensing big data for water environment monitoring: Current status, challenges, and future prospects. https://doi.org/10.1029/2021EF002289

Chow, V. T., Maidment, D. R., & Mays, L. W. (1988). *Applied hydrology*. McGraw-Hill. https://ponce.sdsu.edu/Applied_Hydrology_Chow_1988.pdf

[CivilWeb], C. S. (n.d.). Kirpich Formula. https://civilweb-spreadsheets.com/drainage-design-spreadsheets/runoff-and-rainfall-intensity-calculator-spreadsheet/kirpich-formula/

Climate Investment Funds. (2023, June). *Strengthening disaster risk management in climate resilience action: A learning review of cif-supported projects* (tech. rep.). https://www.preventionweb.net/publication/strengthening-disaster-risk-management-climate-resilience-action

de Smith, M. J., Goodchild, M. F., & Longley, P. A. (2018). *Geospatial analysis: A comprehensive guide to principles, techniques and software tools* (6th) [See chapter on Univariate classification schemes]. Winchelsea Press. https://www.spatialanalysisonline.com

de Vries, M. (1975). A morphological time-scale for rivers [Publication No. 147]. *Proceedings of the XVIth IAHR Congress*. https://scispace.com/pdf/a-morphological-time-scale-for-rivers-20zj4oozr2.pdf

Dilley, M., Chen, R. S., Deichmann, U., Lerner-Lam, A. L., & Arnold, M. (2005). *Natural disaster hotspots: A global risk analysis*. The World Bank. https://doi.org/10.1596/0-8213-5930-4

Dinku, T. (2019). Challenges with availability and quality of climate data in africa. In A. M. Melesse, W. Abtew, & S. G. Setegn (Eds.), *Extreme hydrology and climate variability: Monitoring, modelling, adaptation and mitigation* (pp. 71–80). Elsevier. https://doi.org/10.1016/B978-0-12-815998-9.00007-5

Duró, G., Crosato, A., Kleinhans, M. G., & Uijttewaal, W. S. J. (2018). Bank erosion processes measured with uav-sfm along complex banklines of a straight mid-sized river reach. *Earth Surface Dynamics*, *6*(4), 933–953. https://doi.org/10.5194/esurf-6-933-2018

Eggert, B., Berg, P., Haerter, J. O., Jacob, D., & Moseley, C. (2015). Temporal and spatial scaling impacts on extreme precipitation. *Atmospheric Chemistry and Physics*, *15*(10), 5957–5971. https://doi.org/10.5194/acp-15-5957-2015

Erickson, K., & Reiter, J. (2024). Tropical cyclone hidaya [Accessed: 2025-05-21]. https://satlib.cira.colostate.edu/event/tropical-cyclone-hidaya/

ERM. (2019, August). *Standard gauge railway line (sgr) project: Dar es salaam – makutopora, tanzania - environmental and social management and monitoring plan* (tech. rep.) (Prepared for Tanzania Railway Corporation (TRC), Sokoine Drive/Railway Street, P.O.Box 76959, Dar es Salaam, Tanzania.). ERM. Sokoine Drive/Railway Street, P.O.Box 76959, Dar es Salaam, Tanzania. https://www.erm.com

Esri. (2024). Near (analysis) arcgis pro | documentation [Accessed April 16, 2025]. https://pro.arcgis.com/en/pro-app/latest/tool-reference/analysis/near.htm

European Space Agency [ESA]. (n.d.). About the launch. https://www.esa.int/Applications/Observing_the_Earth/Copernicus/Sentinel-2/About_the_launch

Evarister, S. (2023, October). Tanzania's 2023 el niño outlook: What to expect and how to prepare [Accessed: 2025-05-21]. https://www.digest.tz/tanzanias-el-nino-outlook-what-to-expect-and-how-to-prepare/

Feng, D., Gleason, C. J., Yang, X., Allen, G. H., & Pavelsky, T. M. (2022). How have global river widths changed over time? [First published: 16 August 2022]. *Water Resources Research*, *58*(8), e2021WR031712. https://doi.org/10.1029/2021WR031712

Field, A. (2009). *Discovering statistics using spss* (2nd) [First edition published 2000, second edition published 2005]. SAGE Publications Ltd.

Fleischmann, A., Fan, F., Collischonn, B., Collischonn, W., Pontes, P., & Ruhoff, A. (2019). Precipitation as a proxy for climate variables: Application for hydrological modelling. *Hydrological Sciences Journal*, *64*(3), 361–379. https://doi.org/10.1080/02626667.2019.1587169

Food and Agriculture Organization of the United Nations (FAO). (2024). *United republic of tanzania: El niño impact assessment highlights, may 2024* (Technical Report) (Accessed: 2025-05-21). Food and Agriculture Organization of the United Nations. Rome. https://openknowledge.fao.org/server/api/core/bitstreams/8d8406fd-2799-4815-b1a7-94a8be30c132/content

Frank. (2020, August). Relation between spatial resolution and object size in satellite imaging. https://gis.stackexchange.com/questions/370561/relation-between-spatial-resolution-and-object-size-in-satellite-imaging

Gao, P., Belletti, B., Piégay, H., You, Y., & Li, Z. (2024). Can water-detection indices be reliable proxies for water discharges in mid-sized braided rivers using coarse-resolution landsat archives? [Submission received: 30 November 2023 / Revised: 22 December 2023 / Accepted: 24 December 2023 / Published: 28 December 2023]. *Remote Sensing*, *16*(1), 137. https://doi.org/10.3390/rs16010137

Garbrecht, J. (1991). Effects of spatial accumulation of runoff on watershed response [Symposium Paper]. *Journal of Environmental Quality*, *20*(1), 7–13. https://doi.org/10.2134/jeq1991.00472425002000010007x

Gorelick, N., Hancher, M., Dixon, M., Ilyushchenko, S., Thau, D., & Moore, R. (2017). Google earth engine: Planetary-scale geospatial analysis for everyone. *Remote Sensing of Environment*. https://doi.org/10.1016/j.rse.2017.06.031

Güneralp, İ., & Rhoads, B. L. (2011). Influence of floodplain erosional heterogeneity on planform complexity of meandering rivers. *Geophysical Research Letters*, *38*(L14402). https://doi.org/10.1029/2011GL048134

Hao, Z., Xiang, N., Cai, X., Zhong, M., Jin, J., Du, Y., & Ling, F. (2024). Remote sensing of river discharge from medium-resolution satellite imagery based on deep learning. *Water Resources Research*, *60*. https://doi.org/10.1029/2023WR036880

Hemati, M., Hasanlou, M., Mahdianpari, M., & Mohammadimanesh, F. (2021, August). A systematic review of landsat data for change detection applications: 50 years of monitoring the earth. https://doi.org/10.3390/rs13152869

Himmelstoss, E. A., Henderson, R. E., Kratzmann, M. G., & Farris, A. S. (2021, January). *Digital Shoreline Analysis System (DSAS) version 5.1 user guide*. https://doi.org/10.3133/ofr20211091

Hooke, J. M. (2003). River meander behaviour and instability: A framework for analysis. *Transactions of the Institute of British Geographers*, *28*(2), 238–253. https://doi.org/10.1111/1475-5661.00089

Huffman, G., Bolvin, D., Braithwaite, D., Hsu, K., Joyce, R., & Xie, P. (2014). Integrated multi-satellite retrievals for gpm (imerg), version 4.4. ftp://arthurhou.pps.eosdis.nasa.gov/gpmdata/

Humanitarian OpenStreetMap Team (HOT) & OpenStreetMap contributors. (2025). Roads and transportation data for the united republic of tanzania [Dataset accessed on April 2, 2025. Data is based on Volunteered Geographic Information (VGI) and may not be exhaustive. Updated monthly. Licensed under the Open Database License (ODC-ODbL).]. https://data.humdata.org/dataset/openstreetmap-hot-export-for-tanzania

Igini, M. (2024, May). *Kenya, tanzania hit by first-ever cyclone following weeks of heavy rain, deadly floods* [Accessed: 2025-05-21]. https://earth.org/kenya-tanzania-hit-by-first-ever-cyclone-following-weeks-of-heavy-rain-deadly-floods/

Igulu, B. S., & Mshiu, E. E. (2020). The impact of an urbanizing tropical watershed to the surface runoff. *Global Journal of Environmental Science and Management*, *6*, 245–260. https://doi.org/10.22034/gjesm.2020.02.09

Innoter. (2024). Types of water indixes and their applications. https://innoter.com/en/articles/types-of-water-indixes-and-their-applications/#:~:text=Modified%20Normalized%20Difference%20Water%20Index%20(MNDWI)%20is%20a%20variant%20of,open%20water%20in%20other%20indices.

Iowa Organization of Natural Resources. (2023). Chapter 3-section 3 time of concentration a. introduction.

IPCC. (2014). Climate change 2014: Impacts, adaptation, and vulnerability – contribution of working group ii to the fifth assessment report of the intergovernmental panel on climate change [Accessed April 16, 2025]. https://www.ipcc.ch/report/ar5/wg2/

Izdori, F., Alexander, A., Mulungu, D., & Mugisha, L. (2022). Assessing Morphological Changes of the Msimbazi River Using Satellite Images. *Tanzania Journal of Engineering and Technology*, *41*(4), 15–23. https://doi.org/10.52339/tjet.v41i4.871

James, A., & Lecce, S. A. (2013). Impacts of land-use and land-cover change on river systems. In J. Shroder (Ed.), *Treatise on geomorphology* (pp. 768–793, Vol. 13). Academic Press. https://doi.org/10.1016/B978-0-12-374739-6.00264-5

Kashaigili, J. J., Mdemu, M. V., Nduganda, A. R., & Mbilinyi, B. P. (2013). Integrated assessment of forest cover change and above-ground carbon stock in pugu and kazimzumbwi forest reserves, tanzania. *Advances in Remote Sensing*, *02*, 1–9. https://doi.org/10.4236/ars.2013.21001

Kayitesi, N. M., Guzha, A. C., & Mariethoz, G. (2022). Impacts of land use, land cover change and climate change on river hydro-morphology: A review of research studies in tropical regions. *Journal of Hydrology*, *615*, 128702. https://doi.org/10.1016/j.jhydrol.2022.128702

Kazi, T. (2019, January). The msimbazi opportunity - transforming the msimbazi basin into a beacon of urban resilience. https://s3-eu-west-1.amazonaws.com/s3.sourceafrica.net/documents/119904/Msimbazi-Executive-Summary.pdf

Kibugu, C., Munishi, S., & Kongo, V. (2022). Impacts of land cover change caused by urbanization on the flood regime of msimbazi catchment in dar es salaam, tanzania. *Tanzania Journal of Engineering and Technology*, *41*, 35–51. https://doi.org/10.52339/tjet.v41i2.777

Kinyondo, A. A., & Pelizzo, R. (2018). Poor quality of data in africa: What are the issues? *Politics & Policy*, *46*(6), 1054–1071. https://doi.org/10.1111/polp.12277

Kironde, J. M. L. (2016). Governance deficits in dealing with the plight of dwellers of hazardous land: The case of the msimbazi river valley in dar es salaam, tanzania. *Current Urban Studies*, *04*, 303–328. https://doi.org/10.4236/cus.2016.43021

Knighton, D. (2014). *Fluvial forms and processes: A new perspective* (2nd). Routledge.

Ku, H. H. (1966). Notes on the use of propagation of error formulas. *Journal of Research of the National Bureau of Standards*, *70C*(4), 262. https://doi.org/10.6028/jres.070c.025

Langhorst, T., & Pavelsky, T. (2023). Global observations of riverbank erosion and accretion from landsat imagery. *Journal of Geophysical Research: Earth Surface*, *128*. https://doi.org/10.1029/2022JF006774

Leopold, L., Wolman, M., & Miller, J. (1995). *Fluvial processes in geomorphology* [ISBN: 978-0716701291]. W.H. Freeman; Company.

Li, P., Zhang, Y., Liang, C., Wang, H., & Li, Z. (2024). High spatiotemporal resolution river networks mapping on catchment scale using satellite remote sensing imagery and dem data. *Geophysical Research Letters*, *51*. https://doi.org/10.1029/2023GL107956

Lupala, J. M., Mdemu, M. V., & Butungo, S. P. (2014). Effects of peri-urban land use changes on forest ecosystem services: The case of settlements surrounding pugu and kazimzumbwi forest reserves in tanzania. *Journal of Geography and Geology*, *6*. https://doi.org/10.5539/jgg.v6n4p231

Machiwa, H., Mango, J., Sengupta, D., & Zhou, Y. (2021). Using time series remote sensing images in monitoring the spatial–temporal dynamics of lulc in the msimbazi basin, tanzania. *Land*, *10*. https://doi.org/10.3390/land10111139

Mackin, J. H. (1948). Concept of the graded river. *Bulletin of the Geological Society of America*, *69*, 463–512. https://wpg.forestry.oregonstate.edu/sites/default/files/seminars/1948_MACKIN_GradedRiver_GSABulletin.pdf

Massey Jr, F. J. (1951). The kolmogorov-smirnov test for goodness of fit. *Journal of the American Statistical Association*, *46*(253), 68–78.

Mdee, O. J. (2015). Spatial distribution of runoff in ungauged catchments in tanzania [© 2015 E.W. Publications]. *Water Utility Journal*, *9*, 61–70. https://www.ewra.net/wuj/pdf/WUJ_2015_09_06.pdf

Mehta, O., Kansal, M. L., & Bisht, D. S. (2022). A comparative study of the time of concentration methods for designing urban drainage infrastructure. *Aqua Water Infrastructure, Ecosystems and Society*, *71*, 1197–1218. https://doi.org/10.2166/aqua.2022.107

Mengen, D., Ottinger, M., Leinenkugel, P., & Ribbe, L. (2020). Modeling river discharge using automated river width measurements derived from sentinel-1 time series [Submission received: 31 August 2020 / Revised: 29 September 2020 / Accepted: 1 October 2020 / Published: 5 October 2020]. *Remote Sensing*, *12*(19), 3236. https://doi.org/10.3390/rs12193236

Mirzaee, S., Yousefi, S., Keesstra, S., Pourghasemi, H. R., Cerdà, A., & Fuller, I. C. (2018). Effects of hydrological events on morphological evolution of a fluvial system. *Journal of Hydrology*, *563*, 33–42. https://doi.org/10.1016/j.jhydrol.2018.05.065

Mkilima, T. (2021). The influence of land use and land cover change on stormwater runoff in a highly urbanizing catchment. a case of msimbazi catchment in dar es salaam city, tanzania. *Journal of Geography and Environmental Management*, *63*. https://doi.org/10.26577/jgem.2021.v63.i4.03

Nabeta, L. (2022). Msimbazi basin development project. https://www.worldbank.org/en/country/tanzania/brief/msimbazi-basin-development-project

NASA. (2025). The global precipitation measurement mission (gpm). https://gpm.nasa.gov/missions/GPM

NASA, U., & SERVIR-RCMRD. (2018). Tanzania SRTM DEM 30 meters [Accessed via SERVIR-RCMRD. Shuttle Radar Topography Mission data mosaicked and clipped to Tanzania. Released under the Open Database License (ODbL 1.0)]. https://maps.rcmrd.org/arcgis/rest/services/Tanzania/Tanzania_SRTM30meters/ImageServer

Noh, B., Wani, O., Dunne, K. B., & Lamb, M. P. (2024). Geomorphic risk maps for river migration using probabilistic modeling - a framework. *Earth Surface Dynamics*, *12*, 691–708. https://doi.org/10.5194/esurf-12-691-2024

Nyalusi, A., Chazua, I., & OpenMap Development Tanzania [OMDTZ]. (2025, February). Buildings 2016 and 2025.

Ohio Department of Transportation. (2020, January). *Location & design manual, volume 2 – drainage design*. https://dam.assets.ohio.gov/image/upload/transportation.ohio.gov/hydraulic/ld2/archive/2020-01-LD2.pdf

O'Leary, A., Cabunoc, A., Boughton, A., Mills, W., Michonneau, F., Wilson, G., Allen, J., Blischak, J., Pipitone, J., Hansen, M., Banaszkiewicz, P., Silva, R., Emonet, R., Poisot, T., Bekolay, T., & Trevor King, W. (2019). Sar water body classification. https://mbonnema.github.io/GoogleEarthEngine/07-SAR-Water-Classification/

OpenMap Development Tanzania. (2025). Building block data Dar es Salaam 2016 and 2025.

Pannone, M., & Vincenzo, A. D. (2022). On the prediction of the characteristic times of river meander cutoff sequence: Theoretical model and comparison with laboratory and field observations [Open Access]. *Water Resources Research*, *58*(7), e2021WR031661. https://doi.org/10.1029/2021WR031661

RCMRD-SERVIRESA, Government of the Republic of Tanzania, NASA, USAID, & USEPA. (2018a). Tanzania landcover 2000 scheme ii [Land Cover maps developed for Greenhouse Gas Inventories to support the LULUCF sector. Available under the Open Database License (ODbL). Last updated: 2018-01-31]. https://s3.amazonaws.com/rcmrd-open-data/downloadable_files/Tanzania_Landcover_2000_Scheme_II.zip

RCMRD-SERVIRESA, Government of the Republic of Tanzania, NASA, USAID, & USEPA. (2018b). Tanzania landcover 2010 scheme ii [Land Cover maps developed for Greenhouse Gas Inventories to support the LULUCF sector. Available under the Open Database License (ODbL). Last updated: 2018-01-31]. https://s3.amazonaws.com/rcmrd-open-data/downloadable_files/Tanzania_Landcover_2010_Scheme+_II.zip

Redolfi, M., Carlin, M., & Tubino, M. (2023). The impact of climate change on river alternate bars. *Geophysical Research Letters*, *50*. https://doi.org/10.1029/2022GL102072

Rinaldi, M., Surian, N., Comiti, F., & Bussettini, M. (2013). A framework for the assessment of river morphodynamic alteration and its applications to european rivers [Accessed April 16, 2025]. In *Deliverable 6 of the fp7 european project reform*. European Commission. https://www.reformrivers.eu

Rosgen, D. L. (1996). *Applied river morphology* [ISBN: 978-0991931105]. Wildland Hydrology.

Schwenk, J., Lanzoni, S., & Foufoula-Georgiou, E. (2015). The life of a meander bend: Connecting shape and dynamics via analysis of a numerical model. *Journal of Geophysical Research: Earth Surface*, *120*(4), 690–710. https://doi.org/10.1002/2014JF003252

Shibayama, T., & Esteban, M. (2022). *Coastal disaster surveys and assessment for risk mitigation*. CRC Press. https://books.google.nl/books?id=D5yaEAAAQBAJ

Singh, V. P. (1976). Derivation of time of concentration. *Journal of Hydrology*, *30*(1), 147–165. https://doi.org/https://doi.org/10.1016/0022-1694(76)90095-0

Stone, K., van Duinen, R., Veerbeek, W., & Dopp, S. (2011). *Sensitivity and vulnerability of urban systems: Assessment of climate change impact to urban systems* (tech. rep. No. 1202270-008). Deltares. https://edepot.wur.nl/287808

Tang, Q., & Lettenmaier, D. P. (2012). 21st century runoff sensitivities of major global river basins [Free Access]. *Geophysical Research Letters*, *39*(6), L06403. https://doi.org/10.1029/2011GL050834

TanzaniaInvest. (2024). *Sgr tanzania standard gauge railway (sgr)* [Last Updated: 1st August 2024]. https://www.tanzaniainvest.com/sgr

Tha, T., Piman, T., Bhatpuria, D., & Ruangrassamee, P. (2022). Assessment of riverbank erosion hotspots along the mekong river in cambodia using remote sensing and hazard exposure mapping. *Water (Switzerland)*, *14*. https://doi.org/10.3390/w14131981

Thieler, E. R., Martin, D., & Ergul, A. (2003). *The digital shoreline analysis system, version 2.0: Shoreline change measurement software extension for arcview* (USGS Open-File Report No. 03-076). U.S. Geological Survey. https://pubs.usgs.gov/of/2003/0076/

Timmermans, J. (2024, December). Personal communication [Joris Timmermans, personal communication, 4 December 2024.]. *Delft University of Technology*.

Turner, B., Kasperson, R., Matson, P., McCarthy, J., Corell, R., Christensen, L., Eckley, N., Kasperson, J., Luers, A., Martello, M., Polsky, C., Pulsipher, A., & Schiller, A. (2003). A framework for vulnerability analysis in sustainability science. *Proceedings of the National Academy of Sciences*, *100*(14), 8074–8079. https://doi.org/10.1073/pnas.1231335100

UNDRR. (2017). Terminology on disaster risk reduction [Accessed April 16, 2025]. https://www.undrr.org/terminology

UNDRR. (2018). Envisioning urban resilience for tanzania. *PreventionWeb*. https://www.preventionweb.net/news/envisioning-urban-resilience-tanzania

UNISDR. (2009). 2009 unisdr terminology on disaster risk reduction [Accessed April 16, 2025]. https://www.undrr.org/publication/2009-unisdr-terminology-disaster-risk-reduction

United Nations Department of Economic and Social Affairs, P., Menozzi, C., Spoorenberg, T., Bassarsky, L., Kantorová, V., Zeifman, L., Wheldon, M., Gonnella, G., Gu, D., Chen, Z., Athaluri, S., Castanheira, H. C., Fernandes, F., Kamiya, Y., Lattes, P., Lay, K. K., Palacharla, S. M., Silva, J. H. M. d., Williams, I., … Schoumaker, B. (2024). *World Population Prospects 2024: Summary of Results* (tech. rep.). United Nations Department of Economic and Social Affairs. https://www.un.org/development/desa/pd/sites/www.un.org.development.desa.pd/files/undesa_pd_2024_wpp_2024_advance_unedited_0.pdf

U.S. Geological Survey. (2019). Surface runoff and the water cycle [Accessed: 2025-03-28]. https://www.usgs.gov/special-topics/water-science-school/science/surface-runoff-and-water-cycle

U.S. Geological Survey. (2020, March). Landsat Satellite Missions. https://www.usgs.gov/landsat-missions/landsat-satellite-missions

U.S. Geological Survey. (2024a, January). Digital Shoreline Analysis System (DSAS). https://www.usgs.gov/centers/whcmsc/science/digital-shoreline-analysis-system-dsas

U.S. Geological Survey. (2024b). What is el niño and what are its effects? [Accessed: 2025-05-21]. https://www.usgs.gov/faqs/what-el-nino-and-what-are-its-effects

Van Camp, M., Mtoni, Y. E., Mjemah, I. C., Bakundukize, C., & Walraevens, K. (2014). Investigating seawater intrusion due to groundwater pumping with schematic model simulations: The example of the dar es salaam coastal aquifer in tanzania. *Journal of African Earth Sciences*, *96*, 71–78. https://doi.org/10.1016/j.jafrearsci.2014.02.012

van de Sande, B., & Laboyrie, H. (2021, March). Flood management feasibility study for the msimbazi middle catchment area - vulnerability analysis. https://cdr-international.nl/portfolio/flood-management-feasibility-study-for-the-msimbazi-middle-catchment-area-tanzania-giz/

Vermote, E., Justice, C., Claverie, M., & Franch, B. (2016). Preliminary analysis of the performance of the landsat 8/oli land surface reflectance product. *Remote Sensing of Environment*, *185*, 46–56. https://doi.org/10.1016/j.rse.2016.04.008

Vörösmarty, C. J., Green, P., Salisbury, J., & Lammers, R. B. (2000). Global water resources: Vulnerability from climate change and population growth. *Science*, *289*, 284–288. https://doi.org/10.1126/science.289.5477.284

Wackerly, D., Mendenhall, W., & Scheaffer, R. (2008). *Mathematical statistics with applications* (7th). Thomson Brooks/Cole.

Wania, A., Joubert-boitat, I., Dottori, F., Kalas, M., & Salamon, P. (2021). Increasing timeliness of satellite-based flood mapping using early warning systems in the copernicus emergency management service. *Remote Sensing*, *13*. https://doi.org/10.3390/rs13112114

Ward, P. J., de Moel, H., & Aerts, J. C. J. H. (2011). How are flood risk estimates affected by the choice of return-periods? *Natural Hazards and Earth System Sciences*, *11*, 3181–3195. https://doi.org/10.5194/nhess-11-3181-2011

Westra, S., Fowler, H. J., Evans, J. P., Alexander, L. V., Berg, P., Johnson, F., Kendon, E. J., Lenderink, G., & Roberts, N. M. (2014). Future changes to the intensity and frequency of short-duration extreme rainfall. *Reviews of Geophysics*, *52*(3), 522–555. https://doi.org/10.1002/2014RG000464

Wibig, J., Jaczewski, A., Brzóska, B., Konca-Kędzierska, K., & Pianko-Kluczyńska, K. (2014). How does the areal averaging influence the extremes? the context of gridded observation data sets [Open Access Article]. *Meteorologische Zeitschrift*, *23*(3), 265–276. https://doi.org/10.1127/0941-2948/2014/0470

Wisner, B., Blaikie, P., Cannon, T., & Davis, I. (2004). *At risk: Natural hazards, people's vulnerability and disasters* (2nd). Routledge.

Wohl, E. (2004). Compromised rivers: Understanding historical human impacts on rivers in the context of restoration. *Ecology and Society*, *10*(2). https://doi.org/10.5751/ES-01339-100202

World Bank. (2024). *Crisis response window plus (crw+) eligibility note: Support for tanzania — response to the impact of 2023-2024 el niño and cyclone hidaya* (tech. rep.) (Accessed: 2025-05-21). World Bank. https://documents1.worldbank.org/curated/en/099080124134011985/pdf/BOSIB-33cc9ef5-57a3-498e-a4c5-eb9289e31903.pdf

World Bank Group. (2024, February). Msimbazi basin development project. https://projects.worldbank.org/en/projects-operations/project-detail/P169425?_gl=1*kx3pso*_gcl_au*Nzg5NTcyNjg5LjE3MjYwNDM3NTU.

World Bank Open Data. (2023). https://data.worldbank.org/indicator/SP.POP.GROW?locations=TZ

World Meteorological Organization. (2023, November). El niño expected to last at least until april 2024 [Accessed April 24, 2025]. https://wmo.int/media/news/el-nino-expected-last-least-until-april-2024

Xia, J., Wang, Y., Zhou, M., Deng, S., Li, Z., & Wang, Z. (2021). Variations in channel centerline migration rate and intensity of a braided reach in the lower yellow river. *Remote Sensing*, *13*. https://doi.org/10.3390/rs13091680

Yamazaki, D., O'Loughlin, F., Trigg, M. A., Miller, Z. F., Pavelsky, T. M., & Bates, P. D. (2014). Development of the global width database for large rivers [First published: 11 April 2014]. *Water Resources Research*, *50*(4), 3457–3468. https://doi.org/10.1002/2013WR014664

Zanaga, D., Van De Kerchove, R., Daems, D., De Keersmaecker, W., Brockmann, C., Kirches, G., Wevers, J., Cartus, O., Santoro, M., Fritz, S., Lesiv, M., Herold, M., Tsendbazar, N. E., Xu, P., Ramoino, F., & Arino, O. (2022). ESA WorldCover 10 m 2021 v200 [Accessed via Zenodo]. https://doi.org/10.5281/zenodo.7254221

Zanaga, D., Van De Kerchove, R., De Keersmaecker, W., Souverijns, N., Brockmann, C., Quast, R., Wevers, J., Grosu, A., Paccini, A., Vergnaud, S., Cartus, O., Santoro, M., Fritz, S., Georgieva, I., Lesiv, M., Carter, S., Herold, M., Li, L., Tsendbazar, N. E., … Arino, O. (2021). ESA WorldCover 10 m 2020 v100 [Accessed via Zenodo]. https://doi.org/10.5281/zenodo.5571936

Zwiers, F., Asrar, G., & Hurrell, J. (2013). Climate extremes: Challenges in estimating and understanding recent changes in the frequency and intensity of extreme climate and weather events. In G. Asrar & J. Hurrell (Eds.), *Climate science for serving society* (pp. 213–230). Springer. https://doi.org/10.1007/978-94-007-6692-1_13

A

Applicability of automated waterbody detection

To accurately track the river's position and width, it is essential to detect the waterbody. The boundary between land and water can then be identified as the riverbank line.

Water detection can be accomplished through various methods. In this research, two Remote Sensing methods have been evaluated for their applicability. The first method involves the use of the Modified Normalised Difference Water Index (MNDWI) for better visibility in built-up areas, combined with the Normalised Difference Water Index (NDWI) for vegetated areas. The second method utilises Synthetic Aperture Radar (SAR), which has the advantage of being unaffected by cloud cover, thereby ensuring consistent data availability.

A.1. Applicability of remote sensing

According to Dr. ir. Timmermans (2024), Assistant Professor in Remote Sensing at the Delft University of Technology, the application of Remote Sensing requires a systematic evaluation of the following steps.

1. Determine observables, which involves identifying the specific variables to detect. In this research, the primary observable is the main Msimbazi River. See figure A.1

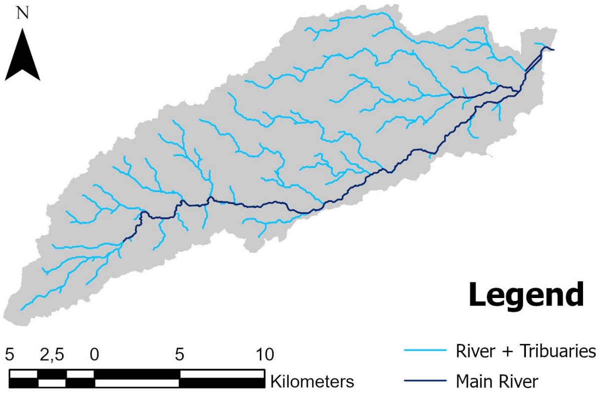

Figure A.1: Main Msimbazi river and its tributaries.

2. Determine the technical requirements. The technical requirements are as follows:

- *Spatial resolution*. Spatial resolution refers to the smallest objects or details that a satellite sensor can distinguish. In the context of river detection, this determines the level of detail captured on the ground. A high spatial resolution, such as 10 meters or smaller, is crucial for detecting narrow rivers or identifying fine-scale features like riverbanks (Frank, 2020). For broader rivers or regional analyses, medium resolutions, such as 30 meters from Landsat, might suffice (Frank, 2020; Li et al., 2024). However, low spatial resolutions exceeding 250 meters are typically inadequate for identifying specific river characteristics but may still serve well for general basin-scale studies (Hao et al., 2024).

- *Spatial extent*. Spatial extent represents the total area covered by the satellite imagery. This is important to ensure the sensor's coverage aligns with the size of the study area. For a localised river segment or catchment, sensors with smaller coverage areas are suitable. However, for entire river basins or transboundary river systems, imagery with broader spatial coverage is required (Vermote et al., 2016).
- *Temporal resolution*. Temporal resolution refers to the frequency with which a satellite revisits the same location on Earth. For rivers subject to dynamic changes, such as seasonal flow variations, sediment deposition, or flooding, high temporal resolution is vital (Casal, 2022). Satellites like Sentinel-2, with a revisit time of five days, are well-suited for monitoring rapidly changing conditions. Conversely, for slower, long-term changes, a revisit time of 16 days, as offered by Landsat, may suffice (Hemati et al., 2021).
- *Temporal extent*. Temporal extent denotes the time span over which satellite data is available. This is particularly important for historical analyses or trend studies. For example, if the goal is to understand past changes in river morphology or flow, data from satellites like Landsat, with archives dating back to 1972, are invaluable (Hemati et al., 2021). Conversely, for current or future monitoring, recent missions such as Sentinel-2 provide the necessary data.
- *Accuracy*. Accuracy refers to how well the satellite data represents real-world conditions. This includes positional accuracy, which ensures the detected river features align with their actual geographic locations, and content accuracy, which differentiates between water and surrounding land (Frank, 2020). For narrow rivers, high spatial resolution is essential to resolve their width accurately. High accuracy is also critical when detecting riverbanks, as positional errors can distort analyses of erosion or migration (Duró et al., 2018).
- *Timeliness*. Timeliness refers to how quickly satellite data becomes available after acquisition. This is particularly significant in scenarios requiring rapid response, such as during flood events or extreme rainfall. Near-real-time data availability within hours is crucial for emergency response, while delays of several days may suffice for long-term research (Wania et al., 2021).

3. Determine the most critical technical requirement, referring to the requirement that imposes the most significant constraint on the analysis. In this research on the Msimbazi River, spatial resolution is clearly the main limiting factor.

4. Match with available detection methods. Based on the determined observable(s), technical requirements, and the most critical requirement(s), an appropriate detection method should be selected. For this research, this selection leads to the MNDWI and NDWI method as well as the SAR method.

A.2. MNDWI & NDWI method

Applying the MNDWI and NDWI methods for water body extraction is conducted using Google Earth Engine, with the code provided below. Evaluations reveal that spatial resolution is a critical factor. Prior to 2018, the Msimbazi River reaches a maximum width of approximately 15 meters during extreme rainfall events, but under typical conditions, it measures around 4 meters wide. With satellite imagery spatial resolutions ranging from 10 to 30 meters, it becomes impossible to detect the river accurately. Furthermore, vegetation often obscures parts of the river, making detection even more challenging.

The MNDWI and NDWI methods leverage the reflective properties of water in specific spectral regions. Using the Normalized Difference Water Index (NDWI) or Modified NDWI (MNDWI), water bodies can be detected based on differences in reflectance between the Green and Near-Infrared (NIR) bands or the Green and Short-Wave Infrared (SWIR) bands, respectively (Innoter, 2024). This approach is particularly suitable for Sentinel-2 imagery (10 m resolution) and Landsat imagery (30 m resolution), which provide multi-year coverage and the required spectral bands (Innoter, 2024). The formulas are defined as follows:

$$NDWI = \frac{(Green - NIR)}{(Green + NIR)} \tag{A.1}$$

$$MNDWI = \frac{(Green - SWIR)}{(Green + SWIR)} \tag{A.2}$$

To reduce work, it is chosen to automate the application of the MNDWI & NDWI method. Below the code which enables this automation is given. The provided code is written in JavaScript for the Google Earth Engine (GEE) platform, automating the process of selecting, filtering, processing, and visualizing satellite imagery. Here's a detailed breakdown of the script's functionality:

Setting Criteria and Variables. The code begins by defining a `criteria` object to filter images based on a specific date range, cloud cover percentage, and area overlap with the region of interest (AOI). The start and end dates are extracted from the criteria object, and the AOI is specified as a geometry.

Defining Functions to select the best image:

- `filterByOverlap`: This function calculates the percentage overlap between an image's geometry and the AOI geometry. It computes the intersection of the image and AOI geometries, calculates their respective areas, and derives the overlap percentage. The overlap percentage is added as metadata to each image.
- `tagLandsat` and `tagSentinel`: These functions tag images with metadata indicating their source satellite (`LANDSAT_X` or `SENTINEL_2`) and ensure the cloud cover value is set (defaulting to -1 if missing).
- Retrieving Image Collections:
  - Landsat Collection: The script merges data from Landsat 4, 5, 7, 8, and 9 collections and applies the following filters:
    - Bounds: Images must intersect the AOI.
    - Date: Images must fall within the specified date range.
    - Cloud Cover: Images must have less than the specified maximum cloud percentage and not be null.

    Each image is processed with `filterByOverlap` to compute overlap percentages and `tagLandsat` to assign metadata.
  - Sentinel-2 Collection: The Sentinel-2 collection is similarly filtered by AOI, date range, and cloud cover. Images must also meet a minimum overlap percentage of 50%. Each image is processed with `filterByOverlap` and `tagSentinel` for metadata assignment.
- Combining and Sorting Collections: The Landsat and Sentinel-2 collections are merged into a single `combinedCollection`. This collection is sorted by the `cloud_cover` property in ascending order to prioritize images with minimal cloud coverage.
- Selecting the Best Image. The first image in the sorted collection (lowest cloud cover) is retrieved.
- `addImageToMap`: This function visualizes an image based on its source satellite. It selects specific spectral bands for true-color visualization, calculates their minimum and maximum values, normalizes the bands, and clips the image to the AOI. Visualization parameters such as color channels, range, and gamma correction are tailored to each satellite type.

Cloud Masking: The `maskClouds` function identifies and masks cloud pixels in an image. It differs for Landsat and Sentinel:

- Landsat, uses the `QA_PIXEL` band to identify cloud pixels. The cloud bit (4th bit) in this band is used to generate a binary mask, setting cloud-covered pixels to 0. The cloud pixels are marked and stored as metadata using `image.set('cloudPixels', cloudPixels)`.

- Sentinel-2, Utilizes the QA60 band for cloud masking and additionally applies a dynamic cloud detection using the brightness of visible bands (B2, B3, B4). It combines these two masking methods to produce a more accurate cloud mask, marking the cloud pixels as metadata similarly.

Shadow Masking: The `maskShadows` function identifies and masks shadow pixels in an image. It differs for Landsat and Sentinel:

- Landsat: It retrieves the cloud pixels from the maskClouds function and uses a focal operation (`focal_max`) to identify potential shadow locations within 30 pixels around cloud areas. This is done to overcome the chance of masking other shadow-like areas that have nothing to do with a cloud. It applies the `QA_PIXEL` band's shadow bit (7th bit) to create a shadow mask, which is then used to mask shadows. The final mask keeps shadow pixels where shadows are detected (`finalMask`).
- Sentinel-2: The process is similar to the Landsat process, it retrieves cloud pixels and identifies shadow potential using a 30-pixel radius. It uses the SWIR band (B11) for shadow detection and applies a typical threshold (e.g., less than 2000) to identify shadows. The final mask is created similarly to the Landsat process, inverting the logic to mask out non-shadow pixels.

Calculating the MNDWI: This is done by the `calculateMNDWI` function:

- Sentinel-2: The function calculates the MNDWI using the Green (B3) and SWIR1 (B11) bands. The formula for MNDWI is the normalized difference between the Green and SWIR1 bands (as given by equation A.2). The resulting index is renamed to `'MNDWI'` before being returned.
- Landsat 8 & 9: The function calculates MNDWI using the Green (SR_B3) and SWIR1 (SR_B6 for Landsat 8 and 9) bands. The normalized difference formula is applied similarly, but using these different band names specific to Landsat 8 and 9 sensors. The resulting index is also renamed to `'MNDWI'`.
- Landsat 4, 5 & 7: The function uses the same calculation method as for Landsat 8 & 9 but with different SWIR1 bands (SR_B5 for Landsat 4, 5, and 7). Again, the resulting index is renamed to `'MNDWI'`.

Determining the appropriate MNDWI image, the function checks the source metadata of the image to determine which type it is: If the source starts with `'SENTINEL'`, it returns the MNDWI for Sentinel-2. If the source starts with `'LANDSAT_8'` or `'LANDSAT_9'`, it returns the MNDWI for Landsat 8 and 9. For other types (Landsat 4, 5, 7), it returns the corresponding MNDWI calculation.

Computing the MNDWI:

1. Compute the MNDWI using the appropriate function (`calculateMNDWI`) on the `shadowMaskedImage`.
2. Clip the MNDWI image to the area of interest (`geometry`).
3. Calculate the histogram for MNDWI values within the area of interest using the `reduceRegion` method with 100 bins for detailed analysis.
4. Visualize the histogram: A User Interface chart is created to visualize the histogram of MNDWI values.
5. Adding MNDWI visualization on the map: The `mndwiClipped` image is added to the map with specific visualization parameters for Sentinel and Landsat images.

Calculating the NDWI: This is done by the `calculateNDWI` function:

- Sentinel-2: The function calculates the NDWI using the Green (B3) and NIR (B8) bands. The formula for NDWI is the normalized difference between the Green and NIR bands (as given by equation A.1). The resulting index is renamed to `'NDWI'` before being returned.
- Landsat 8 & 9: The function calculates NDWI using the Green (SR_B3) and NIR (SR_B5 for Landsat 8/9 or SR_B4 for older Landsat). The normalized difference formula is applied using these specific bands. The resulting index is renamed to `'NDWI'`.
- Landsat 4, 5 & 7: The function uses the same calculation method as for Landsat 8 & 9 but with different NIR bands (SR_B4 for Landsat 4, 5, and 7). Again, the resulting index is renamed to `'NDWI'`.

Determining the appropriate NDWI image: The function checks the source metadata of the image to determine which type it is: If the source starts with `'SENTINEL'`, it returns the NDWI for Sentinel-2. If the source starts with `'LANDSAT_8'` or `'LANDSAT_9'`, it returns the NDWI for Landsat 8 and 9. For other types (Landsat 4, 5, 7), it returns the corresponding NDWI calculation.

Computing the NDWI:

1. Compute the NDWI using the appropriate function (`calculateNDWI`) on the `shadowMaskedImage`.
2. Clip the NDWI image to the area of interest (`geometry`).
3. Calculate the histogram for NDWI values within the area of interest using the `reduceRegion` method with 100 bins for detailed analysis.
4. Visualize the histogram: A User Interface chart is created to visualize the histogram of MNDWI values.
5. Adding MNDWI visualization on the map: The `ndwiClipped` image is added to the map with specific visualization parameters for Sentinel and Landsat images.

Otsu Thresholding for Water Body Detection: In order to determine the optimal reflectance threshold for waterbody detection Otsu Thresholding is applied. This is done by the `otsu` function, which:

- Takes a histogram's data dictionary as input.
- Computes the Otsu's threshold using the between-class variance (BCV) method to find an optimal threshold for separating water from non-water areas.
- Iterates over potential thresholds to find the one with the maximum BCV, which is most suitable for water detection.
- The threshold is then constrained to a sensible range for water reflectance (approximately 0 to 0.35). As negative reflectance corresponds to built-up areas.

Compute Thresholds for MNDWI and NDWI: The function `otsu` is applied to the MNDWI and NDWI histograms to compute the optimal thresholds for water detection. The calculated thresholds (`thresholdMNDWI` and `thresholdNDWI`) are printed to the console.

Create Binary Water Mask for both MNDWI and NDWI by comparing the respective images with their calculated thresholds. These masks are updated to only display areas identified as water. The resulting masks are added to the map with a blue color palette for visualization.

By applying the methodology to the Msimbazi Catchment, it is clear that the river is not sufficiently wide for detection using current Landsat 4-9 or Sentinel 2 imagery. During 2018, when the river reached its widest, a few reaches were detectable, but it was not feasible to detect the river in other years. This limitation obstructs a time-based analysis of river changes. Figures A.2 and A.3 show the output of the model for June 5th, 2018, with a minimum overlap percentage of 50% and a maximum cloud cover of 10%.

According to the Remote Sensing evaluation framework defined by Timmermans (2024), the MNDWI and NDWI methods are not suitable for accurately detecting the main Msimbazi river due to the limitations posed by the spatial resolution of available imagery. Figure A.3b showes the Msimbazi detection quite well, but one should remember that this image is form 2018 when the river was relatively wide. Also, comparing it with figure A.3a, it can be seen that the Msimbazi is only detected for its middle reach. When moving further downstream, the river is not detected anymore.

To address the gaps in the waterbody detection (see figure A.3c), the model can be improved by integrating Machine Learning or Supervised Classification techniques such as k-means clustering. These methods are capable of identifying the linear structure of the river and enabling water body detection even when reflectance alone is inadequate.

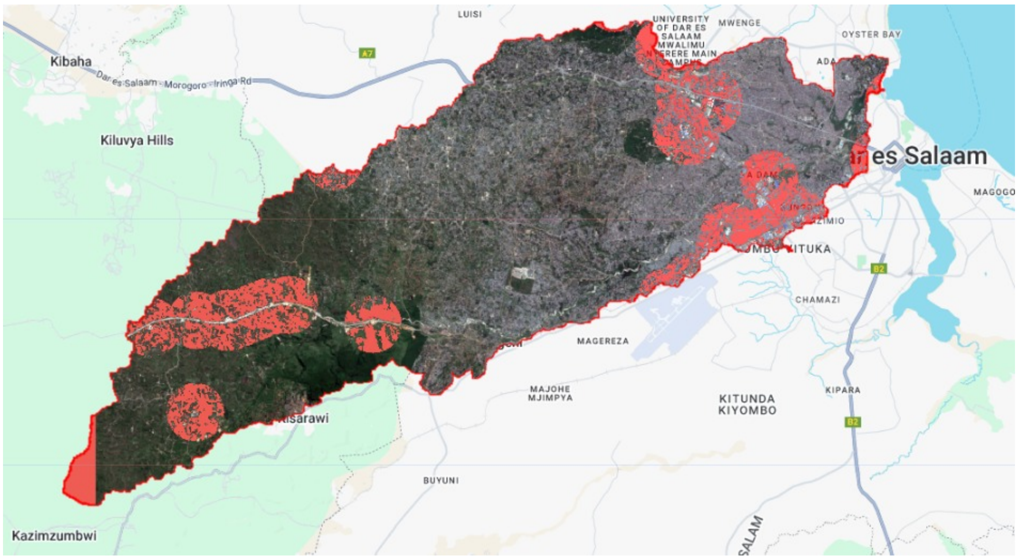

(a) Masked image, red areas represent the areas that are masked by the `cloudMask` and `shadowMask` functions.

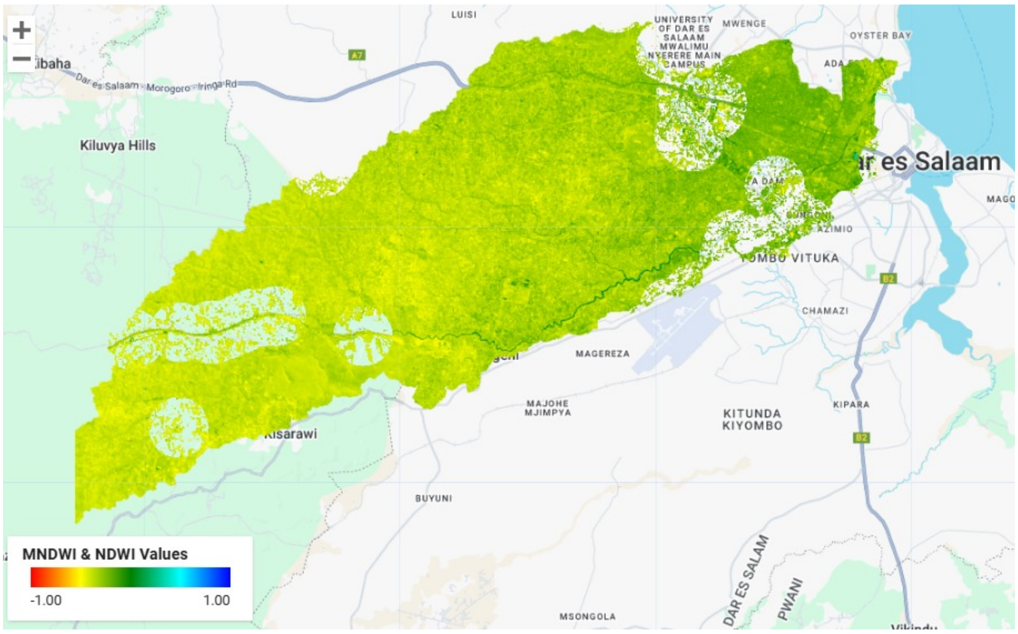

(b) MNDWI Layer

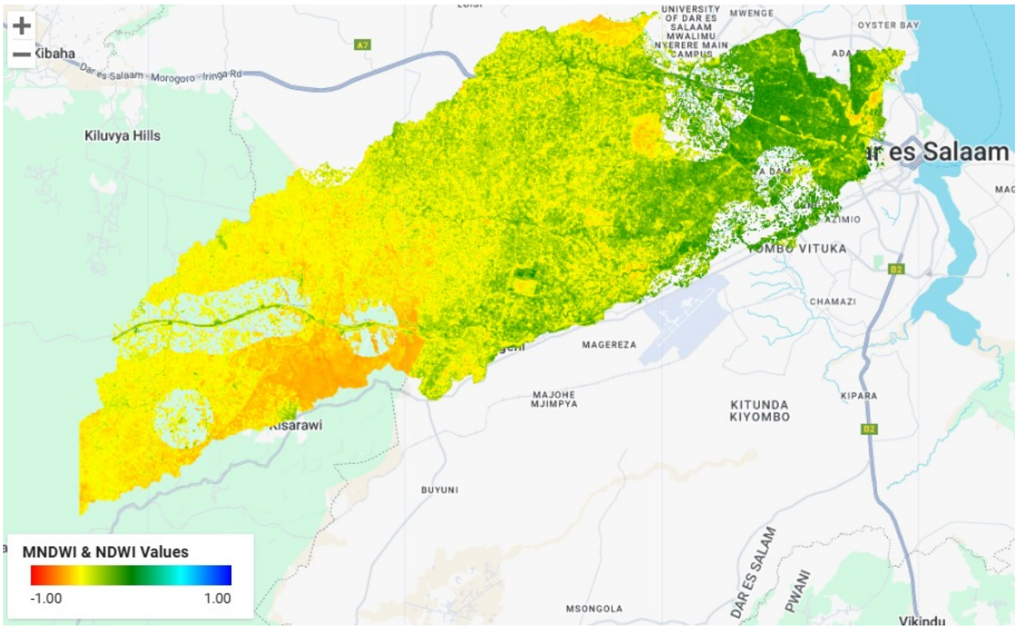

(c) NDWI Layer

Figure A.2: MNDWI & NDWI model output

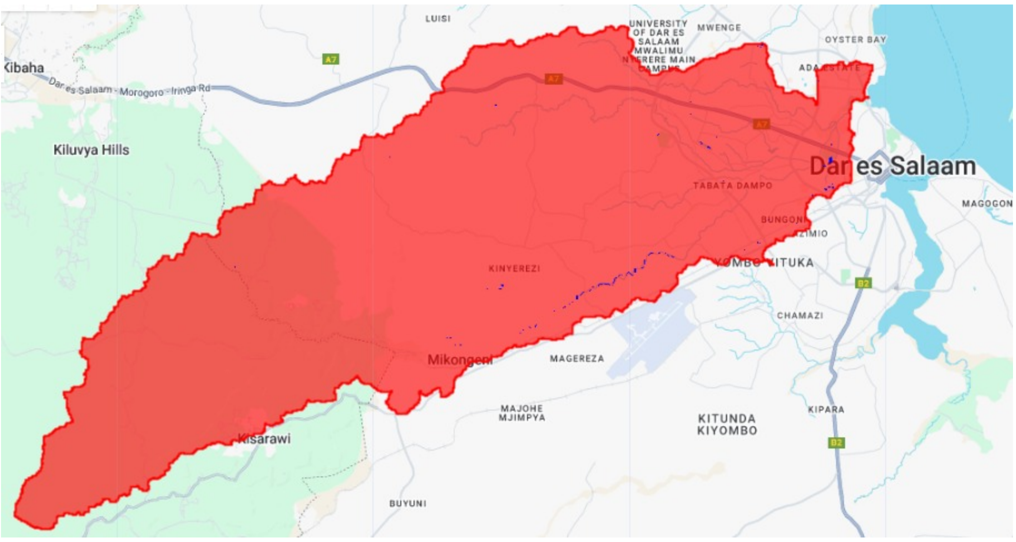

(a) Catchment area (red) and the detected waterbodies (dark blue)

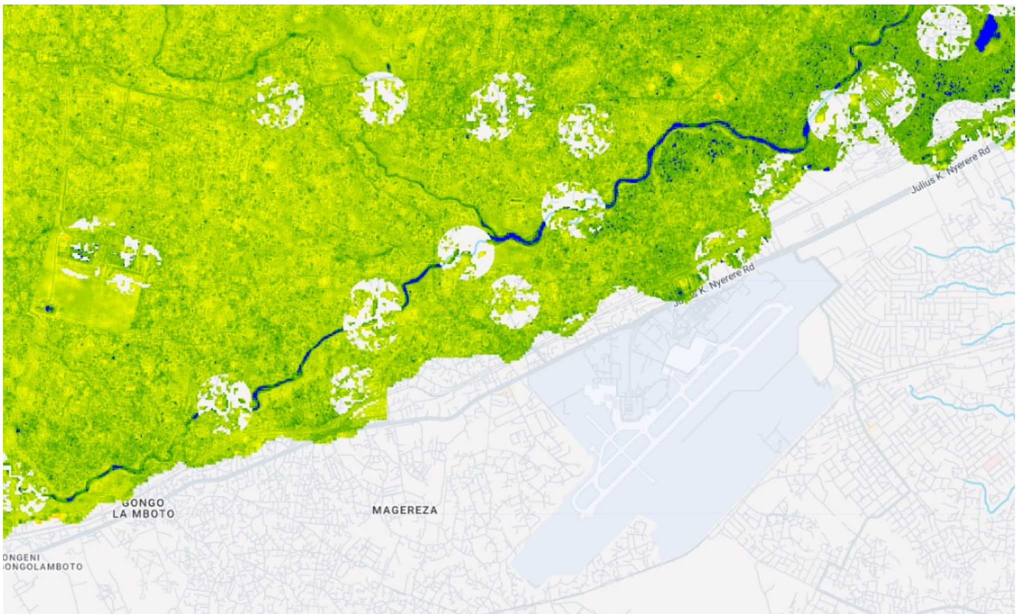

(b) Zoomed in MNDWI layer + Detected waterbody (Dark blue)

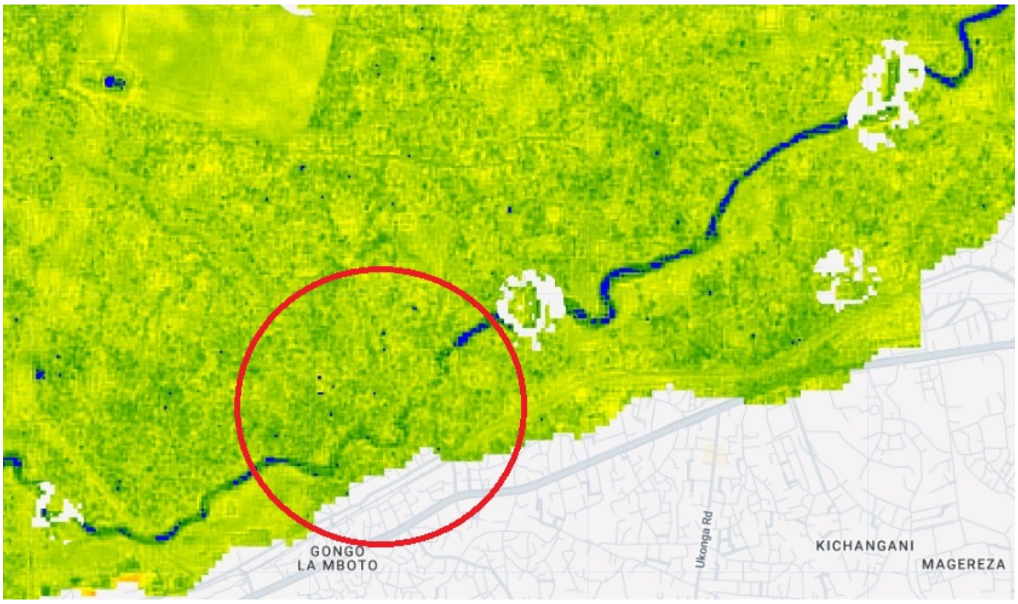

(c) Example of a gap in waterbody detection, although the linear structure is visible in the MNDWI layer. (MNDWI + detected water (dark blue)

Figure A.3: Water extraction based on MNDWI & NDWI

A.3. Sentinel-1 (SAR) image analysis method

This method utilizes Synthetic Aperture Radar (SAR) imagery from the Sentinel-1 satellite to classify water bodies in a region of interest (ROI). SAR sensors are particularly useful in cloudy regions like the Msimbazi catchment where monsoon season blocks visible satellite images. SAR works by transmitting radar waves towards the Earth at an off-nadir angle, allowing it to penetrate clouds and provide clear images of the Earth's surface even during poor weather conditions. The radar signal bounces back from the surface and is measured based on the amount of backscatter, which varies depending on surface roughness. Smooth surfaces like water scatter little radar energy, appearing as dark areas against more scattering land surfaces. Figure A.4 gives a visualisation of how this works (O'Leary et al., 2019)

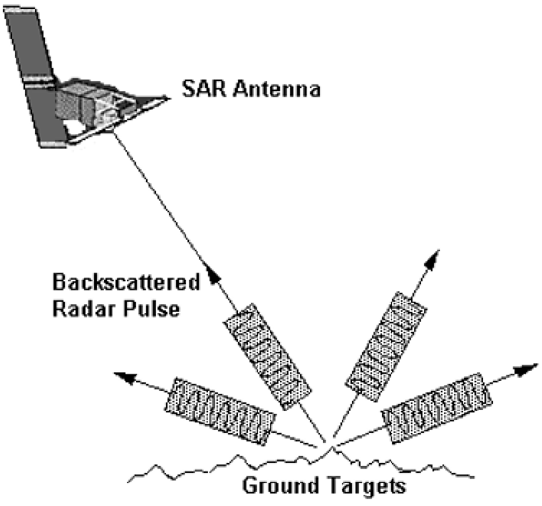

crisp.nus.edu.sg/

Figure A.4: Schematic of SAR application (O'Leary et al., 2019)

The code contains the following functionalities:

Define the Region of Interest (ROI): The code begins by defining the ROI with a specified color visualization, which is added to the map for context.

Loading and filtering Sentinel-1 data: The code loads the Sentinel-1 SAR image collection from the COPERNICUS dataset. It filters the collection to include images from the chosen year within the desired date range. Further filters are applied to retain only images with 'VV' polarization, which involves both the transmission and reception of vertically polarized radar waves. This polarization is optimal for water detection, as variations in backscatter caused by surface roughness do not significantly alter it (O'Leary et al., 2019).

Adding the first SAR image to the map: An initial SAR image is added to the map for visual inspection, giving an idea of how a SAR image appears.

Filtering speckle noise: Speckle noise is a common issue in SAR images, characterized by bright dots that can degrade image quality. The `filterSpeckles` function applies a focal median filter to reduce this noise. This process replaces each pixel with the median value of its neighboring pixels, smoothing out speckle noise without significantly altering the actual features of the image (O'Leary et al., 2019).

Classifying water pixels: The `classifyWater` function identifies water pixels based on a simple threshold of backscatter intensity, with pixels below the -16 threshold classified as water. This rule-based threshold helps distinguish water bodies from surrounding land. The optimal threshold can vary and might be refined using training data or more complex statistical methods. The function creates a binary mask where water pixels are labeled as 1 and non-water pixels as 0, which is then added as a new band to the SAR image (O'Leary et al., 2019).

Adding classified water area to the map: The code maps the water classification process across the Sentinel-1 collection, adding the filtered image to the map for comparison with the original image. This step enhances the visibility of water bodies by removing the speckle noise and clearly defining them against the land (O'Leary et al., 2019).

Creating a Time Series Chart: A time series chart is generated to visualize the number of inundated pixels over time within the ROI. This chart uses the sum of the classified water pixels across all images in the collection as a spatial reducer, which gives the total number of water pixels at each time step. The scale of the chart is set to 100 meters to speed up calculations, though this introduces some error compared to the native 10-meter resolution of Sentinel-1 images (O'Leary et al., 2019).

Interactive Chart: An interactive chart is added to the map, with a callback function triggered when a user clicks on a data point. This function displays the corresponding SAR image and the classified water area for the clicked date on the map, updating a label with the date of the selected image (O'Leary et al., 2019).

Just like with the MNDWI and NDWI method, the SAR method proofs to be poor for the Msimbazi catchment. The critical technical requirement is once again the spatial resolution. To vcalidate the method and correpsonding JavaScript, the Region of Interest has also been changed to the Rufiji river, which is located south of Dar es Salaam. This is a wider river and, as can be seen from figure A.5c, the model is performing well. Un fortunately that cannot be said for the Msimbazi river, as can be seen from figures A.5a and A.5b.

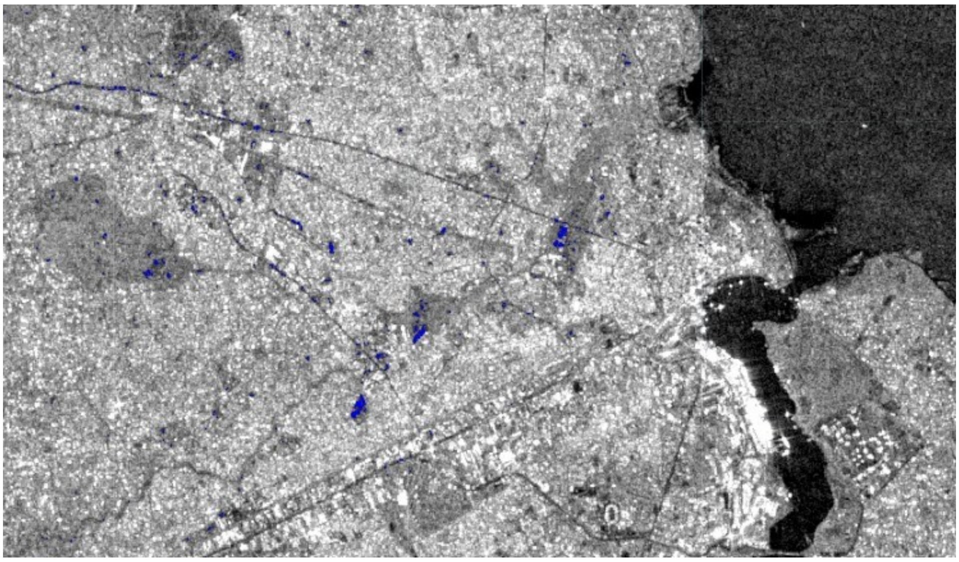

(a) SAR water detection for the Msimbazi River on 26 February 2018.

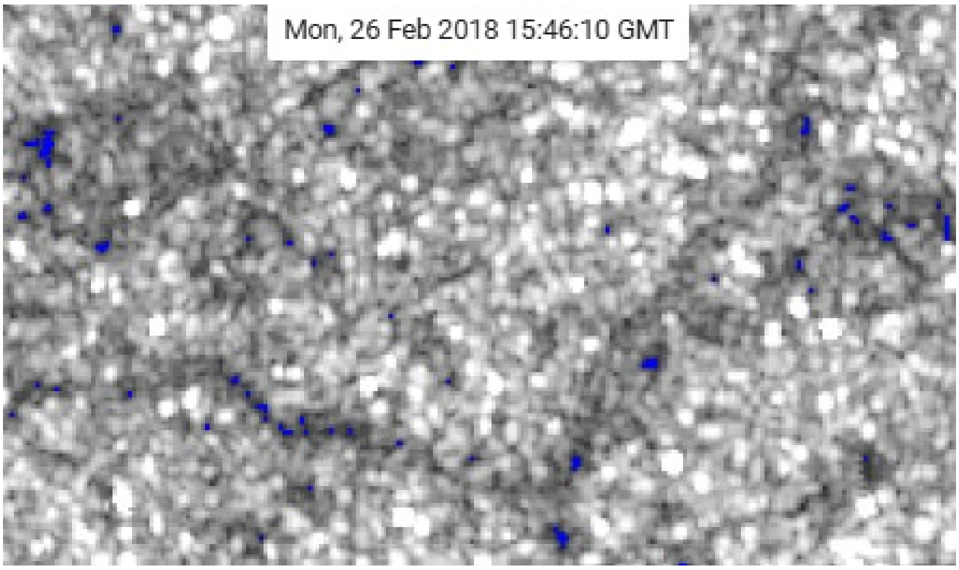

(b) SAR Msimbazi zoomed in.

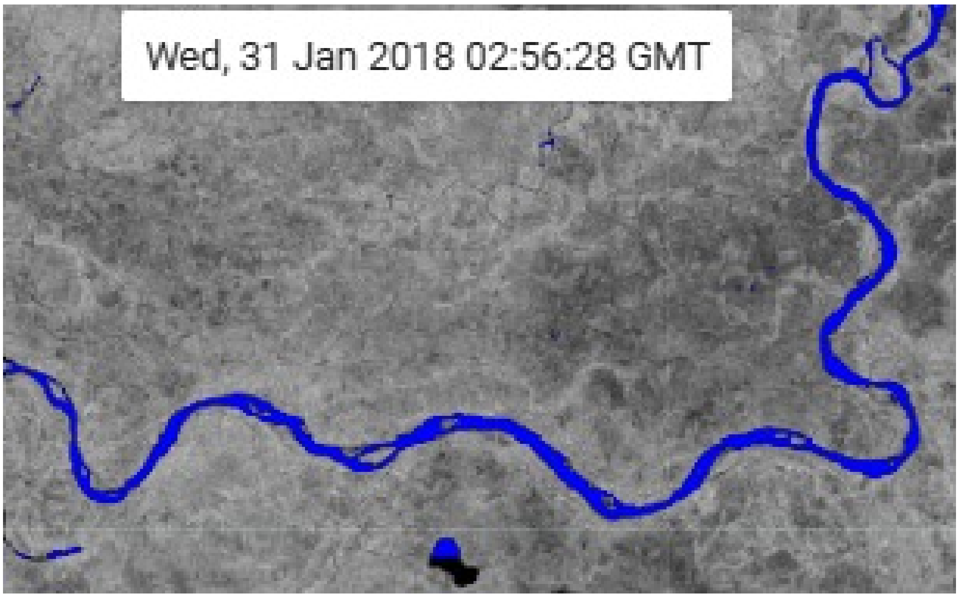

(c) SAR water detection for the Rufiji River.

Figure A.5: Comparison of SAR water detection for the Msimbazi and Rufiji Rivers.

B

Time of concentration

The time of concentration is the duration needed for water from the most distant point in a drainage basin to travel to its outlet, where ”remoteness” is determined by travel time rather than distance (Iowa Organization of Natural Resources, 2023; Mehta et al., 2022).

Several factors influence the time of concentration, including:

Surface roughness: Urban development significantly impacts flow velocity by reducing the delay to flow. In natural, undeveloped areas, slow and shallow overland flow typically occurs through vegetation. However, urbanization alters these conditions, directing flow over paved areas, which speed up runoff transport downstream. Consequently, travel time through the catchment decreases (Iowa Organization of Natural Resources, 2023; Mehta et al., 2022).

Channel shape and flow patterns: In smaller, non-urban catchments, much of the travel time is attributed to overland flow in upstream areas. Urbanization reduces overland flow lengths by channeling runoff into designed channels as early as possible. These engineered channels are hydraulically efficient, increasing flow velocity and further reducing travel time (Iowa Organization of Natural Resources, 2023; Mehta et al., 2022).

Slope: Changes in slope due to urbanization depend on site grading and the extent to which stormwater infrastructure are incorporated. When channels are straightened, slopes tend to increase, whereas directing overland flow into stormwater infrastructure may decrease the effective slope (Iowa Organization of Natural Resources, 2023; Mehta et al., 2022).

The Kirpich formula (1940) provides an empirical method to estimate the time of concentration. It was originally developed for small agricultural catchments and reflects the time required for a stream to transition from its lowest stage to its peak stage during a storm. The formula estimates the time of concentration (T_c) as the time taken for runoff to travel from the most distant point in the catchment to its outlet (Aqua Veo, 2016; Singh, 1976).

The equation is given as:

$$T_c = 0.0195 \cdot L^{0.77} \cdot S^{-0.385} \tag{B.1}$$

Here, T_c represents the time of concentration (minutes), L is the length of the longest flow path (meters), and S is the catchment slope (dimensionless). The coefficient 0.0195 is empirical and specific to SI units, derived from experimental studies.

As watersheds urbanize, the empirical coefficient may decrease, indicating a shorter time of concentration. To have the formula account for land cover variations, adjustment factors can be applied: for overland flow on grassy surfaces, T_c is multiplied by 2.0, while for impervious surfaces like concrete or asphalt, T_c is multiplied by 0.4 (Aqua Veo, 2016; [CivilWeb], n.d.; Singh, 1976). However, in this study slightly overestimating the time of concentration will not do any harm to the analysis.

Applying the Kirpich formula to the Msimbazi catchment is done in two ways. the first method computes the slope by taking the highest elevation of the location of the longest flow path and the elevation of the river outlet and dividing it over the entire flow path distance. This method does not take into account any differences in slope over the river. The second method does take these differences into account by splitting the flow path in reaches of similar slope. The results are given in table B.1.

Table B.1: The time of concntration of the Msimbazi catchment for two different methods

	No splitting of flow path	Splitting of flow path
Minutes	695	790
Hours	11.5	13.2

To ensure that water levels do not influence riverbank detection, all satellite images used for delineation are selected to fall outside the extent of the ToC for different precipitation events.

The ToC values are computed using the following code:

```python
def Kirpich(L, h1, h2, C=0.0195):
    """
    Calculate the time of concentration using the Kirpich formula.

    Parameters:
    L (float): Length of overland flow path in meters.
    h1 (float): Higher elevation point in meters.
    h2 (float): Lower elevation point in meters.
    C (float): Empirical coefficient, default is 0.0195.

    Returns:
    float: Time of concentration in minutes.
    """
    # Calculate the slope (S)
    S = (h1 - h2) / L

    # Calculate the time of concentration (Tc)
    Tc = (C * (L ** 0.77)) / (S ** 0.385)

    return Tc

## No splitting of the river
# Given parameters
L = 51000  # Length of the flow path in meters
h1 = 202   # Higher elevation in meters
h2 = 2.98  # Lower elevation in meters

# Calculate the time of concentration
Tc = Kirpich(L, h1, h2)

# Output
print(f' The Time of Concentration for the river, without splitting for different slopes is: {Tc:.3f} minutes')
print(f' The Time of Concentration for the river, without splitting for different slopes is: {Tc/60:.3f} hours')

## Splitting in 2 reaches with different slope

L_1 = 10000  # Length of the flow path in meters for the upstream reach
h1_1 = 202   # Higher elevation in meters for the upstream reach
h2_1 = 140.29  # Lower elevation in meters for the upstream reach

L_2 = 41000  # Length of the flow path in meters for the downstream reach
```

```
h1_2 = 140    # Higher elevation in meters for the downstream reach
h2_2 = 2.98   # Lower elevation in meters for the downstream reach

# Calculate the time of concentration
Tc_1 = Kirpich(L_1, h1_1, h2_1)
Tc_2 = Kirpich(L_2, h1_2, h2_2)

# Output
print(f'The Time of Concentration for the riverfor the upstream reach is: {Tc_1:.3f} minutes')
print(f'The Time of Concentration for the riverfor the downstream reach is: {Tc_2:.3f} minutes')
print(f'The Time of Concentration for the river for both reaches combined is: {Tc_1+Tc_2:.3f} minutes')

print(f'The Time of Concentration for the riverfor the upstream reach is: {Tc_1/60:.3f} hours')
print(f'The Time of Concentration for the riverfor the downstream reach is: {Tc_2/60:.3f} hours')
print(f'The Time of Concentration for the river for both reaches combined is: {(Tc_1+Tc_2)/60:.3f} hours')
```

C

Centerline detection

This appendix outlines the manual river detection process. It begins with acquiring satellite images, as described in section C.1. Then, the scale at which the detection is performed is evaluated (section C.2). Next, the river's waterbody is identified (section C.3), followed by the detection of edges between land-classified and water-classified pixels (section C.4). The midline between the detected left and right banks, known as the centerline, is then extracted (section C.5). Finally, the uncertainty of these positions is assessed in section C.6.

C.1. Image acquisition

To detect the river manually the satellite images are retrieved outside the time of concentration. As the analysis will focus on both long- and short term changes. The images originate from different satellites. Figure C.1 shows the lifespan of the different satellites.

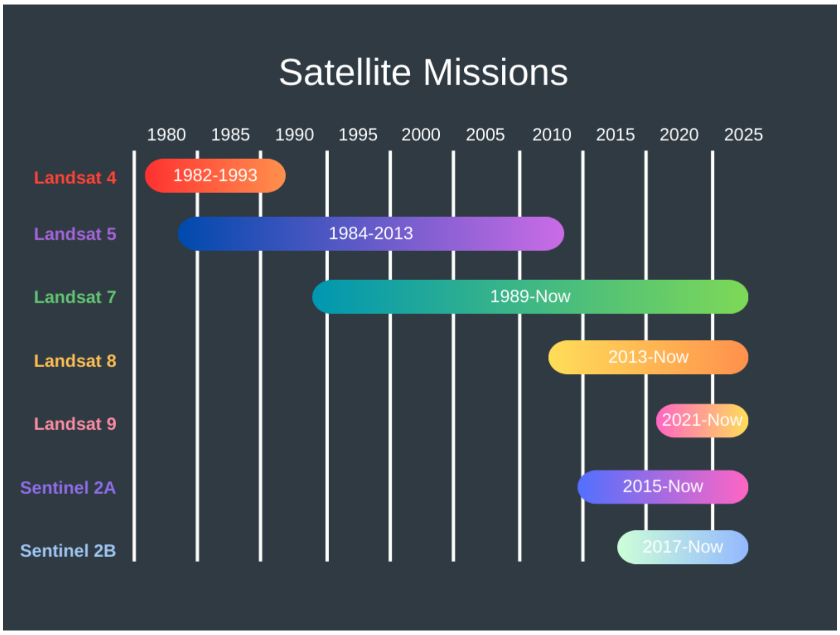

Figure C.1: Lifespan of satellite missions (European Space Agency [ESA], n.d.; U.S. Geological Survey, 2020)

Images are extracted using Google Earth Engine, where the same code is applied as is proposed in appendix A for the automated waterbody detection using the MNDWI & NDWI method. A more precise description of what the extraction process includes is given in section A.2.

The process for selecting and preparing the best satellite image involves several steps tailored to Landsat4-9 and Sentinel2 satellites. Initially, images are filtered based on criteria such as area of interest (AOI), date range, and cloud cover. For each satellite type, functions like `filterByOverlap` and tagging functions (`tagLandsat` for Landsat and `tagSentinel` for Sentinel2) are applied to compute overlap percentages, assign metadata, and ensure cloud cover values are defined. The images from Sentinel2 and Landsat 4, 5, 7, 8, and 9 are combined into a single collection, sorted by cloud cover to prioritize images with minimal cloud coverage. Cloud masking for both satellite types uses different bands: Landsat employs the `QA_PIXEL` band to mask clouds, while Sentinel-2 utilizes the `QA60` band and brightness thresholds. Shadow masking follows a similar procedure: Landsat identifies shadows using the `QA_PIXEL` band's shadow bit, while Sentinel-2 uses the SWIR band (`B11`) with a dynamic threshold. This process selects the best image, i.e., the image with the least cloud cover, from the sorted collection. Additionally, functions like `addImageToMap` are used to visualize the images with SWIR1 (reflectances between 2100-2300 nm), SWIR2 (reflectances between 1550-1750 nm) and Red (reflectances between 630-690 nm) composites and other appropriate adjustments tailored for each satellite's spectral bands. At last the image is exported.

C.2. Scaling

Given the differing spatial resolutions of Landsat (30x30m) and Sentinel (10x10m) satellites, determining the optimal scale for manual riverbank detection is crucial. Observing the imagery at a very small scale reduces accuracy, as smaller river bends become indistinguishable. On the other hand, analyzing imagery at a very large scale also impacts accuracy because it becomes difficult to determine whether a singular pixel represents land or water, especially when transitions between land and water are not sharply defined.

Figure C.2 illustrates various scales. At an excessively small scale (C.2b), river bends are not accurately visible, and the lack of detail makes it difficult to distinguish smaller meanders. On the other hand, at an overly large scale (C.2a), the river appears too coarse, disrupting its linear structure and making manual delineation challenging. Based on these observations, a scale of (C.2c) is identified as optimal, as it provides sufficient resolution to detect linear river features while preserving the visibility of smaller bends.

C.3. Manual river detection

Manual river detection is conducted in ArcGIS Pro (Version 6). To ensure compatibility with the DSAS model, the visible edges of the river are detected and stored according to the requirements specified by DSAS. This involves separately detecting the left and right edges as polylines, with the following attributes: `OBJECTID`, `SHAPE`, `SHAPE_Length`, `DATE_`, and `UNCERTAINTY`.

The manual detection process involves identifying the boundary between pixels classified as water and those classified as land. One advantage of manual detection over automated methods is the ability to interpret ambiguous cases where pixels are not strictly classified as water but still exhibit the linear structure characteristic of a river. This flexibility allows for more accurate identification of riverbanks in such instances.

Since Sentinel imagery has a resolution of 10m × 10m and Landsat imagery 30m × 30m, pixel-based classification of water and land is determined by the average reflectance within each pixel. This can result in discrepancies between the detected river edges and the actual river edges. For example, a pixel adjacent to a water-classified pixel may still contain water but be classified as land due to its dominant reflectance characteristics (Chen et al., 2022). Consequently, the manually delineated riverbanks may deviate by several meters from their true position. Figure C.3 illustrates this effect. Please do note that the in this image the scaling is not optimal for river detection. As discussed in paragraph C.2, this scale is too small and therefore lacks any linear detail. Yet, the image clarifies the discrepancies involved with the reflectance.

Figure C.3a presents the natural river, which is overlaid with a Sentinel grid of 10m × 10m pixels in figure C.3b. The reflectance values of individual pixels influence their classification, as demonstrated in Figures C.3b through C.3e. In Figure C.3b, the first pixel predominantly consists of water, resulting in a strong water classification (dark blue). Figure C.3c contains a mix of land and water, causing

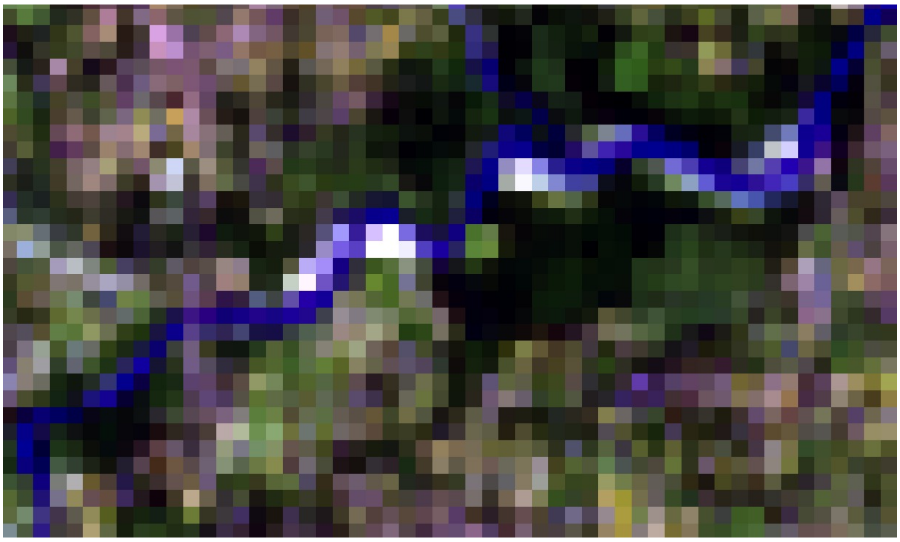

(a) Msimbazi river in June 2018 at a scale of 1:5,000 km.

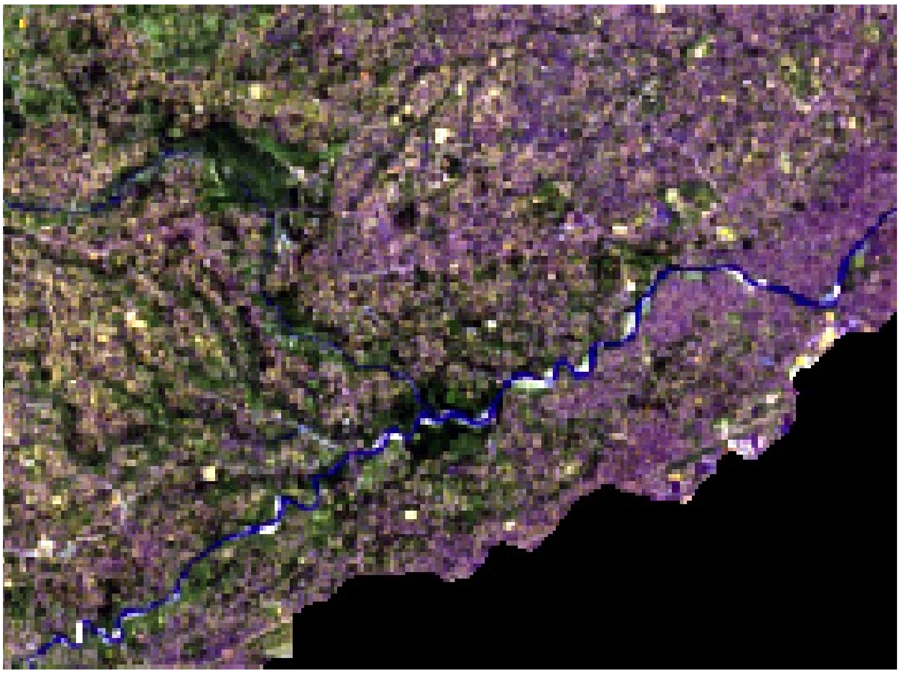

(b) Msimbazi river in June 2018 at a scale of 1:50,000 km.

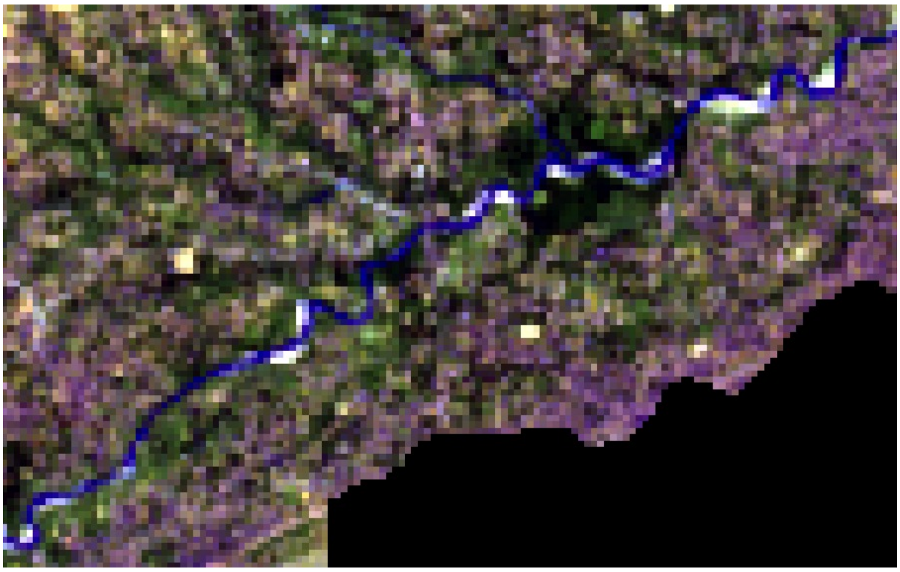

(c) Msimbazi river June 2018 at a scale of 1:17,500 km.

Figure C.2: Msimbazi river in June 2018 at different scales.

a weaker water signal and a transition towards a lighter blue reflectance. Figure C.3d represents a fully land-covered pixel, characterized by a green reflectance, or to be more precise, this reflectance indicates vegetated land. Figure C.3e shows a mixed reflectance of mostly land but also some water, producing an intermediate classification.

As seen in Figure C.3, pixel reflectance directly affect river detection. When delineating the river manually, a pixel such as figure C.3e, which contains both land and water, may be classified entirely as land, despite the river actually running through it. Consequently, small-scale inaccuracies in pixel classification can propagate through manual river detection.

To minimize the impact of these discrepancies on river delineation, both the left and right observable riverbanks are identified. The centerline is then determined by extracting the exact midpoint between these two banks. A detailed explanation of this process is provided in Sections C.4 and C.5.

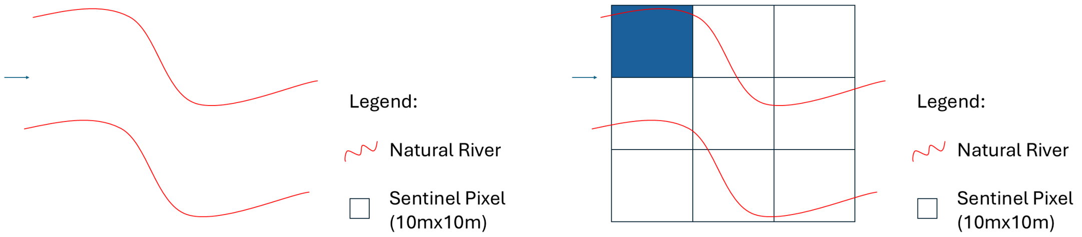

(a) The natural river **(b)** Reflectance of 1st pixel

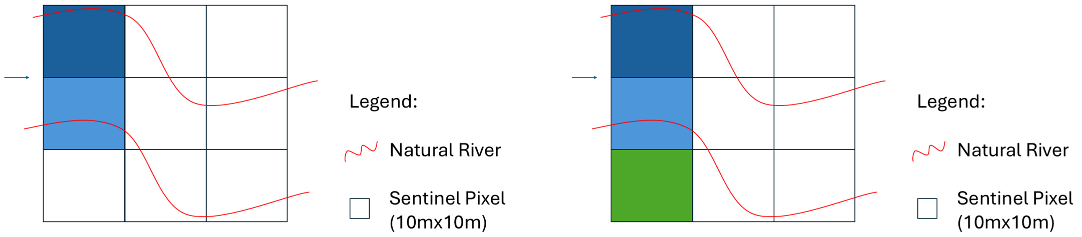

(c) Reflectance of 2nd pixel **(d)** Reflectance of 3rd pixel

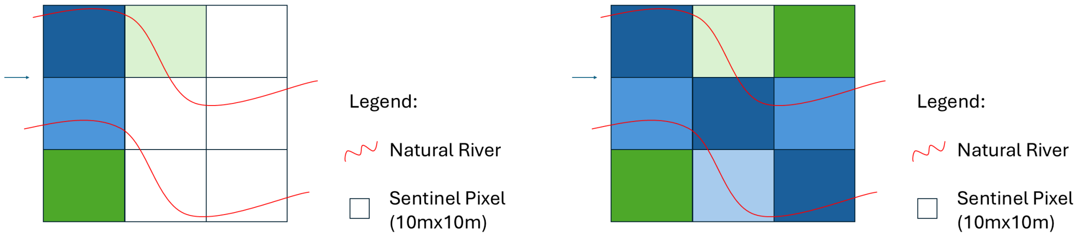

(e) Reflectance of 4th pixel **(f)** Reflectance of all pixels

Figure C.3: Pixel Reflectances

C.4. Riverbank tracking

Given the previously described reflectance characteristics, it is crucial to accurately detect the riverbank. It is important to note that we are referring to the observed riverbanks, which are derived from satellite imagery and may be offset by a few meters from the true riverbank position.

The first three steps in figure C.4 are similar to those in figure C.3. The goal is to avoid being misled by pixel classifications, which is why the optimal scale was applied. The detected riverbank lines should not strictly follow the pixel grid. Instead, during manual river detection, the observable linear structure of the river was prioritized over the pixel boundaries classified as water. This principle is visible in figure C.4d, where the yellow and pink lines extend to include light blue and light green areas, aiming to detect the river's true boundary rather than just a pixel-based classification.

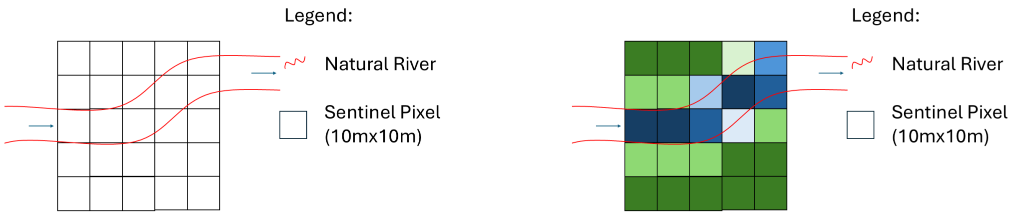

(a) Step 1: The river is located somewhere within the wider catchment area.

(b) Step 2: A satellite image of the catchment is obtained.

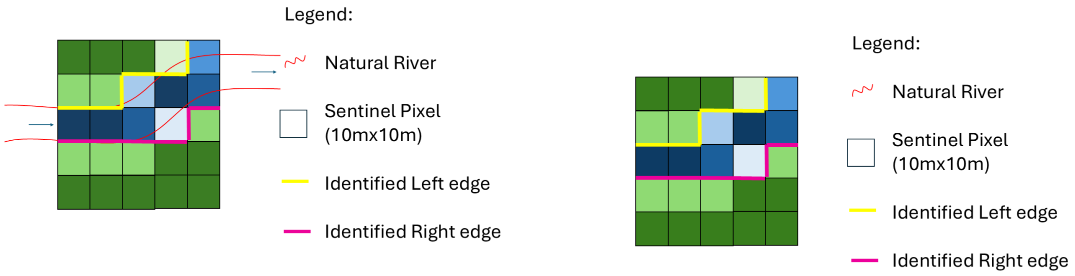

(c) Step 3: Band selection and image enhancement make the river water surface identifiable.

(d) Step 4: The edges of the water surface are delineated, aiding in centerline identification.

Figure C.4: Stepwise method for detecting river water cover boundaries using satellite imagery.

C.5. Centerline generation

Given the detected riverbanks, it is possible to determine the centerline. This method, where the riverbanks are first identified and then the centerline is derived, is preferred as it minimizes the likelihood of errors. During the manual detection of the riverbanks, it is possible that some pixels (or parts of pixels) may have been incorrectly classified as water. However, by manually detecting both the left and right riverbanks, the resulting centerline will be placed more accurately, as any errors made in detecting one bank are likely to be counterbalanced by errors in detecting the other.

Figure C.11 shows the methodology of how the centerline is derived. At first the detected left- and right bank are necessary. On the right bank a perpendicular line is drawn. This perpendicular line intersects with the left bank. The exact middle of the perpendicular line is given by the midpoint. So, each midpoint has similar length to the left bank as to the right bank. For each 10 meters along the right bank a new perpendicular line is drawn and a new midpoint is determined.

Finally, these midpoints are connected by a new line, the so called centerline.

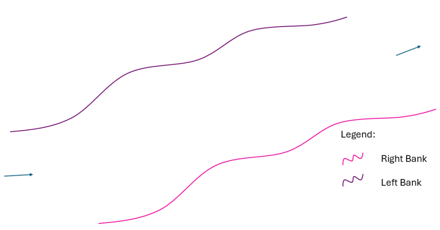

Figure C.5: 1. Natural River.

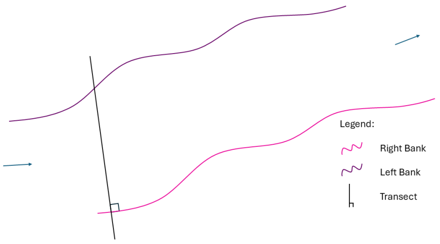

Figure C.6: 2. Draw a line perpendicular to the right bank.

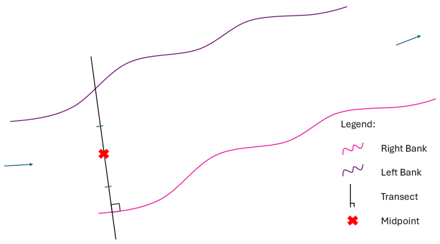

Figure C.7: 3. Identify the midpoint on the perpendicular line with equal distance to right- and left bank.

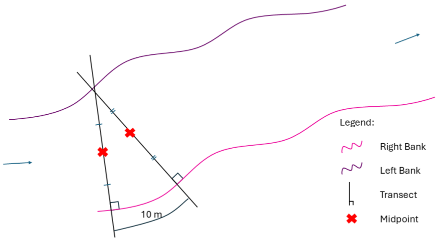

Figure C.8: 4. Repeat after 10 meters along the right bank.

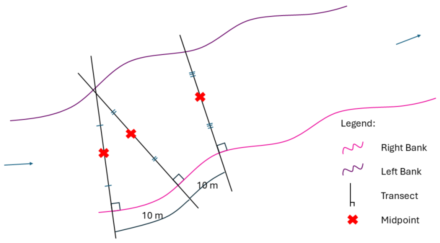

Figure C.9: 5. Keep repeating.

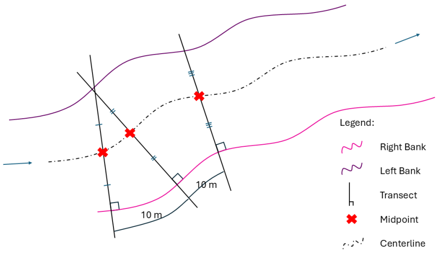

Figure C.10: 6. Connect these midpoints with the Centerline.

Figure C.11: Centerline generation methodology

C.6. Uncertainty

The centerline has been derived from either a Sentinel satellite image, with a resolution of 10 m × 10 m, or a Landsat image, which has a resolution of 30 m × 30 m. Research by Chen et al. (2022) has shown that coarser satellite imagery inherently introduces positional uncertainty when identifying small water bodies, as pixel boundaries may not precisely align with the true shoreline.

To quantify this uncertainty, the error propagation formula for averaging independent measurements is applied (Ku, 1966). Since the centerline is defined as the midpoint between two independently digitized water body edge lines, X_1 and X_2, the centerline position C is given by:

$$C = \frac{X_1 + X_2}{2} \tag{C.1}$$

The uncertainty in C is determined using the general error propagation formula:

$$\sigma_C^2 = \left(\frac{\partial C}{\partial X_1}\right)^2 \sigma_{X_1}^2 + \left(\frac{\partial C}{\partial X_2}\right)^2 \sigma_{X_2}^2 \tag{C.2}$$

Since X_1 and X_2 are independently derived from the same satellite image, they share the same standard deviation, i.e., $\sigma_{X_1} = \sigma_{X_2} = \sigma_X$. The partial derivatives of C with respect to X_1 and X_2 are:

$$\frac{\partial C}{\partial X_1} = \frac{1}{2}, \quad \frac{\partial C}{\partial X_2} = \frac{1}{2} \tag{C.3}$$

Substituting these values into Equation C.2 gives:

$$\sigma_C^2 = \left(\frac{1}{2}\right)^2 \sigma_X^2 + \left(\frac{1}{2}\right)^2 \sigma_X^2 \tag{C.4}$$

$$\sigma_C^2 = \frac{1}{4}\sigma_X^2 + \frac{1}{4}\sigma_X^2 = \frac{2}{4}\sigma_X^2 = \frac{1}{2}\sigma_X^2 \tag{C.5}$$

Taking the square root:

$$\sigma_C = \frac{\sigma_X}{\sqrt{2}} \tag{C.6}$$

Applying this formula to the known spatial resolutions of Landsat and Sentinel imagery, we obtain the final uncertainty values:

$$\sigma_C = \frac{30}{\sqrt{2}} = 21.2 \text{ meters} \quad \text{(for Landsat)} \tag{C.7}$$

$$\sigma_C = \frac{10}{\sqrt{2}} = 7.1 \text{ meters} \quad \text{(for Sentinel)} \tag{C.8}$$

These values represent the expected positional uncertainty of the centerline and account for errors introduced by the resolution of the satellite imagery and the manual digitisation process.

For applicability in the Digital Shoreline Analysis System (DSAS) tool these values are rounded to 21 meters for Landsat and 7 meters for Sentinel, as DSAS does not allow decimal values.

D

Fieldwork

D.1. Fieldwork observations in the Msimbazi basin

During the fieldwork campaign in the Msimbazi Basin, ten key locations (ID 0 - ID 9) were surveyed to assess riverbank characteristics, erosion processes and sediment composition. Observations included sediment types, vegetation cover, visible bank retreat, soil layering, and banks shapes. Below is a detailed account of findings at each location, followed by an in-depth analysis of downstream trends. See figure D.1 for the exact locations at which the measurements have been performed.

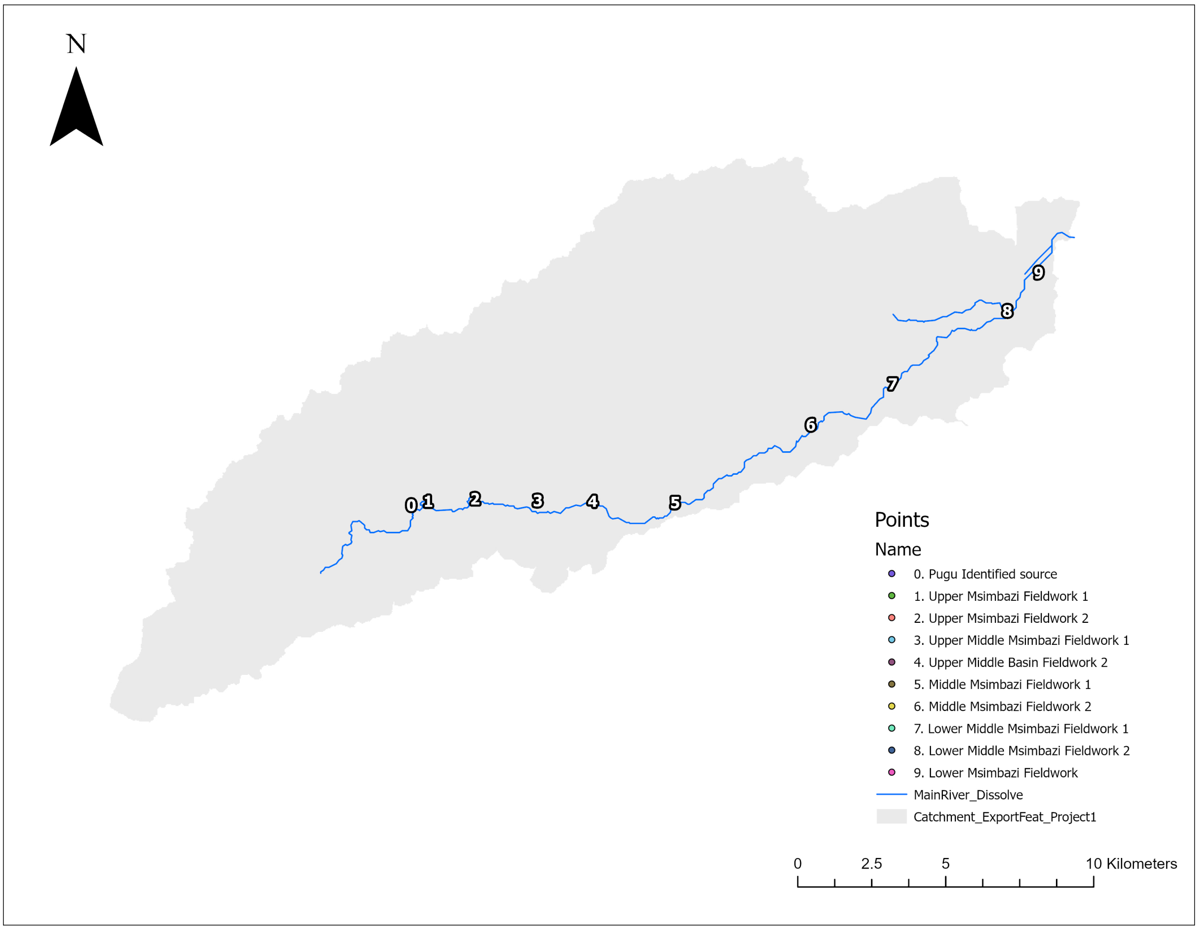

Figure D.1: Fieldwork locations in the Msimbazi catchment

0. Identified Source

Table D.1: 0. Identified Source attribute table

Attribute	Description
Coordinates	(-6.87626, 39.08244)
Elevation	140 m
Material	Hard rock with a thin clay top layer (just a few cm)
Vegetation Cover	80-100% at the bank (grass, bushes, trees). The bank slopes near the dam are less vegetated, as they mainly consist of rock.
Visible Retreat	6 m at the dam; no retreat upstream of the dam
Soil Layers	Digging impossible
Solid Waste	None observed
Remarks	Upstream of this location, several streams converge, with the widest measuring between 3 and 5 meters in width. According to locals, these streams flow into a dam constructed by the government to reduce river discharge. Soil analysis in this area is challenging due to the predominance of rock, with only a thin clay layer deposited over the rock, likely from upstream areas where the soil is predominantly clay and highly vegetated. Locals observe that erosion is minimal in this region, with the exception of the dam area.

Table D.2: 1. Upper Msimbazi Fieldwork 1 Attribute Table

Attribute	Description
Coordinates	(-6.87583, 39.07861)
Elevation	120 m
Material	Rock and cobblestones with a sand overlay. The sand is of medium size, poorly sorted, and sub-angular.
Vegetation Cover	80-90% on top of the bank; less on the slope (0-5%)
Visible Retreat	No imminent retreat visible; gradual widening of the river.
Soil Layers	Digging impossible
Solid Waste	None observed
Remarks	The river width in this area ranges from 10 to 20 meters. The banks near the Railway (SGR) are protected by later boulders, and drainage channels are present. Just downstream of the SGR, sediment accumulation is noticeable, despite the presence of vegetation, which may have been planted.

Table D.3: 2. Upper Msimbazi Fieldwork 2 Attribute Table

Attribute	Description
Coordinates	(-6.87583, 39.07861)
Elevation	110 m
Material	Right bank: The right bank consists of stone and rock with a thin top layer of coarse, poorly sorted sand and it is angular. Left bank: The left bank appears to have similar materials, though it is not accessible for closer examination.
Vegetation Cover	The vegetation cover on both the top and slope of the bank is minimal, ranging from 0 to 5%, primarily consisting of scattered grasses.
Visible Retreat	No retreat visible
Soil Layers	Digging impossible
Solid Waste	None observed
Remarks	The river width in this area is approximately 20 meters, with cliff-like banks reaching a height of about 1.4 meters, gradually sloping downward. The soil is primarily composed of rock, making excavation impossible.

Table D.4: 3. Upper Middle Msimbazi Fieldwork 1 Attribute Table

Attribute	**Description**
Coordinates	(-6.87556, 39.11556)
Elevation	90 m
Material	The point bar is composed of coarse sand, which is sub-angular and moderately sorted. The cut bank, though difficult to observe clearly, appears to be made of clay.
Vegetation Cover	Above the point bar, vegetation coverage ranges from 70 to 100%, while on the point bar itself, it is absent. The cut bank is largely covered by vegetation, with coverage also ranging from 70 to 100%, although it is difficult to assess clearly. Vegetation is also visible on the point bar.
Visible Retreat	At the point bar, a retreat of approximately 3 meters is visible, while at the cut bank, the retreat is around 5 meters.
Soil Layers	A layer of sand, approximately 30 cm thick, is observed before reaching the bottom water level. Beyond this point, further excavation is not possible. The material consists solely of sand, with no distinct layers visible.
Solid Waste	20%
Remarks	This location marks the beginning of urbanization, with the current bank-to-bank width estimated at 40-50 meters. Vegetation consists mostly of bushes and grass. The riverbanks, particularly the cut bank, show layers, though these consist solely of clay, with no evidence of different soil types. While the bank was not accessible for detailed observation, the layers are estimated to range between 30 and 50 cm in height. Remarkably, erosion appears to be equally severe both before the river reaches the urbanized area and after urbanization has occurred. Although the urban area contributes to the presence of solid waste, no such material was found within the soil.

Table D.5: 4. Upper Middle Msimbazi Fieldwork 2 Attribute Table

Attribute	**Description**
Coordinates	(-6.87528, 39.13667)
Elevation	80 m
Material	Coarse sand, moderately sorted, angular
Vegetation Cover	70-80% (depositional bank); 40-50% (Cut bank)
Visible Retreat	At the point bar, the retreat is approximately 3 meters. However, at the cut bank, it was impossible to determine whether retreat is occurring, as locals could not provide any insight into the situation.
Soil Layers	Digging was only possible to a depth of 30 cm. The first 15 cm consists of sand, as previously described under the material section. Below this, the sand becomes slightly finer, with the next 15 cm being well-sorted, rounded, medium sand.
Solid Waste	30%
Remarks	The cut bank features a gradual but steep slope, whereas the point bar consists of straight banks with a terrace and a sandbar. The amount of solid waste at this location has increased compared to the previous site, although the provided percentage is a rough estimation, calculated using the same method as the vegetation cover measurement. This may not have been the most accurate method, as the plastics have not yet spread significantly and are mostly deposited at this location. It was also noteworthy that locals mentioned they did not experience frequent flooding in this area.

Table D.6: 5. Middle Msimbazi Fieldwork Attribute Table

Attribute	**Description**
Coordinates	(-6.87444, 39.14833)
Elevation	70 m
Material	At the point bank, the material is sandy (very coarse, well sorted, and subangular). The material of the cut bank is clay.
Vegetation Cover	The point bank has a vegetation cover of 80-90% on the bank, consisting mostly of bushes and grasses, while on the bar, the cover is around 20%, mainly made up of bushes and grasses. In contrast, the cut bank shows a vegetation cover of 90-100% on both the bank and the bar, with the bank predominantly covered by bushes and grass, and the bar nearly entirely covered by grass.
Visible Retreat	No retreat visible
Soil Layers	At the point bank, the first 20 cm consists of loose sand. Beneath this, a saturated sand layer is observed, which is approximately 20 cm thick, consisting of coarse, moderately sorted, angular sand. Below this layer, the groundwater level is visible. In contrast, the cut bank shows no visible layers.
Solid Waste	The presence is noticeable, but it appears to be less compared to the upstream area.
Remarks	The point bank has a gradual slope between bank and bar. The cut bank consists of a straight, cliff-like bank.

Table D.7: 6. Lower Middle Msimbazi Fieldwork Attribute Table

Attribute	**Description**
Coordinates	(-6.87417, 39.16222)
Elevation	40 m
Material	The material for both the bar and the new bank consists of coarse, subangular, well-sorted sand.
Vegetation Cover	The vegetation cover on top of the bank ranges from 80 to 100%, while the bank slopes are bare. Between the bank slope and the manually constructed bank, vegetation cover is approximately 10%. The manually built bank itself is completely bare. This pattern is consistent for both the point bank and the cut bank.
Visible Retreat	The distance between the toe of the natural bank and the toe of the manually constructed bank is approximately 35 meters.
Soil Layers	The measurement was taken on the bar between the two manually built banks, specifically at the toe of the right bank. The top 20 cm consists of loose, dry sand, exhibiting properties as previously described under the material section. Beneath this layer, there is approximately 10 cm of rock and clay, followed by around 50 cm of the same sand, though this layer is saturated.
Solid Waste	Barely present
Remarks	There are manually built riverbanks present. See figure D.4a

Table D.8: 7. Lower Msimbazi Fieldwork Attribute Table

Attribute	**Description**
Coordinates	(-6.87389, 39.17667)
Elevation	30 m
Material	The upper part of the bank consists of sand. The lower part, closer to the bar, consists of a mix of finer and coarser sand, indicating variations in deposition energy.
Vegetation Cover	The vegetation cover on top of the bank is estimated to be between 70 and 90%. On the slope of the bank, vegetation is sparse, between 10 and 20%.
Visible Retreat	No retreat visible.
Soil Layers	On the bar, digging was possible up to 60 cm. The top 20 cm consists of dry, loose sand. Below that, a saturated sand layer (about 40 cm) was observed, with no visible clay or organic matter.
Solid Waste	Around 20%
Remarks	This site is downstream of the most urbanized parts of the Msimbazi. The bank profile here is flatter, and both banks are relatively wide and low in height. Waste accumulation is notable, especially plastic materials embedded in the bar and lower bank slope.

Table D.9: 8. Estuary Msimbazi Fieldwork Attribute Table

Attribute	**Description**
Coordinates	(-6.86972, 39.19111)
Elevation	<10 m (tidal influence area)
Material	Dominantly silty sand with some organic material. Clearly tidal deposits with laminated structures.
Vegetation Cover	Mangroves and grasses cover 60-80% of the bank.
Visible Retreat	Erosion signs at low-tide level; undermining of mangrove roots.
Soil Layers	Soft, muddy soil. Easily penetrable. First 20 cm contains organic-rich silty sand, followed by more compact fine silt.
Solid Waste	>50%
Remarks	High presence of solid waste, especially plastics. Tidal influence complicates erosion assessment. Area is critical for ecological functions and serves as a buffer between river and ocean.

Table D.10: 9. Msimbazi River Mouth Fieldwork Attribute Table

Attribute	**Description**
Coordinates	(-6.86750, 39.19917)
Elevation	Sea level
Material	Fine sand and silt; beach deposits mixed with organic debris and plastic fragments.
Vegetation Cover	Very limited; some grasses at high tide line.
Visible Retreat	No riverbank visible; transitional zone into ocean.
Soil Layers	Surface layer of 10 cm consists of loose, wet sand. Below that, 20 cm of darker, organic-rich silt.
Solid Waste	Extremely high; >70% surface coverage in some areas.
Remarks	This is the end point of sediment and waste transport in the basin. Accumulation is heavily influenced by tides, waves, and urban waste inflow. River morphology is minimal due to constant tidal reworking.

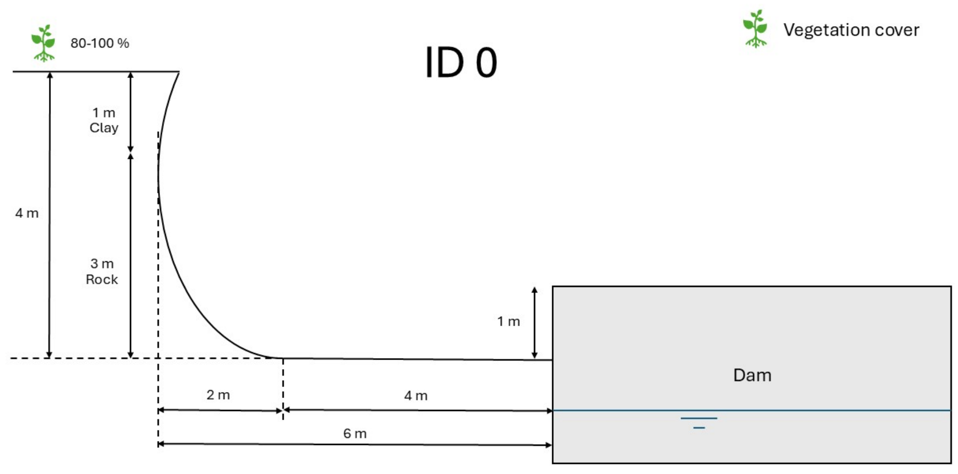

(a) Bank profile and vegetation cover ID 0

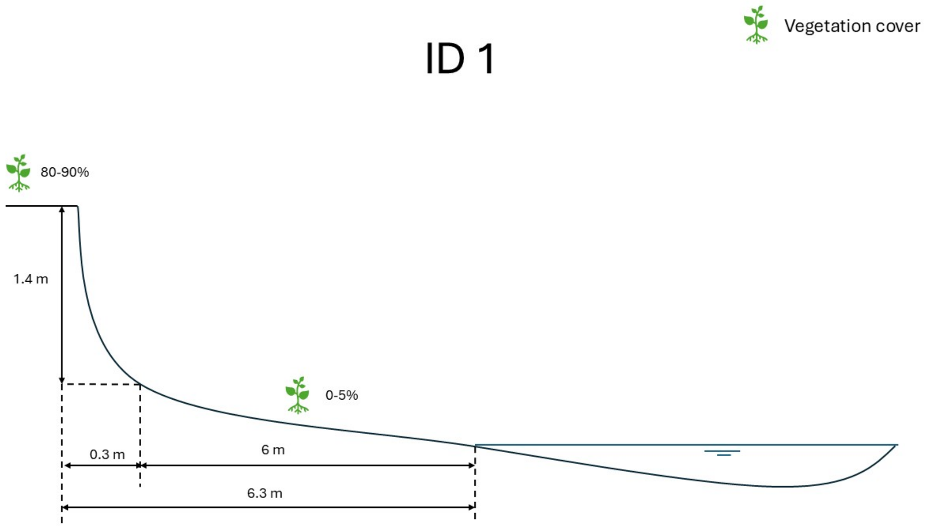

(b) Bank profile and vegetation cover ID 1

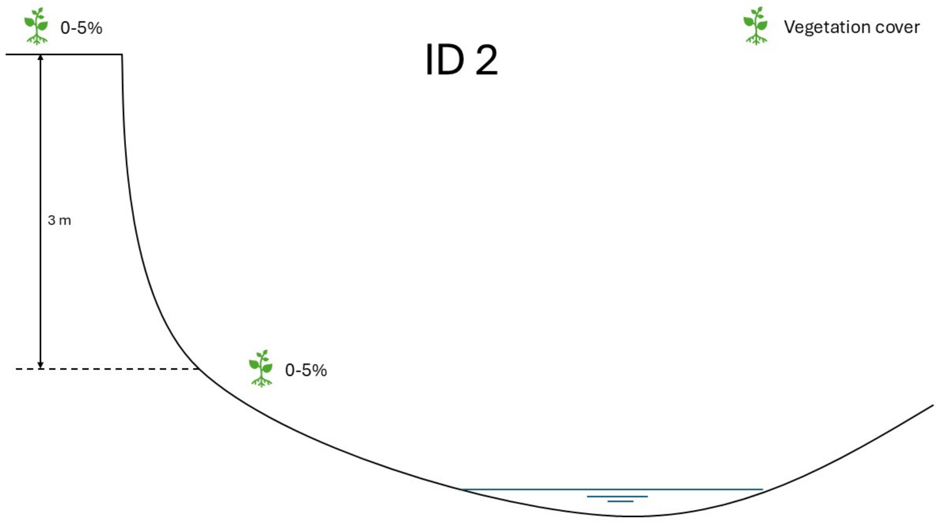

(c) Bank profile and vegetation cover ID 2

Figure D.2: Bank profiles and vegetation cover for Fieldwork ID 0–2

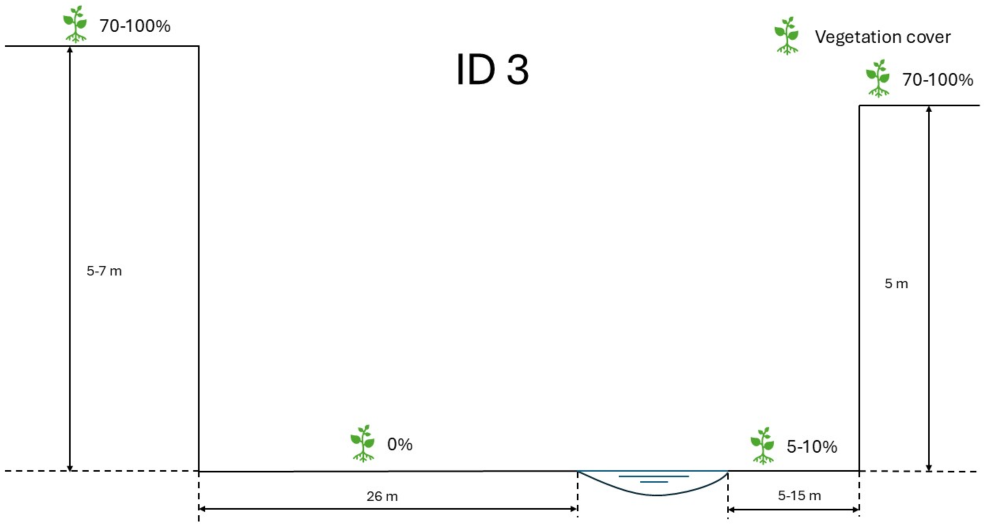

(a) Bank profile and vegetation cover ID 3

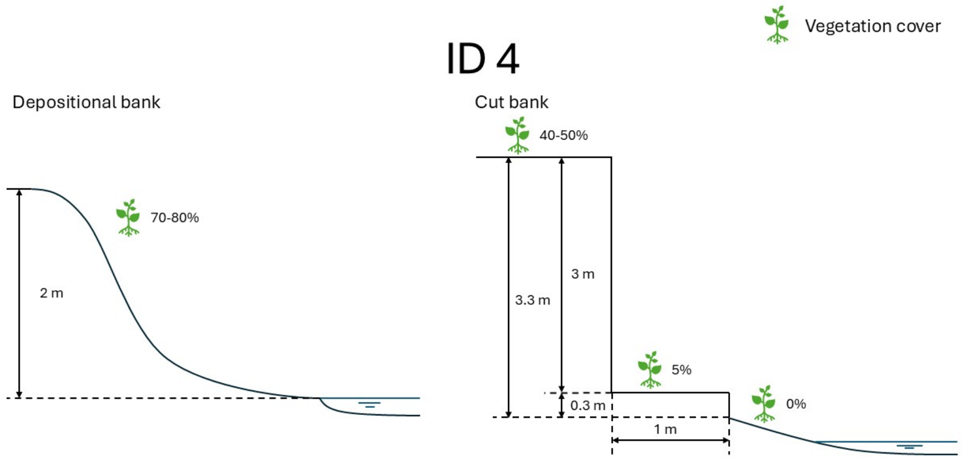

(b) Bank profile and vegetation cover ID 4

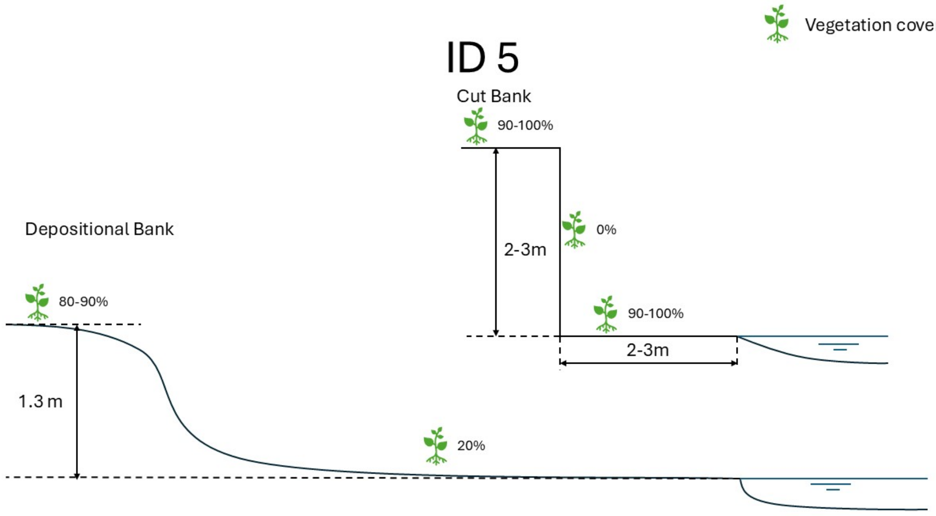

(c) Bank profile and vegetation cover ID 5

Figure D.3: Bank profiles and vegetation cover for Fieldwork ID 3–5

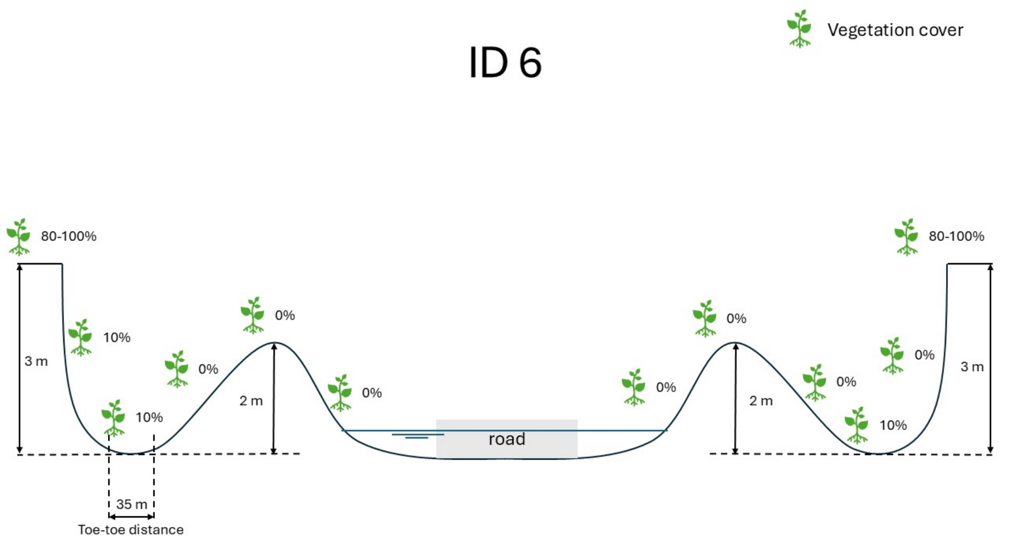

(a) Bank profile and vegetation cover ID 6

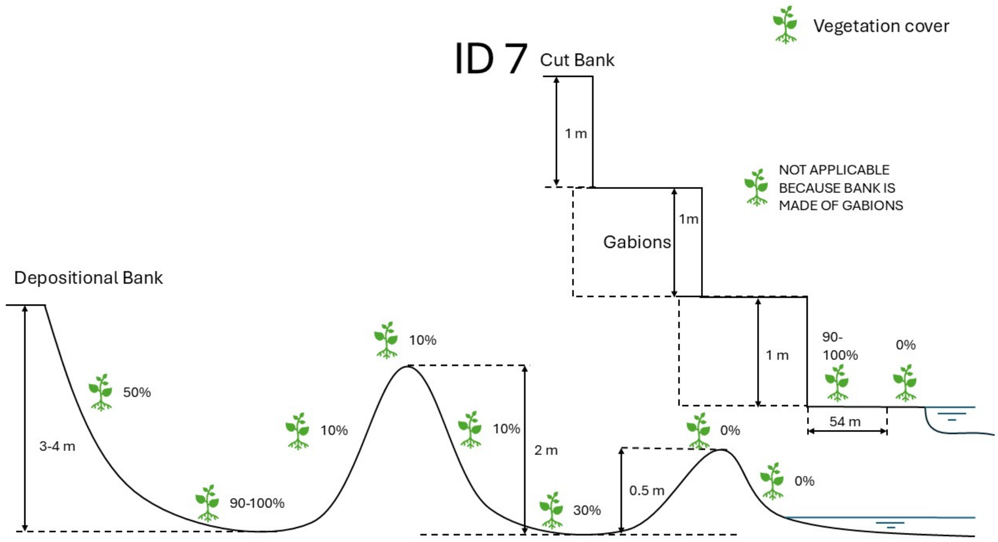

(b) Bank profile and vegetation cover ID 7

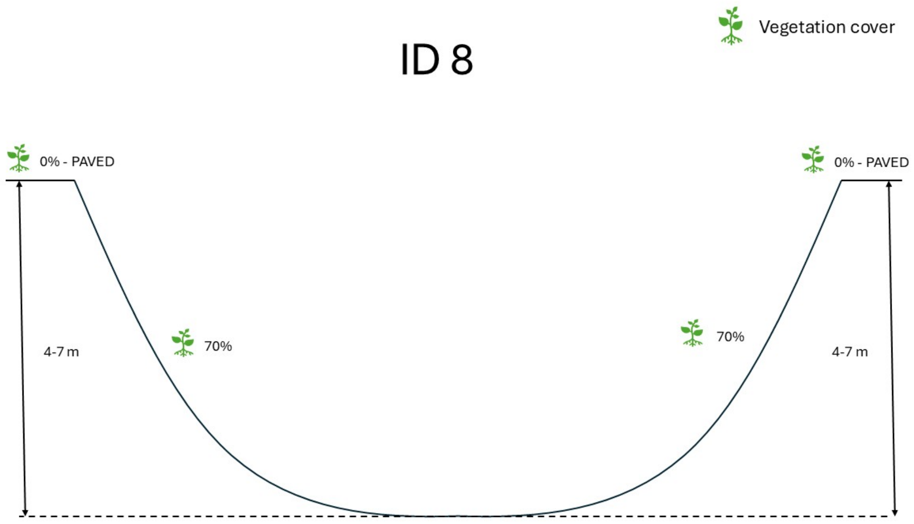

(c) Bank profile and vegetation cover ID 8

Figure D.4: Bank profiles and vegetation cover for Fieldwork ID 6–8

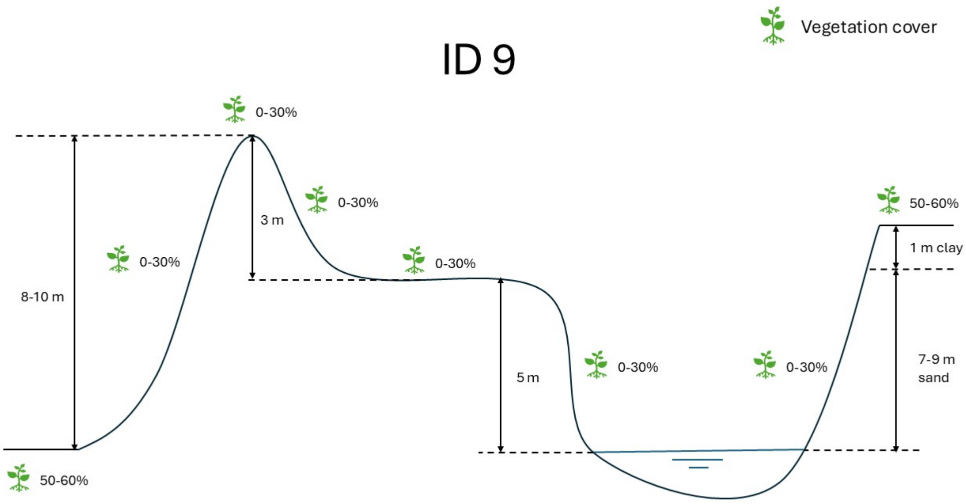

(a) Bank profile and vegetation cover ID 9

Figure D.5: Bank profile and vegetation cover for Fieldwork ID 9

D.2. Downstream analysis

Material properties

The results presented in figure D.6 show an expected decrease in grain size as one moves downstream along the Msimbazi River (figure D.6a). However, it is remarkable that the sediment never reaches medium, fine, or very fine sizes. This observation may be assigned to the relatively short length of the river, which limits the time and spatial extent required for sediment to transition from very coarse to finer sizes before reaching the river mouth. Alternatively, the coarse sediment characteristics observed could suggest that the upstream sediment input itself is predominantly coarse. This may indicate that sediment is not undergoing natural erosion processes from the nearby mountains before entering the river. Human interventions upstream could also contribute to this phenomenon, potentially influencing the sediment composition entering the river.

When observing the angularity (figure D.6b) of sediment along the river, a clear trend emerges: the angularity decreases as one moves downstream, which aligns with expectations of natural degradation. Notably, the sediment remains relatively angular over a significant spatial extent. For instance, at ID 6, located in the lower middle basin, the sediment is still classified as sub-angular. The missing data at ID 0 can be attributed to the fact that the sediment at this location consists solely of rock and boulders, making it impossible to determine the angularity.

Figure D.6c illustrates the sorting of sediment. A decreasing trend in sorting is observed downstream, as expected with natural degradation. However, attention is drawn to the fact that the two most downstream locations (ID 8 and ID 9) exhibit poorly sorted sediment, while the sediment just upstream (ID 7) is well sorted. This phenomenon can be explained by the sand mining activities at locations ID 8 and ID 9, where excavation took place at deeper soil layers. As a result, the sediment at the surface is likely derived from earlier periods.

This observation reinforces the phenomenon of human intervention, which was also noted in the grain size analysis. Should coarse sediment become exposed upstream in the catchment, as could have occurred during the construction of the railway, and then flow downstream through the river, it would be expected that coarse sediment would be found further downstream. A new balance has likely been established by now, as evidenced by the finer material encountered at ID 7, where sand mining is not taking place. This finer sediment would likely be found atop the coarser material. Unfortunately, it was not possible to verify these findings through soil layer measurements. However, this may also explain that the sediment quantity appears substantially higher, and the depth is greater than the 1-meter depth considered during the soil layer measurements.

Presence of solid waste

As anticipated, the results indicate that solid waste begins to appear when the river flows through urbanised areas. The expectation was that the amount of solid waste would increase downstream. Another assumption was that plastics would be scattered across the riverbed as the river would have deposited it when the discharge decreased. However, both expectations were not entirely accurate. At the first settlements (ID 3 to ID 4), the amount of solid waste does appear to increase. However, it was noteworthy that plastic waste was concentrated rather than spread across the riverbed. As the river continues downstream, the scattering of plastic waste does increase, yet considerable concentrations remain. This could be due to the fact that the measurements were taken towards the end of February, well into the dry season. The wet season begins in March/April, which suggests that communities may have been dumping their waste into the river before it had the opportunity to be transported downstream.

The presence of plastic waste varies significantly, ranging from excessive amounts to barely any, without showing a clear trend as one moves downstream. Possible explanations for this include the possibility that certain neighbourhoods may not dump their waste into the river, or variations in river flow velocity may influence the river's ability to transport waste downstream. Unfortunately, the precise reason remains unclear. It is also possible that multiple factors contribute to these inconsistencies.

Bank shape

At ID 0, it is evident that the dam has been bypassed during high-discharge events. From ID 1 to ID 3, a transition can be observed from gradually sloping banks to steep cliffs. This suggests that discharge and flow velocity increase in this section, leading to intensified erosion. As a result, bank failure shifts from gradual erosion to sudden landslides. The presence of these steep, cliff-like banks indicates that erosion occurs through a cantilever beam failure mechanism, particularly in combination with dry, loose sediment such as sand and clay, which contributes to their formation.

Remarkably, these cliff-like banks appear well before the first signs of urbanization along the river. This suggests that increased runoff due to urban development is not the sole driver of erosion. Instead, another factor must be contributing to the increased discharge in the river.

From ID 4 to ID 7, the river begins to meander, and a clear distinction emerges between the depositional and cut banks. The depositional bank exhibits a more gradual slope, while the cut bank continues to display steep, cliff-like formations. However, starting at ID 6, human interventions are visible: local communities have constructed sandbanks between the water and the natural riverbank, effectively modifying the channel. At ID 7, two of these artificial banks have been created, further altering the river's dynamics.

ID 9 presents an even more striking example of human adaptation. Here, people have settled within the river's floodplain, constructing embankments ranging from 8 to 10 meters high to contain the river channel. According to local accounts, these embankments withstand only intermediate discharge levels, with any extreme event likely leading to their failure and subsequent flooding of the surrounding area.

Vegetation cover

Given the significant amount of sediment visible in the river, one might expect the upstream riverbanks to be relatively bare. However, field observations revealed the opposite, these banks were well-vegetated. According to Engineer Mussa Natti from the World Bank (2025), this vegetation results from reforestation efforts initiated after the railway's construction.

Despite this, the extreme erosion observed may still be attributed to a large sediment flux moving through the river. As the banks have been bare previously.

Identifying trends in vegetation cover along the river is challenging due to the localized nature of observations. However, analyzing individual sites provides insight into the stability of specific banks or bars over time based on their vegetation cover.

Bank Retreat

Although it was not possible to retrieve data on riverbank retreat at many locations, it is noteworthy that retreat increases downstream. Measurable retreat at locations ID 3 and ID 4 is approximately 3-5 meters, while at ID 6, it reaches around 35 meters, and at ID 7, it is about 54 meters.

Considering that the bank material is not significantly different across these locations, the variation in retreat is unlikely to be due to substantial differences in bank strength or stability. Instead, the changes in retreat could be attributed to increases in discharge through the river, which aligns with the observed urbanisation within the catchment.

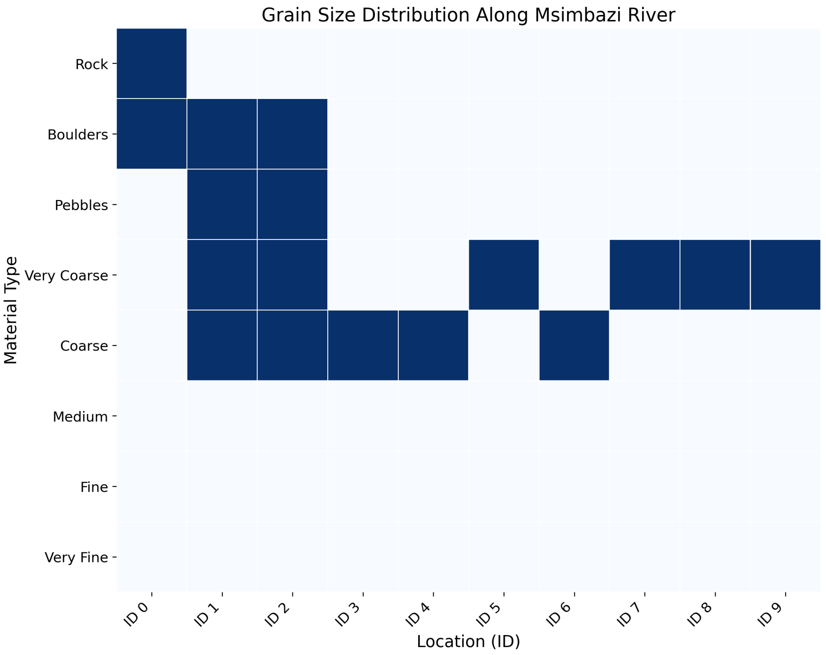

(a) Grainsize distribution along the Msimbazi River.

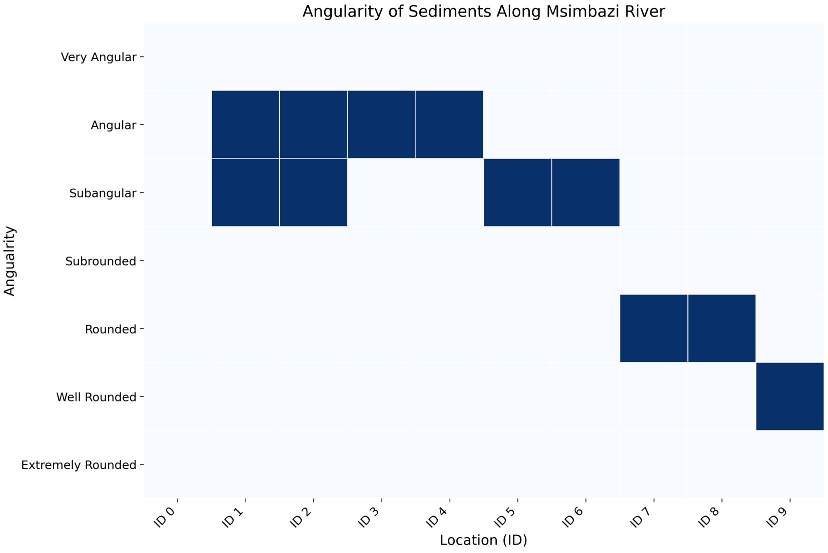

(b) Angularity of sediment along the Msimbazi River.

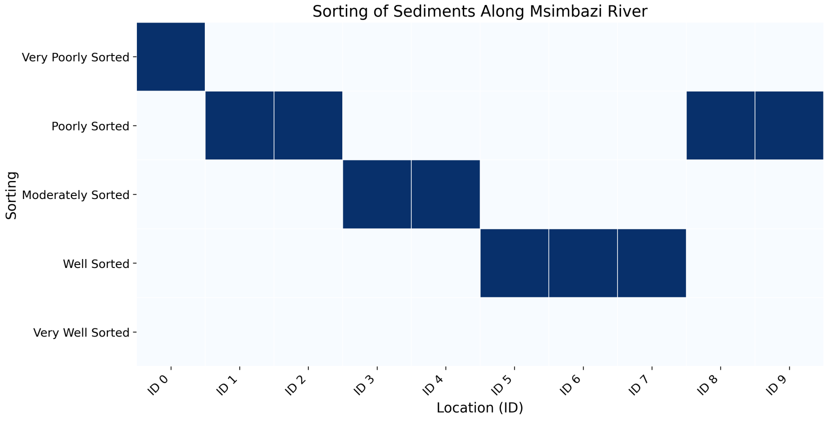

(c) Level of sorting of the sediment along the Msimbazi River.

Figure D.6: Soil characteristics along the Mismbazi River.

E

Digital Shoreline Analysis System (DSAS)

For analyzing migration rates along the Msimbazi River, the Digital Shoreline Analysis System (DSAS) provides a practical method to quantify riverbank erosion and deposition over time (Tha et al., 2022; U.S. Geological Survey, 2024a), despite originally being designed for shoreline analysis.

With a defined baseline and multiple centerlines over time, DSAS can be applied to track changes in riverbank position. In this study, the baseline is treated as an offshore reference, meaning that centerline movement toward the baseline is classified as accretion, while movement away from it is considered erosion (see figure E.1) (Tha et al., 2022; U.S. Geological Survey, 2024a). Figure E.2 shows how this is then applied on centerlines instead of shorelines.

A series of transects is automatically generated at 15-meter intervals along the baseline (Tha et al., 2022; U.S. Geological Survey, 2024a). These transects extend perpendicularly from the baseline to intersect with each year's centerline. However, to prevent transects from overlapping when the baseline curves, a smoothing distance of 500 meters is applied. Various methods exist for handling these intersections, and figure E.3 illustrates how different smoothing distances affect transect orientation. In general, the smoothing distance should be greater than the width of the bends in the centerline (Himmelstoss et al., 2021).

In addition to the transect generation process, the choice of transect length and spacing is crucial for accurately capturing river migration. Given the relatively narrow width of the river, a transect length of 400 meters may seem large compared to the river's current width of approximately 60-70 meters. However, this length is necessary to account for significant migration events, such as bend cut-offs, where the migrated distance can exceed the river width.

A transect spacing of 15 meters is used to ensure a detailed representation of river migration while avoiding overlap between adjacent transects. This spacing provides a high-resolution understanding of migration patterns without excessive redundancy (Himmelstoss et al., 2021).

To compute the rate of migration or absolute distance of migration different methods are available. Table E.1 explains the applicability of these different methods.

From table E.1, it can be concluded that the Linear Regression Rate (LRR) and the Weighted Linear Regression (WLR) methods are the most suitable for determining migration rates of multiple centerlines over time. Both methods calculate migration rates using a regression approach, where LRR fits a straight line through all available centerline positions over time (figure E.4a). The key distinction of WLR (figure E.4b) is that it assigns weights to each data point based on the uncertainty in the centerline location, giving more influence to measurements with lower uncertainty. Given that multiple centerlines are detected in this research and their accuracy depends on the satellite imagery used, Sentinel or Landsat, the Weighted Linear Regression (WLR) method is chosen as the most appropriate approach (Himmelstoss et al., 2021).

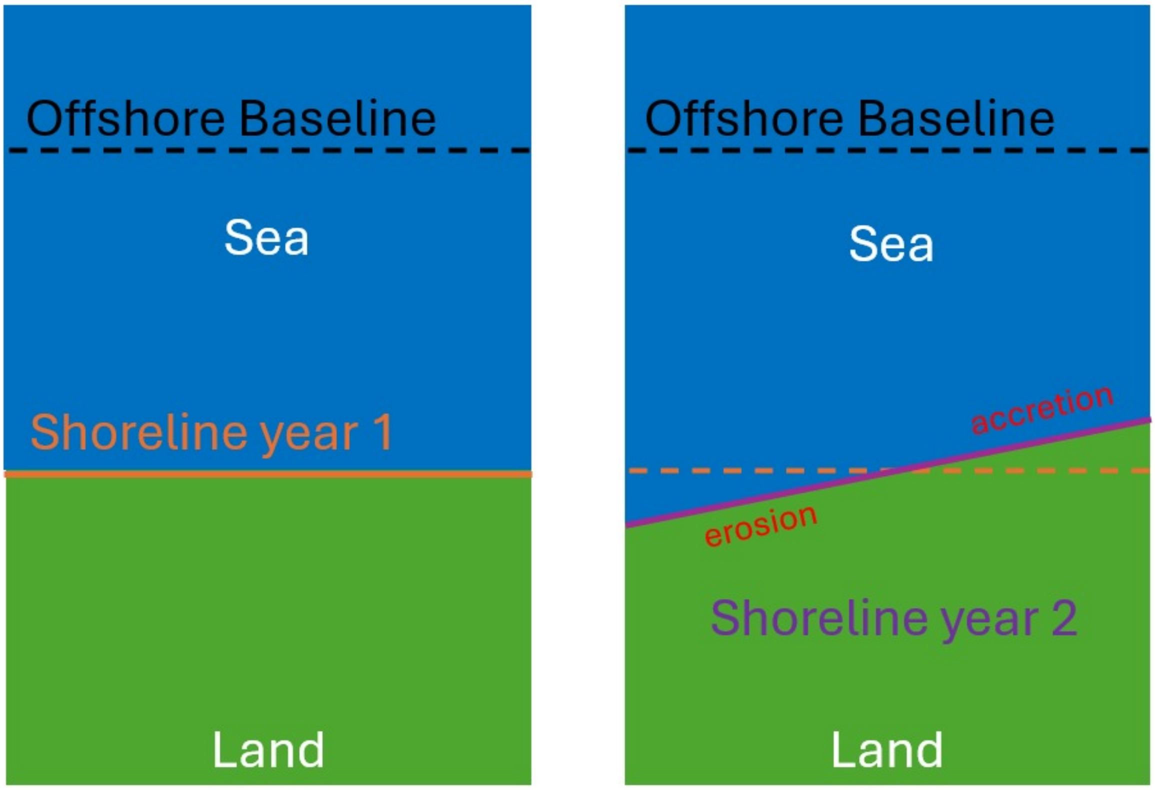

Figure E.1: Functionality of DSAS

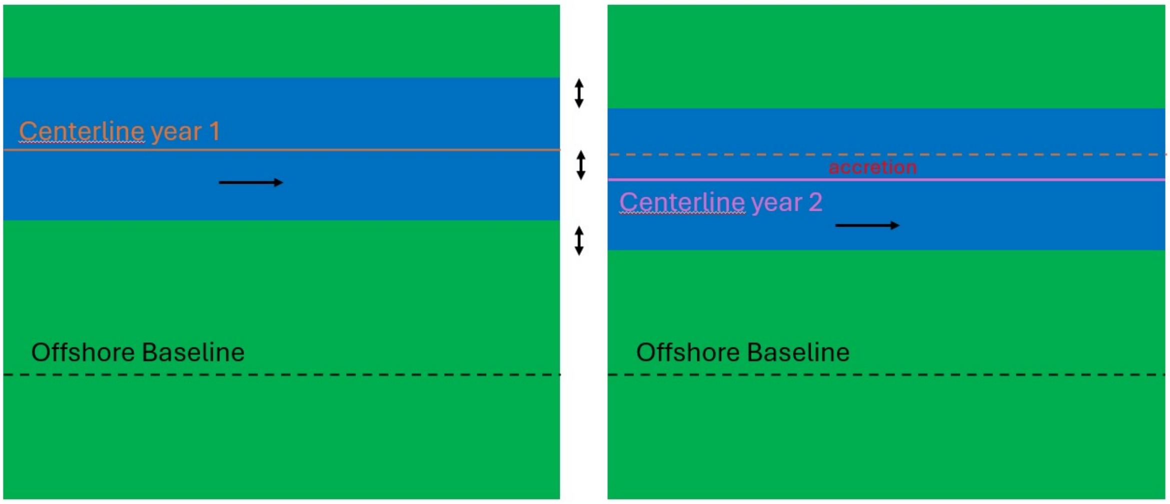

Figure E.2: DSAS applicability on rivers.

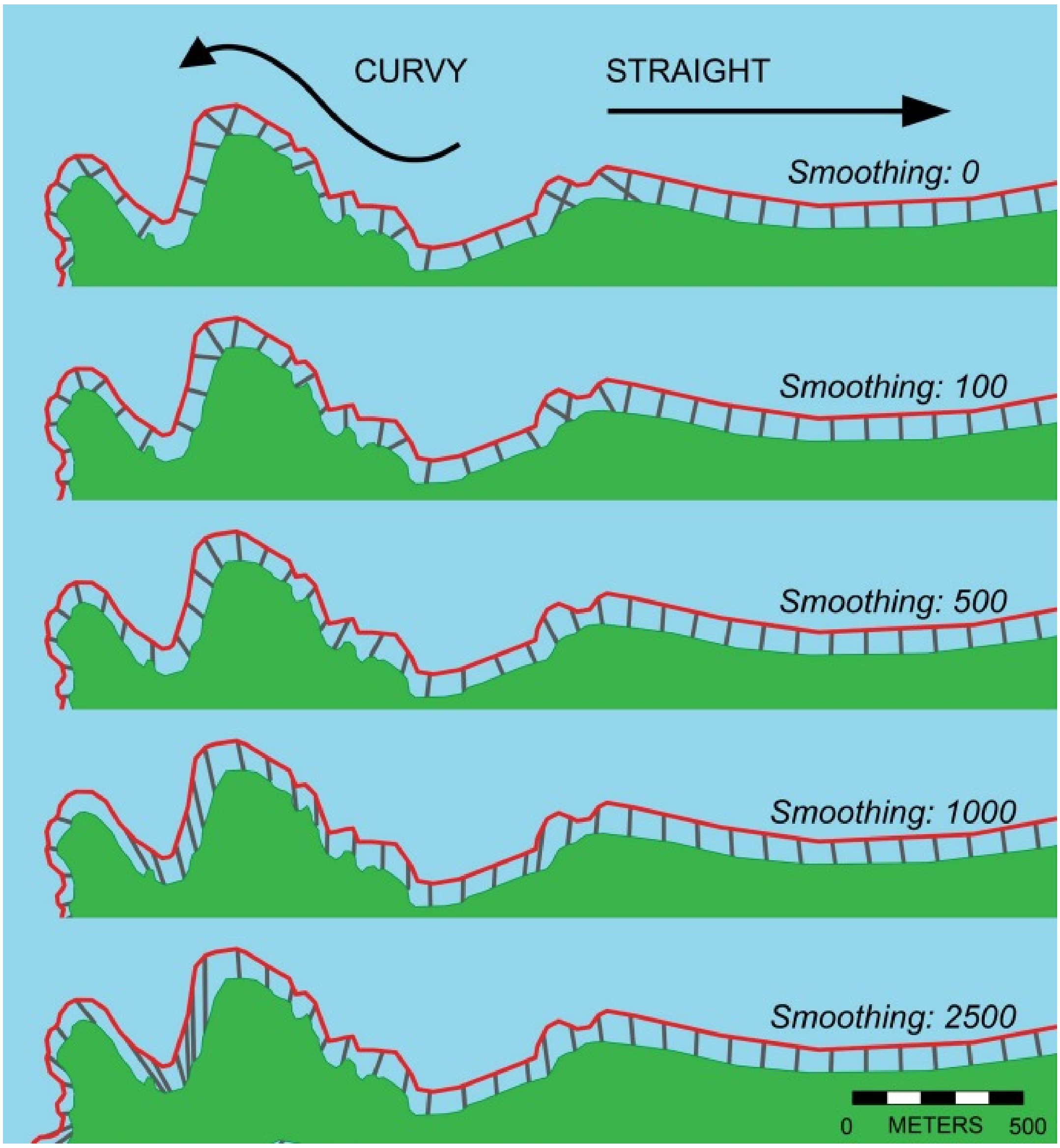

Figure E.3: Sample from the Cast Transects interface, illustrating the effect of smoothing distance on transect orientation for curved and straight coastlines. A smoothing value of 500 meters ensures orthogonal transects for accurate shoreline change measurement (Himmelstoss et al., 2021).

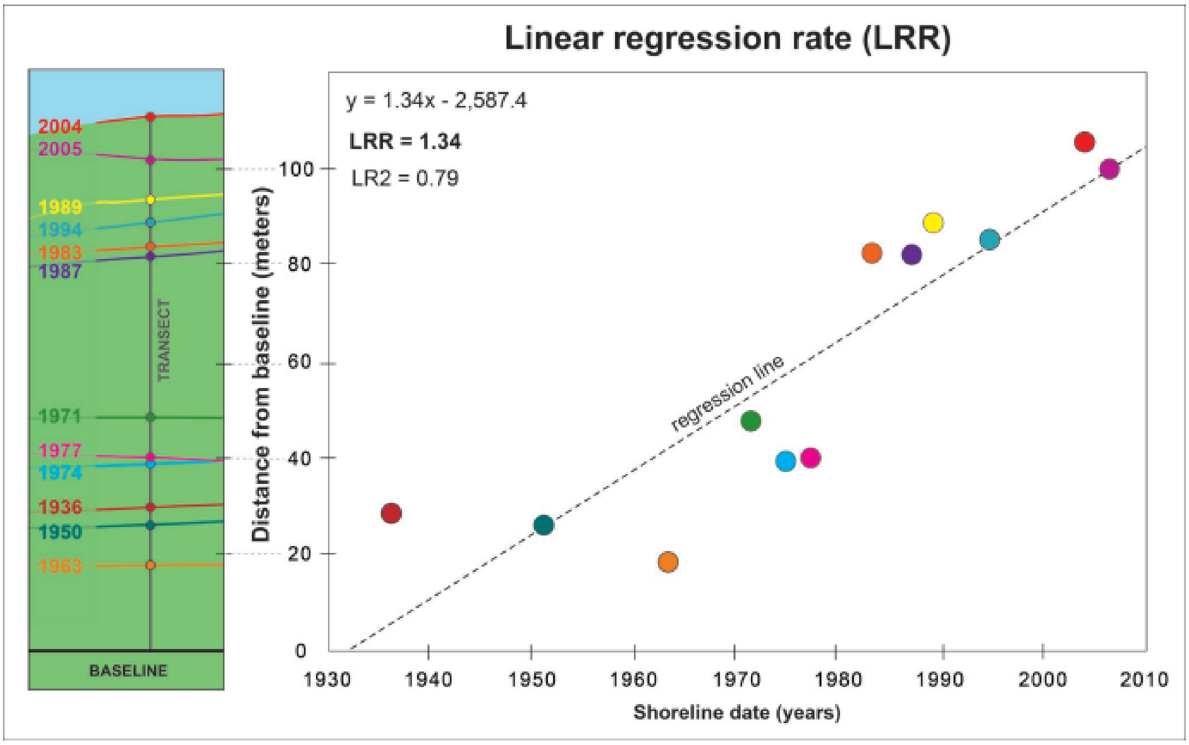

(a) Linear Regression Rate

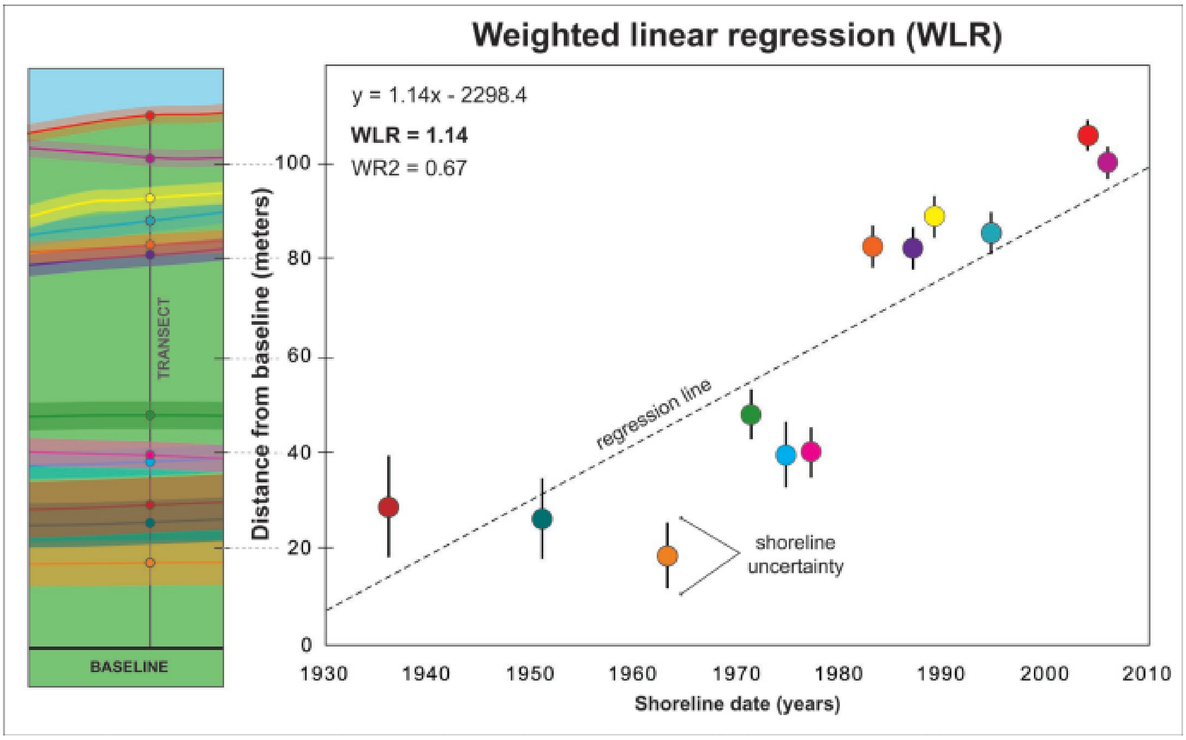

(b) Weighted Linear Regression

Figure E.4: Linear Regression Rate versus Weighted Linear Regression (Himmelstoss et al., 2021).

Table E.1: Comparison of Shoreline Change Measurement Methods in DSAS (Himmelstoss et al., 2021)

Category	Method	What it does	Pros	Cons	Best for	Class Breaks	Meaning of Class Breaks
Rate-Based Methods	**End Point Rate (EPR)**	Measures total shoreline change between the first and last shoreline, divided by years.	Simple, quick, effective for linear trends.	Ignores intermediate shorelines; inaccurate for non-linear trends.	When only two shorelines (start and end) are available.	MIN—(-0.25), -0.25—0.25, 0.25—MAX	Negative values = erosion, positive = accretion.
	Linear Regression Rate (LRR)	Fits a regression line through all shorelines and calculates change rate per year.	Uses multiple shorelines, more reliable trend estimation.	Assumes a linear trend, which may not always be valid.	When multiple shorelines are available and a trend is needed.	MIN—(-0.25), -0.25—0.25, 0.25—MAX	Similar to EPR but more robust due to multiple points.
	Weighted Linear Regression (WLR)	Like LRR but assigns more weight to shorelines with higher accuracy.	More precise when shoreline data has varying reliability.	Requires shoreline uncertainty values.	When shoreline data has different levels of accuracy.	MIN—(-0.25), -0.25—0.25, 0.25—MAX	Negative values = erosion, positive = accretion, both are adjusted for accuracy.
Distance-Based Methods	**Net Shoreline Movement (NSM)**	Measures total shoreline movement between the oldest and newest shoreline.	Simple, easy to interpret.	Doesn't provide a rate, making time-based comparisons difficult.	Measuring absolute shoreline movement rather than yearly rate.	MIN—(-10), -10—10, 10—MAX	Negative values = erosion, positive = accretion.
	Shoreline Change Envelope (SCE)	Measures max shoreline movement considering all shorelines.	Captures full range of shoreline variability.	Doesn't indicate if change is erosional or accretional.	Understanding full extent of shoreline dynamics.	MIN—50, 50—150, 150—MAX	Measures largest observed distance change (meters). High values = significant variation.

F

Weighted Linear Regression (WLR) statistics summary

Table F.1: Short-term Centerline Weighted Linear Regression (WLR) Summary Statistics (Thieler et al., 2003)

Metric	**2007–2017**	**2017–2019**	**2019–2021**	**2021–2023**	**2023–2024**
Total number of transects	1560	1730	1843	1841	1847
Average rate (m/yr)	-0.18	-0.66	0.15	-1.01	-0.49
Average confidence interval	19.77	46.25	15.80	12.63	16.48
Reduced number of independent transects (n_{red})	26.79	212.36	63.63	84.08	50.52
Uncertainty of average rate using n_{red}	3.82	3.17	1.98	1.38	2.32
Average rate with uncertainty (m/yr)	-0.18 ± 3.82	-0.66 ± 3.17	0.15 ± 1.98	-1.01 ± 1.38	-0.49 ± 2.32
Number of erosional transects	798	911	948	1006	941
Percent of transects erosional (%)	51.15	52.66	51.44	54.64	50.95
Statistically significant erosion (%)	9.29	2.20	13.78	5.49	14.89
Maximum erosion rate (m/yr)	-30.33	-71.56	-69.12	-76.79	-138.34
Transect ID (max erosion)	828	745	400	370	528
Average erosional rate (m/yr)	-4.30	-10.05	-11.15	-5.59	-13.65
Number of accretional transects	762	819	895	835	906
Percent of transects accretional (%)	48.85	47.34	48.56	45.36	49.05
Statistically significant accretion (%)	4.62	2.83	17.31	4.67	14.67
Maximum accretion rate (m/yr)	24.57	140.03	69.16	18.68	78.39
Transect ID (max accretion)	108	621	945	836	110
Average accretional rate (m/yr)	4.13	9.78	12.11	4.51	13.18

Table F.2: Short- and Long-term migration of the left Bank (Weighted Linear Regression (WLR) Summary Statistics) (Thieler et al., 2003)

Metric	**2007–2017**	**2017–2019**	**2019–2021**	**2021–2023**	**2023–2024**	**2007–2024**
Total number of transects	1718	1814	1844	1841	1850	1853
Average rate (m/yr)	-0.48	-1.09	0.12	0.03	-1.97	-0.22
Average confidence interval	20.33	26.99	16.52	11.90	19.00	2.72
Reduced number of independent transects (n_{red})	28.79	121.21	75.95	85.51	60.40	64.97
Uncertainty of average rate using n_{red}	3.79	2.45	1.89	1.29	2.44	0.34
Average rate with uncertainty (m/yr)	-0.48 ± 3.79	-1.09 ± 2.45	0.12 ± 1.89	0.03 ± 1.29	-1.97 ± 2.44	-0.22 ± 0.34
Number of erosional transects	893	961	930	879	1022	976
Percent of transects erosional (%)	51.98	52.98	50.43	47.75	55.24	52.67
Statistically significant erosion (%)	6.11	4.19	14.05	4.89	13.89	29.36
Maximum erosion rate (m/yr)	-33.06	-84.61	-75.59	-73.76	-140.80	-17.34
Transect ID (max erosion)	751	1783	401	368	528	528
Average erosional rate (m/yr)	-4.41	-9.42	-12.14	-5.70	-14.33	-3.89
Number of accretional transects	825	853	914	962	828	877
Percent of transects accretional (%)	48.02	47.02	49.57	52.25	44.76	47.33
Statistically significant accretion (%)	5.01	4.36	16.54	9.23	11.35	23.42
Maximum accretion rate (m/yr)	20.86	59.13	77.60	21.72	66.55	18.25
Transect ID (max accretion)	550	620	945	1209	172	946
Average accretional rate (m/yr)	3.76	8.29	12.59	5.27	13.30	3.87

Table F.3: Short- and Long-term migration of the left Bank (Weighted Linear Regression (WLR) Summary Statistics) (Thieler et al., 2003)

Metric	**2007–2017**	**2017–2019**	**2019–2021**	**2021–2023**	**2023–2024**	**2007–2024**
Total number of transects	1715	1807	1844	1841	1845	1852
Average rate (m/yr)	0.71	0.05	-0.04	-1.27	1.05	-0.37
Average confidence interval	21.48	22.82	15.68	11.84	17.92	2.71
Reduced number of independent transects (n_{red})	32.99	61.23	57.14	140.95	53.29	163.76
Uncertainty of average rate using n_{red}	3.74	2.92	2.07	1.00	2.45	0.21
Average rate with uncertainty (m/yr)	0.71 ± 3.74	0.05 ± 2.92	-0.04 ± 2.07	-1.27 ± 1.00	1.05 ± 2.45	-0.37 ± 0.21
Number of erosional transects	839	848	877	1101	844	926
Percent of transects erosional (%)	48.92	46.93	47.56	59.80	45.75	50.00
Statistically significant erosion (%)	8.45	2.99	12.91	9.07	11.33	29.00
Maximum erosion rate (m/yr)	-26.31	-86.91	-72.25	-60.49	-129.53	-19.09
Transect ID (max erosion)	827	1784	836	371	1329	365
Average erosional rate (m/yr)	-3.61	-8.79	-12.20	-5.63	-13.66	-4.13
Number of accretional transects	876	959	967	740	1001	926
Percent of transects accretional (%)	51.08	53.07	52.44	40.20	54.25	50.00
Statistically significant accretion (%)	6.06	5.64	18.06	6.03	15.66	27.11
Maximum accretion rate (m/yr)	31.59	63.24	70.69	44.06	103.93	17.46
Transect ID (max accretion)	769	622	625	369	111	946
Average accretional rate (m/yr)	4.85	7.87	10.98	5.21	13.46	3.39

G

KS-tests for precipitation duration

Table G.1: Results of KS-tests for different thresholds with pre- and post-2007 and pre- and post-2018 comparisons.

Threshold	Pre- vs. Post 2007			Pre- vs. Post 2018		
(mm/hr)	KS-statistic	p-value	Significance	KS-statistic	p-value	Significance
0	0.041	0.047	Yes	0.076	4.0e-6	Yes
1	0.041	0.26	No	0.088	5.1e-5	Yes
2	0.087	0.0033	Yes	0.12	2.0e-6	Yes
3	0.11	0.0011	Yes	0.12	9.0e-5	Yes
4	0.12	0.0026	Yes	0.070	0.11	No
5	0.11	0.037	Yes	0.063	0.36	No
6	0.13	0.032	Yes	0.10	0.068	No
7	0.11	0.21	No	0.070	0.60	No
8	0.14	0.065	No	0.10	0.31	No
9	0.18	0.046	Yes	0.17	0.039	Yes
10	0.14	0.27	No	0.13	0.27	No
11	0.17	0.15	No	0.11	0.57	No
12	0.21	0.12	No	0.12	0.61	No
13	0.17	0.35	No	0.11	0.86	No
14	0.16	0.55	No	0.096	0.96	No
15	0.16	0.62	No	0.099	0.96	No
16	0.12	0.90	No	0.074	1.0	No
17	0.14	0.85	No	0.098	0.99	No
18	0.15	0.83	No	0.093	1.0	No
19	0.073	1.0	No	0.10	0.99	No
20	0.092	1.0	No	0.12	0.98	No
30	0.085	1.0	No	0.13	1.0	No
40	0.20	0.99	No	0.23	1.0	No
50	0.25	0.99	No	-	-	No Data
60	0.50	0.93	No	-	-	No Data
70	-	-	No Data	-	-	No Data
80	-	-	No Data	-	-	No Data
90	-	-	No Data	-	-	No Data
100	-	-	No Data	-	-	No Data

H

Detailed hotspot maps

This appendix provides more detailed images of the different hotspot maps. To offer a more comprehensive understanding, the river is divided into 5 segments, which are illustrated in figure H.1.

The four types of hotspot maps, long-term migration rates, short-term migration rates, long-term widening, and short-term widening hotspot maps, are presented below. Figures H.2 to H.6 correspond to the long-term migration rate hotspot maps. Figures H.7 to H.11 correspond to the short-term migration rate hotspot maps. Figures H.12 to H.16 correspond to the long-term widening rate hotspot maps. Finally, figures H.17 to H.21 correspond to the short-term widening rate hotspot maps.

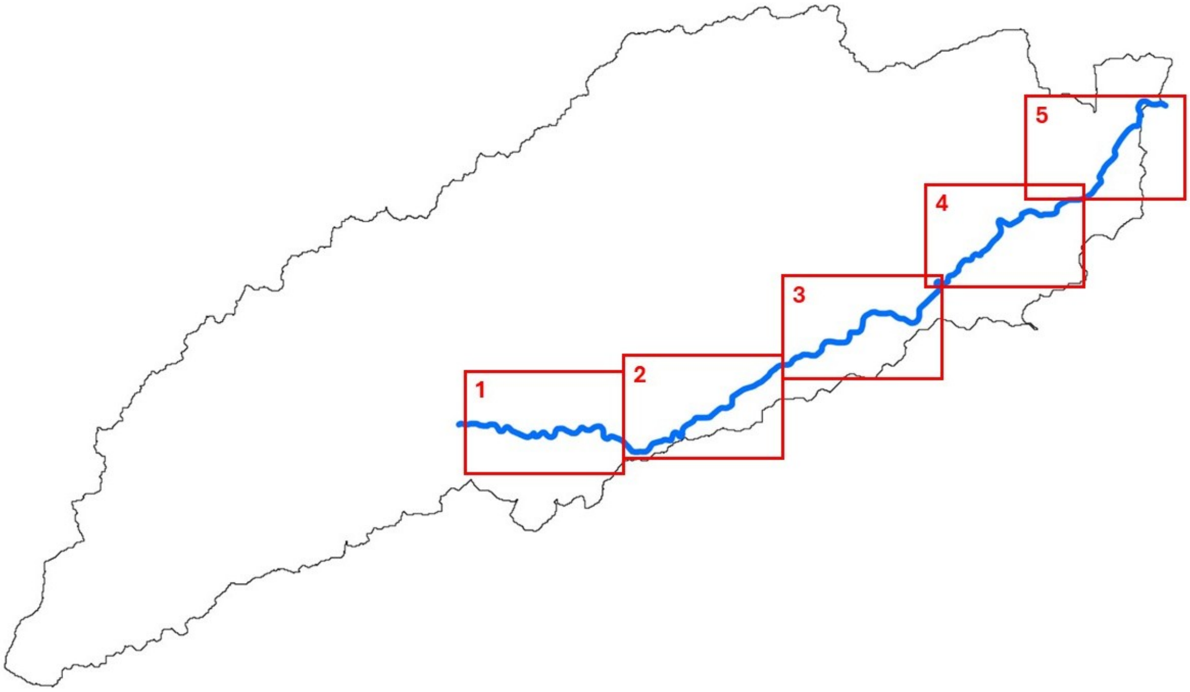

Figure H.1: An overview of the segments (1 through 5) used to present the hotspot maps in a clear and detailed manner.

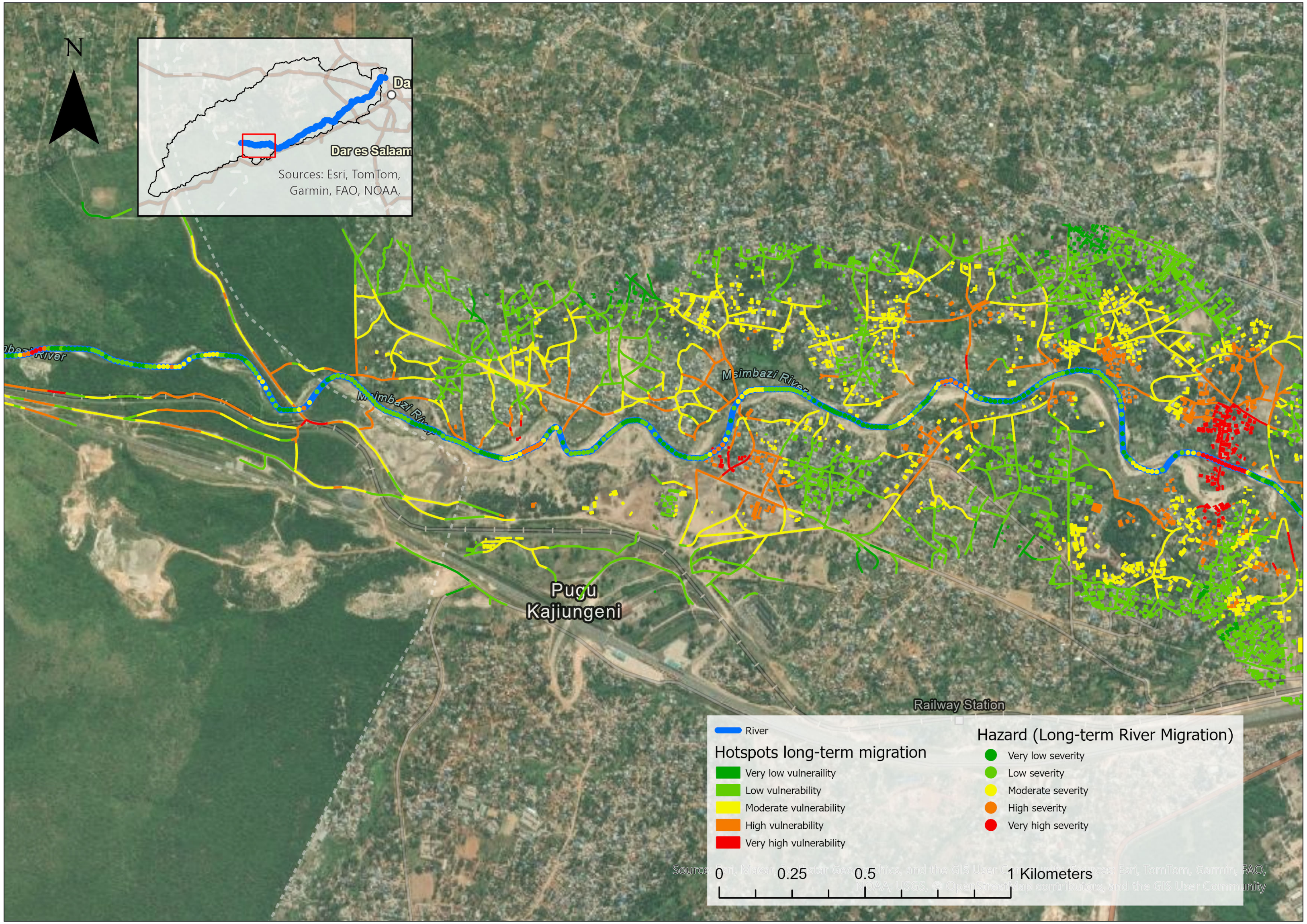

Figure H.2: Hotspot map as a result of long-term (2007-2024) river migration for segment 1 (An overview of all segments is given in figure H.1).

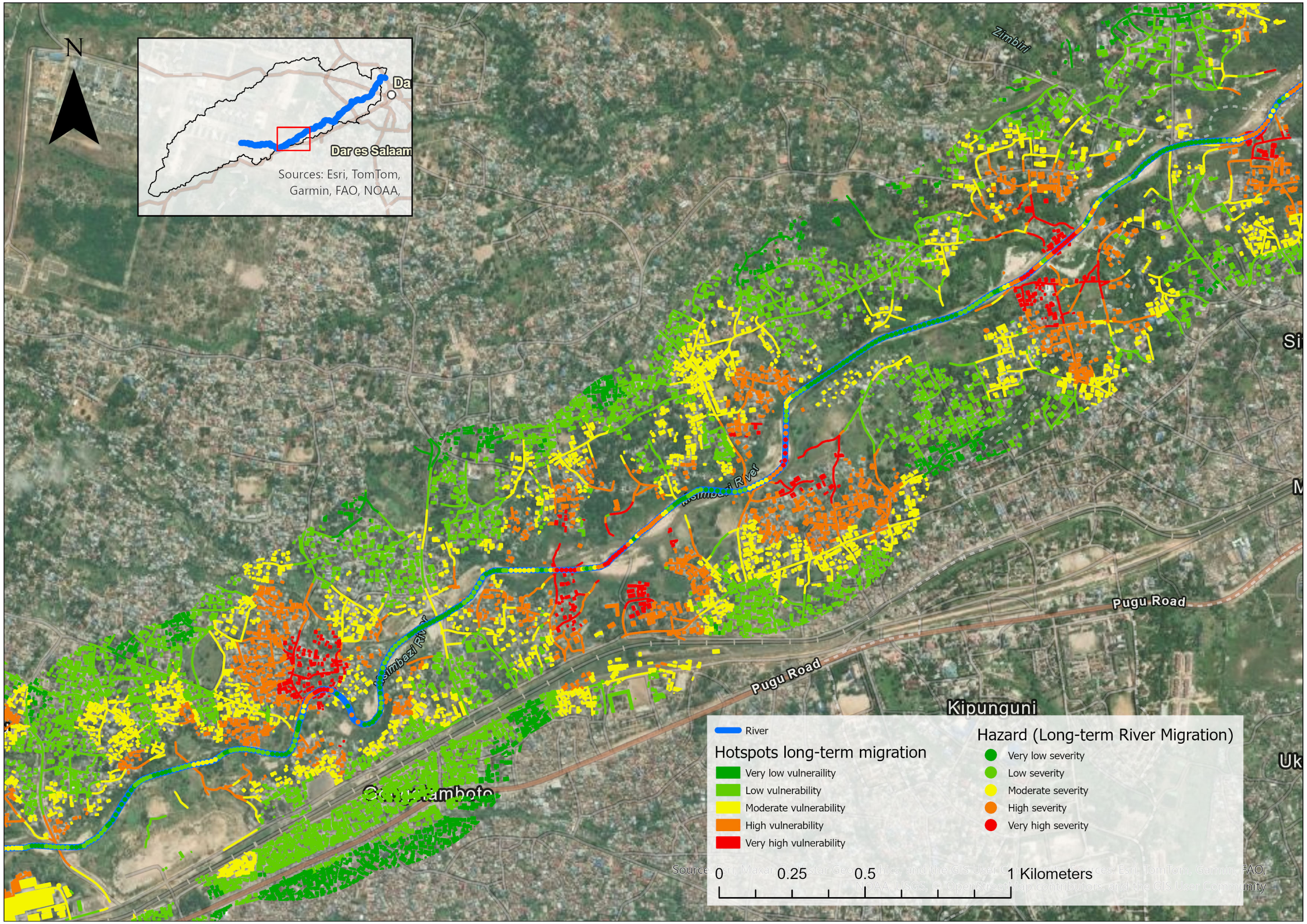

Figure H.3: Hotspot map as a result of long-term (2007-2024) river migration for segment 2 (An overview of all segments is given in figure H.1).

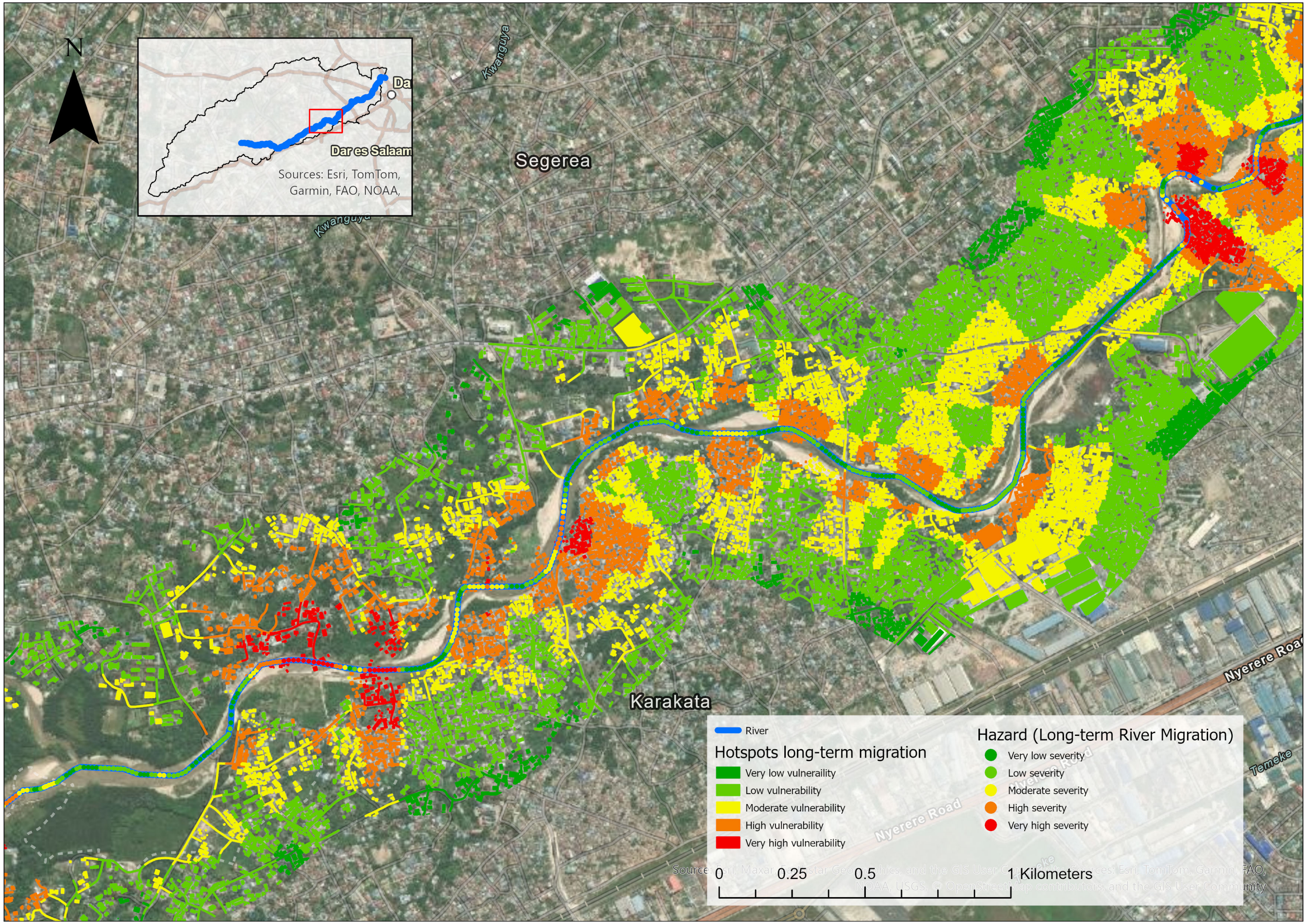

Figure H.4: Hotspot map as a result of long-term (2007-2024) river migration for segment 3 (An overview of all segments is given in figure H.1).

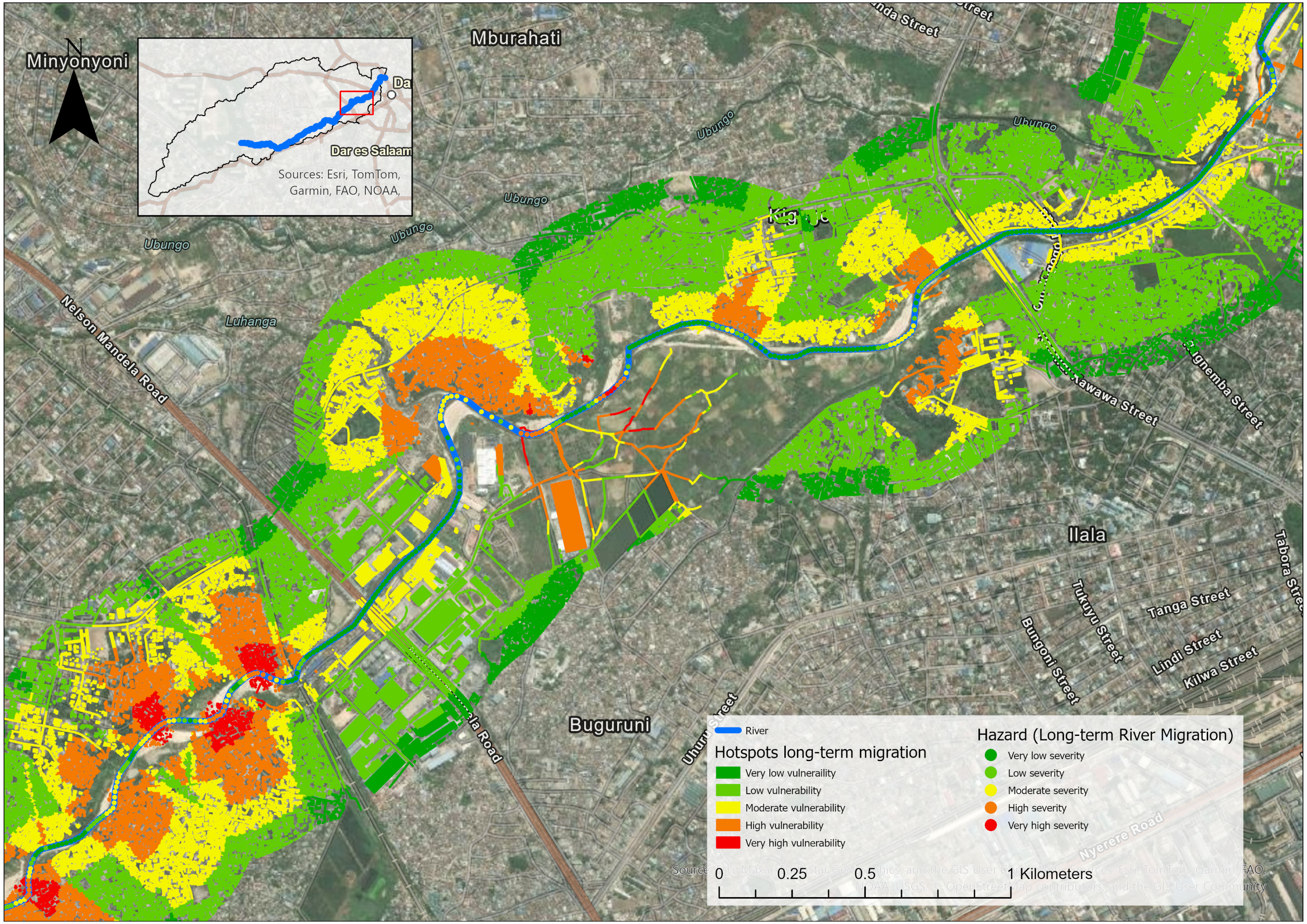

Figure H.5: Hotspot map as a result of long-term (2007-2024) river migration for segment 4 (An overview of all segments is given in figure H.1).

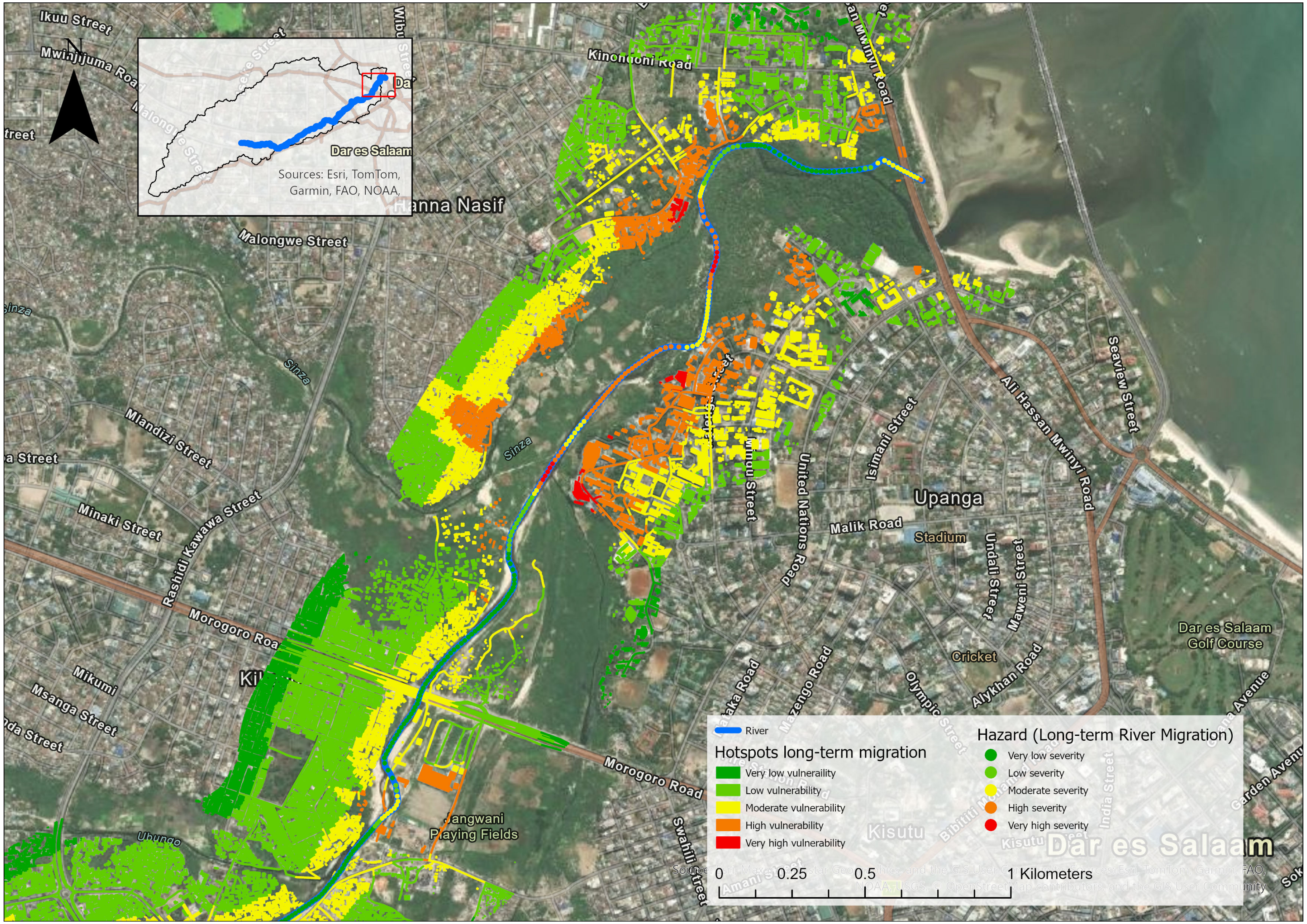

Figure H.6: Hotspot map as a result of long-term (2007-2024) river migration for segment 5 (An overview of all segments is given in figure H.1).

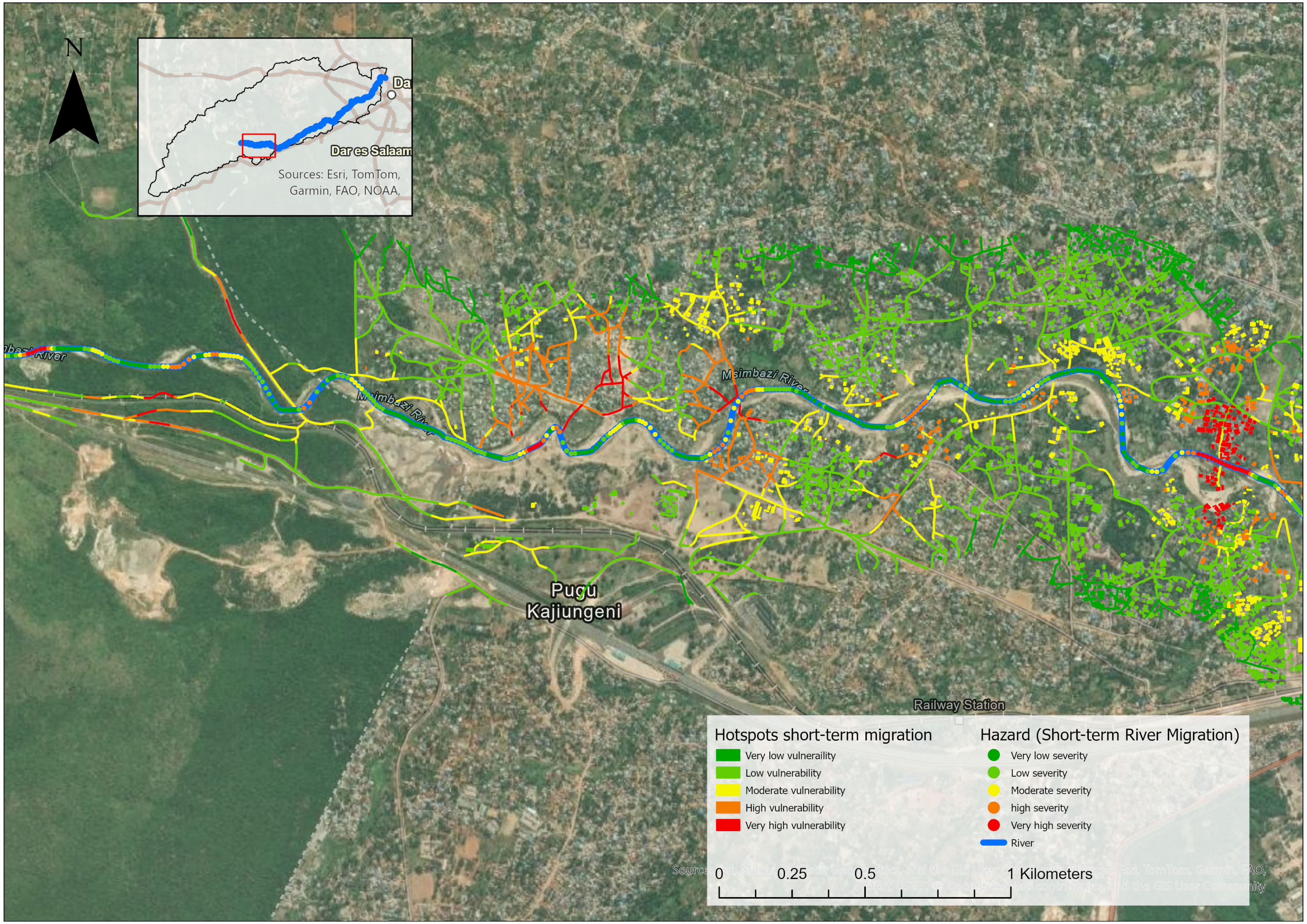

Figure H.7: Hotspot map as a result of short-term (2020-2024) river migration for segment 1 (An overview of all segments is given in figure H.1).

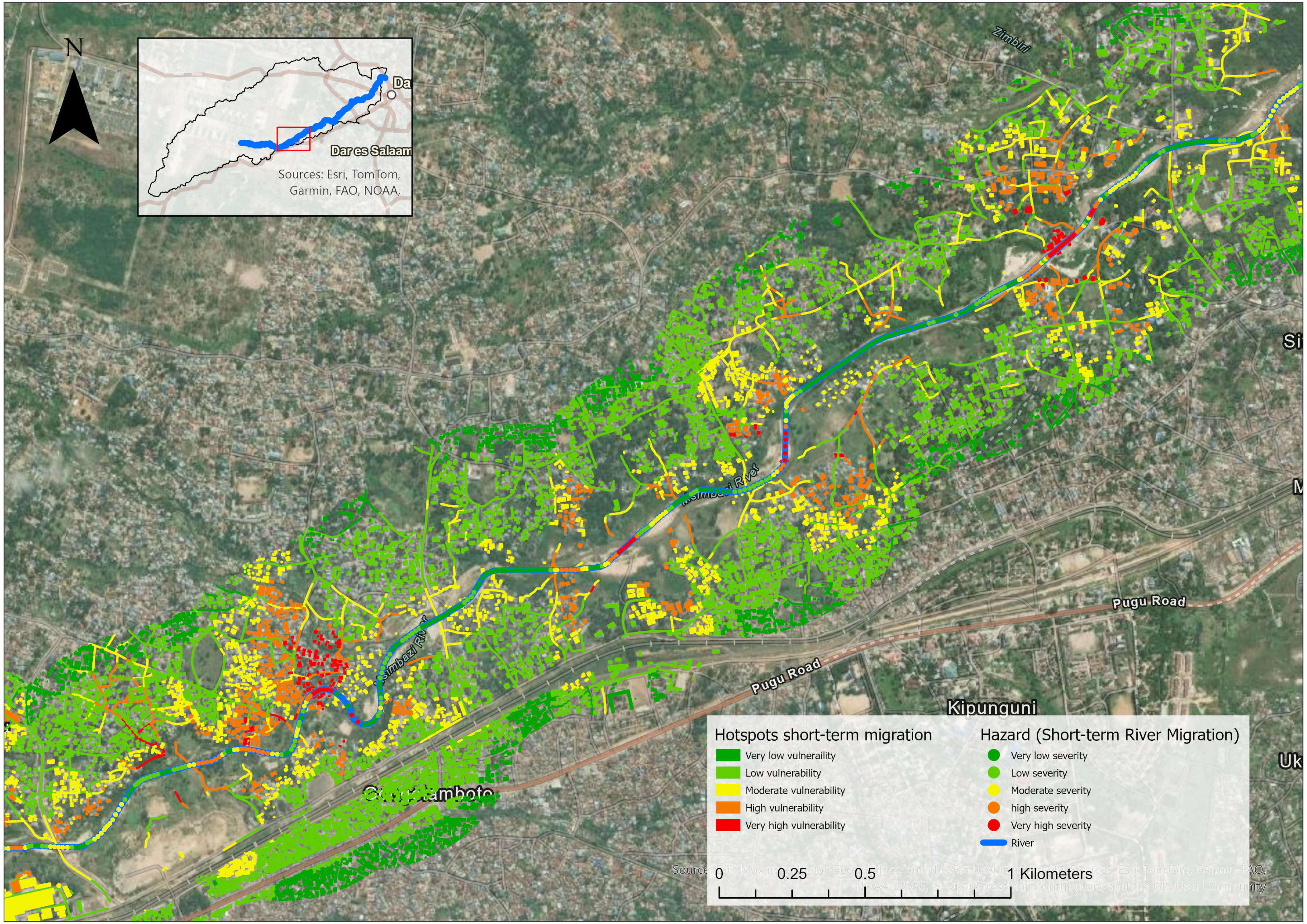

Figure H.8: Hotspot map as a result of short-term (2020-2024) river migration for segment 2 (An overview of all segments is given in figure H.1).

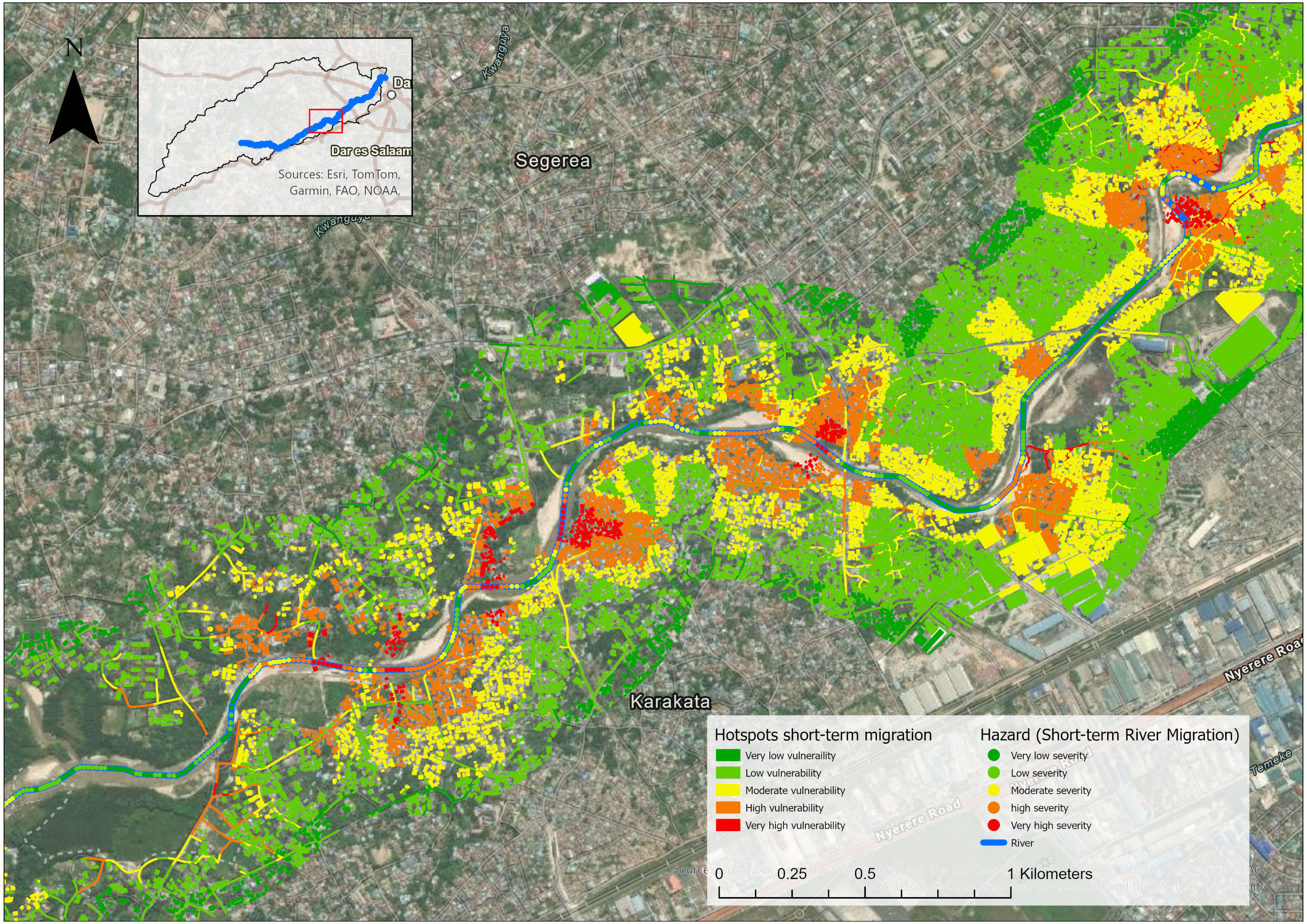

Figure H.9: Hotspot map as a result of short-term (2020-2024) river migration for segment 3 (An overview of all segments is given in figure H.1).

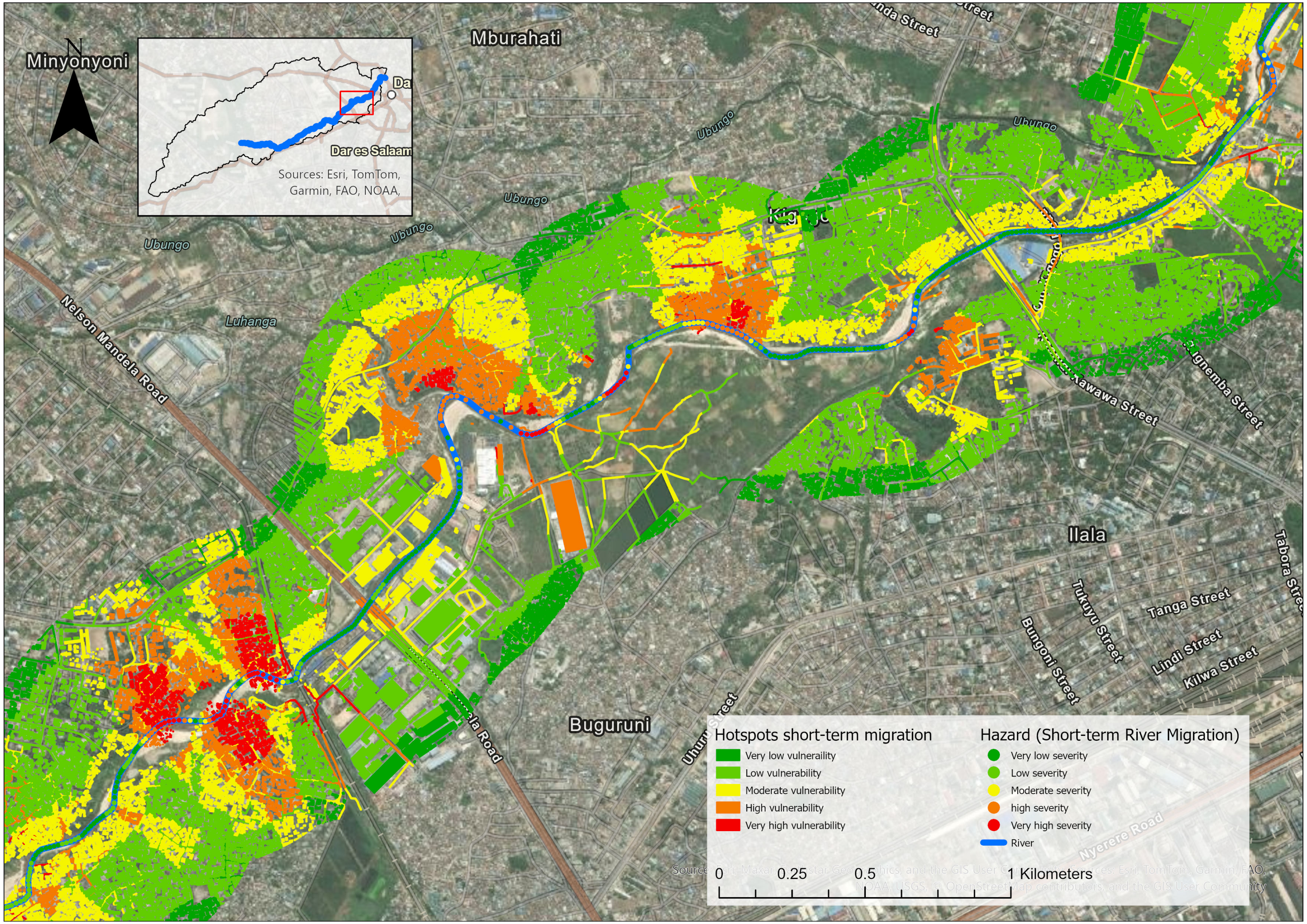

Figure H.10: Hotspot map as a result of short-term (2020-2024) river migration for segment 4 (An overview of all segments is given in figure H.1).

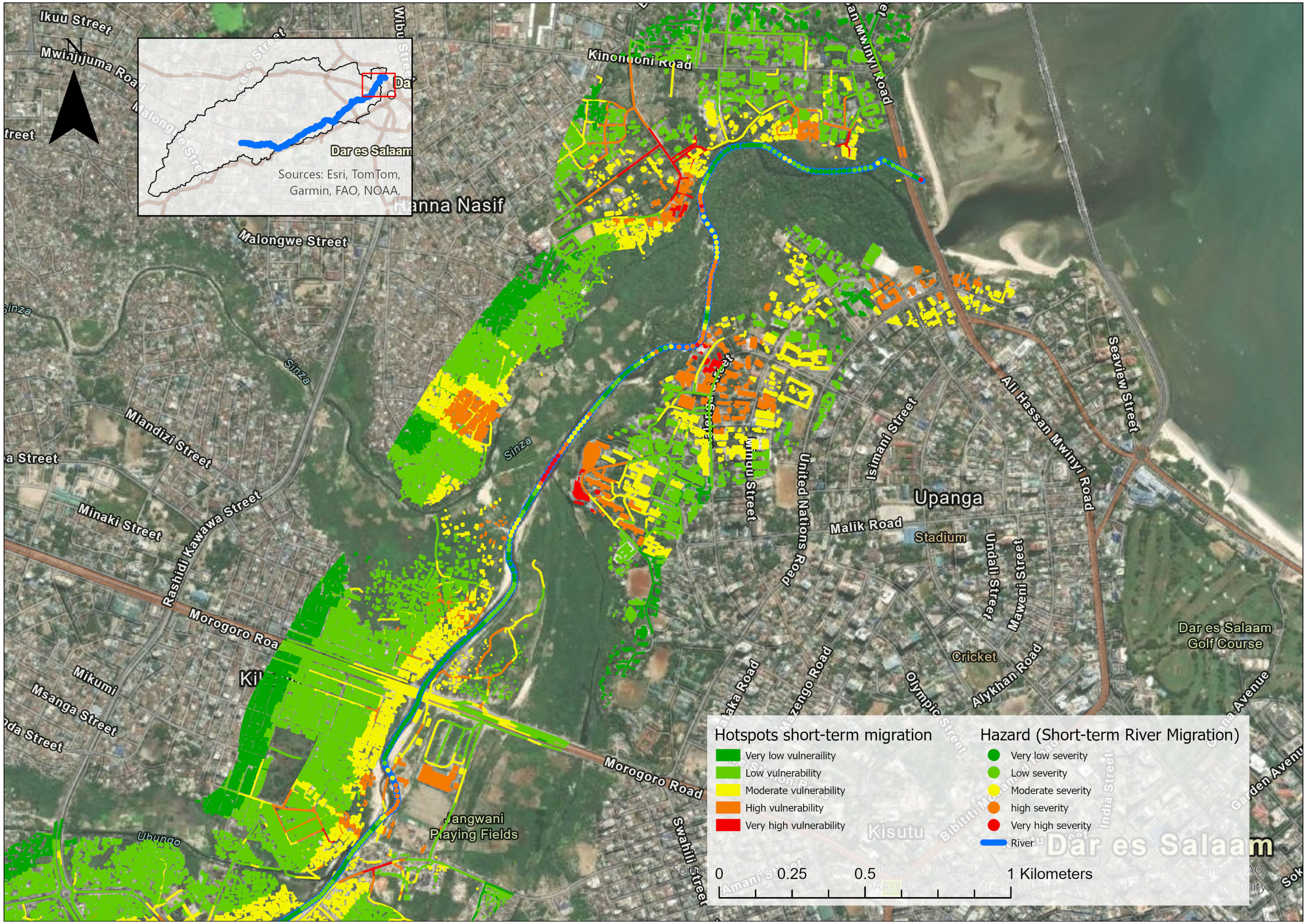

Figure H.11: Hotspot map as a result of short-term (2020-2024) river migration for segment 5 (An overview of all segments is given in figure H.1).

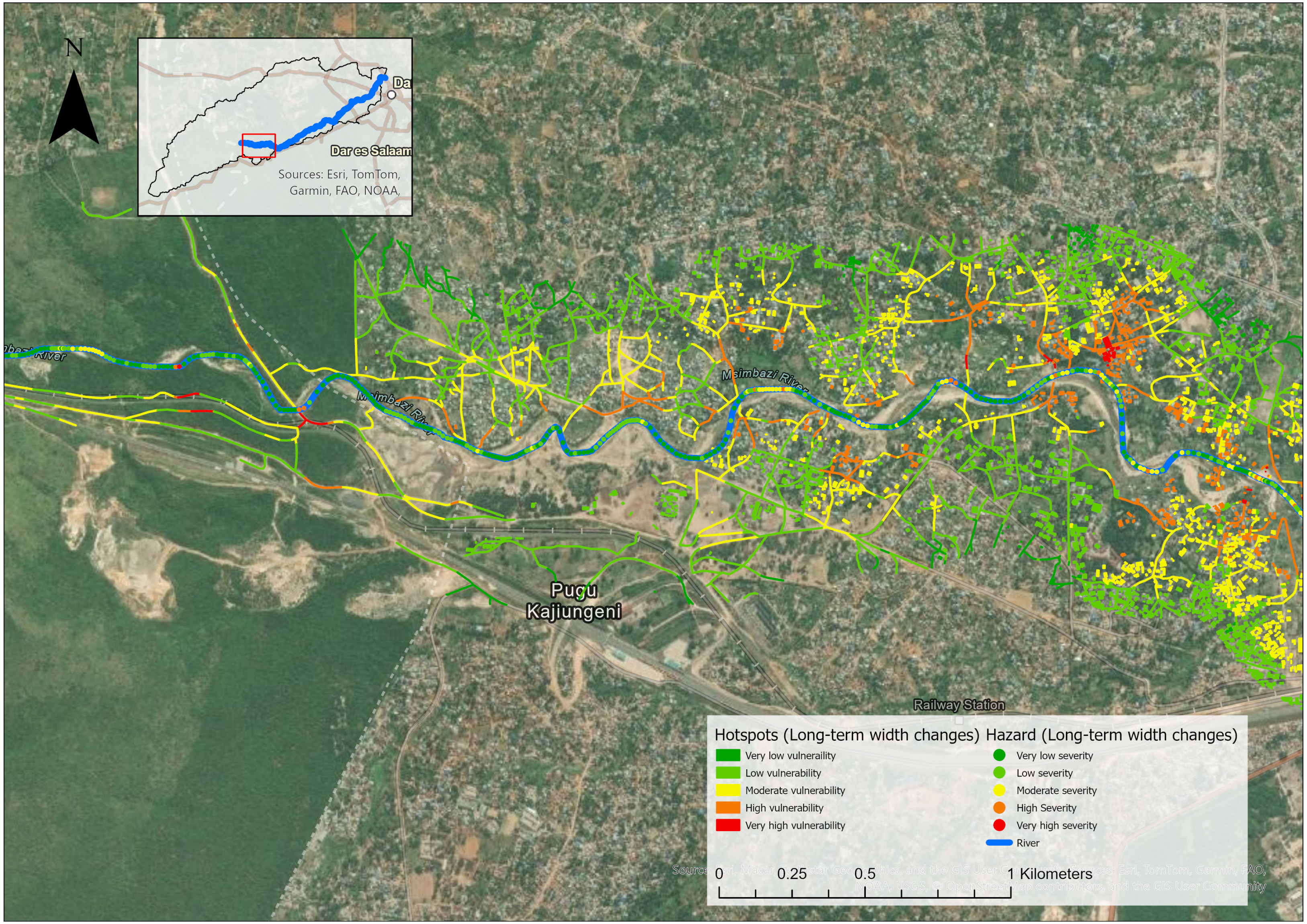

Figure H.12: Hotspot map as a result of long-term (2007-2024) river widening for segment 1 (An overview of all segments is given in figure H.1).

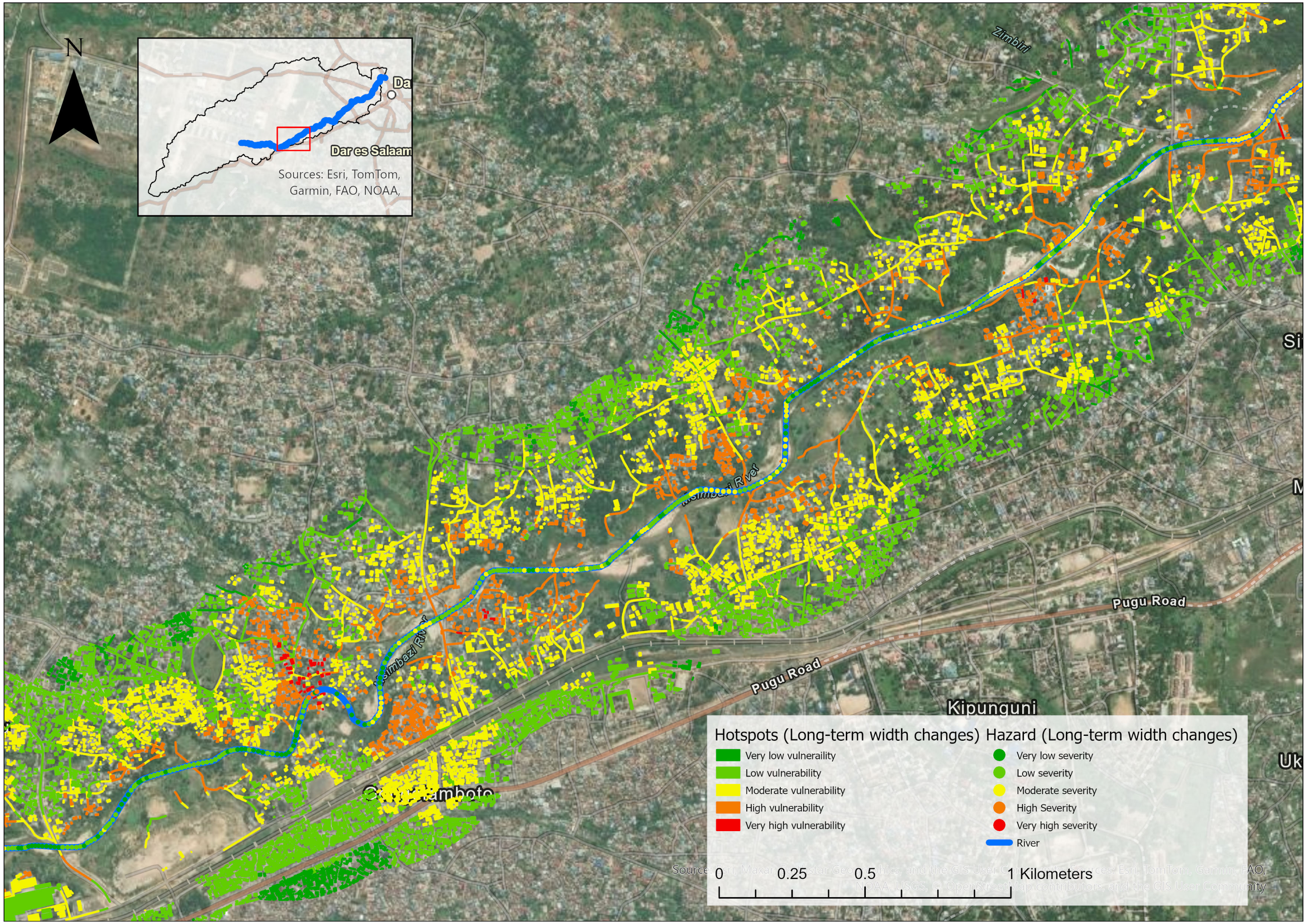

Figure H.13: Hotspot map as a result of long-term (2007-2024) river widening for segment 2 (An overview of all segments is given in figure H.1).

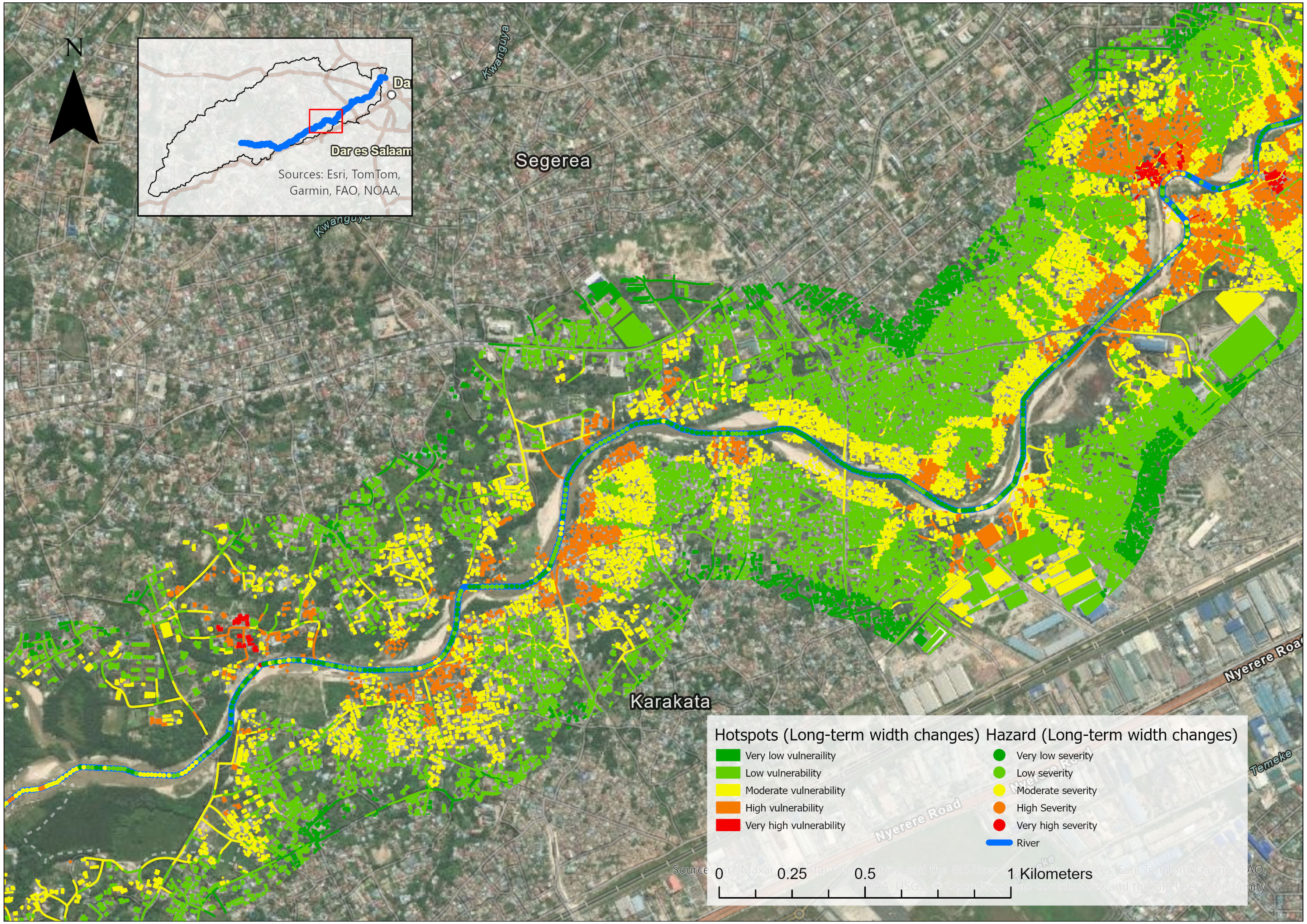

Figure H.14: Hotspot map as a result of long-term (2007-2024) river widening for segment 3 (An overview of all segments is given in figure H.1).

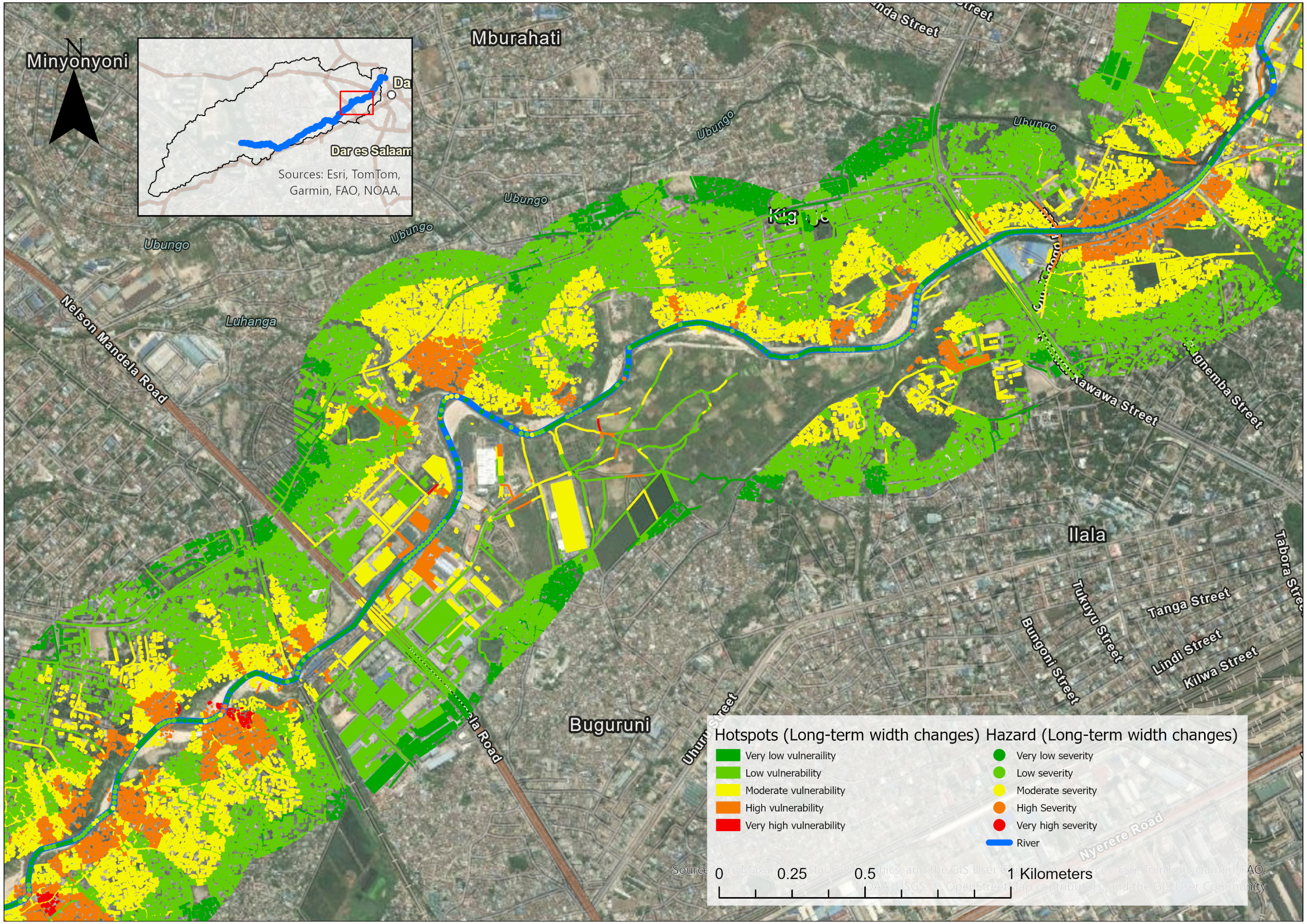

Figure H.15: Hotspot map as a result of long-term (2007-2024) river widening for segment 4 (An overview of all segments is given in figure H.1).

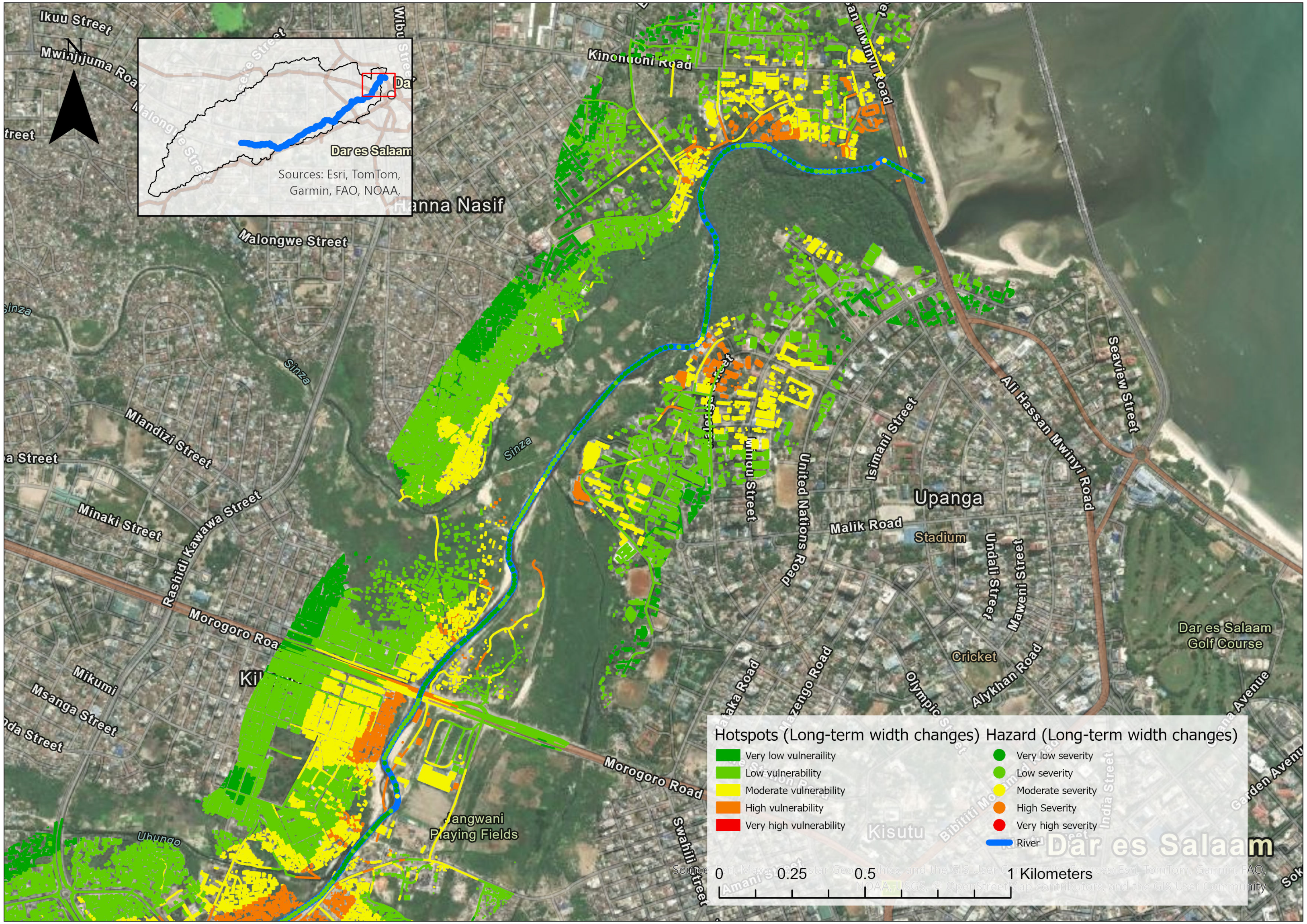

Figure H.16: Hotspot map as a result of long-term (2007-2024) river widening for segment 5 (An overview of all segments is given in figure H.1).

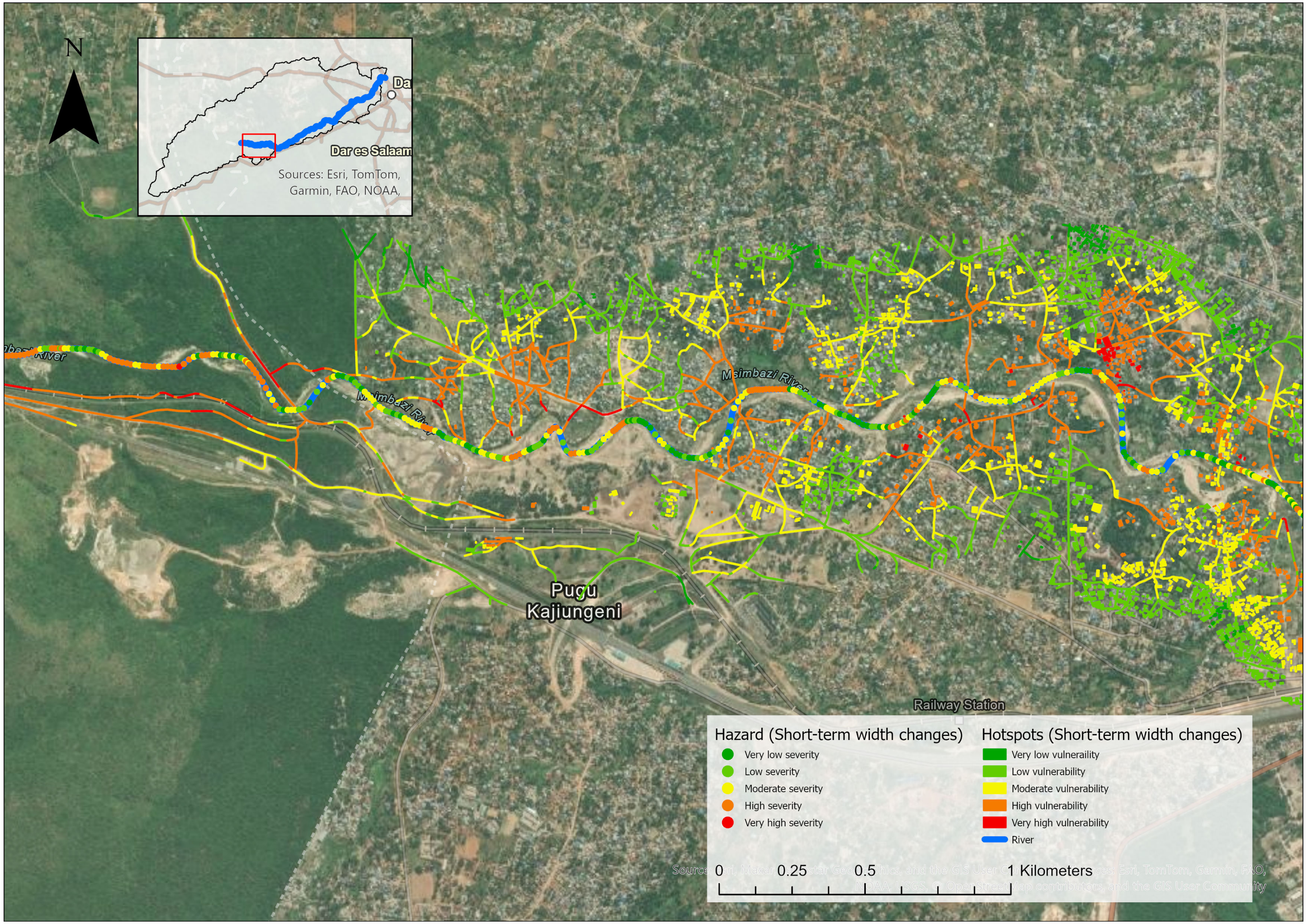

Figure H.17: Hotspot map as a result of short-term (2020-2024) river widening for segment 1 (An overview of all segments is given in figure H.1).

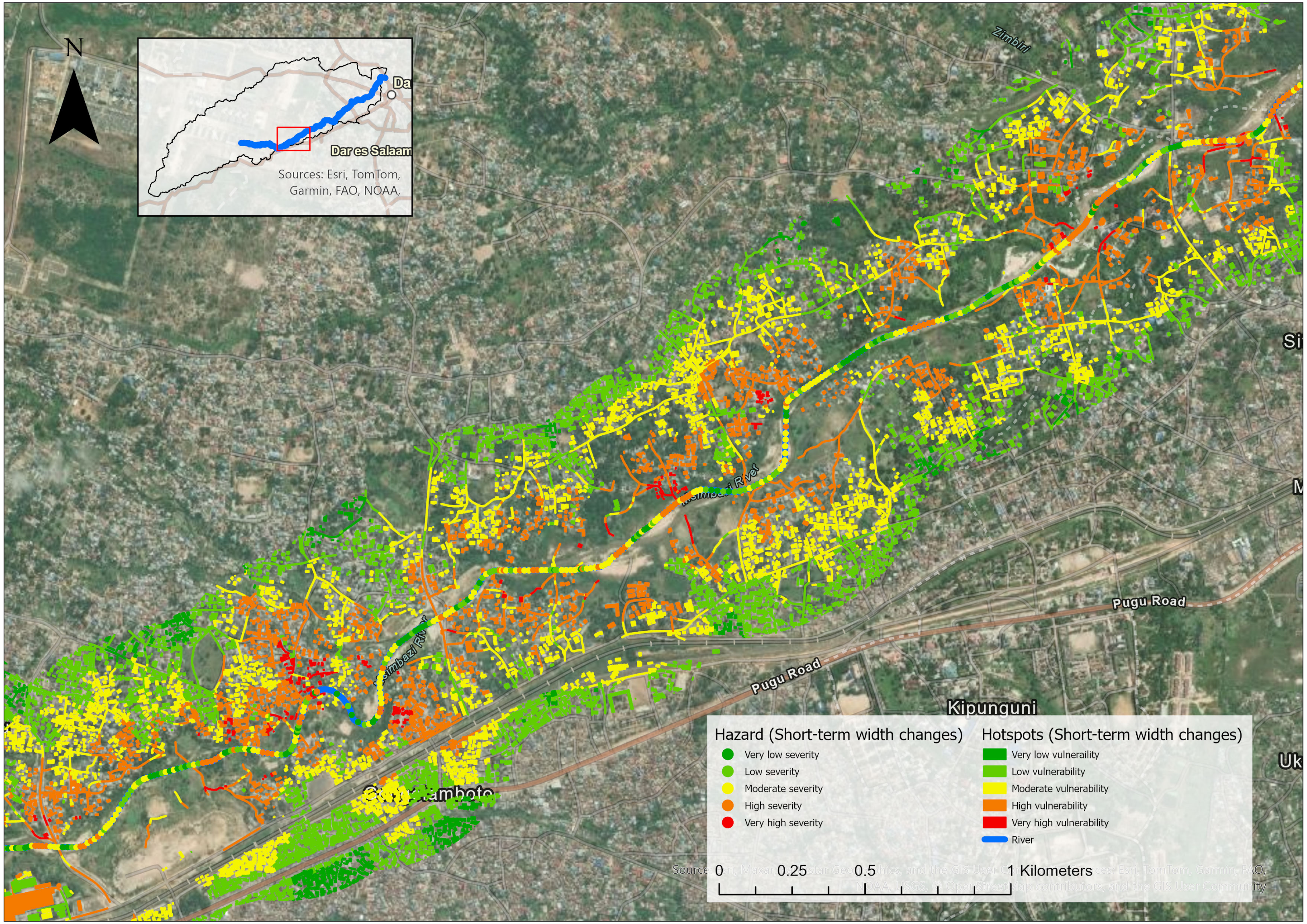

Figure H.18: Hotspot map as a result of short-term (2020-2024) river widening for segment 2 (An overview of all segments is given in figure H.1).

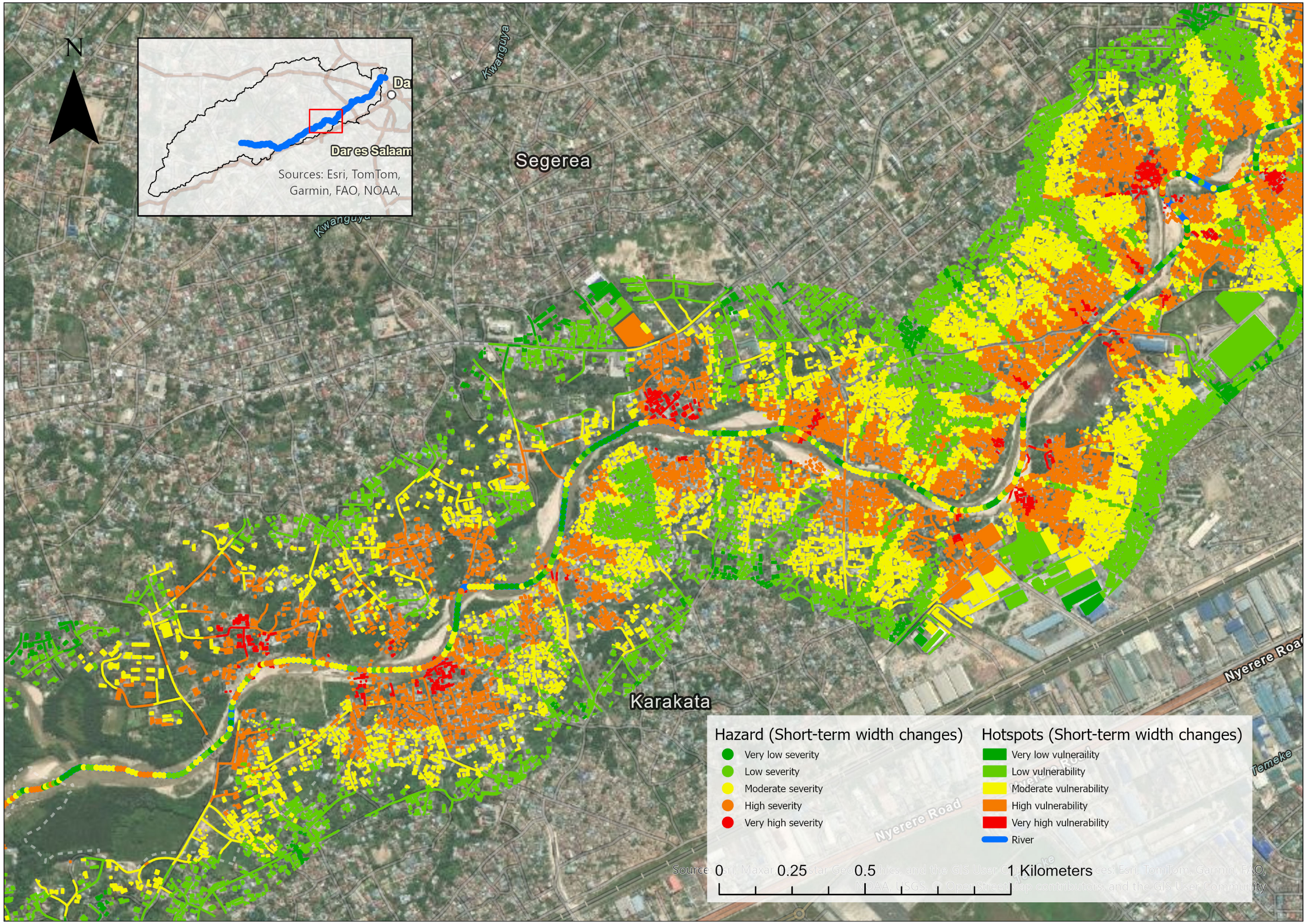

Figure H.19: Hotspot map as a result of short-term (2020-2024) river widening for segment 3 (An overview of all segments is given in figure H.1).

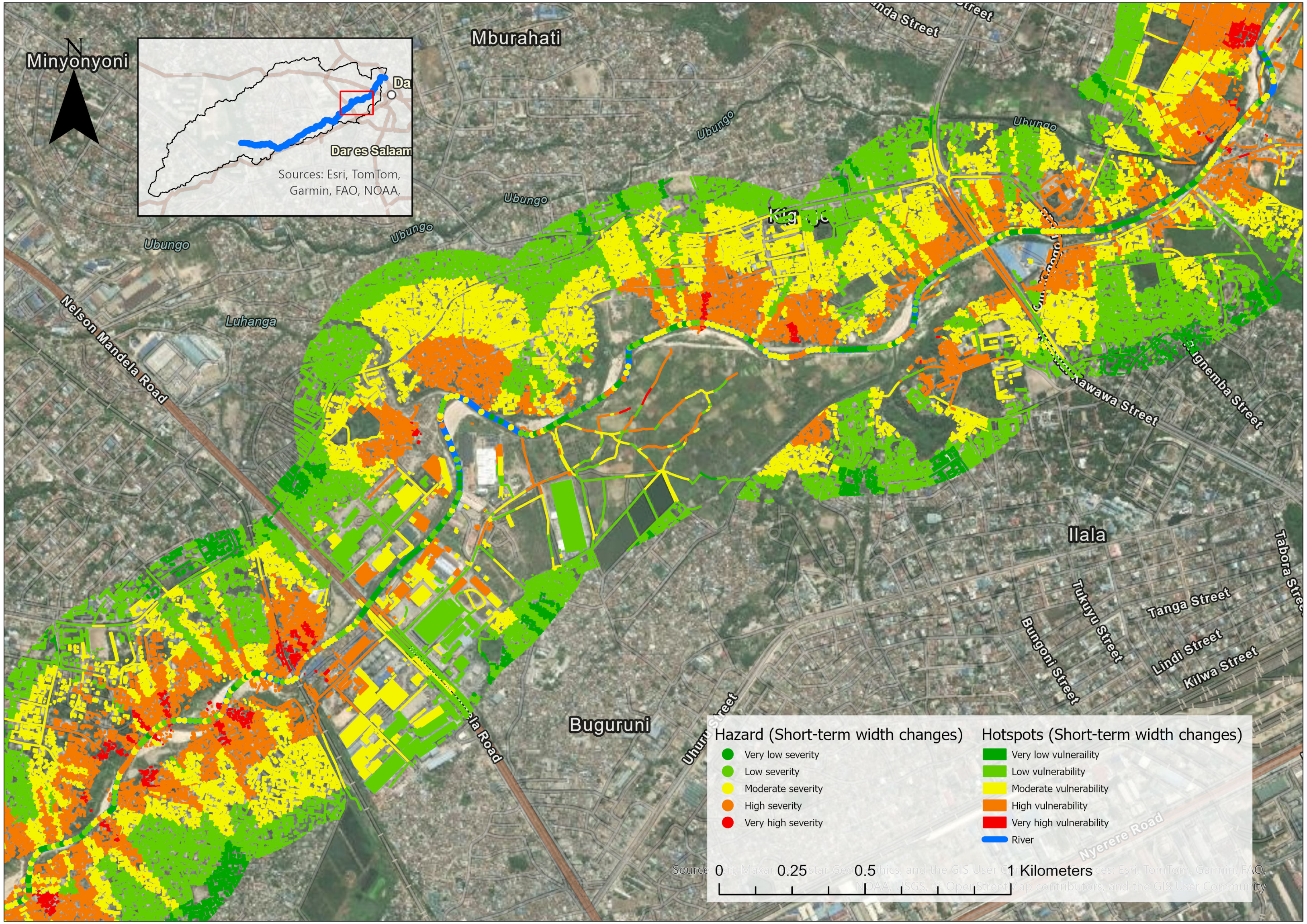

Figure H.20: Hotspot map as a result of short-term (2020-2024) river widening for segment 4 (An overview of all segments is given in figure H.1).

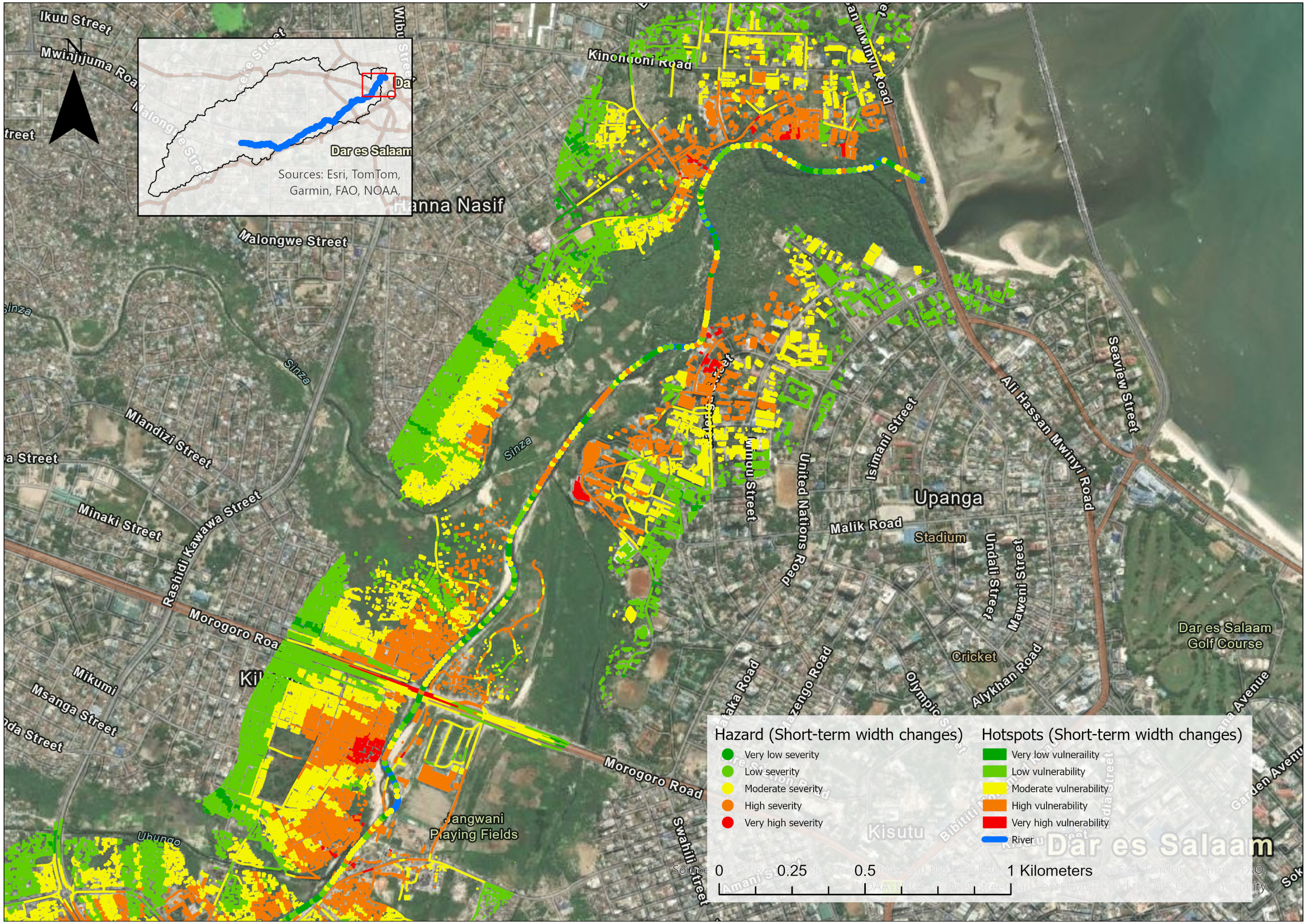

Figure H.21: Hotspot map as a result of short-term (2020-2024) river widening for segment 5 (An overview of all segments is given in figure H.1).